UNIVERSITY OF CALIFORNIA
RIVERSIDE

A Hybrid Density Functional Theory for Solvation and Solvent-Mediated Interactions

A Dissertation submitted in partial satisfaction
of the requirements for the degree of

Doctor of Philosophy

in

Chemical and Environmental Engineering

by

Zhehui Jin

March 2012

Dissertation Committee:
Dr. Jianzhong Wu, Chairperson
Dr. Ashok Mulchandani
Dr. David Kisailus

The Dissertation of Zhehui Jin is approved:

_____

_____

_____

Committee Chairperson

University of California, Riverside

Acknowledgements

This thesis is the result of five years of work whereby I have been accompanied and supported by many people. I would like to express the most profound appreciation to my advisor, Prof. Jianzhong Wu. He led me to the field of statistical thermodynamics and guided me to define research problems and solve these problems through theoretical approaches. I have been greatly benefited from his wide knowledge and logical way of thinking and gained fruitful achievements during my Ph.D. study. His enthusiasms on research and passion for providing high-quality research works have made a deep impression on me.

I am deeply grateful to Dr. Yiping Tang, Prof. Zhengang Wang, Dr. De-en Jiang, Dr. Dong Meng, and Dr. Douglas Henderson who have assisted my research work and led me to different exciting fields of study. I would also thank for Dr. Zhidong Li and Dr. Tao Jiang for significant technical support in my early stage of Ph.D. study. I would also thank for Dr. Shuangliang Zhao for insightful discussions during everyday research works. His passion and strong motivation for research inspired me in my Ph.D. study. Special thanks are given to Profs. Ashok Mulchandani and David Kisailus for helping me in the qualified exam and dissertation defense.

I sincerely appreciate the nonstop support and encouragement from my parents during these years. I would like to thank Ms. Qingyan Jin for accompanying me, encouraging me and supporting me in the study and research.

The text of this dissertation, in part or in full, is a reprint of the material as it appears in Physical Review E (Volume 84, Issue 4, Page 041805, Oct 2010) , Journal of Physical Chemistry B (Volume 115, Issue 6, Page 1450, Jan 2011), Journal of Physical Chemistry B (Volume 115, Issue 21, Page 6971, May 2011), Journal of Chemical Physics (Volume 134, Issue 17, Page 174702, May 2011). This thesis work is financially sponsored by the US Department of Energy (DOE) (DE-FG02-06ER46296), the National Science Foundation (NSF-CBET-0852353; NSF-CMMI-005400), and the National Institute of Health (R21-AI077532). This work utilizes supercomputer from the National Energy Research Scientific Computing Center (NERSC).

ABSTRACT OF THE DISSERTATION

A Hybrid Density Functional Theory for Solvation and Solvent-Mediated Interactions

by

Zhehui Jin

Doctor of Philosophy
Graduate Program in Chemical and Environmental Engineering
University of California, Riverside, March 2012
Professor Jianzhong Wu, Chairperson

Recent years have witnessed a renewed interest in statistical mechanics of solvation directed toward a better understanding of hydration and water-mediated interactions from a molecular perspective. A good understanding of aqueous solvation is essential not only in solution thermodynamics but also for studying functions and interfacial properties of nanostructured materials in a solution environment. Such knowledge is also indispensable for understanding biological processes *in vivo* and *in vitro*.

While conventional theories of solvation are mostly based on a continuous representation of the solvent, due to the lack of fundamental understanding of the properties of solvent molecules near solute surface, the materials fabrication and self-assembly of functional biomacromolecules often rely on costly and time-consuming "trial-and-error" approaches. The objective of this Ph.D. research is to provide a

theoretical framework for efficient investigation of the microscopic structure and thermodynamic properties of flexible and rigid molecules in solution through a unified density functional theory (DFT) and a hybrid method incorporating molecular simulations. Toward that end, I have applied the DFT to the study of the microscopic structure and thermodynamic properties of polymers and polyelectrolytes in in confined geometry. I have tested the numerical performance of the DFT with molecular simulations and scaling analysis and examined the effects of packing densities, the curvature of confinement, the degree of polymerization, the salt concentration and valence on the properties and microscopic structure of confined polymers and polyelectrolytes. In addition, I developed a hybrid method combining the molecular simulations and used the DFT to study the microscopic structure and thermodynamic properties of complex systems. While molecular simulation can provide the microscopic structure, the DFT can connect the microscopic structure to the thermodynamic properties through accurate free energy functional. This efficient hybrid method was extend to the study of colloidal interactions and potential of mean force underlying “lock-and-key” interactions in a solution environment and to ion solvation in water. The numerical performance of hybrid method is very good comparing to molecular simulations, while the new method drastically reduces the calculation time. Furthermore, I studied the solvent distribution and behavior near a solute ranging from microscopic to macroscopic scales, which is closely related to the understanding of hydrophobic phenomena and fabrication of superhydrophobic materials. Lastly, the solvation free energy of

nanoparticles and the shape effect on the nanoparticle solvation were investigated through morphological thermodynamic with negligible computational costs.

Accomplishments from this work contribute toward a better understanding of solvation and solvent-mediated interactions in complicated molecular systems and will have broad impacts on both fundamental research and engineering applications.

Table of Contents

List of Figures

List of Tables

Chapter 1 Introduction

1. 1 Scope of Research

Solvation is a ubiquitous phenomenon in nature and plays an important role in solution chemistry, molecular biology and many aspects of materials science and nanotechnology. While classical thermodynamics describes solvation with a continuous representation of the solvent, the macroscopic approach is inadequate for applications such as structure-based drug design where the solute properties and performance are closely affiliated with the local solvent inhomogeneity. This thesis aims to provide a quantitative description of solvation and solvent-mediated interactions from a microscopic perspective. The main content is decomposed into two parts. One aspect is to study the microscopic structure and thermodynamic properties of flexible molecules in complicated solution environments. In particular, the theoretical study is focused on the structure and thermodynamic properties of various polymers and polyelectrolytes under various confinements. Another aspect of this thesis deals with the microscopic structure and interfacial behavior of solvent molecules near rigid solutes and extended surfaces. The work on solvation of rigid molecules is also extended to studying solvent-mediated interactions as well as solvation free energy calculations.

Whereas most previous work on the microscopic details of solvation and solvent-mediated interactions is based on molecular dynamics (MD) or Monte Carlo (MC) simulations, simulation is not well suited for calculation of thermodynamic properties such as the solvation free energy and potential of mean force. A key theoretical

contribution of this work is development of a hybrid method we call MC-DFT that combines MC/MD simulation for the solvent structure and analytical equations from the classical density functional theory (DFT) to calculate thermodynamic properties. The new theoretical framework utilizes well-established force fields and simulation protocols for obtaining the microscopic details of multi-dimensional systems but avoids lengthy simulation of thermodynamic pathways to calculate the configurational properties. Although in principle the microscopic distribution of solvent molecules can be obtained self-consistently by functional minimization of the grand potential, direct application of the DFT to multi-dimensional systems is often hampered by the expensive computational cost. On the other hand, the computational time in molecular simulations does not scale with the complexity of the solute molecule, while molecular simulations are usually extremely time-consuming in calculation of thermodynamic properties such as solvation free energy. Therefore, a combination of molecular simulations and DFT takes the advantages of both methods and provides a power theoretical tool to study the structural and thermodynamic properties of complex multi-dimensional molecular systems.

1. 2 Theoretical Background

Solvation is a molecular event entailing complex interactions of an ensemble of solvent molecules with a solute at infinite dilution. In contrast to that in vacuum, the physicochemical properties of a solute are sensitive to the local solvent structure that conforms to a statistical distribution dictated by the thermodynamic state of the solvent as well as the microscopic solute-solvent interactions. Characterization of the local distribution of solvent molecules and the solvation free energy often serves as a starting

point to understand the solution behavior of solute molecules. In addition, solvation is closely related to solvent-mediated interactions among many solute molecules or particles.

From a theoretical perspective, a solute molecule is considered as rigid if its conformation does not vary with the interaction with solvent molecules. In that case, solvation depends only on the degrees of freedom of the solvent molecules. Because the solute-solvent interaction can be represented by an effective external potential, the rigid solute model greatly simplifies the computational procedure. The rigid model is most suitable for investigating solvation of small molecules, spherical ions, globular proteins, colloidal particles. For example, Figure 1-1 gives a schematic representation of ion solvation in water. For rigid solutes, the essential task in theoretical investigation of solvation is to calculate the ensemble averages of the solvent molecules in the presence of an external field.

For flexible molecules such as polymer chains, solvation is dependent not only on the properties of solvent and solute-solvent interactions but also on the statistics of the intramolecular configurations. Figure 1-2 presents a schematic representation of a polymer/polyelectrolyte chain surrounded by solvent molecules and small ions. Unlike a rigid solute such as a nanoparticle or a spherical ion whose solvation free energy is fully determined by the properties of solvent and solute-solvent interaction, the polymer configuration plays an important role in determining the solvation free energy and the properties of the dissolved polymer chain. In this case, theoretical calculation should account for the statistics of both polymer configuration and solvent distributions.

Understanding solvent distribution near rigid solutes or particles is pertinent to a broad range of biological, chemical and physical processes in solutions [1-4]. In particular, the solvation free energy is instrumental for controlling the size and shape of nanoparticles during the synthesis and the properties of nanocrystals are often related to their sizes and shapes [5-7]. Solvation of a solvent-phobic solute (e.g., hydrophobic substrate) is also related to the underlying mechanism of hydrophobic phenomena near macroscopic substrates [8] that are important for rational design and fabrication of superhydrophobic materials [9]. As the size of solute increases from microscopic to macroscopic scale, the presence of macroscopic solutes in solvent exerts strong confinement effect and the microscopic structure of solvent is dependent on the curvature and properties of substrates. Whereas current knowledge on solvation of small rigid molecules has been well advanced, quantification of the microscopic structure of the solvent near an extended solute and molecular solvation free energy remains a daunting theoretical challenge. In particular, the colloidal force arising in a solution or colloidal dispersion is difficult to quantify if it entails surface phase transitions [10]. Understanding solvent-mediated interaction is key to colloidal self-assembly processes [11, 12] and the microscopic mechanisms underlying biological processes including protein folding [13] and structure-based rational drug design [14, 15].

A cornerstone for describing solvation of rigid solutes is provided by the scaled-particle theory (SPT) that was originally proposed by Reiss, Frisch and Lebowitz bout 50 years ago [16]. According to this theory, dissolution of a solute molecule into a solvent can be considered as a two-step process: first, formation of a cavity to accommodate the

solute molecule and second, application of the solute-solvent attractions. The first step accounts for the molecular excluded-volume effect; and it can be represented by dissolution of a hard body or cavity that excludes solvent molecules. The second step accounts for the attractive energy between the solute and solvent molecules and its influence on the local solvent structure. While the solvation process is perceived as a two-step process, the total solvation free energy is calculated by using a semi-empirical correlation near the bulk limit [17]. SPT has been successfully applied not only to hard-sphere systems as well documented, but also to liquid crystals [18] and to hydrophobic phenomena [8, 19]. In this thesis, I will discuss an extension of the SPT to solutes with complicated geometry and to solvent-mediated "lock-and-key" interactions.

Like a typical classical thermodynamic method, SPT is not concerned with the solvent structure. In statistical mechanics, the distribution of solvent molecules near a rigid solute and the solvent-mediated interactions are often described by the Ornstein-Zernike (OZ) integral equation theory [20]. The OZ equation defines direct correlation functions in terms of the total correlation functions. To solve direct and total correlation functions, we need a closure approximation [21] or input pair correlation data from computer simulation. With a good closure for the OZ equation, the solvent distribution and subsequently pertinent thermodynamic properties can be obtained following standard equations of statistical mechanics. Integral equation theory has been applied to the study of colloidal interaction and self-assembly [22] and protein solvation [23]. While it is efficient for relative simple systems, integral equation theory is computationally expensive if it requires solving the three-dimensional density profile of solvent molecules

near complex solutes. In addition, a faithful representation of the bridge functional is often difficult [24].

Polymers and polyelectrolytes have been of great interest among scientists and engineers for their broad applications ranging from synthetic plastics and fibers in polymer engineering [25] to biopolymers such as nucleic acids, genome and proteins in many biological systems [26]. In particular, when polymers are under confinement [27, 28], they have been widely used to understand genome packaging [29-33], which is key in virus replication and gene delivery [29-33]. In biological systems, polyelectrolytes (e.g., RNA/DNA) under confinement are solvated in water and surrounded by various salt ions. As a result, the properties of polymers in viral capsid are dependent on the properties of solvent (water) and salt as well as the confined environment.

The theoretical methods for solvation of flexible molecules are quite different from those for rigid solutes. A number of statistical-mechanical theories are available for describing the structure and thermodynamic properties of various polymers at uniform as well as inhomogeneous conditions. The simplest approach is scaling analysis pioneered by de Gennes [34, 35], which is based on analogies with critical phenomena in phase behavior of magnets. Scaling analysis incorporates repulsion between monomers and it may account for important intermolecular interactions beyond the usual mean-field approximations (e.g., Flory-Huggins theory) [36-38]. The scaling methods are most adequate for very long polymers chains whose thermodynamic properties such as the osmotic pressure and the mean-square end-to-end distance have simple power-law dependences on scaling variables [39]. Another popular choice for the study of the

thermodynamic properties of polymer systems is based on the self-consistent field theory (SCFT) [40-43], in which the many-body interaction is replaced by a term where all bodies of the system interact with an effective field [44]. Because SCFT reduces a multi-body problem to an effective one-body problem, it predicts the properties and behavior of complex many-body systems at relatively low computational cost. The SCFT has been applied to many aspects of polymer physics, such as block copolymer and self-assembly [45], polymer adsorption [46], polyelectrolytes [47], and single polymer in solution [48]. However, because SCFT uses Gaussian chains as a reference, the atomistic details are lost. Furthermore, because mean-field approximation simplifies many-body to one-body effective field, it cannot capture the fluctuation effects.

The reference interaction site model (RISM) is applicable to solvation of rigid and flexible polymeric molecules [49]. Indeed, RISM was originally developed by Chandler and Anderson for small rigid molecules and later extended to polymeric systems by Curro and Schweizer [50-52]. The so-called polymer RISM integral equation allows a self-consistent determination of the equilibrium properties of polymer solutions and melts. In principle, RISM-type integral equations require solving the intra- and inter-molecular structure self-consistently [53]. At certain conditions, however, computation of intra-molecular correlations can be avoided by assuming that polymer average conformation is determined only by the chain connectivity [21]. Such approximation is adequate when the excluded-volume interactions between sites far apart are screened by interactions with surrounding chains [54]. For simplified chains, such as freely joined chains, the intra-

molecular correlation can be solved analytically. For complex chains, it can be in turn determined from a single-chain molecular simulation.

Thanks to the rapid surge in computer power in the past several decades, molecular simulation provides an effective approach to study the microscopic structure and thermodynamic properties of complex molecular systems. In general, molecular simulation can be divided into two categories: molecular dynamic (MD) simulation [55] which follows the dynamic trajectories of molecules, and Monte Carlos (MC) simulation [56, 57] which samples the microstates of individual systems based on the ensemble statistics. In MD simulation, the trajectories of molecules are determined by numerically solving the Newton's equation of motion for a system of interacting particles. Toward that end, the interactions between particles are defined by a molecular force field. In MC simulation, the movement of molecules is fully determined by the change in the microscopic probability distribution. The macroscopic properties are evaluated by ensemble averages of microstates after the system reaches a thermodynamic equilibrium. Because molecular simulation is concerned with molecular interactions and potential energy directly, it provides reliable microscopic details for calibration of different theoretical methods.

Molecular simulation has been widely used to study solvation and solve many statistical mechanical problems for polymeric fluids, such as liquid crystals [58], block copolymer and self-assembly [59, 60], protein folding [61], and polyelectrolytes [62]. Molecular simulation has also been widely used to the study of colloids solvation and interaction. Although molecular simulation is able to provide microscopic structure of

solvent for complex systems, it is often very difficult to calculate the thermodynamic quantities because computation of configurational properties requires not only the microscopic details at thermodynamic conditions of interest but also for a pathway connecting the thermodynamic state to a reference condition. While MD and MC simulations are exact in principle, the simulation methods are plagued by the fact that the computational cost scales with the system size and atomistic simulation becomes computationally too expensive for large polymeric systems. At present, molecular simulation for polymers is largely limited to short chain length and relatively small systems with coarse-grained models.

Density functional theory provides an analytical connection between the microscopic structure and thermodynamic properties of complex molecular systems from molecular perspective [63-65]. Conceptually, DFT is formulated on the basis of the Hohenberg-Kohn theorem [66], which states that there is an invertible relation between one-body density profile and the one-body system external potential [63]. Although the Hohenberg-Kohn theorem was originated in quantum mechanics of inhomogeneous electrons, it can be generalized for classical systems including polymers [67]. DFT has been used to investigate colloidal interaction [68], interfacial phenomena [69], ionic liquids [70], and solvation free energy [24]. Unlike a phenomenological method or a mean-field theory such as SCFT, DFT takes into account the segmental level interactions and can provide analytical expressions for the complex many-body correlation effects.

Typically, the free energy functional in DFT is divided into the ideal gas term and excess part that arises from thermodynamic non-ideality due to molecular interactions.

Although the exact formulation of excess free energy functional is unknown, it can be constructed by using different approximations to account various contributions from molecular interactions. Because of the flexibility in construction of the excess Helmholtz free energy functional, DFT can be applied to various aspects of statistical mechanical problems with relatively low computational cost. Thanks to the unique features of DFT, it provides a unified theoretical basis to describe equilibrium and dynamic properties of various complex fluids including polymer science, material and colloid sciences, surface engineering and biological systems [30, 31, 67, 71-76].

1. 3 Thesis Organization

This thesis includes 10 Chapters. After this brief introduction, Chapter 2 describes the basic formulation and numerical implementation of DFT and the hybrid method proposed in this work. Here the emphasis is given to construction of various excess Helmholtz free energy functionals that arise from thermodynamic non-ideality. For most systems considered in this work, the contribution from excess Helmholtz free energy can be divided into hard-sphere repulsion, the chain connectively of polymer, the van der Waals attraction, the direct Coulomb interaction, and the electrostatic correlation for different systems. After the formalism of the DFT, the general procedure and ideas of the hybrid method are also discussed in this chapter.

Chapter 3 examines the structural and thermodynamic properties of individual polymer chains inside fully enclosed environments. The key purpose of this work is to study the confinement effect on the properties of individual polymer chains such as those appeared in gel chromatography and biomacromolecules in capsids. Our study is focused

on the confined hard-sphere chains that represent the chain connectivity and molecular excluded-volume effects. Although hard-sphere chain model is oversimplification of any realistic polymer or biomolecule, it can partially capture the confinement effects on the excluded volume properties of polymers. DFT predictions are in excellent agreement with the simulation results for the distributions of polymer segments as well as the free energy of confinement, especially at high polymer concentration. With the advantage of numerical efficiency, the DFT is also able to reproduce key conclusions from the scaling analysis and recent experimental observations.

Chapter 4 extends DFT calculation to the study of flexible and semi-flexible polyelectrolyte packaging in a spherical cage within the primitive model of electrolyte solutions. Confined flexible and semi-flexible polyelectrolytes were often utilized to study the properties of RNA and DNA in viral capsid. Unlike previous genome packaging calculations, the loaded capsid and its surroundings are explicitly included in the calculation; our calculation is free of the prerequisite of charge neutrality of capsid that is usually assumed in previous calculations. DFT calculation shows a good agreement with Monte-Carlo simulation for the segmental density distributions of polymer segments and small ions. The effects of the density distribution of small ions in the outside environment and discontinuous dielectric constants on the structural properties of polyelectrolyte and small ions as well as the net charge of capsid complex are investigated.

Chapter 5 presents a hybrid DFT method to study the colloidal force and self-assembly of solute in solvent. The hybrid method incorporates the Monte-Carlo

simulation and density functional theory calculation. While computer simulation is difficult to study the solvation free energy, DFT can relate the microscopic structure and thermodynamic properties efficiently. Therefore, unlike conventional method, this new hybrid method can be applied to the study of structural and thermodynamic properties of complex multi-dimensional systems. The numerical performance is tested by extensive comparison with Monte-Carlo simulation and alternative theoretical methods for solvent-mediated interaction in colloidal dispersions and receptor-ligand systems.

Chapter 6 extends the hybrid method to the study of the solvation free energy of ions in water. However, in contrast to Chapter 5, the hybrid method incorporates molecular dynamic (MD) simulation and the classical DFT. Unlike a hard-sphere solvent, the DFT is based on an accurate free energy functional for water that incorporates the simulation results for long-range correlations and the fundamental measure theory for the molecular excluded-volume effects. The numerical performance of the theoretical method has been validated with simulation results and experimental data for the solvation free energies of various cations and anions in water.

Chapter 7 represents a perturbative density functional theory to study the structural and thermodynamic properties of uniform as well as inhomogeneous square-well fluids. The solvation of solute and solute-solvent interactions alter the microscopic structure of solvent and the corresponding thermodynamic properties. The theory yields good agreement with simulation results for the radial distribution function of bulk systems and for the density profiles of square-well fluids near the surfaces of spherical

cavities or in slit pores over a broad range of the parameter space and thermodynamic conditions.

Chapter 8 investigates the solvent behavior and depletion from a non-attractive surface, which is closely related to hydrophobic phenomena and superhydrophobicity of patterned materials. Although the solvent behavior is well understood near microscopic substrates, the prediction of the solvent behavior near an extended surface is more complicated and the nature of drying transition has been a long controversy. To study the essential physics, the theoretical work is focused on a model system that consists of a spherical cavity submerged in a square-well liquid close to saturation. In this chapter, a perturbative density functional theory is used to study the receding of a saturated solvent from microscopic and macroscopic spherical non-attractive surfaces and the nature of drying transition.

Chapter 9 presents morphological thermodynamics for nanoparticle solvation. Within the context of morphological thermodynamics, any thermodynamic quantity which satisfies motion invariance, continuity and additivity can be represented by the bilinear combination of four morphometric measures and the corresponding thermodynamic coefficients. The theory predicts the solvation free energies of nanoparticles in good agreement with alternative theoretical calculations and studies the dependence of free energy of solvation on nanoparticle geometry.

Finally, Chapter 10 summarizes the key conclusions from this dissertation and possible implications.

Figure 1-1 Schematic representation of ion solvation in water.

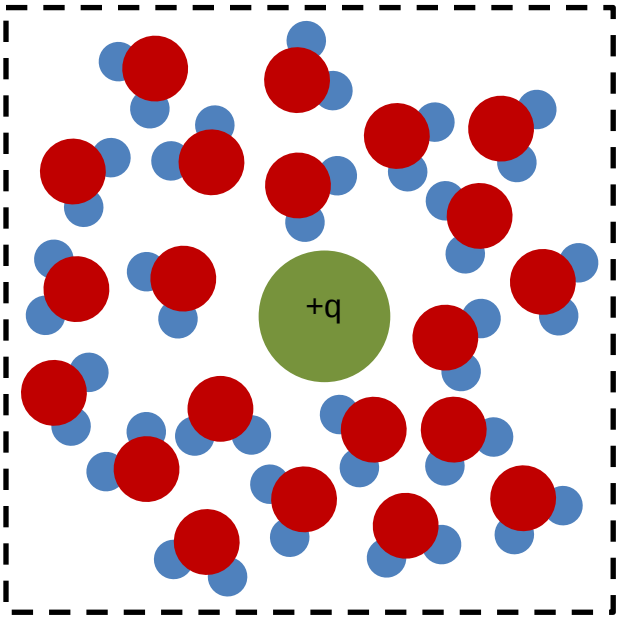

Figure 1-2 Schematic representation of a polyelectrolyte chain in continuous solvent (i.e., water). Polyelectrolyte is represented by a freely joined chain (orange) with positive charge surrounded by cations (pink) and anions (green). Solvent is depicted as continuum.

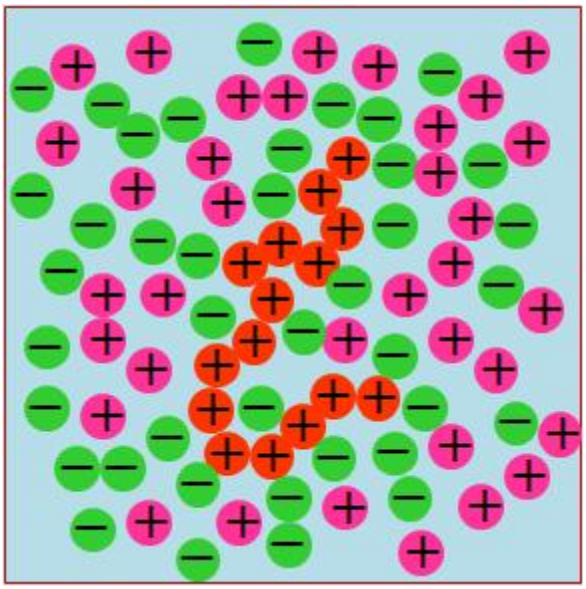

Chapter 2 – Basic Formulism of Classical Density Functional Theory

Density functional theory (DFT) is an effective computational tool to study the microscopic structure and thermodynamic properties of complex fluids, such as polymers, colloids, and ionic liquids at uniform as well as inhomogeneous conditions. Different from molecular simulations, DFT provides analytical relations between the microscopic structure and thermodynamic quantities from a molecular perspective. Also different from simulation methods, practical application of DFT requires the formulation of an approximate free energy functional F in terms of the one-body density profile $\rho(\mathbf{r})$. Its numerical implementation relies on variational calculus to obtain the equilibrium density profile and subsequently thermodynamic variables. While the equilibrium density profile can be obtained from the molecular simulations, simulation of thermodynamic properties such as the free energy calculation is extremely time consuming. On the other hand, direct minimization of the free energy functional with respect to the density profile is also computationally challenging for systems with three-dimensional inhomogeneity. In this work, we propose a hybrid method combining the merits of molecular simulation and the DFT and calibrate the new theoretical procedure through its application to studying solvation. Because molecular simulation for solutes of complicated shapes does not require additional computational cost, combination of molecular simulation and DFT method enables efficient study of the structural and thermodynamic properties of complex multi-dimensional systems. The density functional methods can be naturally applied to systems with multiple length scales and various intermolecular interactions

that are difficult to handle by using alternative computational methods. This chapter presents an overview of the basic concepts of DFT and the hybrid method application of the DFT to various complex fluids.

2. 1 Density Profile

In DFT, thermodynamic properties are often represented in terms of the functionals of the molecular density profiles. A density profile describes the average distribution of molecules in a many-body system. For a system containing N identical particles, the microscopic instantaneous particle density $\hat{\rho}(\mathbf{r})$, which counts the number of particles at a position $\mathbf{r}$ is

$$\hat{\rho}(\mathbf{r}) = \sum_{i=1}^{N} \delta(\mathbf{r} - \mathbf{r}_i), \tag{2.1}$$

where δ is the Dirac-Delta function defined as

$$\delta(\mathbf{r} - \mathbf{r}') = \begin{cases} 0, & \mathbf{r} \neq \mathbf{r}' \\ \infty, & \mathbf{r} = \mathbf{r}' \end{cases}. \tag{2.2}$$

The Dirac-Delta function is subject to the normalization condition

$$\int d\mathbf{r}\delta(\mathbf{r} - \mathbf{r}') = 1. \tag{2.3}$$

The equilibrium density profile is defined as an ensemble average of the instantaneous density [77]

$$\rho(\mathbf{r}) = \hat{\rho}(\mathbf{r}) = \left\langle \sum_{i=1}^{N} \delta(\mathbf{r} - \mathbf{r}_i) \right\rangle. \tag{2.4}$$

For a one-component open system at fixed temperature T and volume V, the equilibrium one-body density profile is related to the Hamiltonian of the system and the grand partition function Ξ

$$\Xi = \sum_N \frac{1}{N!\Lambda^{3N}} \int d\mathbf{r}^N \exp\left\{-\beta\left[\Gamma\left(\mathbf{r}^N\right) + N\mu + \sum_{i=1}^{N}\varphi\left(\mathbf{r}_i\right)\right]\right\} \tag{2.5}$$

where Λ is the thermal wavelength, $\Gamma\left(\mathbf{r}^N\right)$ stands for the total interaction potential of N particles at configuration $\mathbf{r}^N = \left(\mathbf{r}_1, \mathbf{r}_2, ..., \mathbf{r}_N\right)$, μ is the bulk chemical potential of particle, $\beta = 1/\left(k_B T\right)$, k_B is the Boltzmann constant, and $\varphi\left(\mathbf{r}\right)$ is the one-body external potential.

By substituting Eq. (2.4) into Eq. (2.5), the one-body density profile $\rho\left(\mathbf{r}\right)$ is related to the grand partition function

$$\rho\left(\mathbf{r}\right) = \frac{1}{\Xi}\sum_N \frac{1}{N!\Lambda^{3N}} \int d\mathbf{r}^N \sum_{i=1}^{N}\delta\left(\mathbf{r}_i - \mathbf{r}\right)\exp\left\{-\beta\left[\Gamma\left(\mathbf{r}^N\right) + N\mu + \sum_{i=1}^{N}\varphi\left(\mathbf{r}_i\right)\right]\right\}. \tag{2.6}$$

The right hand side of Eq. (2.6) is related to the functional derivative of the grand partition function with respect to the external potential. After rearrangement, the one-body density profile is then given by

$$\rho\left(\mathbf{r}\right) = -\frac{1}{\beta\Xi}\frac{\delta\Xi}{\delta\varphi\left(\mathbf{r}\right)} = -\frac{\delta \ln \Xi}{\beta\delta\varphi\left(\mathbf{r}\right)}. \tag{2.7}$$

The grand potential Ω is defined by the grand partition function given by

$$\beta\Omega = -\ln \Xi. \tag{2.8}$$

Substituting Eq. (2.8) into Eq. (2.7) yields

$$\rho(\mathbf{r}) = \frac{\delta\Omega}{\delta\varphi(\mathbf{r})}. \tag{2.9}$$

2. 2 Density Functional Theory

Although broad application of DFT to quantum and classical statistical mechanical calculations began in the mid-1960s, the basic ideas were proposed by van der Waals in late 19th century, who justified the choice of functional minimization of the free energy as the criterion of equilibrium in a liquid-gas system [78]. However, modern DFT is built upon the Hohenberg-Kohn theorem [66], which states that for an equilibrium system at a given temperature and the chemical potentials of all species, the one-body external potential can be uniquely determined by the one-body density profiles. This mathematical theorem enables a definition of intrinsic Helmholtz free energy F which is independent of the one-body external potential [63]. For a one-component system, the intrinsic Helmholtz free energy is defined as

$$F \equiv A - \int d\mathbf{r}\varphi(\mathbf{r})\rho(\mathbf{r}), \tag{2.10}$$

where A is the Helmholtz free energy. The Helmholtz energy is related to the grand potential by

$$\begin{aligned}\Omega = A - N\mu &= F + \int d\mathbf{r}\varphi(\mathbf{r})\rho(\mathbf{r}) - N\mu \\ &= F + \int d\mathbf{r}\left[\varphi(\mathbf{r}) - \mu\right]\rho(\mathbf{r})\end{aligned}. \tag{2.11}$$

The intrinsic Helmholtz free energy and subsequently the grand potential are functionals of the one-body density profiles of particles/molecules. Such feature allows determination of the equilibrium density profiles by the minimization of the grand potential:

$$\frac{\delta\Omega\left[\rho(\mathbf{r})\right]}{\delta\rho(\mathbf{r})}=0. \tag{2.12}$$

Combining Eq. (2.11) and Eq. (2.12), we have

$$\frac{\delta F\left[\rho(\mathbf{r})\right]}{\delta\rho(\mathbf{r})}=\mu-\varphi(\mathbf{r}). \tag{2.13}$$

The functional derivative of the grand potential with respect to the one-body density profile provides a mathematical framework to solve the microscopic structure and all pertinent thermodynamic properties.

To further illustrate the basic ideas of DFT, we consider a multi-component system consisting of mixture of polymers and monomers with varying intermolecular and intra-molecular interactions at temperature T, total volume V, and bulk chemical potential of polymers μ_M and that of monomers μ_a. According to a standard coarse-grained model, polymers are represented by freely joined spherical segments with the degree of polymerization M and segment diameter σ_p. Within this model, the bond length is the same as the polymer segment diameter. The monomers are represented by spherical particles with diameter σ_a.

If for simplicity we neglect the bending potential and the effects on bond angles on the properties of polymers, the bond potential of a polymer chain $V_b(\mathbf{R})$ is given by

$$\exp\left[-\beta V_b(\mathbf{R})\right]\propto\prod_{i=1}^{M}\delta\left(\left|\mathbf{r}_{i+1}-\mathbf{r}_i\right|-\sigma_p\right), \tag{2.13}$$

where $\mathbf{R} \equiv (\mathbf{r}_1, \mathbf{r}_2, \cdots, \mathbf{r}_M)$ is a set of coordinates specifying the polymer configuration, and $\mathbf{r}_i$ is the i-th segmental position of the polymer chain. The proportionality constant in Eq. (2.13) are determined from the normalization condition

$$\frac{1}{V}\int \exp\left[-\beta V_b(\mathbf{R})\right] d\mathbf{R} = 1. \tag{2.13}$$

Substitution of Eq. (2.13) into Eq. (2.13) yields

$$\exp\left[-\beta V_b(\mathbf{R})\right] = \prod_{i=1}^{M} \frac{\delta\left(|\mathbf{r}_{i+1} - \mathbf{r}_i| - \sigma_p\right)}{4\pi\sigma_p{}^2}. \tag{2.13}$$

The central goal of DFT is to formulate the grand potential Ω, or equivalently, the intrinsic Helmholtz free energy F in terms of the molecular density distributions. For a multi-component system containing polymers and monomers, the grand potential can expressed in terms of intrinsic Helmholtz free energy functional and one-body external potentials,

$$\begin{aligned}\Omega\left[\rho_M(\mathbf{R}), \{\rho_a(\mathbf{r})\}\right] = F\left[\rho_M(\mathbf{R}), \{\rho_a(\mathbf{r})\}\right] + \\ \int\left[\Psi_M(\mathbf{R}) - \mu_M\right]\rho_M(\mathbf{R})\, d\mathbf{R} + \sum_a \int\left[\Psi_a(\mathbf{r}) - \mu_a\right]\rho_a(\mathbf{r})\, d\mathbf{r},\end{aligned} \tag{2.13}$$

in which $d\mathbf{R} = d\mathbf{r}_1 d\mathbf{r}_2 \cdots d\mathbf{r}_M$ represents a set of differential volumes, $\rho_M(\mathbf{R})$ is a multi-dimensional polymer density profile as a function of the polymer configuration $\mathbf{R}$, $\rho_a(\mathbf{r})$ is the segmental distribution of monomers, $\Psi_a(\mathbf{r})$ stands for the external potential of monomers, and $\Psi_M(\mathbf{R})$ is the summation of the external potential of polymer segments, i.e. $\Psi_M(\mathbf{R}) = \sum_{i=1}^{M} \varphi_i(\mathbf{r}_i)$.

2. 3 Intrinsic Helmholtz Free Energy

The intrinsic Helmholtz free energy can be decomposed into two parts: ideal gas term F^{id} that is free of non-bonded interactions and excess term F^{ex} arising from the thermodynamic non-ideality due to inter-molecular and intra-molecular interactions

$$F\left[\rho_M(\mathbf{R}),\{\rho_a(\mathbf{r})\}\right]=F^{id}\left[\rho_M(\mathbf{R}),\{\rho_a(\mathbf{r})\}\right]+F^{ex}\left[\rho_M(\mathbf{R}),\{\rho_a(\mathbf{r})\}\right]. \quad (2.13)$$

The ideal-gas Helmholtz free energy is known exactly for polymer and monomer mixtures. It is dependent on the configuration of polymer and monomers as well as the bond potentials

$$\begin{aligned}\beta F^{id}=&\int\left[\ln\rho_M(\mathbf{R})-1\right]\rho_M(\mathbf{R})\,d\mathbf{R}+\beta\int V_b(\mathbf{R})\,\rho_M(\mathbf{R})\,d\mathbf{R}\\&+\sum_a\int\left[\ln\rho_a(\mathbf{r})-1\right]\rho_a(\mathbf{r})\,d\mathbf{r}\end{aligned} \quad . \quad (2.13)$$

Seeking an accurate representation of excess Helmholtz free energy is key to DFT calculations. Unfortunately, the exact formulation for excess free energy is in general unknown. However, good approximations can be used to calculate F^{ex} arising from thermodynamic non-ideality, i.e., contribution of the intermolecular interactions to the free-energy functional. Detailed representations and approximations about excess Helmholtz free energy will be described later on.

2. 4 Euler-Lagrange Equation

The equilibrium density $\rho_M(\mathbf{R})$ and $\{\rho_a(\mathbf{r})\}$ correspond to the minimum value of the variational grand potential functional Ω as indicated in Eq. (2.12). Following the rules of calculus of variations, we may express the condition of equilibrium by minimization of the grand potential for the mixture

$$\frac{\delta\Omega}{\delta\rho_M(\mathbf{R})} = 0, \tag{2.14}$$

$$\frac{\delta\Omega}{\delta\rho_a(\mathbf{r})} = 0. \tag{2.15}$$

These functional derivatives of the grand potential with respect to the density distributions lead to a set of Euler-Lagrange equations for the segmental density distribution of polymers and monomers,

$$\rho_M(\mathbf{R}) = \exp\left[\beta\mu_M - \beta V_b(\mathbf{R}) - \beta\Psi_M(\mathbf{R}) - \beta\varphi(\mathbf{R})\right], \tag{2.16}$$

$$\rho_a(\mathbf{r}) = \exp\left[\beta\mu_a - \beta\Psi_a(\mathbf{r}) - \frac{\delta\beta F^{ex}}{\delta\rho_a(\mathbf{r})}\right]. \tag{2.17}$$

In Eq. (2.16), $\beta\varphi(\mathbf{R}) = \partial\beta F^{ex} / \partial\rho_M(\mathbf{R})$ represents an effective potential field due to intra- and intermolecular interactions [79]. On the other hand, the functional derivative of excess Helmholtz free energy with respect to the density profile of a monomer yields excess chemical potential of the monomer:

$$\mu_a^{ex}(\mathbf{r}) = \frac{\delta\beta F^{ex}}{\delta\rho_a(\mathbf{r})}. \tag{2.18}$$

The number segment density of polymer segments $\rho_p(\mathbf{r})$ is given by

$$\rho_p(\mathbf{r}) = \sum_{i=1}^{M}\rho_{si}(\mathbf{r}_i) = \sum_{i=1}^{M}\int d\mathbf{R}\,\delta(\mathbf{r}-\mathbf{r}_i)\rho_M(\mathbf{R}), \tag{2.19}$$

where $\rho_{si}(\mathbf{r})$ is the local density of segment i. Using Eq. (2.19), $\varphi(\mathbf{R})$ can be simplified to

$$\varphi(\mathbf{R}) = \frac{\delta F^{ex}}{\delta \rho_M(\mathbf{R})} = \sum_{i=1}^{M} \frac{\delta F^{ex}}{\delta \rho_p(\mathbf{r}_i)}. \tag{2.20}$$

Substitution of Eq. (2.20) into Eq. (2.16) yields

$$\rho_M(\mathbf{R}) = \exp\left[\beta\mu_M - \beta V_b(\mathbf{R}) - \beta\sum_{i=1}^{M}\lambda_i(\mathbf{r}_i)\right], \tag{2.21}$$

where $\lambda_i(\mathbf{r}_i)$ represents an effective one-body potential

$$\lambda_i(\mathbf{r}_i) = \frac{\delta F^{ex}}{\delta \rho_p(\mathbf{r}_i)} + \Psi_i(\mathbf{r}_i). \tag{2.22}$$

and $\Psi_i(\mathbf{r}_i)$ is the external potential for segment *i*. The i-th segment density $\rho_{si}(\mathbf{r})$ can be obtained by combining Eq. (2.19) and Eq. (2.21),

$$\rho_{si}(\mathbf{r}) = \int d\mathbf{R}\,\delta(\mathbf{r}-\mathbf{r}_i)\exp\left[\beta\mu_M - \beta V_b(\mathbf{R}) - \beta\sum_{i=1}^{M}\lambda_i(\mathbf{r}_i)\right]. \tag{2.23}$$

Integration over the all beads in polymer chain gives

$$\rho_p(\mathbf{r}) = \exp(\beta\mu_M)\int d\mathbf{R}\sum_{i=1}^{M}\delta(\mathbf{r}-\mathbf{r}_i)\exp\left[-\beta V_b(\mathbf{R}) - \beta\sum_{j=1}^{M}\lambda_j(\mathbf{r}_j)\right]. \tag{2.24}$$

From Eqs. (2.17) and (2.24), it can be seen that the formalism of one-body effective potential $\lambda_i(\mathbf{r}_i)$ or equivalently excess Helmholtz free energy F^{ex} is key to the DFT calculation.

2. 5 Excess Helmholtz Free Energy

The excess Helmholtz free energy can be decomposed into several contributions due to different molecular interactions and correlations. For polymer systems considered in this work, the excess Helmholtz free energy can be expressed as:

$$F^{ex} = F_{hs}^{ex} + F_{ch}^{ex} + F_{C}^{ex} + F_{el}^{ex} + F_{att}^{ex}, \tag{2.25}$$

where F_{hs}^{ex} represents excess Helmholtz free energy due to the hard-sphere repulsion, F_{ch}^{ex} is that due to the chain connectivity, F_{C}^{ex} is that due to the direct Coulomb energy, F_{el}^{ex} represents the electrostatic correlations, and F_{att}^{ex} depicts that due to the long-range attractions, respectively.

One key advantage of DFT is that it can explicitly represent the contributions to thermodynamic potentials from different components of intermolecular forces. Therefore, within the framework of DFT, these different excess Helmholtz free energy functionals can be easily organized based on the specific system under consideration. As in Eq. (2.18), the functional derivative of excess Helmholtz free energy with respect to the density profile yields the excess chemical potential $\mu^{ex}(\mathbf{r})$,

$$\begin{aligned}\beta\mu^{ex}(\mathbf{r}) &= \frac{\delta\beta F^{ex}}{\delta\rho(\mathbf{r})} = \frac{\delta\beta F_{hs}^{ex}}{\delta\rho(\mathbf{r})} + \frac{\delta\beta F_{ch}^{ex}}{\delta\rho(\mathbf{r})} + \frac{\delta\beta F_{C}^{ex}}{\delta\rho(\mathbf{r})} + \frac{\delta\beta F_{el}^{ex}}{\delta\rho(\mathbf{r})} + \frac{\delta\beta F_{att}^{ex}}{\delta\rho(\mathbf{r})} \\ &= \beta\mu_{hs}^{ex}(\mathbf{r}) + \beta\mu_{ch}^{ex}(\mathbf{r}) + \beta\mu_{C}^{ex}(\mathbf{r}) + \beta\mu_{el}^{ex}(\mathbf{r}) + \beta\mu_{att}^{ex}(\mathbf{r})\end{aligned}, \tag{2.26}$$

where $\mu_{hs}^{ex}(\mathbf{r})$, $\mu_{ch}^{ex}(\mathbf{r})$, $\mu_{C}^{ex}(\mathbf{r})$, $\mu_{el}^{ex}(\mathbf{r})$, and $\mu_{att}^{ex}(\mathbf{r})$ represent the excess chemical potential due to corresponding excess Helmholtz free energies. In the following subsections, we present the detail expressions for the excess Helmholtz free energies and the corresponding excess chemical potentials.

2. 5. 1 Fundamental Measure Theory

The excess Helmholtz free energy due to the hard-sphere repulsion F_{hs}^{ex} accounts for the molecular excluded-volume effect. Hard-sphere interactions are defined by

impenetrable spheres that cannot overlap. Hard-sphere model represents a simple description of the extreme repulsions that spherical molecules experience at very close distances.

For a mixture of hard spheres, the hard-sphere potential between two spherical particles is given by

$$\beta u\left(\mathbf{r}_i,\mathbf{r}_j\right)=\begin{cases}0, & \left|\mathbf{r}_i-\mathbf{r}_j\right|\geq\frac{1}{2}\left(\sigma_i+\sigma_j\right)\\ \infty, & \left|\mathbf{r}_i-\mathbf{r}_j\right|<\frac{1}{2}\left(\sigma_i+\sigma_j\right)\end{cases} \tag{2.26}$$

where $\mathbf{r}_i$ and $\mathbf{r}_j$ are the particle positions , and σ_i and σ_j are the diameters. Although the hard-sphere model is an oversimplification for any realistic fluid, it serves a useful reference to study the structural and thermodynamic properties of complex fluids and solids.

There have been numerous theories to describe the structural and thermodynamic properties of hard-sphere fluids, including the Percus-Yevck (PY) integral equation[80], the scaled-particle theory (SPT) [16], the local density approximation (LDA) [81], and the weighted-density approximation (WDA) [82]. Among these theories, fundamental measure theory (FMT) originally proposed by Rosenfeld [83] has been the most effective approach. Within FMT, the free energy density is taken to be a function not just of one but of several weighted densities that are defined by the geometrical characteristics of the particles. In principle, FMT can be applied to not only spherical particles systems but also to systems containing non-spherical particles. FMT was originally inspired by the link between SPT and PY approximation for hard sphere [21].

While SPT provides the thermodynamic properties of hard-sphere fluids, PY theory describes complementary pair distribution functions.

The excess Helmholtz free energy for a mixture consisting of v species of hard spheres can be obtained from a diagrammatic expansion [21]:

$$-\beta F_{hs}^{ex}\left[\rho_i(\mathbf{r})\right] =$$ 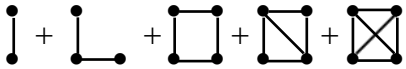 $$+\cdots\cdots, \qquad (2.27)$$

In Eq.(2.27), each line represents a Mayer function, and the closed circles depict multiplication by the average one-body density of specie k, and the integration over all spaces [21].

At the low density limit, higher order terms are negligible and the excess Helmholtz free energy is given by [83, 84]

$$\beta F_{hs}^{ex}\left[\rho_i(\mathbf{r})\right] = -\frac{1}{2}\sum_{i,j}\int\int d\mathbf{r}_i d\mathbf{r}'\rho_i(\mathbf{r})\rho_j(\mathbf{r}')\, f_{ij}\left(\left|\mathbf{r}-\mathbf{r}'\right|\right) \qquad (2.28)$$

where Mayer function f is defined by

$$f_{ij}\left(\left|\mathbf{r}_i-\mathbf{r}_j\right|\right) = \exp\left[-\beta u_{ij}\left(\left|\mathbf{r}_i-\mathbf{r}_j\right|\right)\right]-1 \qquad (2.29)$$

For hard-sphere fluids, the Mayer function for a pair of spheres is equal to negative of the Heaviside step function θ,

$$f_{ij}\left(\left|\mathbf{r}_i-\mathbf{r}_j\right|\right) = -\theta\left[\sigma_i/2+\sigma_j/2-\left|\mathbf{r}_i-\mathbf{r}_j\right|\right]. \qquad (2.30)$$

Eq. (2.30) indicates that the Mayer function is -1 when two spheres overlap and 0 otherwise. Substitution of Eq. (2.30) into Eq. (2.28) gives the exact low density expression for the free energy functional

$$\beta F_{hs}^{ex}\left(\rho_i(\mathbf{r})\right)=\frac{1}{2}\sum_{i,j}\int\int d\mathbf{r}_i d\mathbf{r}'\rho_i(\mathbf{r})\rho_j(\mathbf{r}')\theta\left[\sigma_i/2+\sigma_j/2-\left|\mathbf{r}_i-\mathbf{r}_j\right|\right]. \quad (2.31)$$

The Heaviside step function in Eq. (2.30) can be decomposed into a sum of convolutions of four scalar and two vector weight functions given by the following identity:

$$\theta\left[\sigma_i/2+\sigma_j/2-\left|\mathbf{r}_i-\mathbf{r}_j\right|\right]=\omega_i^{(3)}\otimes\omega_j^{(0)}+\omega_i^{(0)}\otimes\omega_j^{(3)}+\omega_i^{(2)}\otimes\omega_j^{(1)}+\omega_i^{(1)}\otimes\omega_j^{(2)} \\ -\vec{\boldsymbol{\omega}}_i^{(V2)}\otimes\vec{\boldsymbol{\omega}}_j^{(V1)}-\vec{\boldsymbol{\omega}}_j^{(V1)}\otimes\vec{\boldsymbol{\omega}}_i^{(V2)}, \quad (2.32)$$

where

$$\omega_i^{(\alpha)}\otimes\omega_j^{(\beta)}=\int d\mathbf{r}\,\omega_i^{(\alpha)}\left(\mathbf{r}_i-\mathbf{r}\right)\omega_j^{(\beta)}\left(\mathbf{r}_j-\mathbf{r}\right). \quad (2.33)$$

These convolutions are only the functional of the difference vector $\mathbf{r}_i-\mathbf{r}_j$, and $\omega_i^{(\alpha)}$ also applies to vector valued weight functions.

The six weight functions are independent of the density profiles, but are directly related to the geometry of a spherical particle i:

$$\omega_i^{(2)}(r)=\delta\left(\sigma_i/2-r\right), \quad (2.34)$$

$$\omega_i^{(3)}(r)=\theta\left(\sigma_i/2-r\right), \quad (2.35)$$

$$\vec{\boldsymbol{\omega}}_i^{(V2)}(\mathbf{r})=(\mathbf{r}/r)\,\delta\left(\sigma_i/2-r\right), \quad (2.36)$$

Integration of two scalar weight functions $\omega_i^{(2)}(r)$ and $\omega_i^{(3)}(r)$ with respect to position yields the particle surface area and volume, respectively. On the other hand, the integration of the vector weight function $\vec{\boldsymbol{\omega}}_i^{(V2)}(\mathbf{r})$ with respect to position gives the

gradient across the sphere in the **r** direction. Other weight functions are proportional to these three functions,

$$\omega_i^{(0)}(r) = \frac{\omega_i^{(1)}(r)}{\sigma_i/2} = \frac{\omega_i^{(2)}(r)}{\pi\sigma_i^2}, \tag{2.37}$$

and

$$\vec{\omega}_i^{(V1)}(\mathbf{r}) = \frac{\vec{\omega}_i^{(V2)}(\mathbf{r})}{2\pi\sigma_i}. \tag{2.38}$$

The three-dimensional Fourier transform of the weight function are [85]

$$\omega_i^{(0)}(k) = 2\sin(k\sigma_i/2)/k\sigma_i, \tag{2.39}$$

$$\omega_i^{(1)}(k) = \sin(k\sigma_i/2)/k, \tag{2.40}$$

$$\omega_i^{(2)}(k) = 2\pi\sigma_i \sin(k\sigma_i/2)/k, \tag{2.41}$$

$$\omega_i^{(3)}(k) = 4\pi\frac{\sin(k\sigma_i/2) - (k\sigma_i/2)\cos(k\sigma_i/2)}{k^3}, \tag{2.42}$$

$$\overline{\vec{\omega}}_i^{(V1)}(\mathbf{k}) = -\sqrt{-1}\mathbf{k}\omega_i^{(3)}(k)/(2\pi\sigma_i), \tag{2.43}$$

$$\overline{\vec{\omega}}_i^{(V2)}(\mathbf{k}) = -\sqrt{-1}\mathbf{k}\omega_i^{(3)}(k). \tag{2.44}$$

The deconvolution of Eq. (2.32) can be plugged into the expression for the exact low density limit, Eq. (2.31) to yield

$$\beta F_{hs}^{ex}\left(\rho_i(\mathbf{r})\right) = \int d\mathbf{r}\left[n_0(\mathbf{r})n_3(\mathbf{r}) + n_1(\mathbf{r})n_2(\mathbf{r}) - \vec{\mathbf{n}}_{V1}(\mathbf{r})\vec{\mathbf{n}}_{V2}(\mathbf{r})\right] \tag{2.45}$$

where $n_\alpha(\mathbf{r})$ are a set of weighted densities defined as

$$n_\alpha(\mathbf{r}) = \sum_i n_{\alpha i}(\mathbf{r}) = \sum_i \int \rho_i(\mathbf{r}')\omega_i^{(\alpha)}(|\mathbf{r}-\mathbf{r}'|)d\mathbf{r}'. \tag{2.46}$$

For systems with only one-dimensional inhomogeneity, the calculation of weighted densities reduces to one-dimensional integrations. If the density profiles are spherically symmetric, the density profile $\rho(\mathbf{r})$ is only r dependent and the weighted densities are given by [85]

$$n_{2,i}(r)=\frac{\pi\sigma_i}{r}\int_{|r-\sigma_i/2|}^{r+\sigma_i/2}dr'r'\rho_i(r'), \tag{2.47}$$

$$n_{3,i}(r)=\frac{\pi}{r}\int_{|r-\sigma_i/2|}^{r+\sigma_i/2}dr'r'\left[\frac{\sigma_i^{\,2}}{4}-(r-r')^2\right]\rho_i(r'), \tag{2.48}$$

$$\vec{\mathbf{n}}_{V2,i}(\mathbf{r})=\frac{\mathbf{r}}{r}\frac{\pi}{r}\int_{|r-\sigma_i/2|}^{r+\sigma_i/2}dr'r'\left[r^2-r'^2+\frac{\sigma_i^{\,2}}{4}\right]\rho_i(r'), \tag{2.49}$$

$$n_{0,i}(r)=\frac{2n_{1,i}(r)}{\sigma_i}=\frac{n_{2,i}(r)}{\pi\sigma_i^{\,2}}, \tag{2.50}$$

$$\vec{\mathbf{n}}_{V1,i}(\mathbf{r})=\frac{\vec{\mathbf{n}}_{V2,i}(\mathbf{r})}{2\pi\sigma_i}. \tag{2.51}$$

For the case of system with slab geometry, the weighted densities are [85]

$$n_{2,i}(z)=\pi\sigma_i\int_{z-\sigma_i/2}^{z+\sigma_i/2}dz'\rho_i(z'), \tag{2.52}$$

$$n_{3,i}(z)=\pi\int_{z-\sigma_i/2}^{z+\sigma_i/2}dz'\left[\frac{\sigma_i^{\,2}}{4}-(z'-z)^2\right]\rho_i(z'), \tag{2.53}$$

$$\vec{\mathbf{n}}_{V2,i}(z)=-\frac{\mathbf{z}}{z}\pi\sigma_i\int_{z-\sigma_i/2}^{z+\sigma_i/2}dz'(z'-z)\rho_i(z'), \tag{2.54}$$

$$n_{0,i}(z)=\frac{2n_{1,i}(z)}{\sigma_i}=\frac{n_{2,i}(z)}{\pi\sigma_i^{\,2}}, \tag{2.55}$$

$$\vec{\mathbf{n}}_{V1,i}(z) = \frac{\vec{\mathbf{n}}_{V2,i}(z)}{2\pi\sigma_i}. \tag{2.56}$$

A key assumption in the fundamental measure theory (FMT) is that the excess Helmholtz free energy can be described in terms of the excess Helmholtz free energy density:

$$\beta F_{hs}^{ex} = \int \Phi_{hs}^{ex}\left[\{n_\alpha(\mathbf{r})\}\right] d\mathbf{r}, \tag{2.56}$$

where Φ_{hs}^{ex} is the reduced excess energy density.

The precise functional form of the free energy density in Eq. (2.56) remains to be specified. Within the spirit of a virial expansion, the free energy density for inhomogeneous hard-sphere fluid can be expressed by the linear combination of the lowest powers of the weighted densities and their products. Because Φ^{ex} is a scalar with the dimension of density, it can only be a sum of functions $n_0(\mathbf{r})$, $n_1(\mathbf{r})\cdot n_2(\mathbf{r})$, $n_2(\mathbf{r})^3$, $\vec{\mathbf{n}}_{V1}(\mathbf{r})\cdot\vec{\mathbf{n}}_{V2}(\mathbf{r})$, and $n_2(\mathbf{r})\left[\vec{\mathbf{n}}_{V2}(\mathbf{r})\cdot\vec{\mathbf{n}}_{V2}(\mathbf{r})\right]$, with corresponding coefficients that are represented by the functions of packing fraction $n_3(\mathbf{r})$,

$$\Phi_{hs}^{ex}\left[\{n_\alpha\}\right] = \phi_1 n_0 + \phi_2 n_1 n_2 + \phi_3 n_2^3 + \phi_4 \vec{\mathbf{n}}_{V1}\cdot\vec{\mathbf{n}}_{V2} + \phi_5 n_2\left(\vec{\mathbf{n}}_{V2}\cdot\vec{\mathbf{n}}_{V2}\right). \tag{2.56}$$

We note that the last two terms on the right hand side of Eq. (2.56) will vanish for uniform fluid due to the homogeneity in every direction.

The excess Helmholtz free energy functional in Eq. (2.56) is related to the corresponding excess grand potential,

$$\Omega^{ex}\left[\{\rho_i\}\right] = -\int P^{ex}\left[\{\rho_i\}\right] d\mathbf{r} = F^{ex}\left[\{\rho_i\}\right] - \sum_i \int \rho_i(\mathbf{r}) \frac{\delta F^{ex}}{\delta \rho_i(\mathbf{r})} d\mathbf{r}. \tag{2.56}$$

Therefore, the excess pressure P^{ex} is given by the expression

$$\beta P^{ex}\left[\{\rho_i\}\right] = -\Phi_{hs}^{ex} + \sum_{\alpha} n_{\alpha} \frac{\delta \Phi_{hs}^{ex}}{\delta n_{\alpha}}. \tag{2.56}$$

To illustrate the mathematical procedure to derive FMT, we focus on one-component hard-sphere fluid. Within the framework of SPT, which is used to calculate the thermodynamic properties of spherical particle γ with radius R_{γ} solvated in a bulk hard sphere fluid, the excess chemical potential $\mu^{ex} \to PV_{\gamma}$ in the limit $R_{\gamma} \to \infty$, where P is the bulk pressure of hard sphere fluid, and V_{γ} is the volume of the solute. The bulk pressure P can be decomposed into two terms: ideal term P^{id} and excess term P^{ex}. The ideal part of pressure is known exactly,

$$\beta P^{id} = \rho, \tag{2.56}$$

where ρ is the bulk density of hard-sphere fluid. On the other hand, the excess chemical potential of solute is given by

$$\beta \mu^{ex} = \frac{\delta \Phi_{hs}^{ex}}{\delta \rho_{\gamma}} = \sum_{\alpha} \frac{\partial \Phi_{hs}^{ex}}{\partial n_{\alpha}} \frac{\partial n_{\alpha}}{\partial \rho_{\gamma}} = \frac{\partial \Phi_{hs}^{ex}}{\partial n_3} V_{\gamma} + \mathrm{O}\left(R_{\gamma}{}^2\right). \tag{2.56}$$

where R_{γ} is ???. Therefore, we can easily find the equivalence between $\partial \Phi_{hs}^{ex} / \partial n_3$ and βP for a uniform fluid. (not clear). Within the framework of FMT, a further assumption can be made to postulate that such equivalency can be applied to inhomogeneous fluid. Thus,

$$\frac{\partial \Phi_{hs}^{ex}}{\partial n_3} = \beta P^{ex}\left[\{\rho_i\}\right] + n_0. \tag{2.56}$$

Substitution of Eq. (2.56) into Eq. (2.56) yields

$$\frac{\delta\Phi_{hs}^{ex}}{\delta n_3} = -\Phi_{hs}^{ex} + \sum_{\alpha} n_\alpha \frac{\delta\Phi_{hs}^{ex}}{\delta n_\alpha} + n_0 . \tag{2.56}$$

Combination of Eq. (2.56) and Eq. (2.56) leads to determination of five coefficients in Eq. (2.56) which is each function of ϕ_i.

After some simple derivation, the five coefficients are

$$\begin{cases} \phi_1 = -\ln(1-n_3) + c_1 \\ \phi_2 = c_2 / (1-n_3) \\ \phi_3 = c_3 / (1-n_3)^2 \\ \phi_4 = c_4 / (1-n_3) \\ \phi_5 = c_5 / (1-n_3)^2 \end{cases}, \tag{2.56}$$

where c_i are constants. The coefficients of c_1, c_2, and c_4 can be obtained from the low density limit of the free energy functional given in Eq. (2.45). For homogeneous one-component hard-sphere fluid at low density, i.e. $\rho \to 0$,

$$\lim_{\rho\to\infty}\left[-\ln(1-n_3)\right] = n_3, \tag{2.57}$$

$$\lim_{\rho\to\infty}(1-n_3) = 1, \tag{2.58}$$

Substituting Eqs. (2.56), (2.57), and (2.58) into Eq. (2.45) yields

$$c_1 = 0, \quad c_2 = 1, \quad c_4 = -1. \tag{2.59}$$

On the other hand, c_3 can be obtained from the exact 2nd and 3rd virial coefficients for one-component hard spheres,

$$\beta P_{hs} / \rho = 1 + 4n_3 + 10n_3^{\,2} + \cdots . \tag{2.60}$$

For homogeneous one-component hard spheres, the vector terms in Eq. (2.56) vanish. Thus, the bulk pressure can be obtained from the combination of Eqs. (2.56) and (2.56),

$$\beta P_{hs} / \rho = \frac{1 + n_3 + \left(72\pi c_3 - 2\right) n_3^{\,2}}{\left(1 - n_3\right)^3}, \tag{2.61}$$

At low density limit, we have

$$\frac{1}{\left(1 - n_3\right)^3} \approx \left(1 + n_3 + n_3^{\,2} + \cdots\right)^3 = 1 + 3n_3 + 6n_3^{\,2} + \cdots \tag{2.62}$$

Substitution of Eq. (2.62) into (2.61) yields

$$\beta P_{hs} / \rho = 1 + 4n_3 + \left(7 + 72\pi c_3\right) n_3^{\,2} + \cdots. \tag{2.63}$$

Thus, comparison between Eq. (2.60) and (2.63) yields

$$c_3 = \frac{1}{24\pi}. \tag{2.64}$$

Finally, the constant c_5 is obtained from the requirement that the pair direct correlation function $c^{(2)}\left(r\right)$ is regular in the limit $r \to 0$ [84]. The pair direct correlation function is obtained from the second functional derivative of the free energy functional [21],

$$c^{(2)}\left(\mathbf{r}_i, \mathbf{r}_j\right) = -\frac{\delta^2 \beta F_{hs}^{ex}}{\delta\rho\left(\mathbf{r}_i\right)\delta\rho\left(\mathbf{r}_j\right)} = \; i\,j \; + \; i\,j \; + \; i\,j \; + \; i\,j \; + \; i\,j \; + \cdots\cdots \tag{2.65}$$

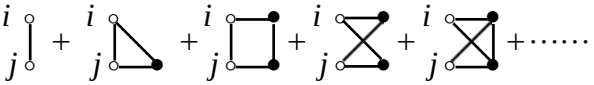

At low density limit, all higher-order diagrams in Eq. (2.65) are negligible [21] and can be obtained from the second diagram:

$$c^{(2)}\left(\mathbf{r}_i, \mathbf{r}_j\right) = \int d\mathbf{r}_k \rho\left(\mathbf{r}_k\right) f_{ik}\left(\mathbf{r}_i, \mathbf{r}_k\right) f_{ij}\left(\mathbf{r}_i, \mathbf{r}_j\right) f_{kj}\left(\mathbf{r}_k, \mathbf{r}_j\right). \tag{2.66}$$

For uniform fluid, we have

$$\rho(\mathbf{r}_k) = \rho\,. \tag{2.67}$$

Combination of Eq. (2.66) and Eq. (2.67) yields

$$\begin{aligned} c^{(2)}(\mathbf{r}_i, \mathbf{r}_j) &= \rho \int d\mathbf{r}_k\, f_{ik}\left(|\mathbf{r}_i - \mathbf{r}_k|\right) f_{ij}\left(|\mathbf{r}_i - \mathbf{r}_j|\right) f_{kj}\left(|\mathbf{r}_k - \mathbf{r}_i|\right) \\ &= \rho\, f_{ij}\left(|\mathbf{r}_i - \mathbf{r}_j|\right) \int d\mathbf{r}_k\, f_{ik}\left(|\mathbf{r}_i - \mathbf{r}_k|\right) f_{kj}\left(|\mathbf{r}_k - \mathbf{r}_i|\right), \\ &= \rho\, f\left(|\mathbf{r}|\right) \int d\mathbf{r}'\, f\left(|\mathbf{r}'|\right) f\left(|\mathbf{r} - \mathbf{r}'|\right) \end{aligned} \tag{2.68}$$

where

$$\mathbf{r} = \mathbf{r}_i - \mathbf{r}_j\,, \tag{2.69}$$

$$\mathbf{r}' = \mathbf{r}_i - \mathbf{r}_k\,. \tag{2.70}$$

The Mayer function for the hard-sphere interaction is given by

$$f(r) = \begin{cases} -1, & r \le \sigma \\ 0, & r > \sigma \end{cases}. \tag{2.71}$$

Substituting Eq. (2.71) into Eq. (2.68) yields

$$c^{(2)}(r) = \begin{cases} -\dfrac{4\pi}{3}\left(1 - \dfrac{3r}{4} + \dfrac{r^3}{16}\right)\rho, & r \le \sigma \\ 0, & r > \sigma \end{cases}, \tag{2.72}$$

where we assume $\sigma = 1$.

In Fourier space, the direct correlation function is given by

$$
\begin{aligned}
c^{(2)}(k) &= \frac{4\pi}{k}\int_0^1 r\sin(kr)\rho\left(-\frac{4\pi}{3}\right)\left(1-\frac{3r}{4}+\frac{r^3}{16}\right)dr \\
&= -\frac{16\pi^2\rho}{3k}\int_0^1 r\sin(kr)\left(1-\frac{3r}{4}+\frac{r^3}{16}\right)dr \\
&= \frac{\pi^2\rho}{3k^6}\begin{bmatrix} 4k^3\sin(k)+5k^4\cos(k)+12k^2\cos(k) \\ +24k\sin(k)+24\cos(k)-24-24k^2 \end{bmatrix}
\end{aligned}
\quad . \tag{2.73}
$$

On the other hand, the direct correlation function of the uniform fluid is [21]

$$
c^{(2)}(k) = -\sum_{\alpha}\sum_{\beta}\frac{\partial^2\Phi_{hs}^{ex}}{\partial n_\alpha \partial n_\beta}\omega_\alpha \otimes \omega_\beta \, . \tag{2.74}
$$

A comparison of Eq. (2.73) and Eq. (2.74) gives

$$
c_5 = -\frac{1}{8\pi} \, . \tag{2.75}
$$

Once we have the coefficients for Eq.(2.56), the free energy density is then given by

$$
\Phi_{hs}^{ex} = -n_0\ln(1-n_3) + \frac{n_1 n_2 - \vec{\mathbf{n}}_{V1}\cdot\vec{\mathbf{n}}_{V2}}{1-n_3} + \frac{n_2^{\,3}/3 - n_2\vec{\mathbf{n}}_{V2}\cdot\vec{\mathbf{n}}_{V2}}{8\pi(1-n_3)^2} \, . \tag{2.75}
$$

To be noted that at the bulk limit, FMT can be reduced to the scaled-particle free energy density given by

$$
\Phi_{hs}^{ex} = \frac{\beta F_{hs}^{ex}}{V} = -n_0\ln(1-n_3) + \frac{n_1 n_2}{1-n_3} + \frac{n_2^{\,3}}{24\pi(1-n_3)^2} \, . \tag{2.76}
$$

On the other hand, the bulk pressure obtained from FMT can reproduce the value from PY equation of state

$$
\beta P_{hs}/\rho = \frac{1}{\rho}\frac{\delta\Phi_{hs}^{ex}}{\delta n_3} = \frac{1+n_3+n_3^{\,2}}{(1-n_3)^3} \, . \tag{2.77}
$$

Boublik [86] and independently Mansoori, Carnahan, Starling, and Leland (BMCSL) [87] found that the thermodynamic properties of a hard-sphere fluid from PY equation can be greatly improved by an empirical combination of the results from the compressibility equation and viral equation [85]. In contrast to original FMT, BMCSL equation of state [87] is given by

$$\beta P_{CS} = \frac{n_0}{1-n_3} + \frac{n_1 n_2}{\left(1-n_3\right)^2} + \frac{{n_2}^3}{12\pi\left(1-n_3\right)^3} - \frac{n_3 {n_2}^3}{36\pi\left(1-n_3\right)^3}. \tag{2.77}$$

In contrast to BMCSL, the final term in Eq. (2.77) is absent in PY equation [88]. Thus, Eq. (2.56) can be modified as

$$\beta P_{CS} = -\Phi_{hs}^{ex} + \sum_{\alpha} n_\alpha \frac{\delta \Phi_{hs}^{ex}}{\delta n_\alpha} + n_0 . \tag{2.77}$$

Correspondingly, the five coefficients are given by [85, 88]

$$\phi_1 = -\ln\left(1-n_3\right), \tag{2.77}$$

$$\phi_2 = \frac{1}{1-n_3}, \tag{2.77}$$

$$\phi_3 = \frac{n_3 + \left(1-n_3\right)^2 \ln\left(1-n_3\right)}{36\pi {n_3}^2 \left(1-n_3\right)^2}, \tag{2.77}$$

$$\phi_4 = -\phi_2 , \tag{2.77}$$

$$\phi_5 = -3\phi_3 . \tag{2.77}$$

The corresponding excess free energy density is formulated as [85, 88]

$$\Phi_{hs}^{ex} = -n_0 \ln\left(1-n_3\right) + \frac{n_1 n_2 - \vec{\mathbf{n}}_{V1} \cdot \vec{\mathbf{n}}_{V2}}{1-n_3} + \left(n_2^{\,3} - 3n_2 \vec{\mathbf{n}}_{V2} \cdot \vec{\mathbf{n}}_{V2}\right) \frac{n_3 + \left(1-n_3\right)^2 \ln\left(1-n_3\right)}{36\pi n_3^{\,2}\left(1-n_3\right)^2} \quad . \tag{2.77}$$

Eq.(2.77) is the modified fundamental measure theory (MFMT) [85] or FMT of the White Bear version [88]. It generally improves the performance on the density profiles of inhomogeneous hard-sphere fluids and the pair distribution function over original FMT. MFMT represents the best available DFT for strongly inhomogeneous hard-sphere fluids at all densities, especially at high density. To be noted that MFMT is obtained from the empirical plugging of BMCSL equation of state rather than derived self-consistently. The results from original FMT and MFMT can be applied to not only uniform as well as inhomogeneous one-component system but also mixtures.

The functional derivative of excess Helmholtz free energy due to the hard-sphere repulsion yields the excess chemical potential $\mu_{hs,i}^{ex}$ given by

$$\begin{aligned} \beta\mu_{hs,i}^{ex}\left(\mathbf{r}\right) = \frac{\delta\beta F_{hs}^{ex}}{\delta\rho_i\left(\mathbf{r}\right)} &= \int d\mathbf{r}' \frac{\delta\Phi_{hs}^{ex}}{\delta\rho_i\left(\mathbf{r}\right)} \\ &= \sum_\alpha \int d\mathbf{r}' \frac{\partial\Phi_{hs}^{ex}}{\partial n_\alpha\left(\mathbf{r}'\right)} \frac{\delta n_\alpha\left(\mathbf{r}'\right)}{\delta\rho_i\left(\mathbf{r}\right)} \\ &= \sum_\alpha \int d\mathbf{r}' \frac{\partial\Phi_{hs}^{ex}}{\partial n_\alpha\left(\mathbf{r}'\right)} \omega_i^{(\alpha)}\left(\mathbf{r}'-\mathbf{r}\right) \end{aligned} \quad . \tag{2.78}$$

A set of $\delta\Phi_{hs}^{ex} / \delta n_\alpha\left(\mathbf{r}\right)$ from MFMT are given by

$$\frac{\partial\Phi_{hs}^{ex}}{\partial n_0\left(\mathbf{r}\right)} = -\ln\left(1-n_3\right), \tag{2.79}$$

$$\frac{\partial \Phi_{hs}^{ex}}{\partial n_1(\mathbf{r})} = \frac{n_2}{1-n_3}, \tag{2.80}$$

$$\frac{\partial \Phi_{hs}^{ex}}{\partial n_2(\mathbf{r})} = \frac{n_1}{1-n_3} + \left[\frac{\ln(1-n_3)}{n_3} + \frac{1}{(1-n_3)^2}\right]\frac{{n_2}^2 - \vec{\mathbf{n}}_{V2}^{\,2}}{12\pi n_3}, \tag{2.81}$$

$$\frac{\partial \Phi_{hs}^{ex}}{\partial n_3(\mathbf{r})} = -\left[\frac{\ln(1-n_3)}{18\pi {n_3}^3} + \frac{1-3n_3+(1-n_3)^2}{36\pi {n_3}^2(1-n_3)^3}\right]\left({n_2}^3 - 3n_2\vec{\mathbf{n}}_{V2}^{\,2}\right) + \frac{n_0}{1-n_3} + \frac{n_1 n_2 - \vec{\mathbf{n}}_{V1}\cdot\vec{\mathbf{n}}_{V2}}{(1-n_3)^2}, \tag{2.82}$$

$$\frac{\partial \Phi_{hs}^{ex}}{\partial \vec{\mathbf{n}}_{V1}(\mathbf{r})} = -\frac{\vec{\mathbf{n}}_{V2}}{1-n_3}, \tag{2.83}$$

$$\frac{\partial \Phi_{hs}^{ex}}{\partial \vec{\mathbf{n}}_{V2}(\mathbf{r})} = -\frac{\vec{\mathbf{n}}_{V1}}{1-n_3} - \left[\frac{\ln(1-n_3)}{n_3} + \frac{1}{(1-n_3)^3}\right]\frac{n_2\vec{\mathbf{n}}_{V2}}{6\pi n_3}. \tag{2.84}$$

2. 5. 2 Thermodynamic Perturbation Theory for Chain Connectivity

The excess Helmholtz free energy due to chain connectivity exists only in polymeric fluids. In other words, for pure monomeric fluids, this term vanishes. The thermodynamic properties due to chain connectivity can be described by the perturbation theory using the corresponding monomeric system as a reference. For uniform systems, the thermodynamic perturbation theory (TPT) was first proposed by Wertheim [89] to the study of associating hard-sphere molecules by using monomeric hard-sphere fluids as the reference. Although there are many different versions of TPT, this subsection gives a brief derivation of the extension of the first-order thermodynamic perturbation theory (TPT1) for inhomogeneous systems.

For simplicity, we consider a mixture of hard-sphere chains and hard spheres. In this case, the thermodynamic non-ideality comes from the hard-sphere repulsion and the constraint of chain connectivity. The formation of the bond is essentially to bring two monomers from infinite separation to contact; and this work is equivalent to the potential of mean force [90].

The potential of mean force W is given by

$$\beta W\left(\sigma_p\right) = -\ln y_{MM}\left(\sigma_p\right), \tag{2.84}$$

where $y_{pp}\left(\sigma_p\right)$ is the contact value of the cavity correlation function (CCF) of the polymer segments when they are disconnected. W can be understood as the Helmholtz energy required to link two polymer segments together in the medium.

The CCF is given by

$$y(r) \equiv g(r)\exp\left[\beta u(r)\right], \tag{2.84}$$

in which $g(r)$ is the pair distribution function (PDF), and $u(r)$ is the pair interaction potential. In case of hard-sphere chains, $u(r) = 0$ for $r \geq \sigma_p$, the contact value of CCF is equal to that of PDF:

$$y_{pp}\left(\sigma_p\right) = g_{pp}\left(\sigma_p\right). \tag{2.84}$$

If we further assume that all bonds of the hard-sphere chains are independent of each other, the excess Helmholtz free energy F_{ch}^{ex} for forming a hard-sphere chain of polymerization M is

$$\beta F_{ch}^{ex} = -(M-1)\ln y_{pp}\left(\sigma_p\right), \tag{2.84}$$

where $M-1$ represents the number of bonds within a hard-sphere chain. Thus, the total excess Helmholtz free energy due to chain connectivity for a mixture of N hard-sphere chains with the same degree of polymerization is

$$\beta F_{ch}^{ex} = -N(M-1)\ln y_{pp}(\sigma_p). \tag{2.84}$$

In generalization of TPT1 for inhomogeneous systems, we can present F_{ch}^{ex} in a similar manner of Eq. (2.56),

$$\beta F_{ch}^{ex} = \int \Phi_{ch}^{ex}\left[\{n_\alpha(\mathbf{r})\}\right] d\mathbf{r}, \tag{2.84}$$

where Φ_{ch}^{ex} is the free energy density due to the chain connectivity.

For a mixture of uniform hard-sphere chains and hard-sphere monomers, Φ_{ch}^{ex} is homogeneous and is given by [79]

$$\Phi_{ch}^{ex,b} = \frac{1-M}{M}\rho_{p,b}\ln y_{pp}^{b}(\sigma_p), \tag{2.84}$$

where $\rho_{p,b}$ is the bulk polymer segment density. To extend Eq. (2.84) to inhomogeneous polymeric fluids, the bulk density and CCF can be represented by the weighted densities of FMT. $\rho_{p,b}$ in Eq. (2.84) is replaced by $n_{0p}\zeta_p$ and the cavity correlation function for inhomogeneous fluid is represented by [79, 91]

$$y_{pp}(\sigma_M, n_\alpha) = g_{pp}(\sigma_p, n_\alpha) = \frac{1}{1-n_3} + \frac{n_2\sigma_M\zeta}{4(1-n_3)^2} + \frac{{n_2}^2{\sigma_M}^2\zeta}{72(1-n_3)^3}, \tag{2.84}$$

where $\zeta_p = 1-\vec{\mathbf{n}}_{V2p}\cdot\vec{\mathbf{n}}_{V2p}/{n_{2p}}^2$ and $\zeta = 1-\vec{\mathbf{n}}_{V2}\cdot\vec{\mathbf{n}}_{V2}/{n_2}^2$. Thus, the free energy density due to the chain connectivity for inhomogeneous hard-sphere chains and hard-sphere mixture is given by

$$\Phi_{ch}^{ex} = \frac{1-M}{M} n_{0p} \zeta_p \ln y_{pp}\left(\sigma_p, n_\alpha\right). \tag{2.84}$$

Now we consider a mixture of homo-polyelectrolytes and ions in a solvent which is treated as dielectric continuum with dielectric constant ε. Polyelectrolyte is composed of charged hard-sphere chain of each segment with electric charge $Z_p e$, and ions are consisting of charged hard spheres with cation charge $Z_+ e$ and anion charge $Z_- e$. Here e stands for elementary charge.

The pair potential in a system composed of charged hard spheres is given by

$$\beta u_{ij}\left(r\right) = \begin{cases} \infty, & r < \sigma_{ij} \\ l_B \dfrac{Z_i Z_j}{r}, & r \geq \sigma_{ij} \end{cases}, \tag{2.84}$$

where $l_B = \beta e^2 / \varepsilon$ is Bjerrum length.

Because the pair potential does not vanish at contact point and the exact PDF is elaborate to obtain, it is more subtle to get the free energy density for charged polymer. One popular way to obtain the contact value of the PDF function is from Blum's mean-spherical approximation (MSA) [92-94] for charged hard spheres. The contact value of PDF from MSA for inhomogeneous polyelectrolyte solution is given by [95, 96]

$$g_{pp}^{MSA}\left(\sigma_p, n_\alpha\right) = \frac{1}{1-n_3} + \frac{n_2 \sigma_p \left(1 - \vec{\mathbf{n}}_{V2} \cdot \vec{\mathbf{n}}_{V2} / n_2^{\,2}\right)}{4\left(1-n_3\right)^2} - \frac{\Gamma^2 a_p^{\,2}}{4\pi\sigma_p l_B}, \tag{2.84}$$

where

$$\Gamma^2 = \pi l_B \sum_{i=p,+,-} n_{0i} \left(\frac{1}{1+\Gamma\sigma_i}\right)^2 \left(Z_i - \frac{\pi P_n \sigma_i^{\,2}}{2\left(1-n_3\right)}\right)^2, \tag{2.84}$$

and

$$P_n = \frac{\sum_{i=p,+,-} \frac{2n_{1i}Z_i}{1+\Gamma\sigma_i}}{1+\frac{3}{1-n_3}\sum_{i=p,+,-}\frac{n_{3i}}{1+\Gamma\sigma_i}}. \tag{2.84}$$

In the above three equations, we use weighted densities of FMT to replace the bulk density contribution.

The pair potential at contact is known exactly

$$u_{pp}\left(\sigma_p\right) = \frac{l_B Z_p^{\ 2}}{\sigma_p}. \tag{2.84}$$

Substitution of Eq. (2.84) and Eq. (2.84) into Eq. (2.84) yields

$$y_{pp}\left(\sigma_p, n_\alpha\right) = g_{pp}^{MSA}\left(\sigma_p, n_\alpha\right)\exp\left(\frac{l_B Z_p^{\ 2}}{\sigma_p}\right). \tag{2.84}$$

However, it has been shown that $g_{pp}^{MSA}\left(\sigma_p, n_\alpha\right)$ from MSA is not very accurate for high coupling and low polymer segment density [96]. A major improvement over PDF at contact is from the EXP approximation [97-99]given by

$$g_{pp}^{EXP}\left(\sigma_p, n_\alpha\right) = g_{pp}^{hs}\left(\sigma_p, n_\alpha\right)\exp\left[g_{pp}^{MSA}\left(\sigma_p, n_\alpha\right) - g_{pp}^{hs}\left(\sigma_p, n_\alpha\right)\right], \tag{2.84}$$

where $g_{pp}^{hs}\left(\sigma_p, n_\alpha\right)$ is the PDF for hard-sphere at contact from MSA given by

$$g_{pp}^{hs}\left(\sigma_p, n_\alpha\right) = \frac{1}{1-n_3} + \frac{n_2\sigma_p\left(1-\vec{\mathbf{n}}_{V2}\cdot\vec{\mathbf{n}}_{V2}/n_2^{\ 2}\right)}{4\left(1-n_3\right)^2}. \tag{2.84}$$

Please note that Eq. (2.84) is different from Eq. (2.84), because Eq. (2.84) is solved from MSA route, while Eq. (2.84) is from FMT. By substituting both Eq. (2.84) and Eq. (2.84) into Eq. (2.84), the CCF of polyelectrolyte is given by [67, 76]

$$y_{pp}\left(\sigma_p, n_\alpha\right)=\left[\frac{1}{1-n_3}+\frac{n_2\sigma_p\left(1-\vec{\mathbf{n}}_{V2}\cdot\vec{\mathbf{n}}_{V2}/n_2^{\,2}\right)}{4\left(1-n_3\right)^2}\right]\times\exp\left(-\frac{\Gamma^2 a_p^{\,2}}{4\pi\sigma_p l_B}\right)\exp\left(\frac{l_B Z_p^{\,2}}{\sigma_p}\right). \quad (2.84)$$

Thus the free energy density due to chain connectivity of homo-polyelectrolyte can be obtained from the combination of Eqs. (2.84) and (2.84).

The expression for the excess Helmholtz energy density is complicated for heterogeneous polymers, e.g. polyelectrolytes composed of segments with different charges and sizes. To illustrate the free energy density due to chain connectivity for heteropolymers, as an example, we consider a mixture consisting of m_p species of block copolymers and m_a species of monomers. Each block copolymer is made of p_k blocks of polymerized monomers, i.e., the k-th block copolymer has M_i^k number of segments with diameter σ_i^k and point charge Z_i^k ($i=1,2,\cdots,p_k$). Thus, within k-th type of block copolymer, there are M_i^k-1 number of $B_i^k-B_i^k$ bonds for identical bead i, p_k-1 number of $B_i^k-B_{i+1}^k$ bonds for different consecutive beads. The schematic representation of block copolymer is shown in Figure 2-1.

Similar to Eq. (2.84), the free energy density due to k-th type of block copolymer $\Phi_{ch,k}^{ex}$ is given by

$$\Phi_{ch,k}^{ex} = -\frac{n_0^k \zeta^k}{\sum_{i=1}^{p_k} M_i^k} \left[\sum_{i=1}^{p_k} \left(M_i^k - 1 \right) \ln y_{i,i}^k \left(\sigma_{i,i}^k, n_\alpha \right) + \sum_{i=1}^{p_k - 1} \ln y_{i,i+1}^k \left(\sigma_{i,i+1}^k, n_\alpha \right) \right], \tag{2.85}$$

where

$$n_0^k = \sum_{i=1}^{p_k} n_{0,i}^k , \tag{2.86}$$

$$\zeta^k = 1 - \frac{\vec{\mathbf{n}}_{V2}^k \cdot \vec{\mathbf{n}}_{V2}^k}{n_2^k \times n_2^k} = 1 - \frac{\sum_{i=1}^{p_k} \vec{\mathbf{n}}_{V2,i}^k \cdot \sum_{i=1}^{p_k} \vec{\mathbf{n}}_{V2,i}^k}{\left(\sum_{i=1}^{p_k} n_{2,i}^k \right)^2}, \tag{2.87}$$

$$\sigma_{i,j}^k = \frac{1}{2} \left(\sigma_i^k + \sigma_j^k \right). \tag{2.88}$$

The CCF in Eq. (2.85) is given by

$$\begin{aligned} y_{i,j}^k \left(\sigma_{i,j}^k, n_\alpha \right) = & \left[\frac{1}{1 - n_3} + \frac{n_2 \sigma_i^k \sigma_j^k \left(1 - \vec{\mathbf{n}}_{V2} \cdot \vec{\mathbf{n}}_{V2} / n_2^2 \right)}{4 \left(1 - n_3 \right)^2 \sigma_{i,j}^k} \right] \cdot \\ & \times \exp\left(-\frac{\Gamma^2 a_i^k a_j^k}{4\pi \sigma_{i,j}^k l_B} \right) \exp\left(\frac{l_B Z_i^k Z_j^k}{\sigma_{i,j}^k} \right) \end{aligned} \tag{2.89}$$

The total free energy density is a sum of all polymers:

$$\Phi_{ch}^{ex} = \sum_{k=1}^{m_p} \Phi_{ch,k}^{ex} . \tag{2.90}$$

In all cases, the excess chemical potential $\mu_{ch,t}^{ex}$ due to chain connectivity is given by

$$\beta \mu_{ch,t}^{ex} \left(\mathbf{r} \right) = \frac{\delta \beta F_{ch}^{ex}}{\delta \rho_t \left(\mathbf{r} \right)} = \sum_\alpha \int d\mathbf{r}' \frac{\partial \Phi_{ch}^{ex}}{\partial n_{\alpha,t} \left(\mathbf{r}' \right)} \omega_t^{(\alpha)} \left(\mathbf{r}' - \mathbf{r} \right). \tag{2.91}$$

For block copolymers, t applies to all species of block copolymer segments and monomers. Unlike Eq. (2.78), $n_{\alpha,t}(\mathbf{r})$ in Eq. (2.91) are not total weighted densities but weighted densities of t-th specie. The detailed expressions of $\mu_{ch,t}^{ex}$ can be found in Appendix A.

2. 5. 3 Excess Helmholtz Energy Due to Van der Waals Attraction

In this subsection, we present the derivation of excess Helmholtz free energy due van der Waals attraction. For simplicity, van der Waals force is represented by a pairwise attractive inter-particle force between two spherical particles. Typical examples of van der Waals fluids include Square-Well [100] (SW), Lennard-Jones [101] (LJ), and Yukawa [102] potentials. To illustrate the basic idea for formulation of the excess Helmholtz free energy due to van der Waals attraction, SW potential is used as a model fluid.

In the SW model, the pair potential is the combination of a hard-sphere potential and a fixed attractive energy of finite distance right beyond the hard core [103]. For a one-component system, the intermolecular interaction $u(r)$ is given by

$$u(r)=\begin{cases}\infty & r<\sigma \\ -\varepsilon & \sigma\le r<\lambda \\ 0 & r\ge\lambda\end{cases}, \tag{2.91}$$

where σ is the hard-core diameter, λ denotes the range of attraction, and $\varepsilon>0$ represents an attractive energy or the attraction well depth.

The simplest way to construct the excess Helmholtz free energy for inhomogeneous fluid is from the mean-field theory (MFT), which ignores the density

correlation and reduces many-body system to an effective simple one-body system. Within the framework of MFT, the excess Helmholtz free energy due to van der Waals attraction is given by

$$\beta F_{att}^{ex} = \frac{1}{2}\int\int d\mathbf{r}d\mathbf{r}' u_{att}\left(\left|\mathbf{r}-\mathbf{r}'\right|\right)\rho\left(\mathbf{r}\right)\rho\left(\mathbf{r}'\right), \tag{2.91}$$

in which the attractive potential is $u_{att}(r) = -\varepsilon$ for $r < \lambda$. Thus, the excess chemical potential due to long-range attraction $\mu_{att}^{ex}\left(\mathbf{r}\right)$ from mean-field theory is given by

$$\beta\mu_{att}^{ex}\left(\mathbf{r}\right) = \frac{\delta\beta F_{att}^{ex}}{\delta\rho\left(\mathbf{r}\right)} = \int u_{att}\left(\left|\mathbf{r}-\mathbf{r}'\right|\right)\rho\left(\mathbf{r}'\right)d\mathbf{r}'. \tag{2.92}$$

A more accurate way to formulate the excess Helmholtz free energy of an inhomogeneous fluid is from the functional expansion. The functional Taylor expansion of the excess Helmholtz free energy due to van der Waals attraction with respect to that of a bulk fluid at constant temperature, system volume and chemical potential yields

$$\begin{aligned}\beta F_{att}^{ex}\left[\rho\left(\mathbf{r}\right)\right] = \beta F_{att}^{ex}\left[\rho_b\right] + \int d\mathbf{r}\Delta\rho\left(\mathbf{r}\right)\left.\frac{\delta\beta F_{att}^{ex}\left[\rho\left(\mathbf{r}\right)\right]}{\delta\rho\left(\mathbf{r}\right)}\right|_{\rho(\mathbf{r})=\rho_b} \\ + \frac{1}{2}\int\int d\mathbf{r}_1 d\mathbf{r}_2 \Delta\rho\left(\mathbf{r}_1\right)\Delta\rho\left(\mathbf{r}_2\right)\left.\frac{\delta^2\beta F_{att}^{ex}\left[\rho\left(\mathbf{r}\right)\right]}{\delta\rho\left(\mathbf{r}_1\right)\delta\rho\left(\mathbf{r}_2\right)}\right|_{\rho(\mathbf{r}_1)=\rho(\mathbf{r}_2)=\rho_b} + \cdots\end{aligned}, \tag{2.92}$$

where $F_{att}^{ex}\left[\rho_b\right]$ is the excess Helmholtz free energy due to attraction of bulk fluid, ρ_b is the bulk density, and $\Delta\rho\left(\mathbf{r}\right) = \rho\left(\mathbf{r}\right) - \rho_b$. At equilibrium, terms beyond the second-order have little contribution to total excess Helmholtz free energy. In other words, the first-order and second-order derivatives of excess Helmholtz free energy are related to the

first-order and second-order direct correlation functions (DCF) of the bulk fluid, respectively,

$$\left.\frac{\delta\beta F_{att}^{ex}\left[\rho(\mathbf{r})\right]}{\delta\rho(\mathbf{r})}\right|_{\rho(\mathbf{r})=\rho_b} = -\Delta C_{att}^{(1)}, \tag{2.92}$$

$$\left.\frac{\delta^2\beta F_{att}^{ex}\left[\rho(\mathbf{r})\right]}{\delta\rho(\mathbf{r}_1)\delta\rho(\mathbf{r}_2)}\right|_{\rho(\mathbf{r}_1)=\rho(\mathbf{r}_2)=\rho_b} = -C_{att}^{(2)}\left(\left|\mathbf{r}_1-\mathbf{r}_2\right|\right). \tag{2.92}$$

The first-order direct correlation function $\Delta C_{att}^{(1)}$ is equal to bulk excess chemical potential due to van der Waals attraction μ^{att}; the second-order direct correlation function due to van der Waals attraction $C_{att}^{(2)}\left(\left|\mathbf{r}_1-\mathbf{r}_2\right|\right)$ is simply called direct correlation function due to van der Waals attraction and labeled as $c^{att}\left(\left|\mathbf{r}_1-\mathbf{r}_2\right|\right)$.

With expressions for the first- and second-order direct correlation functions, Eq. (2.92) can be rewritten as

$$\begin{aligned}\beta F_{att}^{ex}\left[\rho(\mathbf{r})\right] = \beta F_{att}^{ex}\left[\rho_b\right] + \beta\mu^{att}\int d\mathbf{r}\Delta\rho(\mathbf{r}) \\ -\frac{1}{2}\int\int d\mathbf{r}_1 d\mathbf{r}_2\Delta\rho(\mathbf{r}_1)\Delta\rho(\mathbf{r}_2)c^{att}\left(\left|\mathbf{r}_1-\mathbf{r}_2\right|\right)\end{aligned}. \tag{2.92}$$

while the first term on the right hand side of Eq. (2.92) vanishes in functional derivative of excess Helmholtz free energy, and the second term cancels out combined with the bulk chemical potential, derivation of $c^{att}\left(\left|\mathbf{r}_1-\mathbf{r}_2\right|\right)$ is more difficult.

One popular way to solve $c^{att}\left(\left|\mathbf{r}_1-\mathbf{r}_2\right|\right)$ is from the Ornstein-Zernike (OZ) equation. For one-component homogeneous systems, direct correlation function *c* and total correlation function h are related within OZ equation [103],

$$h(\mathbf{r}_1,\mathbf{r}_2) = c(\mathbf{r}_1,\mathbf{r}_2) + \rho_b \int c(\mathbf{r}_1,\mathbf{r}_3) h(\mathbf{r}_3,\mathbf{r}_2)\, d\mathbf{r}_3, \tag{2.92}$$

where $h(\mathbf{r}_1,\mathbf{r}_2) = g(\mathbf{r}_1,\mathbf{r}_2) - 1$. The total direct correlation function includes hard-sphere repulsion part c^{hs} and van der Waals attraction c^{att},

$$c(\mathbf{r}_1,\mathbf{r}_2) = c^{hs}(\mathbf{r}_1,\mathbf{r}_2) + c^{att}(\mathbf{r}_1,\mathbf{r}_2). \tag{2.92}$$

Because there are two unknowns in one equation in OZ equation, a closure is necessary to solve Eq. (2.92). Mean spherical approximation has been an effective tool to solve h and c analytically. The MSA is defined in terms of the PDF and DCF by

$$g(r) = 0, \qquad r < \sigma, \tag{2.92}$$

$$c(r) = -\beta u(r), \quad r > \sigma. \tag{2.92}$$

Combining with MSA, OZ equation can be solved analytically. However, the solution of OZ equation is non-trivial. For SW fluids, the DCF has been recently derived by Tang [100] for $\sigma < \lambda \le 2\sigma$ and by Hlushak et al. [104] for $2\sigma < \lambda \le 3\sigma$. The DCF of LJ [101] and Yukawa [102] fluids are also derived by Tang. The detailed derivations of DCF are referred to above cited papers.

The excess chemical potential due to long-range attraction $\mu_{att}^{ex}(\mathbf{r})$ from quadratic expansion is given by

$$\beta\mu_{att}^{ex}(\mathbf{r}) = \frac{\delta\beta F_{att}^{ex}}{\delta\rho(\mathbf{r})} = \beta\mu^{att} - \int \Delta\rho(\mathbf{r}')\, c^{att}\left(|\mathbf{r}-\mathbf{r}'|\right) d\mathbf{r}'. \tag{2.93}$$

2. 5. 4 Excess Helmholtz Energy Due to Direct Coulomb Interaction

The excess Helmholtz free energy due to the Coulomb interactions can be separated into two parts: one is the direct Coulomb interaction and the second part

accounts for the correlation of charge distributions. In this subsection, we present the derivation of excess Helmholtz free energy due to direct Coulomb interaction F_C^{ex} . The excess Helmholtz energy due to charge correlation will be described in next subsection.

The excess Helmholtz energy due to direct Coulomb Interaction F_C^{ex} appears in conventional Poisson-Boltzmann (PB) equation [105]. It is identical to that from the mean-field given bytheory

$$\beta F_C^{ex} = \frac{l_B}{2} \sum_{i,j=p,+,-} \int\int d\mathbf{r} d\mathbf{r}' \frac{Z_i Z_j \rho_i(\mathbf{r}) \rho_j(\mathbf{r}')}{|\mathbf{r}-\mathbf{r}'|}. \tag{2.93}$$

It should be noted that because of the long-range nature of the Coulomb potential, the integrals on the right side of Eq. (2.93) diverges for any pair potential. To avoid the numerical problem, the electrostatic energy is often calculated from the local mean electrostatic potential $\psi(\mathbf{r})$,

$$\psi(\mathbf{r}) = \int d\mathbf{r}' \sum_{j=p,+,-} \frac{Z_j e \rho_j(\mathbf{r}')}{4\pi\varepsilon|\mathbf{r}-\mathbf{r}'|}. \tag{2.93}$$

The local mean electrostatic potential satisfies the Poisson equation

$$\nabla^2 \psi(\mathbf{r}) = -\frac{4\pi e}{\varepsilon} \rho_c(\mathbf{r}), \tag{2.93}$$

where $\rho_c(\mathbf{r}) = \sum_{i=p,+,-} Z_i \rho_i(\mathbf{r})$. Eq. (2.93) can be solved analytically for a one-dimensional system with appropriate boundary conditions and numerically for a three-dimensional system. The detailed solutions of Poisson equation in one-dimension are discussed in Appendix B.

The Helmholtz energy functional given by Eq. (2.93) alone would lead to the conventional Boltzmann distribution for charged species. Thus, the PB equation for electrostatic systems can be understood as a simple application of the DFT.

The excess chemical potential due to direct Coulomb interaction $\mu_{C,i}^{ex}(\mathbf{r})$ is given by

$$\beta\mu_{C,i}^{ex}(\mathbf{r}) = \frac{\delta\beta F_C^{ex}}{\delta\rho_i(\mathbf{r})} = \beta Z_i e\psi(\mathbf{r}). \tag{B.94}$$

To be noted that the excess chemical potential in bulk vanishes because of charge neutrality in bulk electrolyte solution.

2. 5. 5 Electrostatic Correlation

In this subsection, we discuss the formulation of excess Helmholtz free energy due to electrostatic correlation F_{el}^{ex}. Similar to the calculation of F_{att}^{ex}, F_{el}^{ex} is approximated by a quadratic functional Taylor expansion with respect to that for a monomeric bulk fluid of densities $\{\rho_i^b\}$ [106],

$$\begin{aligned}\beta F_{el}^{ex}\left[\{\rho_i(\mathbf{r})\}\right] = \beta F_{el}^{ex}\left[\{\rho_i^b\}\right] + \sum_{i=+,-}\beta\mu_i^{el}\int d\mathbf{r}\Delta\rho_i(\mathbf{r}) \\ -\frac{1}{2}\sum_{i,j=+,-}\int\int d\mathbf{r}_1 d\mathbf{r}_2 \Delta\rho_i(\mathbf{r}_1)\Delta\rho_j(\mathbf{r}_2)c_{ij}^{el}(|\mathbf{r}_1-\mathbf{r}_2|)\end{aligned}, \tag{2.94}$$

where μ_i^{el} is a set of bulk excess chemical potential due to electrostatic correlation of specie i, and c_{ij}^{el} is DCF due to electrostatic correlation. In writing (2.94), it is assumed that the effect of chain connectivity on the electrostatic part of the DCF can be neglected [76]. Thus, $c_{ij}^{el}(r)$ can be obtained from MSA [106],

$$c_{ij}^{el}(r) = c_{ij}(r) - c_{ij}^{C}(r) - c_{ij}^{hs}(r), \tag{2.94}$$

in which $c_{ij}(r) = -\beta u_{ij}(r)$ is total DCF from MSA, $c_{ij}^{C}(r) = -l_B Z_i Z_j / r$ is the DCF due to direct Coulomb interaction and $c_{ij}^{hs}(r)$ is that due to hard-sphere repulsion from PY approximation [80]. One interesting feature of $c_{ij}^{el}(r)$ is that it vanishes when $r > \sigma_{ij} = (\sigma_i + \sigma_j)/2$. Therefore, only inside core part is important to the DFT calculation.

The DCF due to Coulomb interaction $c_{ij}^{el}(r) + c_{ij}^{C}(r)$ from MSA is derived by Blum [93] and later by Hiroike[107] for asymmetric electrolytes. When $0 \le r \le |\sigma_i - \sigma_j|/2$, the DCF is [107]

$$c_{ij}(r) - c_{ij}^{hs}(r) = -2l_B\left[-Z_i N_j + X_i\left(N_i + \Gamma X_i\right) - (\sigma_i/3)\left(N_i + \Gamma X_i\right)^2\right], \tag{2.94}$$

and when $|\sigma_i - \sigma_j|/2 \le r \le \sigma_{ij}$,

$$c_{ij}(r) - c_{ij}^{hs}(r) = l_B\left[\left(\sigma_i - \sigma_j\right)L_1 - rL_2 + r^2 L_3 + r^4 L_4\right], \tag{2.94}$$

where,

$$\begin{aligned}
L_1 &= \frac{X_i + X_j}{4}\left(S_i - S_j\right) - \frac{\sigma_i - \sigma_j}{16}\left[\left(S_i + S_j\right)^2 - 4N_i N_j\right] \\
L_2 &= \left(X_i - X_j\right)\left(N_i - N_j\right) + \left(X_i^{\,2} + X_j^{\,2}\right)\Gamma + \left(\sigma_i + \sigma_j\right)N_i N_j \\
&\quad + \left[\sigma_i S_i^{\,2} + \sigma_j S_j^{\,2}\right]/3 \\
L_3 &= \frac{X_i}{\sigma_i}S_i + \frac{X_j}{\sigma_j}S_j + N_i N_j - \left[S_i^{\,2} + S_j^{\,2}\right]/2 \\
L_4 &= \frac{S_i^{\,2}}{6\sigma_i^{\,2}} + \frac{S_j^{\,2}}{6\sigma_j^{\,2}}
\end{aligned} \tag{2.94}$$

and

$$S_i = N_i + \Gamma X_i \,. \tag{2.94}$$

The parameter Γ is given by

$$\Gamma = \left(\pi l_B \sum_i \rho_i^b X_i^{\,2} \right)^{1/2}, \tag{2.94}$$

and the parameter N_i can be obtained from

$$N_i = \frac{X_i - Z_i}{\sigma_i}, \tag{2.94}$$

where X_i is solved from the system of linear equations

$$\left(1 + \Gamma \sigma_i\right) X_i + v \sigma_i^{\,2} \sum_j \rho_j^b \sigma_j X_j = Z_i, \tag{2.94}$$

$$v \equiv \left(\pi / 2\right) \left[1 - \left(\pi / 6\right) \sum_i \rho_i^b \sigma_i^{\,3} \right]^{-1}. \tag{2.94}$$

The quadratic expansion is sufficient to capture counter-intuitive electrostatic phenomena such as attraction between like charges and charge inversion in the presence of multivalent ions, which defy predictions for conventional mean-field theories.

The excess chemical potential due to electrostatic correlation $\mu_{el,i}^{ex}\left(\mathbf{r}\right)$ of specie i is given by

$$\beta \mu_{el,i}^{ex}\left(\mathbf{r}\right) = \frac{\delta \beta F_{el}^{ex}}{\delta \rho_i\left(\mathbf{r}\right)} = \beta \mu_i^{el} - \sum_{j=+,-} \int \Delta \rho_j\left(\mathbf{r}'\right) c_{ij}^{el}\left(\left|\mathbf{r} - \mathbf{r}'\right|\right) d\mathbf{r}'. \tag{2.95}$$

2. 6 Numerical Method

For three-dimensional system where the density profile is non-symmetric, the direct solution of Eqs. (2.14) and (2.15) is computationally expensive. For multi-

dimensional systems, the density profile and thermodynamic properties can be obtained from a hybrid method [10] which we will discuss later on. For one-dimensional systems, the calculation time can be drastically reduced.

For a system with spherical geometry, the density distribution varies only in *r* direction. In that case, Eqs. (2.17) and (2.24) can be simplified to

$$\rho_a(r) = \exp\left[\beta\mu_a - \beta\Psi_a(r) - \frac{\partial\beta F^{ex}}{\partial\rho_a(r)}\right], \tag{2.96}$$

$$\rho_p(r) = \exp(\beta\mu_M)\int d\mathbf{R}\sum_{i=1}^{M}\delta(r-r_i)\exp\left[-\beta V_b(\mathbf{R}) - \beta\sum_{j=1}^{M}\lambda_j(\mathbf{r}_j)\right]. \tag{2.96}$$

Substituting Eq. (2.13) into Eq. (2.96) yields

$$\rho_p(r) = \exp(\beta\mu_M)\sum_{j=1}^{M}\exp\left[-\beta\lambda_j(r_j)\right]G^i(r)G^{M+1-i}(r), \tag{2.96}$$

where the propagator functions $G^i(r)$ arise from the connection of the polymer segments due to the bond connectivity. They are identical to the Green functions used in a typical polymer SCFT [108]. The propagator functions are determined from the recurrence relation [29]

$$G^i(r) = \int dr'\exp\left[-\beta\lambda_i(r')\right]\frac{\theta(\sigma_p - |r-r'|)}{2\sigma_p}G^{i-1}(r'), \tag{2.96}$$

for $i = 2,...,M$ with $G^1(r) = 1$.

If the chain length approaches infinity, the effect of end segments becomes less significant and all segments in polymer are indistinguishable. In this case, the Green

function uniformly approaches a limiting function $G(r)$ and can be solved self-consistently by the relation [109],

$$G(r) = \int dr' \exp\left[-\beta\lambda(r')\right] \frac{\theta\left(\sigma_p - |r - r'|\right)}{2\sigma_p} G(r'), \tag{2.96}$$

and accordingly, Eq. (2.96) can be simplified as

$$\rho_p(r) = M \exp\left(\beta\mu_M - \beta\lambda(r)\right)\left[G(r)\right]^2. \tag{2.96}$$

On the other hand, for a slab system where the density profile is only z dependent, the density distributions of monomers and polymer segments are given by

$$\rho_a(z) = \exp\left[\beta\mu_a - \beta\Psi_a(z) - \frac{\partial\beta F^{ex}}{\partial\rho_a(z)}\right], \tag{2.97}$$

$$\rho_p(z) = \exp\left(\beta\mu_M\right)\sum_{j=1}^{M} \exp\left[-\beta\lambda_j(z_j)\right] G^i(z) G^{M+1-i}(z) \tag{2.98}$$

where

$$G^i(z) = \int dz' \exp\left[-\beta\lambda_i(z')\right] \frac{\theta\left(\sigma_p - |z - z'|\right)}{2\sigma_p} G^{i-1}(z'), \tag{B.99}$$

for $i = 2, ..., M$ with $G^1(z) = 1$. For long chain, these Green functions are the same,

$$G^i(z) = G(z), \tag{B.100}$$

and Eq. (2.98) can be simplified as

$$\rho_p(z) = M \exp\left(\beta\mu_M - \beta\lambda(z)\right)\left[G(z)\right]^2. \tag{B.101}$$

For mixture of polymers and monomers, the chemical potentials of both components can be extended from Wertheim's TPT1 equation of state for bulk hard-sphere-chain fluids [110],

$$\begin{aligned}\beta\mu_a &= \ln\rho_a^b + \beta\mu_a^{hs}\left(\rho_a^b,\rho_p^b\right) + \beta\mu_a^{att} + \beta\mu_a^{C} + \beta\mu_a^{el} \\ &\quad + \frac{1-M}{M}\rho_p^b \frac{\partial \ln y_{pp}^b\left(\sigma_a,\sigma_p\right)}{\partial\rho_a^b}\end{aligned}, \tag{2.101}$$

$$\begin{aligned}\beta\mu_M &= \ln\rho_M^b + M\beta\mu_M^{hs}\left(\rho_a^b,\rho_p^b\right) + M\beta\mu_M^{att} + M\beta\mu_M^{C} \\ &\quad + (1-M)\left[\ln y_{pp}^b\left(\sigma_a,\sigma_p\right) + \rho_p^b \frac{\partial \ln y_{pp}^b\left(\sigma_a,\sigma_p\right)}{\partial\rho_p^b}\right].\end{aligned} \tag{2.101}$$

To be noted that, both $\beta\mu_a^C$ and $\beta\mu_M^C$ vanish due to charge neutrality.

In this work, the density profiles of polymer segments and monomers are solved by the conventional Picard iteration method [91]. The iteration starts from an initial guess (i.e., bulk densities) for density profiles of polymer segments and monomers. The effective fields $\lambda_i(r)$ and the Green function $G^i(r)$ can be obtained from Eq. (2.96) for short polymer and from Eq. (2.96) for long polymer where end effect can be neglected. The new set of density profiles obtained from Eqs. (2.96) and (2.96) or (2.96) are then mixed with the previous results as new input. The iteration repeats until the difference between input and output density profile at all points is smaller than 1×10^{-6}. After obtaining the equilibrium density profile, the thermodynamic properties can be derived by inputting density profiles into Eqs. (2.13) and (2.25).

2. 7 Hybrid Method

As mentioned above, it would be time-consuming for DFT to obtain three-dimensional (3D) density profiles from Eqs. (2.16) and (2.17), when a simple geometry is not applicable. Because extension of molecular simulation from simple geometry systems to anisotropic systems requires essentially no increase of the computational cost and becasue DFT provides an efficient link between the microscopic structure and thermodynamic potentials, a combination of simulation and DFT takes advantages of the good features of both methods.

The main idea of the hybrid method is as following: first, we use molecular simulation to obtain the microscopic structure. For example, in solvation studies, we simulate one system containing the solute and solvent molecules. To obtain the solvent distribution near the solutes, in MC simulation the solute molecule is usually fixed while the trial moves are only applied to the solvent molecules, and in MD simulation we concern the pair distribution function between the solute and solvent molecules. After all of simulation cycles finished we output the density profile. In the second step, we will use the density profile from the molecular simulation as an input to calculate the thermodynamic properties of the system based on the DFT equations. With accurate free-energy functionals for inter-molecular and intra-molecular interactions, the numerical accuracy of the hybrid method is on the same level of molecular simulations, while drastically reduce calculation time.

In this work, the hybrid method has been applied to the study of solvent-mediated colloidal interactions, lock-and-key interaction [10], and ion solvation in water [24]. More details about hybrid method are given in Chapter 5 and 6.

Figure 2-1 Schematic representation of block copolymer.

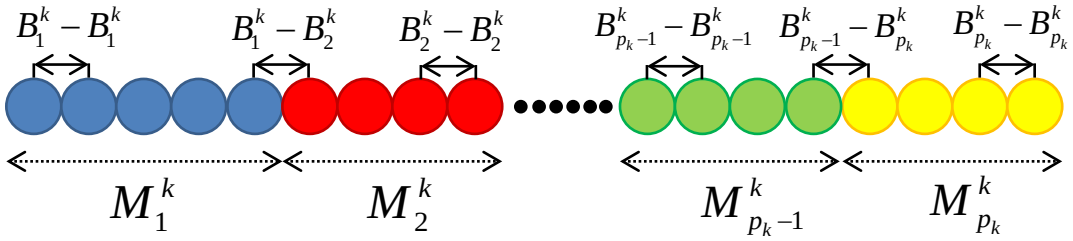

Chapter 3 Entropic forces of single-chain confinement in spherical cavities

Abstract

Thermodynamic properties of a single chain in a confined space have been studied before with the polymer scaling theory and computer simulations. However, a comprehensive understanding of the entropic effects due to the molecular excluded volume and chain connectivity is emerging only recently, especially in the limit of large polymer packing densities as often encountered in biological systems. In this work, we propose a polymer density functional theory (DFT) to study the entropic forces for the confinement of single polymer chains in spherical cavities. At conditions accessible to Monte Carlo simulations, we show that the DFT predictions are in excellent agreement with the simulation results for the distributions of polymer segments as well as the free energy of confinement. The numerical efficiency of the DFT allows us to unify key conclusions from various theoretical analyses and experimental observations.

3. 1 Introduction

A number of recent theoretical investigations have been reported on the properties of polymers in confined spaces [27, 28]. The renewed interest is motivated primarily by the close connection of polymers under confinement to biological processes such as

genome packaging in viral capsids or chaperone-assisted protein folding [111, 112]. While the knowledge for the bulk and interfacial behavior of polymers has been well advanced [34], much less known is the spatial organization and the thermodynamic properties of single polymer chains inside fully enclosed environments. Unlike polymers near a macroscopic surface or interface, the behavior of a fully confined biomacromolecule depends not only on the geometry of confinement (that restricts the chain conformation) but also on the properties of the local cellular environment (that often favors the packaging of biomacromolecules). Despite the poor characterization of molecular details in a typical biological milieu, it has been well established that the confinement effect can be partially described by simple molecular models that captures the local geometry and the thermodynamic properties of the surroundings [27, 28].

The main purpose of this work is to investigate the confinement entropy for single polymer chains in spherical cavities. The problem has been studied before in different contexts using the scaling analysis [36], self-consistent-field theory (SCFT) [113], or molecular simulations [27]. Whereas good progress has been made at low and intermediate polymer concentrations, a comprehensive understanding of the entropic effects is yet to be established, in particular at conditions of interest for biological systems [28]. To capture the effects of confinement on chain configuration and the excluded-volume interactions over a broad range of polymer conditions, we consider in this work a simple coarse-grained model where a confined polymer chain is represented by tangentially-connected hard spheres and the confinement is due to a spherical cavity. A polymer density functional theory (DFT) is used to calculate the spatial distributions of

the polymer segments, the free energies of confinement, and the surface osmotic pressures of the system at different cavity sizes, polymer chain lengths and packing fractions. The DFT predictions are validated by extensive comparison with those from alternative approaches and from Monte Carlo (MC) simulations.

The remainder of this article is organized as follows. In section 2, we introduce briefly the thermodynamic model and the theoretical/simulation methods used in this work. The detail equations for the polymer DFT have been reported in our previous publications [79]. Section 3 compares the DFT predictions with the simulation results for the density profiles of polymer segments and the free energies of packaging at different polymer chain lengths and cavity sizes. In this section, we will also present other thermodynamic properties of confined polymer chains and compare the DFT predictions with those from the scaling analysis and the SCFT calculations. In section 4, we summarize the key conclusions.

3. 2 Polymer Model and Methods

To study the influence of a spherical cavity on polymer conformation, we assume that the polymer can be represented by a linearly-connected chain of identical hard spheres dispersed in a continuous medium. The model mimics a single confined polymer chain in a good solvent. Within this model, the bond length is the same as the segment diameter and the intra-chain bonding potential satisfies [79]

$$\exp[-\beta V_b(\mathbf{R})] = \prod_{i=1}^{N-1} \frac{\delta\left(|\mathbf{r}_{i+1} - \mathbf{r}_1| - \sigma\right)}{4\pi\sigma^2}, \tag{3.1}$$

where N stands for the number of hard-sphere segments, $\mathbf{R} \equiv \left(\mathbf{r_1}, \mathbf{r_2}, ..., \mathbf{r_N}\right)$ denotes a set of coordinates describing the segmental positions, σ is the hard-sphere diameter, and δ stands for the Dirac-delta function. In a spherical cavity of radius R_c, each hard-sphere segment is subject to a "hard-wall" potential

$$\varphi(r) = \begin{cases} \infty & r > R_c - \sigma/2 \\ 0 & r \le R_c - \sigma/2 \end{cases}. \tag{3.2}$$

Qualitatively, the hard-sphere-chain model is equivalent to other coarse-grained models of self-avoiding polymer chains commonly used in the polymer literature. For example, it differs from a conventional bead-spring model of flexible polymers (e.g., FENE) mainly in terms of the bonding potential, i.e., instead of having a flexible bond length, here the separation between nearest-neighboring segments is fixed equal to the segment diameter. In both cases, neither the bending energy nor the angular constraint is applied to the neighboring bonds. It has been shown in our previous work [30] that, augmented with electrostatic and van der Waals forces among polymer segments, the hard-sphere-chain model can be generalized to describe the structure and thermodynamic properties of realistic biomacromolecules under confinement. Nevertheless, this work is focused on the athermal model for the confined chain (and the external potential) because in this case, the free energy of polymer confinement is exclusively due to the entropy effects.

We are interested to calculate the structure and thermodynamic properties of a fully confined hard-sphere chain in a hard spherical cavity by using both the polymer density functional theory (DFT) and Monte Carlo (MC) simulations. In the DFT calculations, we assume that the density of polymer segments varies only in the radial

direction. For a single chain of N tangentially connected hard spheres in a cavity of radius R_c, the local segment density is determined from the Euler-Lagrange equation:

$$\rho(r)=\frac{N\sum_{i=1}^{N}\exp\left[-\beta\lambda(r)\right]G^{i}(r)G^{N+1-i}(r)}{4\pi\int_{0}^{R_c}\sum_{i=1}^{N}\exp\left[-\beta\lambda(r)\right]G^{i}(r)G^{N+1-i}(r)r^{2}dr}, \tag{3.3}$$

where $\beta=1/(k_BT), k_B$ is the Boltzmann constant, T is the absolute temperature, $\lambda(r)$ represents an effective one-body potential affiliated with the inter-segment interactions, and $G^{i}(r)$ is a propagator function related to the chain connectivity. If the polymer chain is relatively short, $G^{i}(r)$ can be calculated from the recurrence relation

$$G^{i}(r)=\int dr'\exp\left[-\beta\lambda(r')\right]\times\frac{\theta(\sigma-|r-r'|)}{2\sigma}G^{i-1}(r'), \tag{3.4}$$

for $i=2,...,N$ with $G^{1}(r)=1$. Because the propagator function, $G^{i}(r)$, is defined in terms of individual polymer segments, the numerical iteration becomes computationally intensive for a very long polymer chain. Fortunately, the end effect becomes insignificant as the chain length increases, i.e., for a sufficiently long homogeneous polymer chain, $G^{i}(r)\approx G(r)$ becomes independent of the segment index. In that case, Eq. (3.3) is simplified to

$$\rho(r)=\frac{N\exp\left[-\beta\lambda(r)\right]G^{2}(r)}{4\pi\int_{0}^{R_c}\exp\left[-\beta\lambda(r)\right]G^{2}(r)r^{2}dr}, \tag{3.5}$$

with

$$G(r)=\int dr'\exp\left[-\beta\lambda(r')\right]\times\frac{\theta\left(\sigma-|r-r'|\right)}{2\sigma}G(r'). \tag{3.6}$$

The no-end-effect approximation (NEA) drastically accelerates the convergence of the iterations and thus enables us to investigate the properties of confined polymers of arbitrary chain length. To ensure the numerical accuracy, we will check the end effect by comparing the results from the full DFT calculations.

The one-body segment potential is related to the excess Helmholtz energy F^{ex} of the system by

$$\lambda(r)=\delta F^{ex}/\delta\rho(r). \tag{3.7}$$

For a hard-sphere-chain system, F^{ex} includes contributions due to the segment excluded volume effect the intra-chain correlations. The former is represented by a modified fundamental measure theory [85, 88], and the latter is accounted for by the first-order thermodynamic perturbation theory [79]. The explicit expression for the excess Helmholtz energy functional can be found in our previous publication [63]. With an analytical expression for F^{ex}, we can calculate the one-body density profile of polymer segments $\rho(r)$ via the Picard iteration method [101].

From the density distribution of the polymer segments, it is straightforward to calculate the Helmholtz energy and subsequently other thermodynamic properties including the entropy of confinement. The free energy of polymer confinement corresponds to the potential of mean force to “ghost” a single polymer chain from an infinite dilution into the confined space. Similar to the potential of mean force between two rigid particles, the confinement free energy is independent of the translational

entropy of the entire polymer chain. It is determined by the difference between the Helmholtz energy of a single chain in the spherical cavity and that of the same chain without the confinement:

$$\Delta F = F\left(T,V,N,\varphi\right) - F_0\left(T,V,N\right). \tag{3.8}$$

In Eq. (3.8), the reference Helmholtz energy F_0 corresponds to that of a single chain free of confinement; F_0 is related to system volume V that is accessible to the polymer center of mass, an effective thermal wavelength Λ, and the intra-molecular partition function ω_0 at infinite dilution

$$\beta F_0\left(T,V,N\right) = -\ln\left(V/\Lambda^3\right) - \ln\omega_0. \tag{3.9}$$

In calculation of the confinement free energy, both the effective thermal wavelength and the intra-molecular partition function are immaterial because the former cancels with that of the confined state and the latter is simply affiliated with the boundary condition, i.e., $\Delta F\left(V\to\infty\right) = 0$.

From the density profile of polymer segments, we can also estimate the osmotic pressure *p* inside the cavity by following the contact-value theorem [85, 114]

$$p \approx \rho_c k_B T, \tag{3.10}$$

where ρ_c is the segment density at the cavity inner surface. In writing Eq. (3.10), we neglect the interfacial tension between the polymer and the cavity surface, presumably to be small for an athermal hard-sphere chain in contact with a hard cavity.

To calibrate the numerical performance of the DFT, we have also performed the configurational-biased Monte Carlo (MC) simulations for a single hard-sphere chain confined in a spherical cavity with various combinations of the cavity size and the polymer chain length. Different MC moves, including the chain re-growth and the cut-and-rebridging methods, are used with approximately equal frequency of sampling. Each simulation runs over 5×10^8 MC steps, with the one third of MC steps for the system to reach equilibrium and rest for ensemble averages. The free energy of confinement is related to an ensemble average of the system free of confinement

$$\beta\Delta F = -\ln\left[\frac{1}{V}\int d\mathbf{r}\left\langle \exp\left(-\beta\varphi\right)\right\rangle_0\right], \tag{3.11}$$

where $\left\langle \ \right\rangle_0$ stands for an ensemble average over all polymer configurations in the free space. Because the confinement is represented by a hard-wall potential, Eq. (3.11) is implemented by generating a large number of polymer configurations in free space and enumerating the probability of the polymer insertion in the spherical cavity without overlapping with the surface.

3. 3 Results and Discussions

3. 3. 1 Comparison between MC and DFT

For a comprehensive comparison between the MC and the DFT calculations, we consider a number of different combinations of the polymer chain length and the cavity size. The thermodynamic conditions to be discussed below correspond to three representative regimes of the polymer concentration, i.e., the concentrated regime ($R_c << R_g$), the semi-dilute regime ($R_c \approx R_g$), and the dilute regime ($R_c >> R_g$). For a

tangent hard-sphere chain at infinite dilution, the radius of gyration R_g can be estimated from an empirical correlation of the simulation results [68, 115]

$$\ln\frac{R_g}{\sigma} = 0.62405\ln N - 0.87535 . \tag{3.12}$$

Eq. (3.12) is obtained by best fitting of the simulation results for relatively short hard-sphere chains. The Flory exponent (0.588) would be recovered if the polymer chain length approaches infinite. To check the thermodynamic properties of the polymer chain within different density regimes, we calculate the radial distribution of polymer segments and the confinement free energy by varying the polymer chain length at a given cavity radius and by varying the cavity size at a given polymer chain length.

Figure 3-1 shows the density profiles of polymer segments calculated from the MC simulations and from the DFT. Here the cavity radius is fixed at $R_c = 10\sigma$, and the polymer chain lengths are $N = 50$, 150 or 2400 . According to Eq. (3.12), the polymer radii of gyration are $R_g \approx 5\sigma$, 10σ and 54σ, suggesting that the average concentrations of the confined polymers correspond to the dilute, the semi-dilute, and the concentrated conditions, respectively. For the case with a long polymer chain ($N = 2400$), the DFT calculations were based on the no-end-effect assumption [Eq. (3.5)] or by replacement of the single chain with 12 identical short chains, each with $N = 200$ segments. As shown in a previous work [30], division of a long single chain into several short chains does not alter the radial distribution of the polymer segments as long as the total number of polymer segments or the polymer concentration remains unchanged. The good agreement of the density profile of a single chain with that of several “broken chains” affirms a key

hypothesis in the scaling analysis [28], i.e. the correlation length of a confined polymer is bounded by the cavity size. In all cases, the DFT predictions are in excellent agreement with the simulation data.

At high polymer density, accumulation of the polymer density near the cavity surface is due to the strong short-range repulsion among the polymer segments. The excluded-volume effect becomes less significant as the polymer concentration or the chain length decreases. At low polymer concentrations, the segment density near the cavity wall is smaller than that in the center. As well documented, the depletion effect is due to the surface constriction of the polymer configurations. Because the depletion is affiliated with the long-range intra-chain correlations but the DFT captures only the bond connectivity and short-range non-bonded correlations, the density profile predicted by the DFT becomes less accurate as the polymer concentration decreases. Fortunately, at very low polymer density, the system becomes an ideal solution so that the effect of non-bonded correlation on the thermodynamic non-ideality is less important.

Figure 3-2 shows another comparison of the DFT with the MC simulation results for the density profiles of hard-sphere segments. Different from Fig. 3-1, here the polymer chain length is fixed at $N = 150$ but the cavity radius is changed such that the overall polymer concentration corresponds to the dilute regime ($R_c = 15\sigma$), the semi-dilute regime ($R_c = 10\sigma$), and the concentrated regime ($R_c = 4\sigma$). The overall agreement between the theory and simulation is similar to that observed in Fig. 3-1. Whereas the distribution of the polymer segments near a hard surface is mainly determined by the overall polymer concentration inside the cavity, the polymer size and the cavity radius are

two independent parameters of the inhomogeneous system. At a fixed polymer density, the structures of the bulk and the confined systems have different dependences on the polymer chain length due to the cavity size or the surface curvature effect.

Figure 3-3 (a) and (b) compare the theory and simulation results for the confinement free energies at a fixed chain length and at a fixed cavity radius, respectively. In both cases, the DFT predictions are again in good agreement with the MC simulations. At a fixed chain length ($N = 200$), the free energy of confinement falls monotonically with the cavity size. The confinement free energy vanishes as the cavity radius approaches to infinite. Conversely, the total confinement free energy increases with the chain length at a fixed cavity radius ($R_c = 20\sigma$). The good agreement between the DFT and the MC simulations for both the structure and thermodynamic properties of a single chain in a cavity, in particular at high polymer packing fractions, allows us to examine systematically the dependences of the confinement entropy on the polymer chain length and on the cavity radius.

3. 3. 2 Comparison with The Scaling Analysis

The scaling analysis provides a conventional way to describe the configurational entropy, or equivalently the free energy of confinement, for a single polymer chain in a confined space. At semi-dilute concentrations, the free energy of a confined chain can be derived within the framework of the self-avoiding-chain model [36]. The free energy of confinement for a self-avoiding chain in a spherical cavity of diameter D is [113]

$$\beta\Delta F \cong \left(\frac{R_g}{D}\right)^{3/(3\nu-1)}, \tag{3.13}$$

where $\nu \approx 0.588$ is the Flory exponent [116]. For a self-avoiding chain, the radius of gyration R_g is related to the monomer diameter σ and the degree of polymerization N by $R_g \cong \sigma N^{\nu}$. The scaling analysis predicts that the confinement free energy is on the order of $k_B T$, depending only on the Flory exponent and the ratio of the polymer chain length or the cavity radius. At a fixed cavity diameter, the reduced confinement free energy per segment scales with the polymer chain length as $\beta\Delta F / N \cong N^{1.31}$. For a given polymer, the reduced free energy of confinement scales with the cavity radius as $\beta\Delta F \sim D^{-3.93}$. On the other hand, the SCFT predicts that the free energy of confinement depends on the degree of polymerization N and on the average volume fraction of the confined chain [113]

$$\beta\Delta F \sim N\eta = N^2\sigma^3 / D^3, \tag{3.14}$$

where $\eta = N\sigma^3 / D^3$. The discrepancy between the SCFT and the scaling analysis mainly arises from the mean-field approximation for describing the polymer excluded-volume effect. At low polymer concentrations, the power-law dependence of the confinement free energy on the chain length has been confirmed by Monte Carlo simulation within a bead-spring representation of a polymer chain in a spherical cavity [27].

Whereas the power-law dependences of the confinement free energy on the polymer chain length and on the cavity diameter have been validated by molecular simulations, the agreement between the theory and simulation data is by no mean quantitative. Indeed, the absolute value of the confinement free energy calculated from molecular simulation can be larger than that predicted from Eq. (3.13) by several orders

of magnitude. Besides, simulation and experimental investigations [27, 117] revealed noticeable deviations from the power-law relations at high polymer concentrations. To our knowledge, no comprehensive theoretical analysis has been reported to capture the properties of a single confined polymer in a cavity at both semi-dilute and concentrated concentrations. As indicated earlier, the high concentration region is particularly relevant to the packaging of biopolymers in a cellular environment. For example, the volume fraction of RNA/DNA in a fully packaged viral capsid is typically in the range of $0.32-0.49$ [118].

Figure 3-4 shows the confinement free energy per polymer segment $\beta\Delta F / N$ versus the chain length N predicted by the DFT. Here the cavity radius is fixed at $R_c = 10\sigma$ in the DFT calculations. For comparison, also shown in Fig. 3-4 are predictions from the scaling analysis and from the SCFT. Whereas the three different theoretical methods show similar power-law dependence of the reduced free energy on the polymer chain length, the confinement free energy predicted by the DFT exceeds that from the scaling analysis or from the SCFT by orders of magnitude. Nevertheless, the DFT yields a scaling exponent in excellent agreement with the scaling analysis at moderate polymer concentrations. Because the Flory exponent is not valid at high polymer concentration, the slope predicted by DFT is noticeably different from the scaling analysis. As indicated before[27], the discrepancy can be corrected by replacing using $\nu = 0.5$, which is more appropriate for concentrated polymer solutions. As shown in Fig. 3-4, the modified scaling analysis yields good agreement with the DFT calculation at high polymer densities. However, at high density the confinement free energy per segment predicted by

the DFT shows a curve up shape in contrast to the tangent straight line predicted from the scaling fitting. Whereas the scaling exponent from the SCFT is quite different, quantitatively the overall free energy predicted by the DFT is much closer to that from the SCFT. The scaling analysis drastically under-estimate the free energy of packaging because in the blob-based method, the major source of the free energy increase arises from the confinement of a pseudo ideal chain within the cavity [119]. While the interaction among the blobs is neglected in the scaling analysis, the DFT takes into account not only non-bonded interactions among monomers but also the entropic loss due to the restriction of polymer configurations near the cavity surface. As a result, the confinement free energy predicted by the DFT is much larger than that from the scaling analysis. On the other hand, the SCFT underestimates the free energy of confinement because the mean-field approximation under-estimate the excluded-volume effects.

Figure 3-4 also shows that the discrepancy between the DFT and the scaling analysis magnifies as the polymer chain length increases. In the blob-scaling description, the number of monomers in each blob N_b is given by [119]

$$N_b \cong \eta^{1/1-3\nu}. \tag{3.15}$$

Eq. (3.15) indicates that the number of monomers in a blob decreases with the polymer packing fraction. The scaling analysis becomes unreliable at high polymer concentrations because the des Cloizeaux exponent $1/(3\nu-1)$, derived from the polymer behavior at semi-dilute conditions, becomes invalid. As a result, at a fixed cavity radius, the scaling relation deteriorates as the chain length increases [27]. Because the long-range correlations are screened by the confinement, the DFT reproduces the non-mean-field

dependence of the confinement free energy on the chain length even at low and moderate polymer densities.

Figure 3-5 shows the dependence of the confinement free energy on the cavity diameter D. According to the scaling analysis [Eq. (3.13)], the reduced confinement free energy, $\beta\Delta F\left(\sigma / R_g\right)^{3/(3\nu-1)}$, is a universal function of the reduced cavity diameter D/σ, independent of the polymer chain length. The DFT calculations indicate, however, that the universal relation is true only for very long polymer chains in large cavities. Noticeable deviations from the scaling relation are observed for polymers in small cavities. If we allow the Flory exponent to change from 0.588 to 0.5 at different polymer concentrations, the slope predicted by the DFT is in good agreement with the scaling analysis. Nevertheless, because the scaling analysis ignores the inhomogeneous distribution of polymer segments under confinement and the strong excluded volume effect at high polymer density, it predicts erroneously that the confinement free energy depends only on the ratio of the polymer radius of gyration and the cavity radius.

Figure 3-6 shows the influence of the polymer packing fraction η on the confinement free energy. Here the DFT calculations were performed both at a given cavity radius ($R_c = 10\sigma$) and at a given polymer chain length ($N = 2000$). As predicted by the scaling analysis and by the SCFT, the DFT calculations show that the confinement free energy per segment ($\beta\Delta F / N$) is primarily determined by the polymer packing fraction up to moderate concentrations ($\eta \le 0.2$). At high polymer concentrations ($\eta > 0.2$), however, the confinement free energy per monomer depends not only on the

average polymer packing fraction but also noticeably on the cavity size. The increase of the scaling exponent at high polymer concentrations ($\eta > 0.2$) is consistent with the simulation results from a bead-spring chain model of polymers in a spherical cavity [27]. An increased scaling exponent for the dependence of the confinement free energy on the polymer concentration is also consistent with experimental results on the partitioning of polyethylene glycol in protein nanopores [120].

At a given polymer concentration, variation of the confinement free energy per segment with the cavity size is mainly due to the polymer-surface contact area. The free energy per segment for the confined chain can be expressed in terms of that of the bulk fluid plus an excess arising from the polymer-wall surface tension

$$F / N = F_b / N + 4\pi R^2 \gamma / N = F_b / N + 3\gamma / (R\rho). \quad (3.16)$$

While for a bulk fluid the free energy per segment depends only on the average polymer concentration, the free energy per segment for a confined chain is inversely proportional to the cavity radius, provided that the surface tension γ is independent of the curvature. Because the surface tension is positive, the confinement free energy per segment increases as the cavity becomes smaller. The scaling analysis ignores the polymer inhomogeneity at the cavity surface and thus does not capture the effect of cavity size on the confinement free energy.

Finally, Figure 3-7 compares the osmotic pressure p of a confined polymer predicted by the contact value theorem [Eq. (3.10)] with that from scaling analysis [28, 113]

$$p \sim \eta \Delta F / N \sim \eta^{3\nu/(3\nu-1)}. \tag{3.17}$$

If the Flory exponent is fixed, we observe noticeable deviation from the power-law relation at both low and high polymer densities. As well documented, the deviation at low density arises from the mean-field nature of the theory for describing the intra-chain correlations. On the other hand, the DFT predicts a "curve up" shape at high polymer packing fraction, implying a higher power-law relation in comparison to the scaling fitting with exponent $\nu = 0.5$. Figure 3-7 also compares the osmotic pressure of a confined chain with that of a bulk polymer at the same average packaging fraction [28, 113]. It shows that that the osmotic pressure is little influenced by the hard-cavity confinement, especially in the high density limit. The weak dependence of the osmotic pressure on confinement is in part due to the fact that the surface tension effect was neglected in our application of the contact value theorem.

3. 4 Conclusions

In summary, we have shown that the polymer density functional theory (DFT) is capable of predicting both the structural and thermodynamic properties for individual polymer chains confined in spherical cavities. The theoretical predictions are in quantitative agreement with simulation results at dilute, semi-dilute, and concentrated polymer densities. While the theoretical calculations discussed in this work are only concerned with athermal systems where the confinement free energy is solely determined by the entropic effects, we expect that the theoretical framework can be extended to realistic polymeric systems with an explicit consideration of the solvent effects.

From a theoretical point of view, the DFT is equivalent to the SCFT except that the former is convenient to account for the segment-level interactions and short-range correlations explicitly [79]. Although for bulk systems, both the DFT and the SCFT exhibit mean-field characteristics such as the molecular weight dependence of the osmotic second viral coefficient for long polymer chains, DFT is able to capture short-range correlations in particular the segment-level excluded-volume effects that are important at high polymer concentrations [85]. Besides, recent scaling analysis revealed that in the semi-dilute regime, a long polymer chain inside a spherical cavity becomes equivalent to multiple shorter chains with the radius of gyration comparable to the cavity size [28]. In other words, the range of intra-chain correlation for a confined polymer is bounded by the cavity size. As a result, by capturing the short-range correlations and exact polymer topology, the DFT provides a reasonable representation of the thermodynamic properties of a long polymer in a spherical cavity in both semi-dilute and concentrated regimes.

As suggested by early scaling analysis, the long-range intra-chain correlation at semi-dilute regime is suppressed by the finite size of the confining space. As a result, the DFT is able to reproduce the scaling exponents for both the confinement free energy and the osmotic pressure in excellent agreement with the scaling analysis at moderate concentrations. However, the DFT and the scaling relations give drastically different values of the thermodynamic properties at high polymer concentration where the excluded-volume effect is predominant. Because the scaling analysis does not fully account for the polymer inhomogeneity and the excluded-volume effects, and also

ignores the curvature of the confinement surface, it significantly underestimates, sometimes by several orders of magnitude, on the confinement free energy. Unlike the scaling analysis, the DFT predicts that the confinement free energy per segment depends both on the average polymer density and on the cavity size. At high polymer densities, the DFT calculations agree well with simulation and experimental results.

Figure 3-1 The segment-density profiles for three hard-sphere chains ($N = 50,\ 150,\ 2400$) confined in a spherical cavity of radius $R_c = 10\sigma$. For clarity, the density profiles for $N = 150$ are up shifted by 0.2 units. Symbols represent MC simulation results and the solid lines are from the DFT predictions.

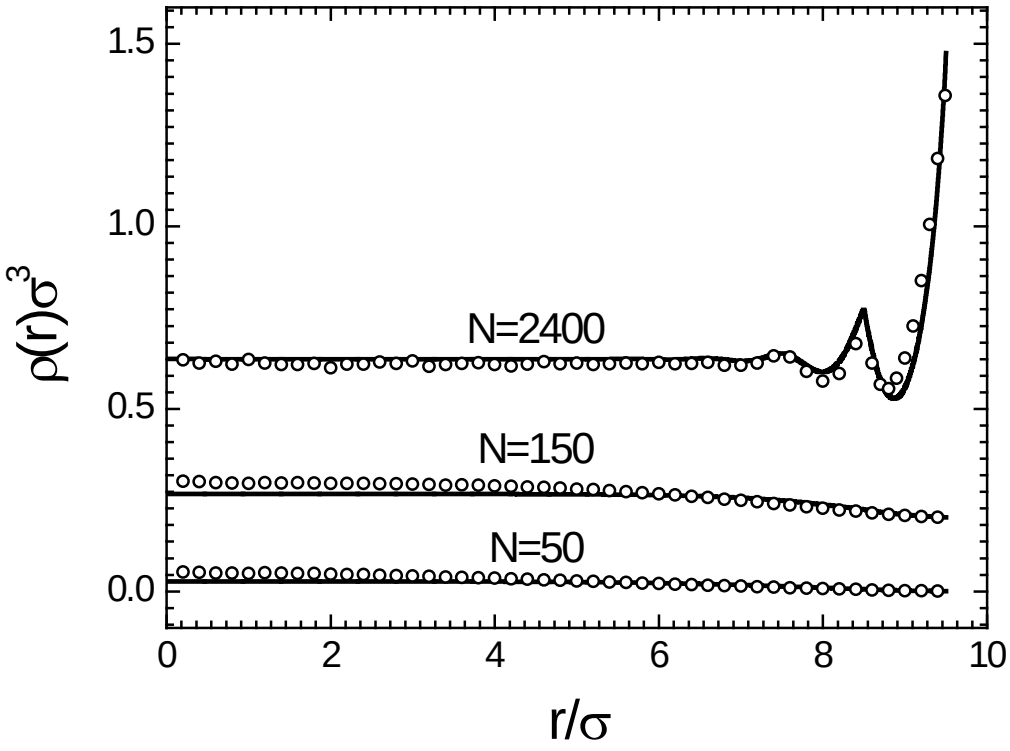

Figure 3-2 The same as Fig. 3-1 but for a single hard-sphere chain ($N = 150$) encapsulated in three different spherical cavities 4σ with $R_c = 15\sigma$, 10σ and 4σ , respectively. For clarity, the density profiles for $R_c = 15\sigma$ are up shifted by 0.2 units.

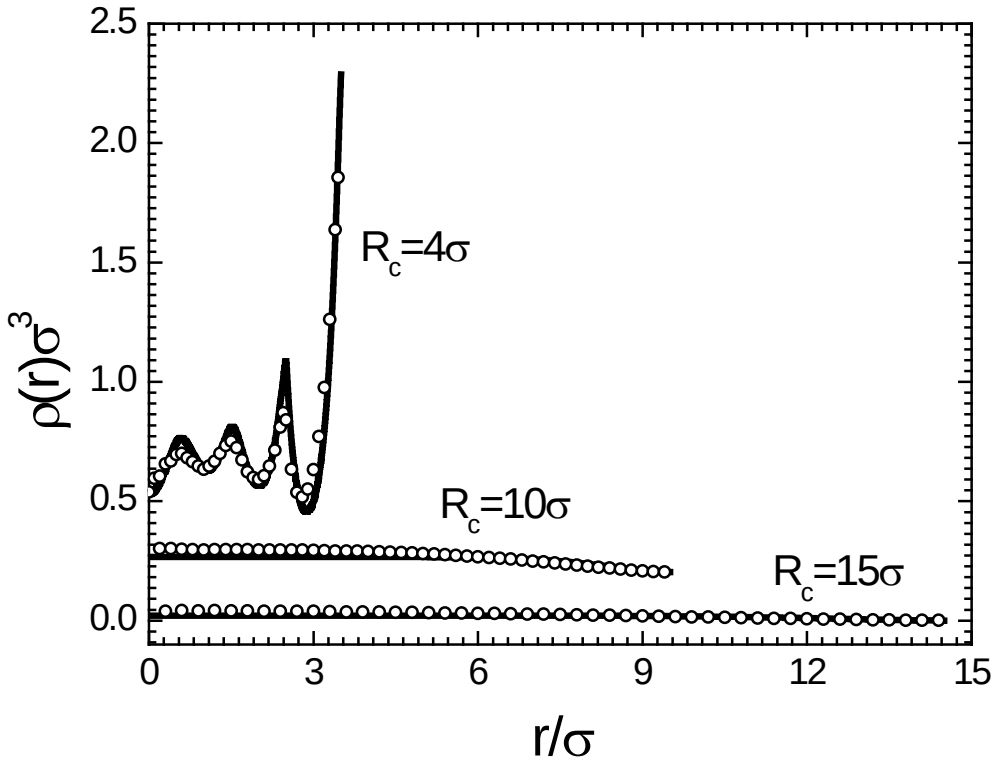

Figure 3-3 (a) The confinement free energy of a single chain ($N = 200$) versus the cavity radius. (b) Effect of the polymer chain length on the confinement free energy in a spherical cavity of radius $R_c = 20\sigma$. Symbols represent MC simulation results and the solid lines are from the DFT predictions.

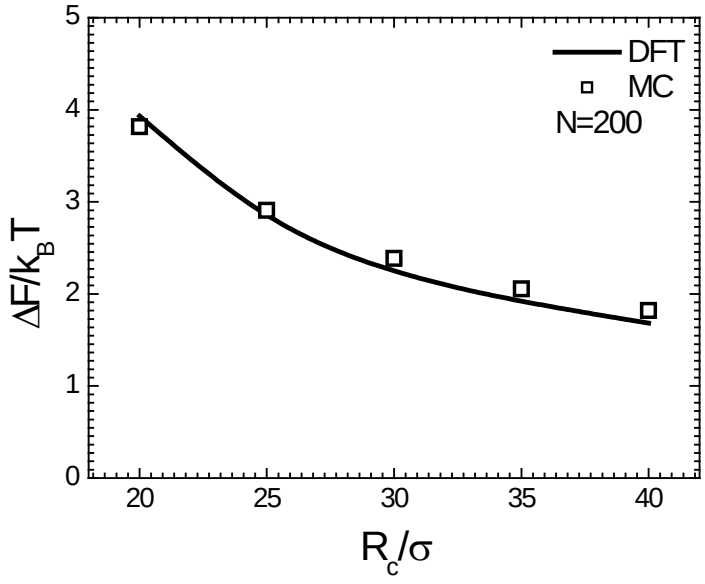

(a)

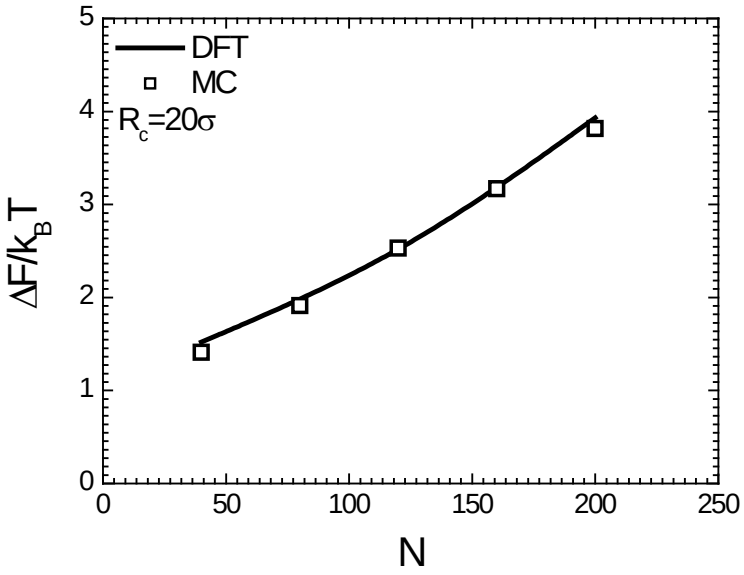

(b)

Figure 3-4 The reduced packaging free energy per segment $\beta\Delta F / N$ versus the chain length N at a fixed cavity radius $R_c = 10\sigma$. The solid line is from DFT, the dashed line is from scaling analysis, the dotted line is from SCFT, and the dash dotted line is the scaling fitting by imposing the exponent $\nu = 0.5$, while the dash dot dotted line with exponent $\nu = 0.588$.

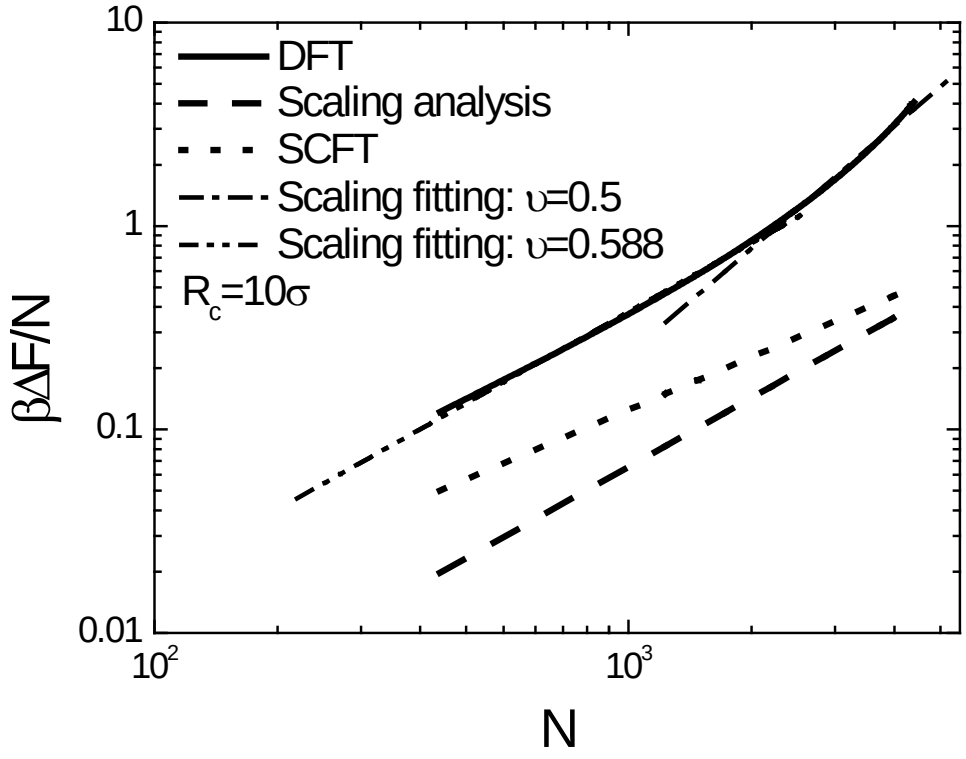

Figure 3-5 The reduced packaging free energy $\beta\Delta F\left(\sigma / R_g\right)^{3/(3\nu-1)}$ versus the cavity radius R_c at different chain lengths, $N=1000$ (Red line), $N=2000$ (Green line), and $N=3000$ (Cyan line). The dash dotted lines are the scaling fitting by imposing the exponent $\nu=0.5$ and dash dot dotted lines are the scaling fitting with exponent $\nu=0.588$. Note that the scaling analysis predicts that $\beta\Delta F\left(\sigma / R_g\right)^{3/(3\nu-1)}$ is independent of N.

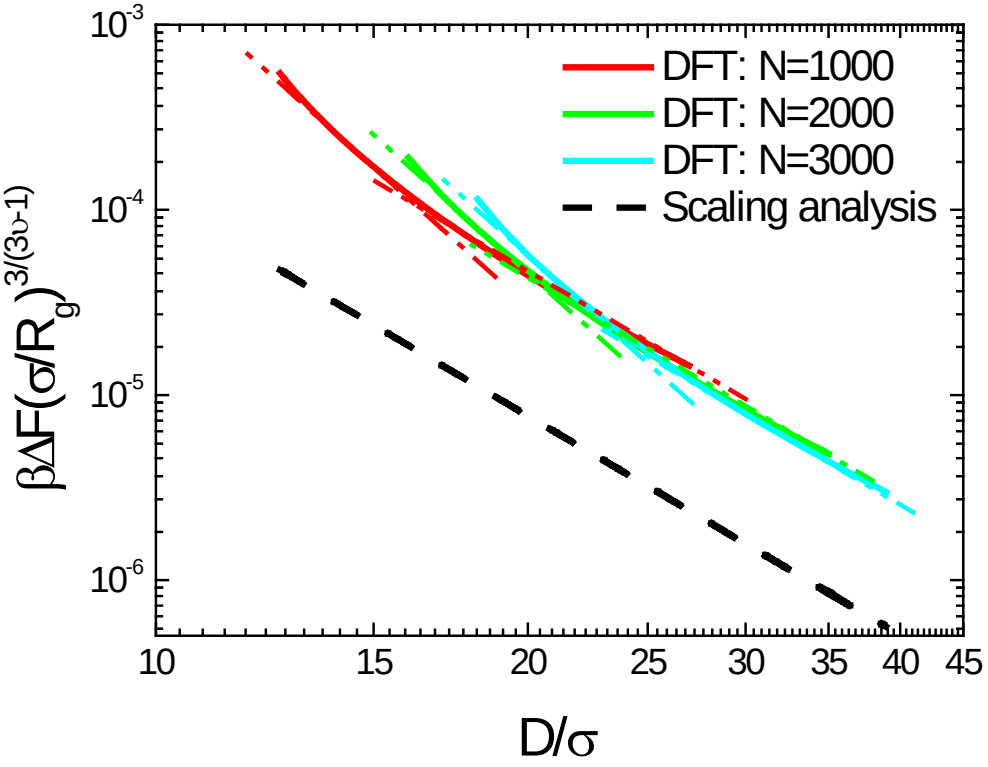

Figure 3-6 The reduced packaging free energy per segment $\beta\Delta F / N$ versus the polymer packing fraction η. The DFT results are given at a fixed cavity radius $R_c = 10\sigma$ (Solid line) and at a fixed chain length $N = 2000$ (dotted line). The dashed line is from the scaling analysis, and the dash dotted line is by fitting of the DFT results (i.e., $\beta\Delta F / N \sim \eta^{1.31}$).

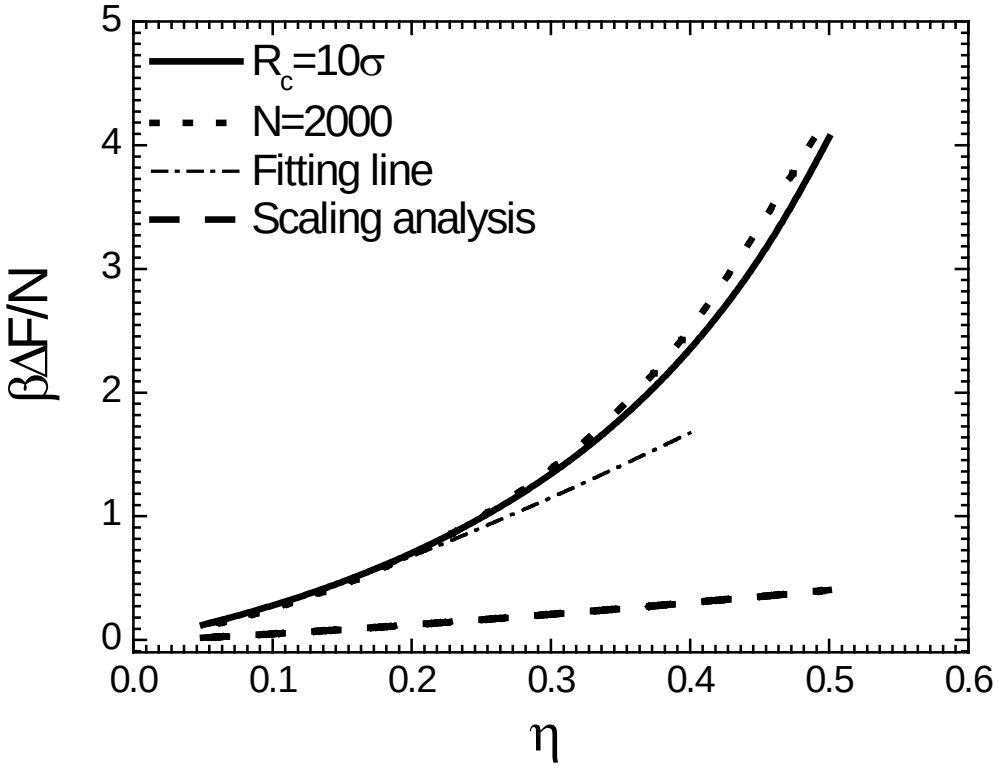

Figure 3-7 The reduced osmotic pressure $p\sigma^3 / k_B T$ versus the polymer packing fraction η. The dash dotted line represents the scaling fitting with exponent $v = 0.5$ and the dash dot dotted line is the scaling fitting with exponent $v = 0.588$ of the DFT calculations. The red line represents the DFT results for a given chain length $N = 2000$ and the green line is for a given cavity radius $R_c = 10\sigma$. The dotted line represents the bulk osmotic pressure for a hard-sphere chain fluid with chain length $N = 2000$ from the bulk equation of state.

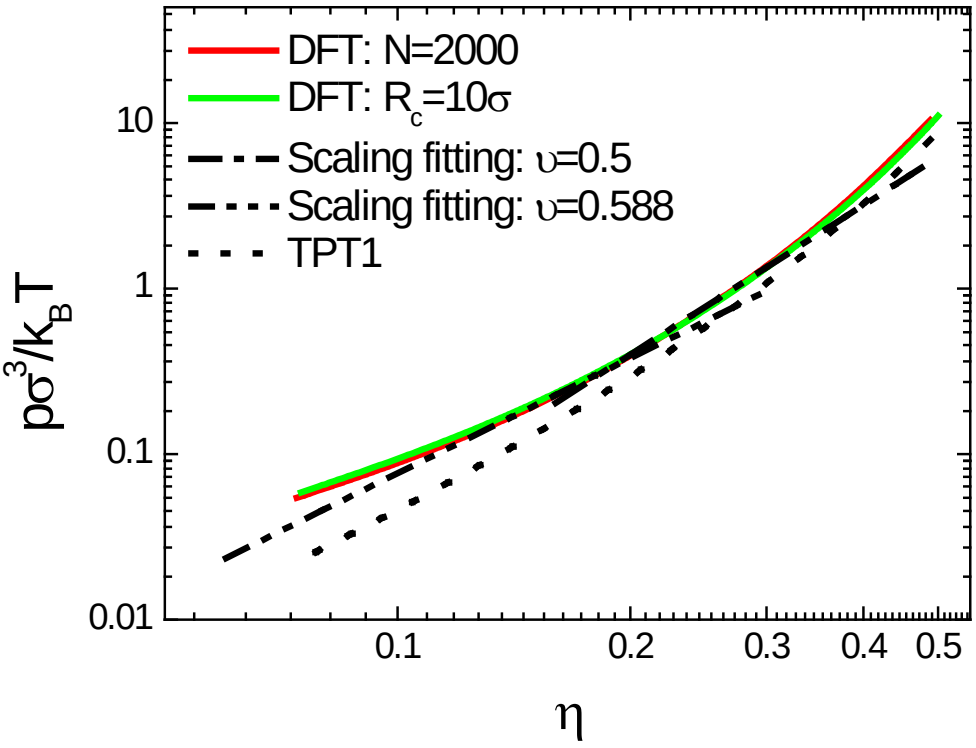

Chapter 4 Density Functional Theory for Encapsidated Polyelectrolytes

Abstract

In this chapter, we used the classical density functional theory (DFT) to investigate packaging of flexible and semi-flexible polyelectrolytes in a spherical capsid permeable to small ions but not the confined polymer. The thermodynamic system is represented by an extension of the primitive model for electrolyte solutions in which the solvent is a dielectric continuum and the polymeric segments and small ions are described as charged hard spheres. Flexible and semi-flexible polyelectrolytes were treated as tangentially connected charged hard spheres without and with a bending potential along the polymer backbone, respectively. The thermodynamic system was used by others in molecular simulations and it provides an idealized representation of genome packaging in viral particles. The DFT predictions were found in good agreement with Monte Carlo simulation for the density distributions of polymer segments and small ions at a wide variety of conditions. After extensive comparison with simulation results, the DFT was then used to study the density distributions of small ions coexisting with the viral capsid and the effect of dielectric inhomogeneity of the capsid on the structure and surface properties of polyelectrolyte segments and small ions as well as the net charge of polyelectrolyte-capsid complexes. The DFT predicts that the net charge of a vrial particle is sensitive to solution conditions and presumption of local charge neutrality may lead to erroneous conclusions. Because of the finite thickness of the capsid walls, it appears that the dielectric inhomogeneity has insignificant effect on viral packaging. The numerical

efficiency and good agreement of the DFT with MC simulations allows quantification of the structural and thermodynamic properties of virus packaging and gene delivery in realistic systems.

4. 1 Introduction

Genome encapsidation is a critical step during virus replication in vivo and has been studied extensively by biologists, physicists as well as engineers [121-125]. While analytical tools for determining the genomic sequence and the structures of capsid proteins are well advanced, much more difficult is characterization of the internal structure in particular conformation of flexible biomolecules inside a nucleocapsid under various physiological conditions. A theoretical description of genome packaging will be helpful to unravel microscopic details that involves entropic, electrostatic as well as bending energies of genome molecules (DNA or RNA) that are sensitive to the local environment [126].

Recently, it was found that the genome encapsidation is regulated by strong electrostatic interactions between nucleic acids and oppositely charged capsid proteins [33]. However, many questions remain unanswered such as how the non-bonding molecular forces regulate genome packaging, what the internal conformations are for biomolecules in a viral capsid, and how non-electrostatic forces affect the charge neutrality of viral capsids. Because genome encapsidation is a microscopic process difficult to be address directly with experiments, theoretical and computational approaches are helpful for the study of RNA/DNA encapsidation as well as the internal structures and thermodynamic properties.

Numerous computer simulations and analytical calculations have already been reported to address the genome conformation in viral capsids [127-135]. Because a typical viral capsid is made of billions of atoms and viral packaging is sensitive to the background solution conditions, most theoretical investigations are based on coarse-grained models. For example, RNA molecules were modeled as flexible charged hard-sphere chains, while DNA molecules were depicted as semi-flexible charged hard-sphere chains with bending energy for the backbone rigidity. For all of these studies, only molecules inside the capsid were considered and the local charge neutrality was imposed for the viral capsid. It has been well documented that local charge neutrality is not valid for inhomogeneous electric systems and the total charge of a virus is in general not neutral [136, 137] Under physiological conditions, viral particles coexist with a background electrolyte solutions such that small ions can move into or out of the capsid freely [31].

Recently Angelescu et al [131, 132] reported a coarse-grained model for genome packaging and studied the structure of confined polyelectrolyte and encapsidation free energy. The model system takes into account not only molecules the inside capsid but also small ions in the outside environment [33, 134]. Monte Carlo simulation of the model system indicates that the capsids loaded with genome molecules are in general not neutral [131]. On the other hand, theoretical investigation of viral packaging often rely on the overused Debye-Huckel approximation [135]. It has been shown that the mean-field theory is insufficient to account for the correlation effect among charged particles [33]. Likewise, the Poisson-Boltzmann equation is insufficient to predict charge inversion and

attraction between like charged particles [106, 138]. Some theoretical investigations [133, 134] ignored the excluded-volume effect. Considering that the volume fraction of biomolecules is substantial in a typical viral capsid, we believe that molecular excluded volume effect plays an important role in genome encapsidation.

In previous work, we proposed Density Functional Theory (DFT) to study properties of inhomogeneous polyelectrolytes near charged surfaces [67, 76] and in viral capsids [33]. Here we extend DFT calculations to flexible and semi-flexible polyelectrolyte in spherical capsids. After extensive comparison of the DFT predictions with simulation data, we examine the effect of the solution condition on viral packaging by comparing the density distributions of polyelectrolytes and small ions of an open (with surroundings) system with that of a semi-open (without surroundings under charge neutrality assumption) system defined in Ref. [33]. While the small ions are freely moving into and out of the viral capsid for the open system, the small ions are completely confined in viral capsid for the semi-open system with the average density defined by a chemical potential in the bulk solution. We find that the outside environment drastically influences the structural and thermodynamic properties of the confined polyion as well as small ions. In the open system, the net charge of capsid complex is not neutral as erroneously assumed in many theoretical investigations but dependent on the density distribution of polyelectrolyte segments, and the dimensions of viral capsid and small ions. In this work, we will study the effects of these parameters on the net charge of polyelectrolyte-capsid complex systematically. In addition, we will study the effect of dielectric inhomogeneity on the properties of confined polyions. This part of work is

motivated by the fact that the viral capsid is mainly composed of proteins that have a dielectric constant different from that of an aqueous solution. Discontinuity in dielectric constants would influence the distributions of all charged species. In different contexts such effect has been studied by the computer simulations [139, 140] by using image charge effects. More recently, Gillespie [141] applied classical DFT to study the image charge effect and made comparison with MC simulation. However, to our knowledge there is no previous report on the effect of dielectric discontinuity on viral packaging. Because explicit consideration of dielectric discontinuity is complicated for viral capsids and the DFT calculation is computationally very extensive, in this work we will solve the generalized Poisson equation [142] to minimize the computational time. Although it does not include the fluctuation force, the generalized Poisson equation gives a good first-order approximation on the effect of discontinuous dielectric constant on viral packaging.

The remainder of this chapter is organized as the following. In section 2, we introduce the molecular model and density functional theory. In section 3, we first calibrate our DFT calculations by comparing with previous computer simulation results. After the calibration, we will study the effects of the outside environment on the density distributions of confined polyelectrolytes and small ions as well as the net charges of polyelectrolyte-capsid complexes and the dependence of density profiles on the dielectric inhomogeneity of the capsid. In section 4, we summarize the key conclusions.

4. 2 Molecular Model and Theory

4. 2. 1 Molecular Model

In this work, we follow a model viral system originally proposed by Angelescu et al [131, 132] to investigate a polyelectrolyte chain confined in a spherical capsid with inner radius R_c, wall thickness D_c. The capsid bears positive charge Q_c uniformly placed at a surface with the radial distance of R_q from the capsid center. The model system has been applied to studying $T = 3$ virus such as cowpea chlorotic mottle virus (CCMV) [131, 132, 143]. Although it is not concerned with a specific real virus, theoretical investigations of the model system have provided useful insights into the generic features of genome packaging in realistic viral systems [131].

The primitive model [67, 76] is used to represent the polyelectrolyte chain and small ions. The polymer is made of tangentially-connected charged hard spheres of diameter σ and each with a unit negative charge, i.e., the valence of a polyion segment is $Z_p = -1$. In addition to the bond connectivity defined by a tangent chain, the neighboring segments are subject to a bond bending potential E_b [144]:

$$E_b = \phi_0 \left(1 + \cos\gamma\right), \tag{4.1}$$

where ϕ_0 characterizes the bending energy, and γ is the bond angle between two immediate neighboring bonds. In the primitive model, the solvent (water) is represented by a dielectric continuum.

The capsid wall is impermeable to the polyelectrolyte segments but permeable to small ions. In contrast to our previous work for HBV [33], the monomeric polyelectrolyte and capsid counterions that separately neutralize the charges of polyelectrolyte and capsid are depicted as charged hard spheres with valence Z_+ and Z_- and can pass across

the capsid freely. For simplicity, the diameter of small ions is set to be identical to that of polyion segments. We set a spherical cell with radius R_{cell} which is far from the outer capsid surface to make sure that it reaches the bulk solution properties. Therefore, the net charge of the whole cell is zero instead of the charge of the capsid itself. Such settings represent a thermodynamic equilibrium between a polyelectrolyte containing capsid and a bulk salt solution, which resembles that experienced by genome capsids in physiological conditions. The schematic representation of this coarse-grained system is depicted in Fig. 4-1.

Similar to the previous primitive model [33], the reduced interaction potential between any pair of charged spheres (i and j) is given by

$$\beta u_{ij}(r) = \begin{cases} \infty, & r < \sigma \\ Z_i Z_j \dfrac{l_B}{r}, & r \geq \sigma \end{cases}, \tag{4.2}$$

where $\beta = 1/(k_B T)$, k_B is the Boltzmann constant, T stands for the absolute temperature, r is the center-to-center distance, and Z_i stands for the valence of particle i. The Bejrrum length $l_B \equiv e^2 / 4\pi\varepsilon k_B T$, characterizes the distance where the electrostatic potential between two monovalent spheres (small ions or polymer segments) is equal to the thermal energy $k_B T$ and ε is the dielectric constant of solvent. In aqueous solution at temperature $T = 298K$, the Bejrrum length is $l_B = 0.715$. The bonding potential $V_b(\mathbf{R})$ of flexible and semi-flexible polyelectrolyte chain is given as [145]

$$\exp\left[-\beta V_{\mathrm{b}}\left(\mathbf{R}\right)\right]=\prod_{i=1}^{M-1}\frac{\delta\left(\left|\mathbf{r}_{i+1}-\mathbf{r}_{i}\right|-\sigma\right)}{4\pi\sigma^{2}} \times\prod_{i=2}^{M-1}\exp\left[-\phi_{0}\left(1+\frac{\left|\mathbf{r}_{i}-\mathbf{r}_{i-1}\right|\times\left|\mathbf{r}_{i+1}-\mathbf{r}_{i}\right|}{\sigma^{2}}\cos\gamma\right)\right], \tag{4.3}$$

where M is the degree of polymerization, $\mathbf{R}=\left(\mathbf{r}_{1},\mathbf{r}_{2},\cdots,\mathbf{r}_{M}\right)$ is a set of coordinates representing the polymer configuration, and δ is Dirac-delta function. Therefore, the local polyelectrolyte segmental density $\rho_{p}\left(\mathbf{r}\right)$ is determined from

$$\rho_{p}\left(\mathbf{r}\right)=\sum_{i=1}^{M}\rho_{\mathrm{si}}\left(\mathbf{r}\right)=\sum_{i=1}^{M}\int d\mathbf{R}\delta\left(\mathbf{r}-\mathbf{r}\right)\rho_{\mathrm{M}}\left(\mathbf{R}\right). \tag{4.4}$$

In the first case, the dielectric constant of the capsid wall ε_{c} is assumed to be the same as that of the solvent, i.e., $\varepsilon_{c}=\varepsilon$. For an open system, the effective potentials exerted on polyion segments $\Psi_{p}\left(r\right)$ and monomeric ions $\Psi_{+,-}\left(r\right)$ due to the capsid wall can then be expressed as

$$\beta\Psi_{p}\left(r\right)=\begin{cases}\dfrac{Z_{p}Q_{c}l_{B}}{R_{c}+\dfrac{\sigma}{2}}, & r\le R_{c}-\dfrac{\sigma}{2}\\ \infty, & r>R_{c}-\dfrac{\sigma}{2}\end{cases}$$

$$\beta\Psi_{+,-}\left(r\right)=\begin{cases}\dfrac{Z_{+,-}Q_{c}l_{B}}{R_{c}+\dfrac{\sigma}{2}}, & r\le R_{c}-\dfrac{\sigma}{2}\\ \infty, & R_{c}-\dfrac{\sigma}{2}<r<R_{c}+D_{c}+\dfrac{\sigma}{2}\\ \dfrac{Z_{+,-}Q_{c}l_{B}}{r}, & r\ge R_{c}+D_{c}+\dfrac{\sigma}{2}\end{cases}. \tag{4.5}$$

On the other hand, for a semi-open system, the small ions are confined in the spherical capsid with chemical potentials determined by a bulk solution. The effective potentials from capsid surface of semi-open system are given as

$$\beta\Psi_p(r)=\begin{cases}\dfrac{Z_pQ_cl_B}{R_c+\dfrac{\sigma}{2}}, & r\le R_c-\dfrac{\sigma}{2}\\ \infty, & r>R_c-\dfrac{\sigma}{2}\end{cases}$$
$$\beta\Psi_{+,-}(r)=\begin{cases}\dfrac{Z_{+,-}Q_cl_B}{R_c+\dfrac{\sigma}{2}}, & r\le R_c-\dfrac{\sigma}{2}\\ \infty, & r>R_c-\dfrac{\sigma}{2}\end{cases}. \tag{4.6}$$

Similar to our previous work [33], the electrostatic interaction due to the capsid is accounted within the overall electrostatic potential of the entire system. Besides, the viral capsid exerts excluded-volume effect to polyelectrolyte segments and small ions.

4. 2. 2 Polymeric Density Functional Theory

The performance of DFT hinges on accurate formulation of the grand potential Ω in terms of molecular density profiles. In this work, the grand potential is given by [76]

$$\Omega\left[\rho_M(\mathbf{R}),\{\rho_\alpha(\mathbf{r})\}\right]=F\left[\rho_M(\mathbf{R}),\{\rho_\alpha(\mathbf{r})\}\right]+\int\left[\Psi_M(\mathbf{R})-\mu_M\right]\rho_M(\mathbf{R})d\mathbf{R}+\sum_{\alpha=+,-}\int\left[\Psi_\alpha(\mathbf{r})-\mu_\alpha\right]\rho_\alpha(\mathbf{r})d\mathbf{r}, \tag{4.7}$$

where $d\mathbf{R}=d\mathbf{r}_1d\mathbf{r}_2\cdots d\mathbf{r}_M$ represents a set of differential volumes, $\rho_M(\mathbf{R})$ is the polyelectrolyte density as a function of the polymer configuration $\mathbf{R}$, $\rho_\alpha(\mathbf{r})$ is the density profile of small ion α, and μ_M and μ_α are the chemical potentials of polyelectrolyte and small ion, respectively. F is the intrinsic Helmholtz free energy of

mixture. $\Psi_M(\mathbf{R})$ is the external potential on polyelectrolyte, which can be separated into individual segments of polyion, i.e. $\Psi_M(\mathbf{R})=\sum_{i=1}^{M}\Psi_M(\mathbf{r}_i)$; $\Psi_\alpha(\mathbf{r})$ is the external potential for small ions.

The intrinsic Helmholtz free energy can be divided into an ideal-gas term F^{id} that include bond potentials and molecular configuration and an excess term F^{ex} that accounts for thermodynamic non-ideality due to different non-bonded inter-segment interactions. In general, the intrinsic Helmholtz free energy F can be divided into five distinct contributions:

$$F = F^{id} + F_{hs}^{ex} + F_{ch}^{ex} + F_{C}^{ex} + F_{el}^{ex}, \tag{4.8}$$

where F^{id} is the ideal-gas term of intrinsic Helmholtz free energy without non-bonded interactions, F_{hs}^{ex} is the excess Helmholtz free energy due to hard-sphere repulsion, F_{ch}^{ex} is the excess Helmholtz free energy due to chain connectivity, F_{C}^{ex} is the excess Helmholtz free energy due to direct Coulomb interaction, and F_{el}^{ex} is the excess Helmholtz free energy due to electrostatic correlation.

The ideal-gas term F^{id} depends on the chain configuration, bonding potential and segmental distribution of small ions,

$$\beta F^{id} = \int d\mathbf{R}\rho_M(\mathbf{R})\left[\ln\rho_M(\mathbf{R})-1\right]+\beta\int d\mathbf{R}\rho_M(\mathbf{R})V_b(\mathbf{R})+ \sum_{\alpha=+,-}\int d\mathbf{r}\rho_\alpha(\mathbf{r})\left[\ln\rho_\alpha(\mathbf{r})-1\right] . \tag{4.9}$$

The hard-sphere-like short-range repulsion plays a key role in determining the structure of a condensed matter and thus is important in virtually all classical DFT

calculations. The excess Helmholtz free energy due to hard-sphere repulsion F_{hs}^{ex} can be accurately represented by modified fundamental measure theory (MFMT) [85, 88],

$$\beta F_{hs}^{ex} = \int \Phi^{hs}\left[n_w(\mathbf{r})\right] d\mathbf{r}, \tag{4.10}$$

where the reduced excess free energy density Φ^{hs} is represent by six weighted densities $n_w(\mathbf{r})$ [83]

$$\begin{aligned}\Phi^{hs} = & -n_0 \ln(1-n_3) + \frac{n_1 n_2 - \mathbf{n}_{V1}\mathbf{n}_{V2}}{1-n_3} \\ & + \frac{1}{36\pi}\left[n_3 \ln(1-n_3) + \frac{n_3^2}{(1-n_3)^2}\right]\frac{n_2^3 - 3n_2\mathbf{n}_{V2}\mathbf{n}_{V2}}{n_3^3}\end{aligned}. \tag{4.11}$$

The detailed expression of weighted densities $\{n_w, w = 1,2,3,V1,V2\}$ can be found in Rosenfeld's original work [83].

In addition to the excluded-volume effects represented by the hard-sphere interactions, the excess Helmholtz energy includes also contributions due to the intra-chain correlations. According to an extension of the first-order thermodynamic perturbation theory (TPT1) [76, 79], the excess Helmholtz free energy due to chain connectivity F_{ch}^{ex} is given by

$$\beta F_{ch}^{ex} = \frac{1-M}{M}\int n_{0p}\zeta_p \ln y(\sigma, n_\omega)\, d\mathbf{r}, \tag{4.12}$$

where $\zeta_p = 1 - \mathbf{n}_{\mathbf{V2p}}\mathbf{n}_{\mathbf{V2p}} / n_{2p}^2$ accounts for the effect of local density variation, and $y(\sigma, n_\omega)$ is the contact value of the cavity correlation function (CCF) of the polymeric segments.

A key assumption of TPT1 is that CCF can be represented by that corresponding to a monomeric reference system [95, 96]

$$y\left(\sigma,n_{\omega}\right)=\left[\frac{1}{1-n_3}+\frac{n_2\sigma\left(1-\mathbf{n}_{\mathbf{V2}}\mathbf{n}_{\mathbf{V2}}/n_2^2\right)}{4\left(1-n_3\right)^2}\right]\exp\left(-\frac{\Gamma^2a_p^2}{4\pi^2l_B\sigma}\right)\exp\left(\frac{l_BZ_p^2}{\sigma}\right). \tag{4.13}$$

where parameters Γ and a_p are calculated from

$$\Gamma=\sqrt{\pi l_B\sum_{k=p,+,-}n_{0k}\left(\frac{1}{1+\Gamma\sigma}\right)^2\left(Z_k-\frac{\pi P_n\sigma^2}{2\left(1-n_3\right)}\right)^2}\,, \tag{4.14}$$

$$a_p=\frac{2\pi l_B\left(Z_p-\dfrac{\pi P_n\sigma^2}{2\left(1-n_3\right)}\right)}{\Gamma\left(1+\Gamma\sigma\right)}, \tag{4.15}$$

with

$$P_n=\sum_{k=p,+,-}\frac{2n_{1k}Z_k}{1+\Gamma\sigma}\Bigg/\left(1+\frac{3}{\left(1-n_3\right)}\sum_{k=p,+,-}\frac{n_{3k}}{1+\Gamma\sigma}\right). \tag{4.16}$$

The excess Helmholtz free energy due to the electrostatic interactions includes two parts: one is due to the direct Coulomb interaction as that appeared in the Poisson-Boltzmann (PB) equation [146], and the other part accounts for the electrostatic correlations [76]. Given the distributions of charged species, the energy due to the direct Coulomb interactions can be written as

$$\beta F_C^{ex}=\frac{l_B}{2}\sum_{i,j=p,+,-}\iint d\mathbf{r}d\mathbf{r}'\frac{Z_iZ_j\rho_i\left(\mathbf{r}\right)\rho_j\left(\mathbf{r}'\right)}{\left|\mathbf{r}-\mathbf{r}'\right|}, \tag{4.17}$$

where p, $+$, $-$ stand for polyion segments, cations and anions respectively. Because of the long-range nature of the electrostatic potential, the integrals on the right side of Eq. (4.17) diverge for any pair interactions.

To avoid numerical problems, we calculate the electrostatic energy from the local mean electrostatic potential

$$\psi(\mathbf{r}) = \int d\mathbf{r}' \sum_{j=p,+,-} \frac{Z_j e \rho_j(\mathbf{r}')}{4\pi\varepsilon |\mathbf{r} - \mathbf{r}'|}, \tag{4.18}$$

where e is the unit charge. Eq. (4.18) is the integrated form of the Poisson equation

$$\nabla^2 \psi(\mathbf{r}) = -\frac{\rho_c(\mathbf{r})}{\varepsilon}, \tag{4.19}$$

where $\rho_c(\mathbf{r})$ is the local net charge density. Because the Helmholtz energy functional given by Eqs. (4.9) and (4.17) alone would lead to the conventional Boltzmann distribution for charged species, the Poisson-Boltzmann equation for electrostatic systems can be understood as a simple application of the DFT.

The excess Helmholtz free energy due to electrostatic interaction F_{el}^{ex} can be obtained by a quadratic functional expansion of excess Helmholtz free energy with respect to that for a bulk fluid of uniform densities $\{\rho_i^b\}$ [106, 147],

$$\begin{aligned} \beta F_{el}^{ex} = \beta F_{el}^{ex}\left[\{\rho_i^b\}\right] - \int d\mathbf{r} \sum_{i=p,+,-} \Delta C_i^{(1)el}\left[\rho_i(\mathbf{r}) - \rho_i^b\right] \\ - \frac{1}{2}\int\int d\mathbf{r} d\mathbf{r}' \sum_{i,j=p,+,-} \Delta C_{ij}^{(2)el}\left(|\mathbf{r} - \mathbf{r}'|\right)\left[\rho_i(\mathbf{r}) - \rho_i^b\right]\left[\rho_j(\mathbf{r}) - \rho_j^b\right] \end{aligned}, \tag{4.20}$$

where $\Delta C_i^{(1)el}$ and $\Delta C_{ij}^{(2)el}$ are the first-order and the second-order direct correlation functions (DCF) due to the electrostatic correlations in the reference system,

$$\Delta C_i^{(1)el} = -\beta\mu_i^{el} = -\delta\beta F_{el}^{ex} / \delta\rho_i(\mathbf{r})\big|_b , \tag{4.21}$$

$$\Delta C_{ij}^{(2)el}\left(\left|\mathbf{r}-\mathbf{r}'\right|\right) = -\delta^2\beta F_{el}^{ex} / \delta\rho_i(\mathbf{r})\delta\rho_j(\mathbf{r})\big|_b . \tag{4.22}$$

Here, we assume that the electrostatic correlation due to the chain connectivity can be ignored [76]. In this work, the DCF is obtained from mean-spherical approximation (MSA) of simple electrolytes [93, 96].

At equilibrium, the grand potential is minimized with respect to the density profiles of polyions segments and small ions as required by the second law of thermodynamics, leading to the Euler-Lagrange equations:

$$\rho_{\mathrm{M}}(\mathbf{R}) = \exp\left\{\beta\mu_{\mathrm{M}} - \beta V_{\mathrm{b}}(\mathbf{R}) - \sum_{i=1}^{M}\left[\beta\Psi_p(\mathbf{r}_i) + \frac{\delta\beta F^{ex}}{\delta\rho_p(\mathbf{r}_i)}\right]\right\}, \tag{4.23}$$

$$\rho_\alpha(\mathbf{r}) = \exp\left[\beta\mu_\alpha - \beta\Psi_\alpha(\mathbf{r}) - \frac{\delta\beta F^{ex}}{\delta\rho_\alpha(\mathbf{r})}\right]. \tag{4.24}$$

For the polyelectrolyte systems considered in this work, the segmental density profiles of polyions and monomeric ions vary only in the *r* direction, i.e. the radial direction of a spherical capsid. As a result, the Euler-Lagrange equations [Eqs. (4.23), (4.24)] can be simplified to

$$\rho_\alpha(r) = \exp\left[\beta\mu_\alpha - \beta\lambda_\alpha(r)\right], \tag{4.25}$$

and for segmental distribution of flexible polyelectrolyte,

$$\rho_{p,\,flex}(r)=\frac{M\sum_{i=1}^{M}\exp\left[-\beta\lambda_{p,\,flex}(r)\right]G_{flex}^{i}(r)G_{flex}^{M+1-i}(r)}{\int 4\pi r^{2}dr\exp\left[-\beta\lambda_{p,\,flex}(r)\right]G_{flex}^{i}(r)G_{flex}^{M+1-i}(r)}, \tag{4.26}$$

where $\lambda_{\alpha}(r)$ and $\lambda_{p,\,flex}(r)$ present the effective one-body potential for a small ion and flexible polyelectrolyte segment, respectively, $G_{flex}^{i}(r)$ stands for a polymer propagator function (i.e., Green function) of flexible polyion, determined from the recursive relation

$$G_{flex}^{i}(r)=\int dr'G_{flex}^{i-1}(r')\exp\left[-\beta\lambda_{p,\,flex}(r')\right]\frac{\theta\left(\sigma-\left|r-r'\right|\right)}{2\sigma}, \tag{4.27}$$

for $i=1,2,\cdots,M$ with $G_{flex}^{1}(r)=1$.

For a sufficiently long homopolymer, we may use the no-end-effect approximation [29]. In that case, the Green function becomes indistinguishable for each segment: $G_{flex}^{i}(r)\approx G_{flex}(r)$. Therefore, Eq. (4.26) can be simplified as

$$\rho_{p,\,flex}(r)=\frac{M\exp\left[-\beta\lambda_{p,\,flex}(r)\right]G_{flex}{}^{2}(r)}{\int 4\pi r^{2}dr\exp\left[-\beta\lambda_{p,\,flex}(r)\right]G_{flex}{}^{2}(r)}, \tag{4.28}$$

with

$$G_{flex}(r)=\int dr'G_{flex}(r')\exp\left[-\beta\lambda_{p,\,flex}(r')\right]\frac{\theta\left(\sigma_{p}-\left|r-r'\right|\right)}{2\sigma_{p}}. \tag{4.29}$$

Similar to the density distribution of flexible polyelectrolyte, the segmental distribution of a semi-flexible polyelectrolyte is given by

$$\rho_{p,semi}(r)=\frac{\exp\left[-\beta\lambda_{p,semi}(r)\right]S(r)}{\int 4\pi r^{2}dr\exp\left[-\beta\lambda_{p,semi}(r)\right]S(r)}, \tag{4.30}$$

where

$$S(r)=\int_{|\sigma_p-r'|}^{\sigma_p+r'} dr'\,r'G_{semi}(r,r')\exp\left[-\beta\lambda_{p,semi}(r')\right]G_{semi}(r',r). \tag{4.31}$$

With the assumption of no-end-effect [31, 109], the chain propagator of semi-flexible polyelectrolyte is given as

$$G_{semi}(r,r')=\frac{1}{2\sigma_p r}\int_{|r-\sigma_p|}^{r+\sigma_p} dr''\,r''G_{semi}(r'',r)P(\alpha,\theta,r''), \tag{4.32}$$

where

$$P(\alpha,\theta,r'')=\exp\left[-\beta\lambda_{p,semi}(r'')-\phi_0(1+\cos\theta\cos\alpha)\right]I_0(\sin\theta\sin\alpha). \tag{4.33}$$

α and θ are the inside angles formed by the i-th bond and $i-1$-th bond with vector $\mathbf{r}_i$ and $\mathbf{r}_{i-1}$, respectively. $I_0(x)=\frac{1}{2\pi}\int_0^{2\pi}\exp(-x\cos\Phi)d\Phi$ is a modified Bessel function. More details about the segmental distribution function of semi-flexible polyelectrolyte can be referred to the supplementary materials of Ref. [31].

The effective one-body potential λ depends on the external potential $\Psi(r)$ in Eq. (4.7), the mean electrostatic potential $\psi(r)$ in Eq. (4.18), and local excess chemical potentials due to hard-sphere repulsion, chain connectivity and electrostatic correlation effects:

$$\lambda_k(r)=\Psi_k(r)+Z_k e\psi(r)+\delta\left(F_{hs}^{ex}+F_{ch}^{ex}+F_{el}^{ex}\right)/\delta\rho_k(r). \tag{4.34}$$

The mean electrostatic potential is given by

$$\psi^*(r)\equiv\beta e\psi(r)=\psi^*(r=0)-4\pi l_B\int_0^r dr'\left(r'-\frac{r'^2}{r}\right)\sum_{k=p,+,-}Z_k\rho_k(r'). \tag{4.35}$$

Eq. (4.35) can be derived from the integration of Poisson equation (Eq. (4.19)) by applying boundary condition $d\psi(r)/dr|_{r=0}=0$ at the capsid center. On the other hand, by applying another boundary condition $\psi(r=\infty)=0$, we can obtain mean electrostatic potential at capsid center, e.g. $\psi^*(r=0)$.

We solve the density distributions of polyion segments and small ions with the Picard iteration method. The numerical procedure starts with an initial guess for the density profiles of polyions and monomeric ions based on their bulk densities. The reduced electrostatic potential $\psi^*(r)$, the effective fields for polyion segments and monomeric ions, $\lambda_k(r)$, and the Green function $G^i(r)$ for polyions are then calculated. Subsequently, new density profiles are updated by using Eqs. (4.25) and (4.26). The new density profiles are mixed with the previous results as the new inputs. The iteration procedure repeats until the change in the input and output density profiles of polyions and monomeric ions is smaller than 0.01% at all positions.

4. 3 Results and Discussions

4. 3. 1 Comparison between MC and DFT

In this section, we validate the numerical performance of the polyelectrolyte density functional theory (DFT) with molecular simulations for polyelectrolytes in spherical capsids. To explore a broad parameter space, we consider polyelectrolytes with different bending energies and electrolyte solutions with various salt concentrations and ionic valences. We compare the density profiles of polyions and small ions to those obtained from Monte Carlo (MC) simulations.

Because of numerical challenges in calculation of electrostatic interactions in an extended environment, simulation results are rare for confined polyelectrolytes. Fortunately, Angelescu, *et, al.* [131, 132] reported a series of studies on thermodynamics and electrostatics of a single polyion confined in a charged capsid using MC simulations. For the sake of comparison, the parameters in our DFT calculations are chosen to be the same as those used in their studies, i.e., $\sigma = 0.4\text{nm}$ for ionic and segment diameters, $R_c = 5.0\text{nm}$ for the inner radius of the spherical capsid, and $D_c = 1.2\text{nm}$ for the capsid thickness. For numerical convenience, our DFT calculations are based on the tangent chain model for polymer backbone but the simulation uses the bead spring model. With a reasonable choice of the parameters for the bond connectivity, we expect that the difference between these two models is insignificant. Because the simulations were performed in the NVT ensemble, the cut-off distance in the DFT calculations (or the size of calculation cell) is chosen to be the same as the simulation cell. We use the chemical potentials as the Lagrange multipliers to impose number conservations for all species inside the calculation cell.

4. 3. 1. 1 Flexible Polyelectrolyte Encapsidation

In this subsection, we compare the density profiles of polyelectrolyte segments and small ions with the MC simulation results. For a flexible polyelectrolyte chain, the parameter specifying the intrinsic bending stiffness satisfies $\beta\phi_0 = 0$.

Figure 4-2 shows the distributions of polyion segments obtained from the DFT calculations and from MC simulations for flexible polyelectrolytes of different chain lengths in a spherical capsid. The total capsid charge is $Q_c = +250$, and the valences of

cations and anions are $Z_+ = +1$ and $Z_- = -1$, respectively. As in MC simulation, we consider three different polyion chains with length $M = 100$, $M = 250$ and $M = 400$; the corresponding calculation cell radii are $R_{cell} = 50\,\text{nm}$, $R_{cell} = 56.3\,\text{nm}$ and $R_{cell} = 61.4\,\text{nm}$, respectively, to ensure that the small ions reach bulk properties near the boundary. In MC simulations, the number of anions is fixed at $N_- = 250$, the same as the number of charges of the spherical capsid, and the number of cations are $N_+ = 100$, $N_+ = 250$ and $N_+ = 400$ for three different polyion chain lengths. The total cation charge is the same as the charge of the polyelectrolyte. The model system mimics capsids dispersed in an aqueous electrolyte solution with low bulk salt concentration.

Despite different models for the polymer backbone, the DFT is able to reproduce the MC results near quantitatively. However, the distinctive features of soft and hard potentials are noticeable near the hard-wall surface within a distance comparable to the diameter of polymer segments. While the density profile generated by the soft potential used in MC for molecular excluded volume and chain connectivity is smooth, the tangent hard-sphere chain model exhibits sharp edges at the hard wall and the bond length and such edges are more visible as the polymer concentration/chain length increases. The polyelectrolyte segments accumulate near the inner surface of capsid due to strong electrostatic attraction from the positively charged surface. The density of polymer segments is near zero until the total charge of polyelectrolyte is larger than the capsid charge (e.g. $M = 400$). Despite the opposite charge at the capsid surface, the DFT

predicts that the polymer segments are slightly repelled from inner surface due to the intra-chain correlations. Such depletion was less apparent in the simulation results.

Figure 4-3 and 4-4 show, respectively, the density profiles of monomeric anions and cations for the systems considered above. The agreement between DFT and MC simulation is excellent for both cases. Because the cations are coupled with polyelectrolyte segments, the difference between DFT and MC simulation shown in Figure 4-4 is probably due to discrepancies on polymer segment distributions near the inner capsid surface. When the polyion net charge is less than that of the capsid, the capsid contains more anions than cations. However, when the polyelectrolyte has equal or more net charge than the capsid, strong accumulation of polyions near the inner capsid surface makes the integrated charge distribution function $P(r)=\int_0^r \mathrm{d}r' \sum_{k=p,+,-} Z_k \rho_k (r')$ negative at $r \approx R_c - \sigma/2$. In this case, the electric field produced by such charge distribution (according to the Gauss law) points inward to the capsid center and therefore repels the anions from accumulating at the inner capsid surface and attracts cations. On the other hand, the positive electric field from the capsid out surface has opposite effect and the competitions among various electric field and excluded-volume effect results in a maximum in the distribution of cations at $r = 4\,\mathrm{nm}$.

When $M = 100$, the polyelectrolyte-capsid complex is positively charged and thus attracts anions to and repels cations from the outer capsid surface, shown in Figure 4-3 (a) and 4-4 (a) respectively. On the other hand, when $M = 400$, the complex is negatively charged and thus attracts cations to and repels anions from the outer capsid

surface (case c). The overcharged capsid attracts extensive number of cations into the capsid, as shown in Figure 4-4 (c). Although electrostatic interactions facilitate the polymer segments to reside at the inner surface of the capsid, the polymer segments extend into the capsid center due to strong excluded-volume effect and chain connectivity. For the case such that the polyelectrolyte and capsid have the same electric charge ($M = 250$), some anions are released from the capsid and some cations reside inside the capsid, making the net charge of the complex slightly positive. Overall, the small ion distributions inside the capsid do not compensate the net charge of polyelectrolyte and capsid complex and the overall net charges are $108e$, $6e$, and $-23e$, respectively, in good agreement with the simulation data [131]. Our DFT calculation affirms that the overall charge of a capsid complex is not neutral. The charge neutrality is valid only for the entire system that includes both polymer-containing capsid and small ions in the bulk solution.

4. 3. 1. 2 Effects of Chain Rigidity

In this subsection, we validate the DFT results for confined semi-flexible polyelectrolytes with MC simulation data [131] by comparing the density profiles for the polymer segments as well as for small ions. The model parameters are similar to those used in the previous subsection except that now the potential for chain connectivity takes in to account the bending stiffness ($\beta\phi_0 = 10$).

Figure 4-5 shows the DFT and MC simulation results for the density distributions of semi-flexible polyelectrolyte segments in a spherical capsid. Here the model parameters are the same as those used in Figure 4-2 but with the bending stiffness. By

comparing to Figure 4-2, we see noticeable influences of the chain stiffness on the density distributions of polymer segments. In contrast to flexible polyelectrolytes, the density profiles for semi-flexible polyions do not exhibit sharp edges and they are more attracted towards the inner capsid surface. It appears that the bending rigidity suppress the penalty of chain configurational entropy. Furthermore, the contact density of semi-flexible polymer at inner capsid surface is slightly higher than that of flexible polyelectrolyte. Although we take into account the bending energy on the mean-field basis, the DFT shows good agreement with simulation data [131].

Figure 4-6 and 4-7 present the density profiles of anions and cations for the confined semi-flexible polyelectrolytes, respectively. Similar to encapsidation of intrinsically flexible polyions discussed above, the agreement between DFT and MC simulation is very good. Unlike polymer segment distributions, the effect of chain stiffness on the distribution of small ions is insignificant. Because a semi-flexible polyelectrolyte chain is closer to the inner surface of capsid, the capsid contains slightly fewer cations in comparison to the case of flexible polymer. Because the chain stiffness has little effects on the microscopic structure, at the same condition the net charge of semi-flexible polyion-capsid complex remains similar to that of flexible polyion-capsid complex.

Overall, the segmental density distributions of polymer monomers and small ions are in good agreement with MC simulation for both semi-flexible and flexible polyelectrolytes.

4. 3. 1. 3 Effects of Salt Valences

In this subsection, we compare the DFT calculations with MC simulation for the segmental distributions of polyelectrolytes in electrolyte solutions with various ionic valences. In this case, the valences of polyion segment and anion remain the same (-1), while we consider three different cation valences (Z_+=1, 2, 3). Because the effect of chain stiffness was considered in the previous subsection, our comparison here is focused on flexible polyelectrolytes.

Figure 4-8 shows the DFT and MC simulation results for the density distributions of flexible polyelectrolyte segments in a spherical capsid surrounded by electrolytes of different cation valences [132]. In all cases, the cell radius is fixed at $R_{cell} = 10\,\text{nm}$. As the cation valence increases, the polyion segments are more depleted from the inner surface because of stronger screening effects. The total packing density inside the capsid falls as the cation valence increases; and more anions are attracted to the inner surface. While qualitatively the DFT results agree well with MC simulation, the discrepancy clearly increases with the cation valence. The difference can be attributed in part to approximations of the DFT and in part due to small simulation range [132]. The small cell size makes the properties of small ions near the boundary different from those in the bulk and because of the small ionic concentration, such difference has a drastic effect on the density profiles. Furthermore, the interaction between the small ions and the cell wall was represented by a hard-wall potential that truncates the long-ranged electrostatic interactions. Due to the long-ranged nature of electrostatic interactions, such cell would influence the distributions of small ions and polymer segments in MC simulation but has little effects in the DFT calculation that is based on the grand canonical ensemble [132].

While the size effect is significant in MC simulation, the DFT calculation fully incorporates the long-ranged electrostatic interactions so that the properties of small ions at the boundary are the same as those in the bulk limit.

Figures 4-9 and 4-10 present the density distributions of anions and cations, respectively for the system discussed above. As the valence of cation decreases, the capsid contains more anions to neutralize the positively charged capsid surface. The cations are accumulated approximately at $r = 4\,\mathrm{nm}$ due to the interplay between excluded-volume effect and electrostatic interactions. In general, DFT results agree with MC simulation qualitatively, but not quantitatively probably due to the reason we explained above.

Figure 4-9 and 4-10 present the density distributions of anions and cations, respectively. As the valence of cation decreases, more anions are attracted to the inner surface to neutralize the positively charged capsid surface. The cations accumulated approximately at $r = 4\,\mathrm{nm}$ as a result of the interplay between excluded-volume effect and electrostatic interaction. In general, DFT calculations agree with MC simulation qualitatively, but not quantitatively probably due to the reason we explained above.

4. 3. 2 Effects of The Outside Environment

Unlike more previous theoretical investigation of polyelectrolyte packaging [33, 134], this work takes into account the solution environment outside the capsid explicitly. In other words, we do not impose the condition of charge neutrality to space occupied by the capsid but to the overall thermodynamic system. We find that the local charge neutrality would have huge impact on the distributions of polyion segments and small

ions. To illustrate the effects of the solution environment outside the capsid, we compare the density profiles of polyelectrolyte and small ions with and without explicit consideration of the background electrolyte solution. For convenience, the former is referred to as an open system and the latter as semi-open system because the ionic distributions outside the capsid are not explicitly considered. In the latter case, the charge neutrality condition is imposed for the capsid and the small ions are confined in spherical capsid with chemical potentials defined by the bulk solution.

Figure 4-11 compares the density distributions of polyelectrolyte segments with and without considering the outside environment. To be consistent, we assume that the bulk properties of small ions for the semi-open system are set to be the same as those of the open system. At low polyelectrolyte concentration ($M = 100$ and $M = 250$), the assumption of capsid charge neutrality results in a distribution of polyion segments qualitatively different from that without the assumption. With the charge neutrality assumption for the capsid, the DFT predicts that the polyion is depleted from the oppositely charged surface, in sharp contrast to strong accumulation of the polyion segments without that assumption. As shown later in Figures 4-12, the semi-open system (with the charge neutrality assumption) contains much more small ions, screening the electrostatic attraction from the capsid surface. The increased small ion concentration is primarily because the outer surface of the viral capsid is unavailable to small ions. At large polyelectrolyte concentrations, the polyion distribution is mainly determined by direct electrostatic interaction and the excluded-volume effects. In that case, the anions are depleted from the capsid in the semi-open system, and as indicated in Fig. 4-4(c), the

cations are mostly attracted inside the capsid to neutralize the excess charge of the polyion for the open system. As a result, the difference in the segmental density distributions of polyelectrolytes is small.

Figures 4-12 and 4-13 compare the semi-open and open systems for the density distributions of anions and cations, respectively. Because no ions are outside for the semi-open system, we present the density profiles only inside the capsid. As mentioned above, the capsid in the semi-open system contains more anions and cations when the net polyion charge is less or equal to that of the capsid. However, the opposite is true if the net polyelectrolyte charge is larger than that of the viral capsid. Due to strong electrostatic interactions from the polyelectrolyte, anions are almost completely depleted from the viral capsid in the semi-open system.

In comparison to the open system, the capsid surface area accessible to counterions is greatly reduced for the semi-open system. As a result, the small ions are more attracted inside the viral capsid for the semi-open system except when the polyelectrolyte charge is much larger than that of the viral capsid. Because of the difference in the ionic concentration, the distribution of polyelectrolyte segments varies drastically. Therefore, the outside environment dramatically affects the structural and thermodynamic properties of confined polyelectrolytes.

4. 3. 3 Net Charge of Spherical Capsid

In this section, we study the net charges of polyelectrolyte-capsid complexes at different polymer chain lengths and ionic concentrations. The net charge Q_N of a polyelectrolyte complex is defined by

$$Q_N = Q_c + MZ_p + N_+^{in} Z_+ + N_-^{in} Z_-, \tag{4.36}$$

where N_+^{in} and N_-^{in} are the numbers of cations and anions inside the capsid, respectively. In most previous studies of polyelectrolyte packaging [33, 134], the outside environment was not considerably explicitly and the net charge of viral capsid was presumed neutral. Explicit consideration of the outside environment allows us to assess the local charge neutrality assumption and to examine how the net charge varies with the properties of the confined polyelectrolyte, viral capsid size and charge density, and the concentration and valences of small ions.

Figure 4-14 shows the DFT predictions for the net charge of a polyelectrolyte-capsid complex varying with the polyelectrolyte chain length at different salt concentrations. At high salt concentration ($C_{salt} = 550\,\text{mM}$), the net charge of the polyelectrolyte complex decreases slowly with the polyelectrolyte chain length but remains positive even though the total charge of the polyelectrolyte is larger than that of the viral capsid. When the salt concentration is low ($C_{salt} = 11\,\text{mM}$), however, the net charge decreases quickly with the polyion chain length, and after a certain point the net charge is inversed due to the increased excluded-volume and screening effects originated from the polyelectrolyte backbone. Interestingly, charge inversion is most likely in monovalent solutions. In all cases, the net charge of a polyelectrolyte complex is clearly not neutral; it varies with the polyelectrolyte chain length as well as the salt concentration.

Figure 4-15 shows the DFT predictions for the net charge of a polyelectrolyte-capsid complex changing with the polyion chain length. Here the capsid is surrounded by

electrolyte solutions of different cation valences. For the system containing monovalent cations, the net charge of the polyelectrolyte-capsid complex decreases with the polymer chain length; but for the system containing trivalent cations, the net charge of the complex reaches a plateau after a certain polymer chain length. Similar to the case of high salt concentration, the net charge of capsid complex remains positive for trivalent cations, even though the polyion charge is larger than that of the capsid. As shown in Figure 4-14, the charge neutrality is not satisfied for a polyelectrolyte-capsid complex; the net charge depends on the polyion chain length and the valences of small ions.

4. 3. 4 Discontinuity of Dielectric Constant

In both DFT calculations and MC simulations, we have assumed that the dielectric constant of the capsid is the same as that of an aqueous solution. In reality, however, the viral capsid may have a dielectric constant (ε_c) quite different from that of an aqueous solution (ε). In this subsection, we study the effect of inhomogeneous dielectric constants on the density distributions of polyelectrolyte segments and small ions.

For simplicity, we assume that the position dependence of the dielectric constant $\varepsilon(\mathbf{r})$ inside the capsid is given by

$$\varepsilon(\mathbf{r}) = \begin{cases} \varepsilon_c = 4, & R_c < r < R_c + D_c \\ \varepsilon = 78.4, & \text{otherwise} \end{cases}, \tag{4.37}$$

where D_c is the capsid wall thickness, the capsid dielectric constant $\varepsilon_c = 4$ is typical for the hydrophobic domain of a protein, and $\varepsilon = 78.4$ corresponds to the dielectric constant

for water at ambient conditions. With the discontinuity of the dielectric constant defined above, we can obtain the electric potential by solving the generalized Poisson equation

$$\nabla^2\psi(\mathbf{r}) = -\frac{\rho_c(\mathbf{r})}{\varepsilon(\mathbf{r})}. \tag{4.38}$$

using two boundary conditions, e.g., $\left.\frac{\mathrm{d}\psi(r)}{\mathrm{d}r}\right|_{r=0} = 0$ and $\psi(r = R_{cell}) = 0$ as well as the continuous nature of electrostatic potential. From the mean electrostatic potential from Eq. (4.38), we can subsequently the distributions of polymer segments and small ions. We note that the generalized Poison equation neglects the "image charge" effect due to the discontinuity of the dielectric constant.

Figure 4-16 shows the density distribution of polyelectrolyte segments with the dielectric discontinuity specified by Eq. (4.37). For comparison, we also present the density profile with a uniform dielectric constant. When the polyelectrolyte charge is less or equal to that of the capsid, the dielectric inhomogeneity makes polyion slightly closer to the inner surface; but the opposite is true when the polyion charge is larger than that of the capsid. For smaller dielectric constant, it needs more polyelectrolyte segments to neutralize the charge of capsid when the charge of polyion is not larger than that of capsid surface. In both cases, the effect of capsid dielectric constant on the distribution of polyion segments is rather insignificant, which justifies in part the extensive use of uniform dielectric model in the literature.

We observe a similar trend for the effect of dielectric discontinuity on the anion distribution. As shown in Figure 4-17, introduction of the dielectric discontinuity makes

anions more attracted to the capsid inner surface but more repelled from the outer surface when the polyion charge is less or equal to that of the capsid. When the polyelectrolyte charge is larger than that of the capsid, however, the dielectric inhomogeneity makes anions more attracted to the outer surface of the capsid but has only negligible effect on the anion distribution near the inner surface of the capsid.

Figure 4-18 shows that the effect of dielectric discontinuity on cation distribution is completely opposite to that of anions. Cations become more depleted from inner surface of the capsid when the polyion charge is less or equal to that of the capsid and more attracted to the inner surface when the polyion charge is more than that of the cage. The trend is opposite for cations outside the shell. Overall, the DFT calculations indicate that the inhomogeneous dielectric constants have insignificant effect on the density distributions of polyelectrolyte segments and small ions.

4. 4 Conclusions

In this chapter, we have used the density functional theory (DFT) to study the structural and surface properties of flexible and semi-flexible polyelectrolytes confined within spherical capsids. Unlike most previous work [33, 134], we consider the polyelectrolyte containing capsids in equilibrium with a bulk salt solution. After extensive comparison of the density profiles of polymer segments and small ions predicted by DFT with MC simulation data [131], we investigated in detail the effects of solution conditions and capsid dielectric inhomogeneity on the overall capsid charge and the polyelectrolyte segment and ionic distributions.

The DFT equations are similar to those used in our previous works for inhomogeneous polyelectrolyte solutions [33, 76]. Specifically, we adopted the modified fundamental measure theory to account for the excess Helmholtz energy functional due to the hard-sphere repulsion. The extended first-order thermodynamic perturbation theory accounts for the excess Helmholtz free energy functional due to the polyion chain connectivity. The mean-spherical approximation accounts for the excess Helmholtz energy functional due to the electrostatic correlation. The mean electrostatic potential from Poisson equation takes into account the excess Helmholtz energy functional due to direct Coulomb interactions.

Extensive comparison of the DFT and simulation results indicates that the DFT provides an efficient and reliable way to describe the density distributions of polyelectrolyte segments and small ions as well as net charges of capsid complex for different chain lengths and bending stiffness. Similar to our previous work for inhomogeneous polyelectrolytes, the agreement between DFT and MC simulation [131] is near quantitative over a broad range of the parameter space pertinent to polyelectrolyte encapsidation. The numerical performance is less satisfactory only when there is certain discrepancy in the thermodynamic conditions defining the DFT and MC calculations. Similar to MC simulation [131], the DFT calculations reveal that the small ions do not compensate the net charge of the polyelectrolyte and capsid complex and the assumption of local charge neutrality is in general not valid.

We also examined the dependence of density distributions of polyelectrolyte segments and small ions on the outside solution conditions. Our DFT calculations

indicate that the outside environment has significant impact on the distributions of both polyelectrolyte segments and small ions especially when the polymer concentration is low. In comparison with the calculation based on the local charge neutrality, the capsid contains fewer amounts of small ions when the outside environment is explicitly considered. The reduction of small ion content can be explained by neutralization of the capsid charge by counterions outside of the capsid surface that is not accounted for in the charge neutrality assumption. Because we consider the outside environment explicitly in our DFT calculations, the charge neutrality is imposed to the entire thermodynamic system instead of the space inside the capsid. As a result, we are able to examine whether or not the net charge of capsid complex is neutral and how the net charge varies with the polyelectrolyte chain length, the salt concentration and ionic valences. At high ionic strength, the net charge of capsid complex is insensitive to the polyelectrolyte chain length due to the strong screening effect. At low ionic strength, however, the trend is opposite. The DFT predicts that charge inversion occurs at low salt concentration and large polyelectrolyte chain length. We find that in general the local charge neutrality is not valid for a viral capsid. The outside solution environment has significant effects on the net charge of polyelectrolyte-capsid complex and the distributions of polyelectrolyte and small ions.

We also studied the influences of the dielectric constant of the capsid wall on the density profiles of polyion segments and small ions. Our DFT calculations indicate that the dielectric inhomogeneity has opposite effects the charge distributions at low and high polyions concentrations. Although the image charge effect was not considered in our

calculations, it appears that the inhomogeneity in dielectric constants has insignificant effect on the structural and thermodynamic properties of polyelectrolyte packaging.

Figure 4-1 A schematic picture of the model system studied in this work. The dark blue spheres stand for polyelectrolyte segments, the green spheres for anions, the red spheres for cations, and the dark red shell with shaded background for a semi-permeable protein capsid. The entire system is embedded in a spherical cell such that the boundary (solid line) has negligible effects.

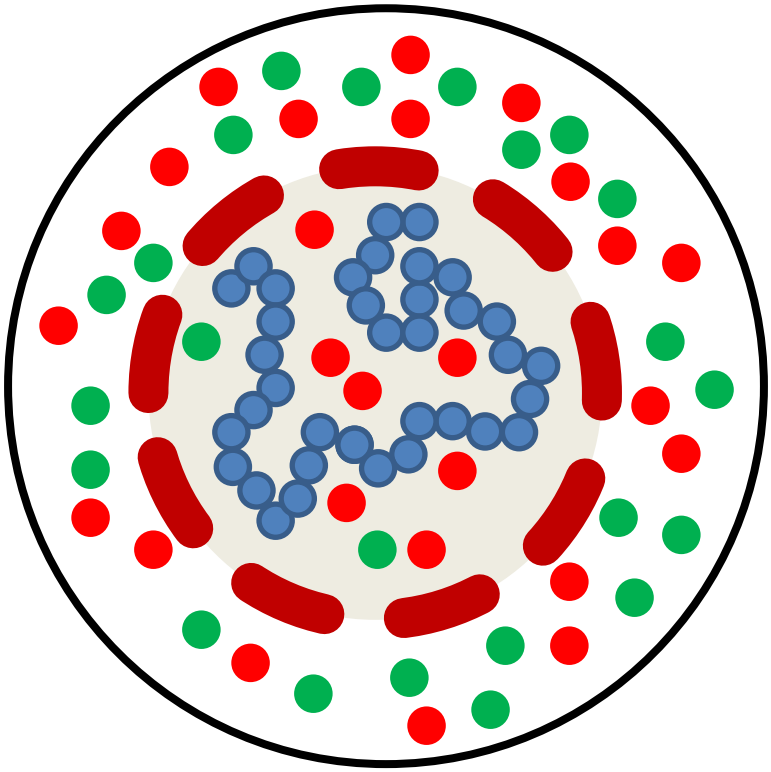

Figure 4-2 (a) Density distribution of polymer segments $\rho_p(r)$ is plotted as a function of radial distance r for a flexible polyelectrolyte confined in a spherical shell with total charge $Q_c = +250$. Here the polymer chain length is $M = 100$ and each segment carries unit negative charge, the valences of cations and anions are $Z_+ = +1$ and $Z_- = -1$, respectively. In MC simulation [131], the cell radius is $R_{cell} = 50\,\text{nm}$, the numbers of cations and anions simulated are $N_+ = 100$ and $N_- = 250$, respectively. (b) The same as Fig. 4-2 (a) except that the polymer chain length is $M = 250$, cell radius $R_{cell} = 56.3\,\text{nm}$, and the number of cations simulated is $N_+ = 250$. (c) The same as Fig. 4-2 (a) except that the chain length is $M = 400$, the cell radius is $R_{cell} = 61.4\,\text{nm}$, and the number of cations simulated is $N_+ = 400$.

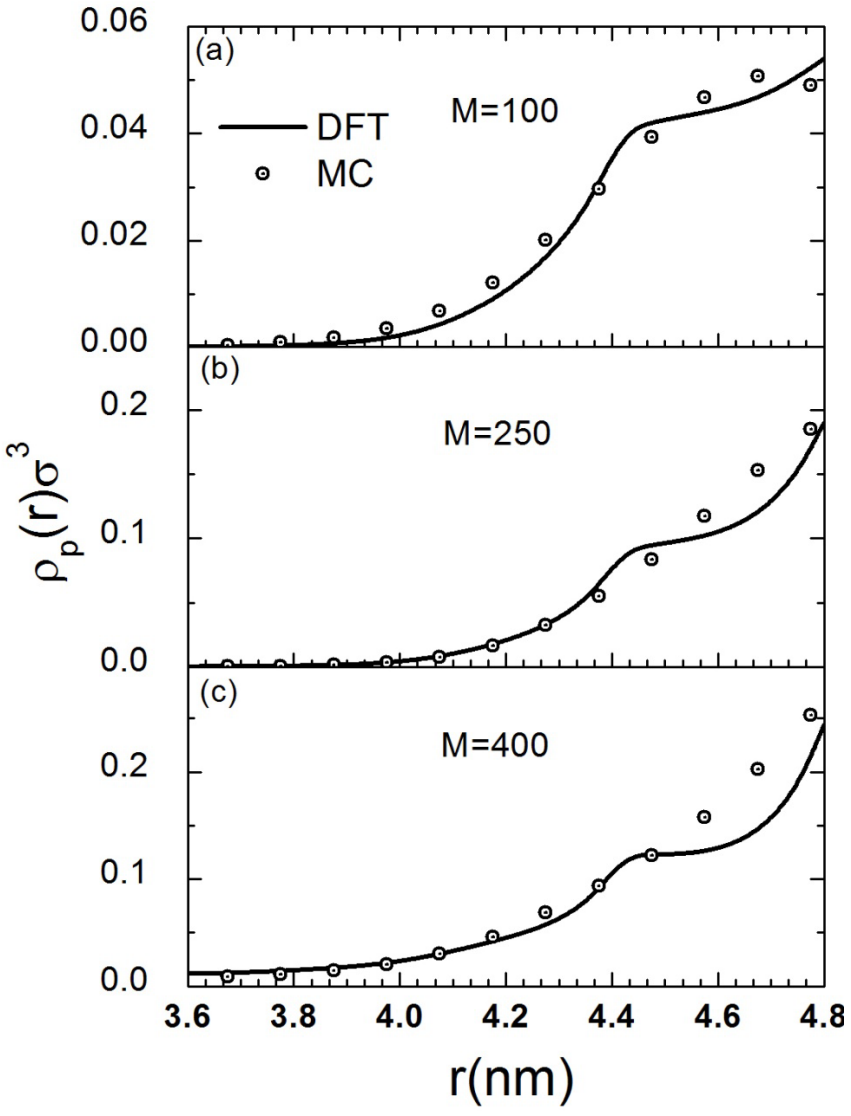

Figure 4-3 The same as Fig. 4-2 but for the density profiles of anions.

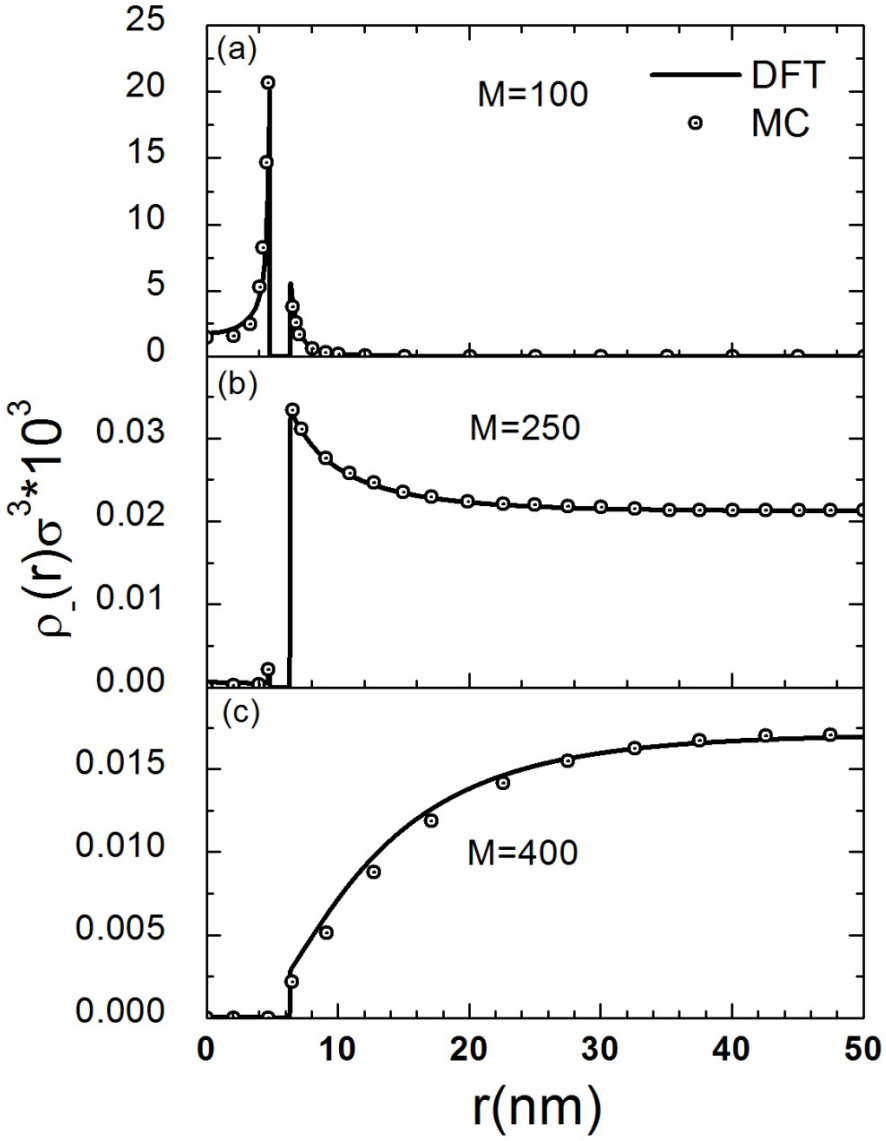

Figure 4-4 The same as Fig. 4-2 but for the density profiles of cations.

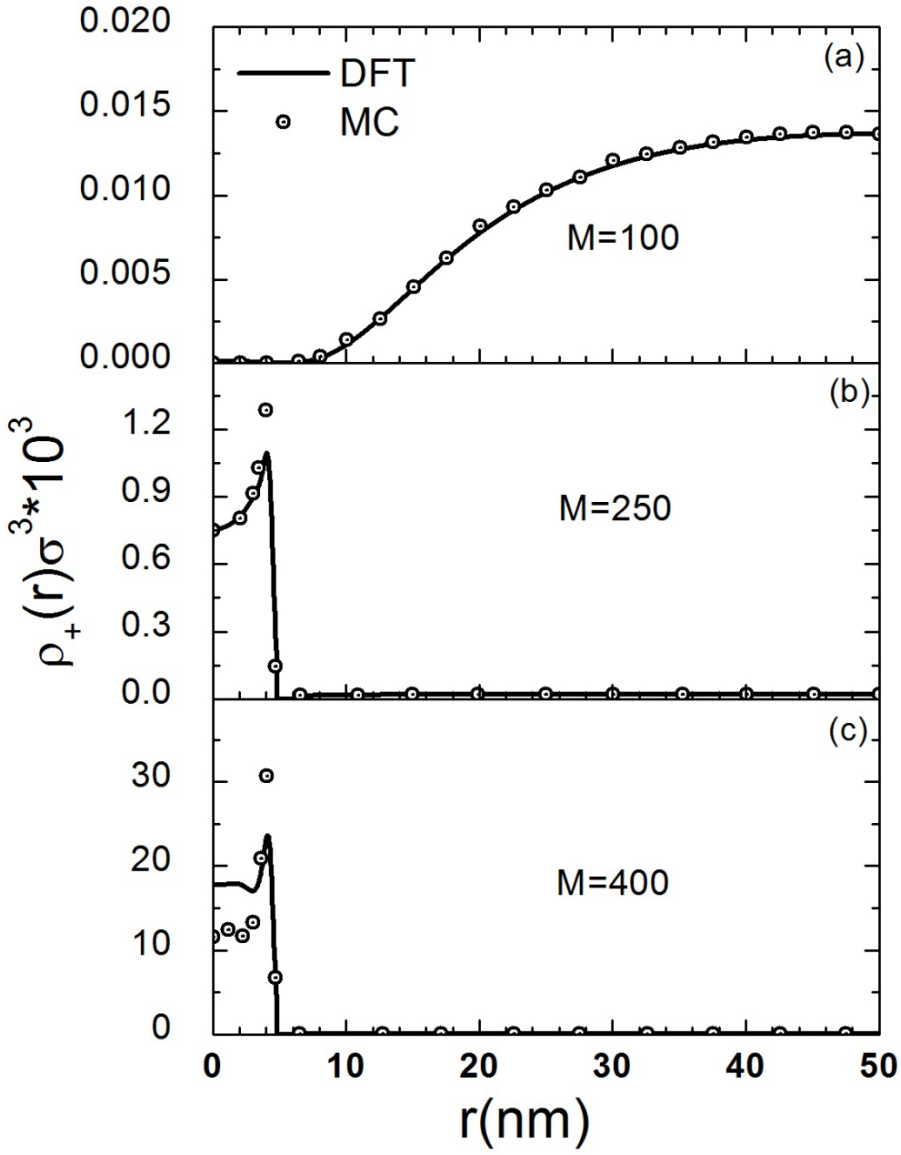

Figure 4-5 The same as Fig. 4-2 but for a semi-flexible polyelectrolyte with bending stiffness parameter $\beta\phi_0 = 10$.

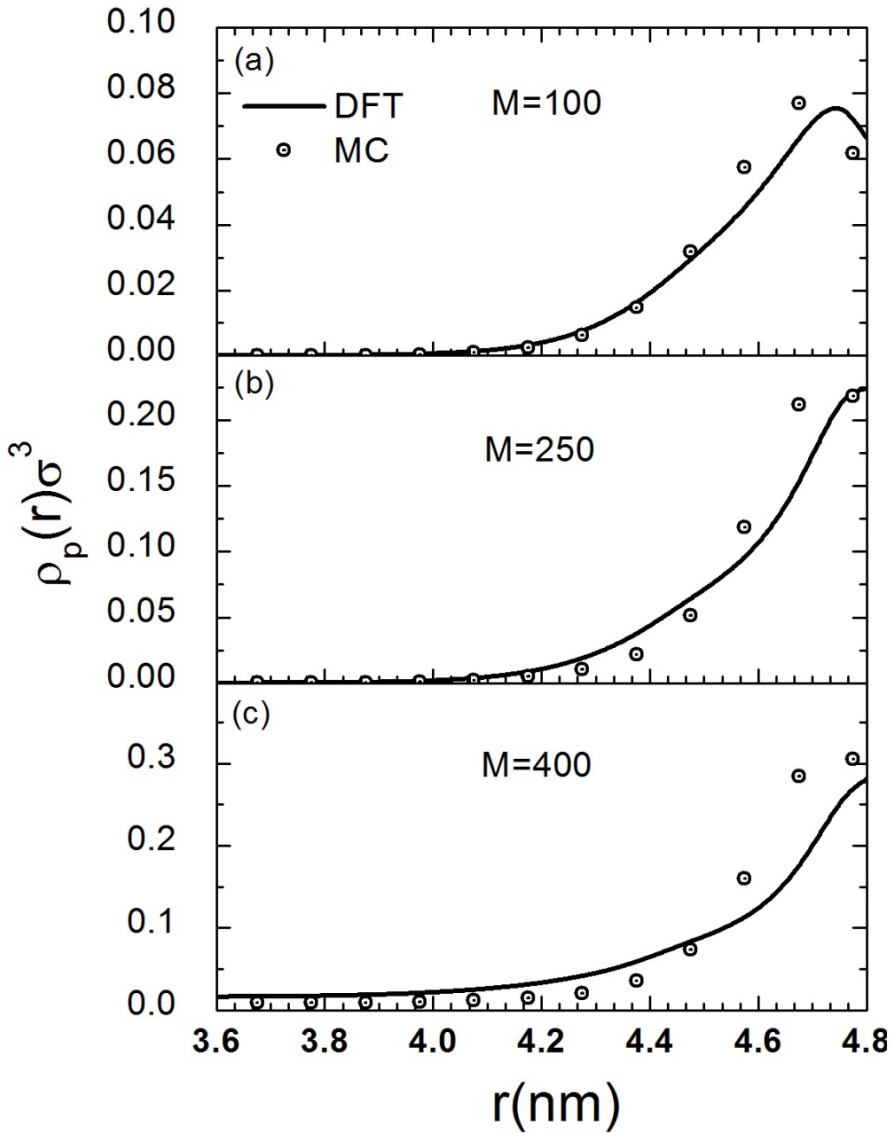

Figure 4-6 The same as Fig. 4-5 but for the density profiles anions.

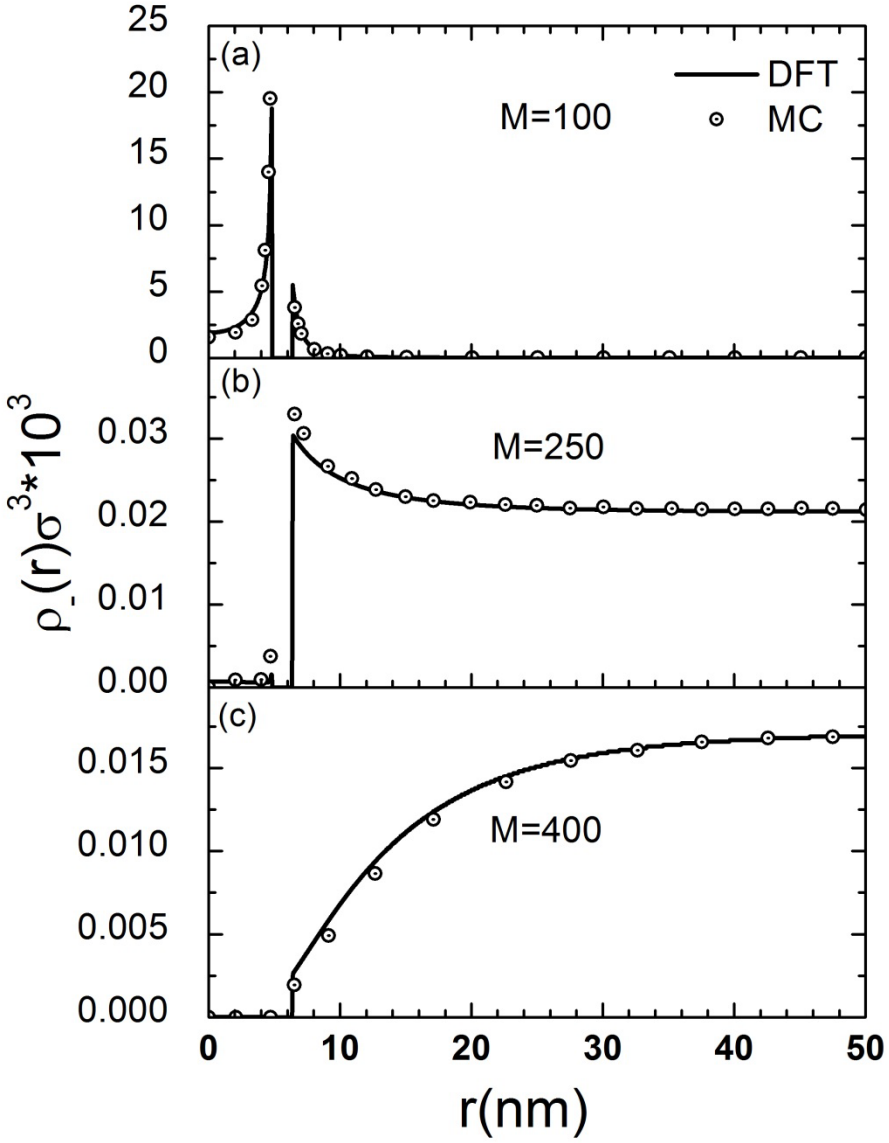

Figure 4-7 The same as Fig. 4-5 but for the density profiles of cations.

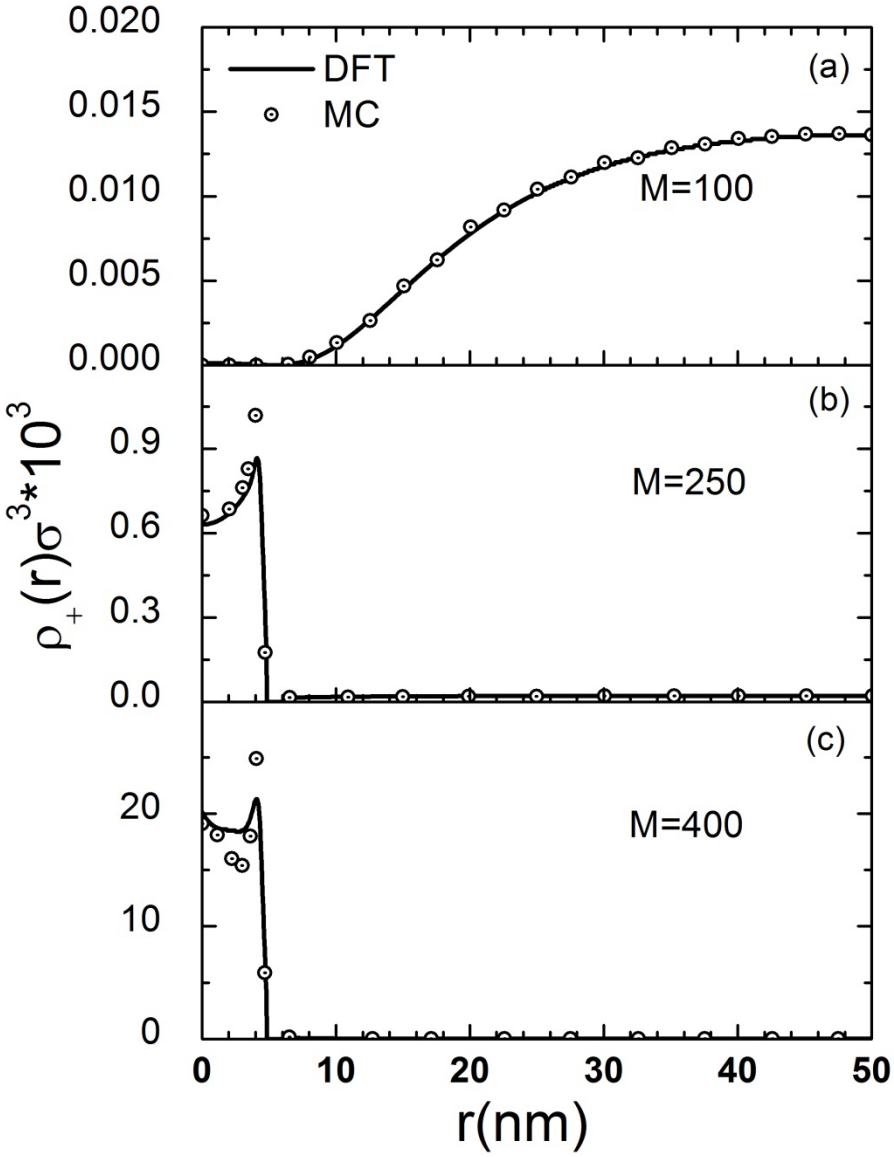

Figure 4-8 (a) Density distribution of polymer segments $\rho_p(r)$ versus radial distance r for a flexible polyelectrolyte in a spherical shell. Here the polyelectrolyte chain length is $M = 252$ and each segment carries unit negative charge. The total charge of the spherical shell is $Q_c = +252$. In MC simulation, the cell radius is $R_{cell} = 10\,\text{nm}$, the numbers of cations and anions simulated are $N_+ = 252$ and $N_- = 252$, respectively, and the valences of cations and anions are $Z_+ = +1$ and $Z_- = -1$, respectively. The solid lines represent results from the DFT calculation and symbols are from MC simulation [132]. (b) The same as (a) except for $Z_+ = +2$ and that the number of cations used in the simulation is $N_+ = 126$. (c) The same as (a) except for $Z_+ = +3$ and that the number of cations simulated is $N_+ = 84$.

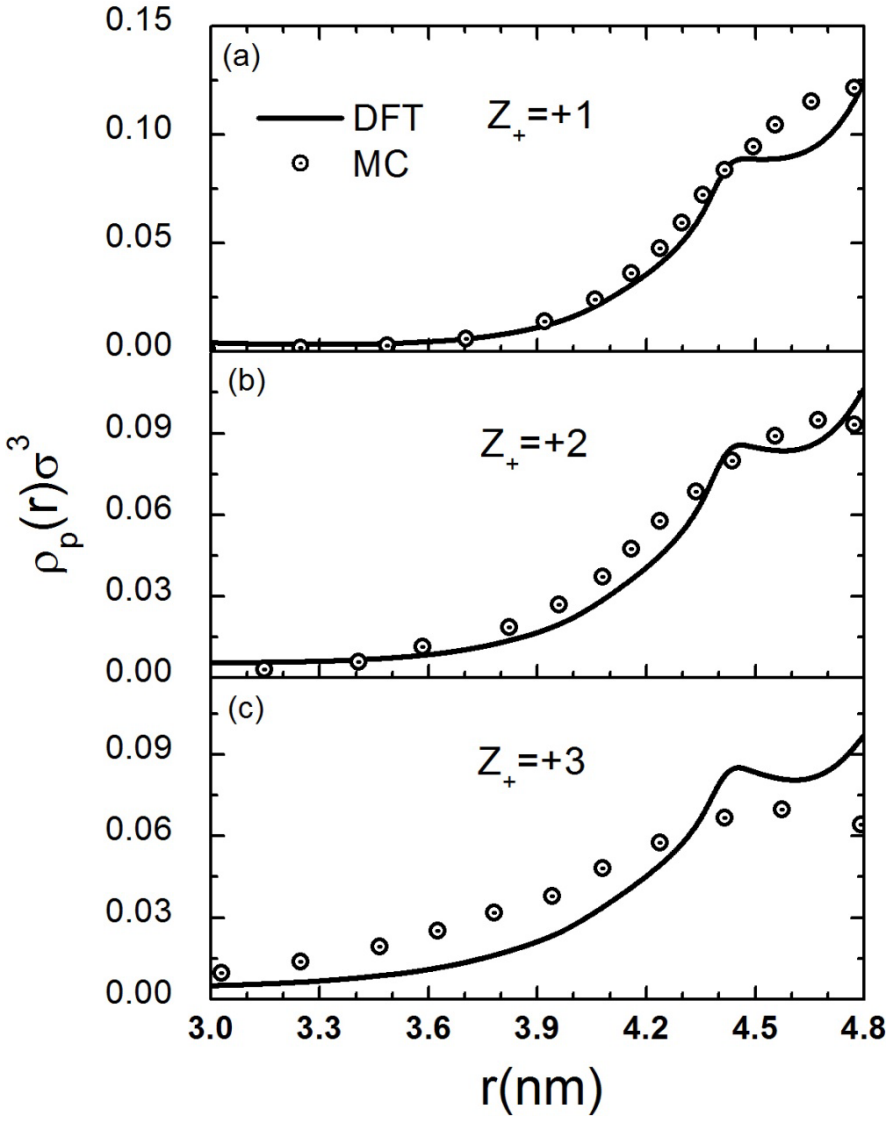

Figure 4-9 The same as Fig. 4-8 but for the density distributions of monomeric anions.

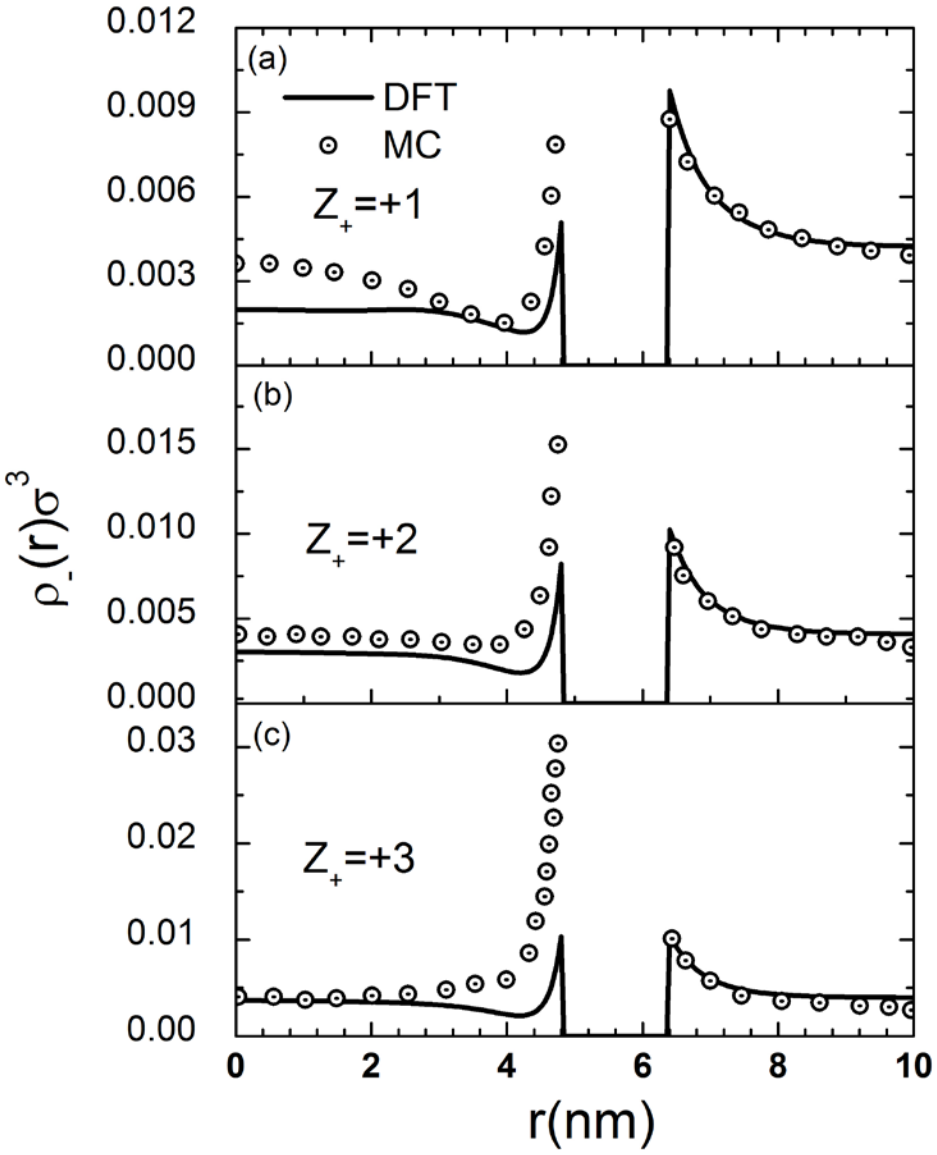

Figure 4-10 The same as Fig. 4-8 but for the density distributions of cations.

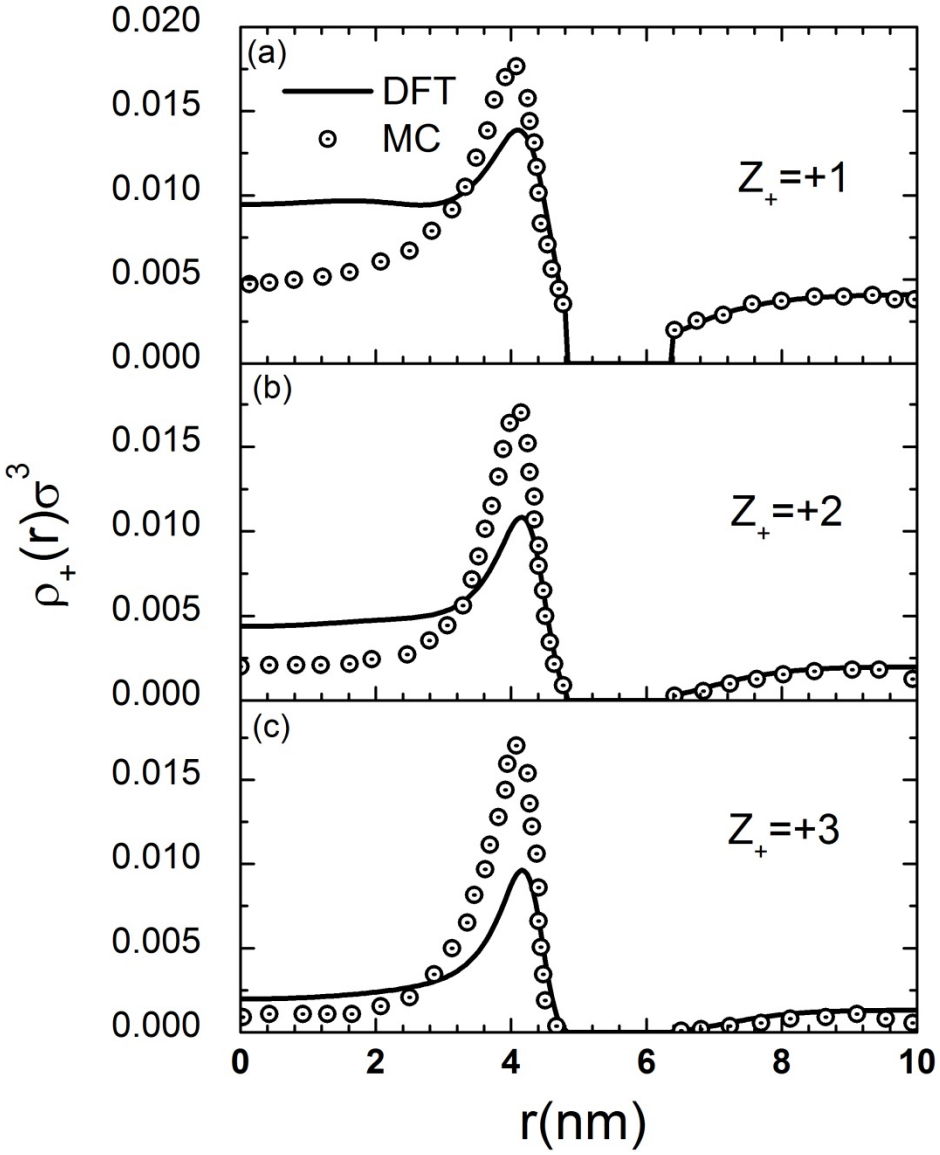

Figure 4-11 (a) The density distribution of polyelectrolyte segments $\rho_p(r)$ as a function of radial distance r for a flexible polyelectrolyte with chain length $M = 100$ in a spherical shell with a total charge $Q_c = +250$. The cell radius is $R_{cell} = 56.5\,\text{nm}$, the valences of cations and anions are $Z_+ = +1$ and $Z_- = -1$, respectively, and the bulk salt concentration is $C_{salt} = 110\,\text{mM}$. The black line is the density profile predicted by the DFT with explicit consideration of the outside environment, i.e., without the assumption of the charge neutrality within the shell; and the red line depicts that without considering the outside environment but assuming the capsid is overall neutral. (b) The same as (a) except for $M = 250$. (c) The same as (a) except for $M = 400$.

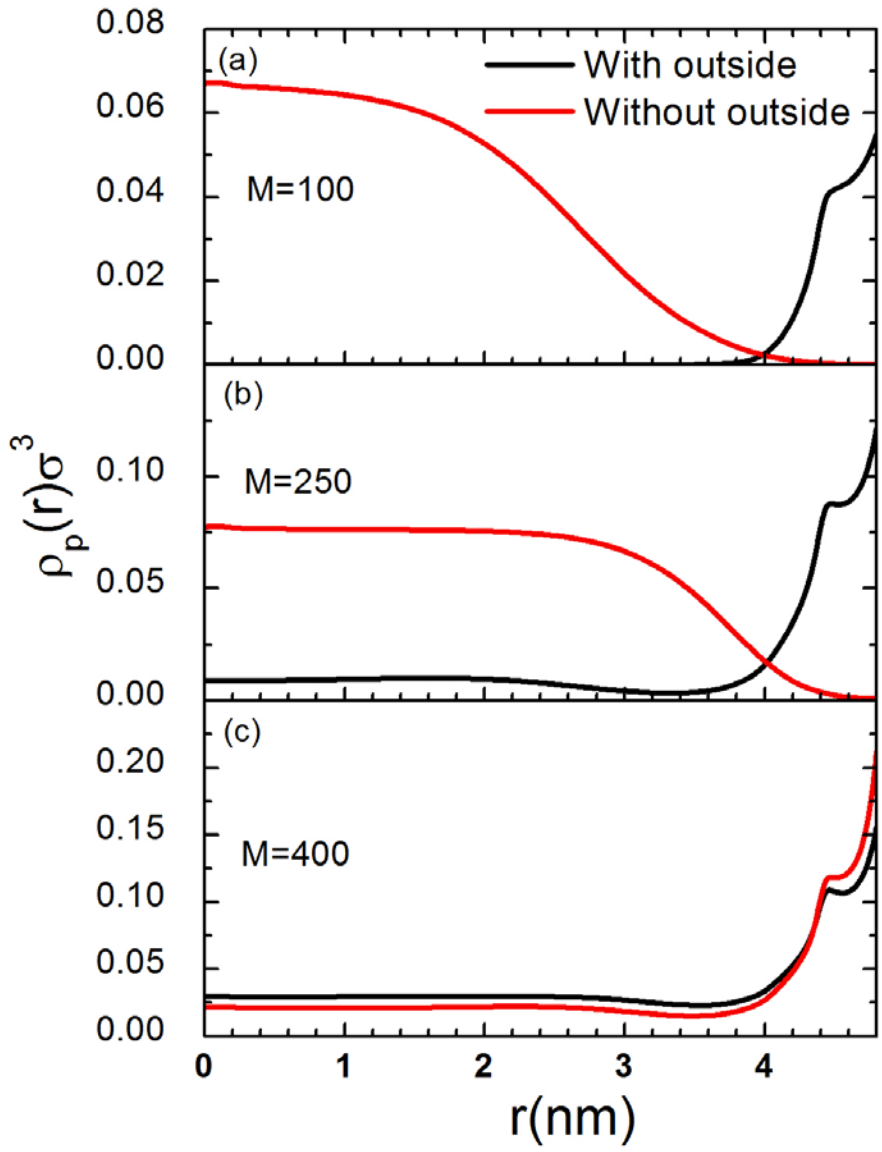

Figure 4-12 The same as Fig. 4-11 but for the density distributions of monomeric anions.

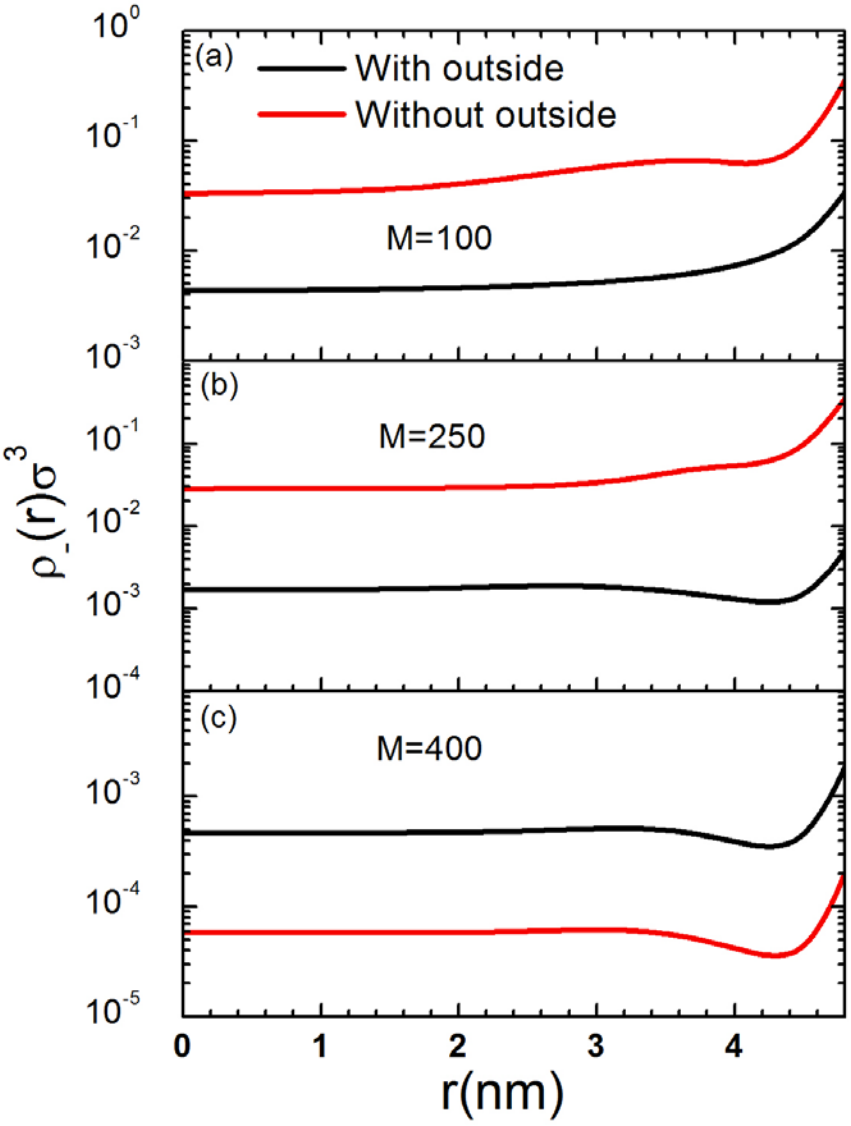

Figure 4-13 The same as Fig. 4-11 but for the density distributions of monomeric cations.

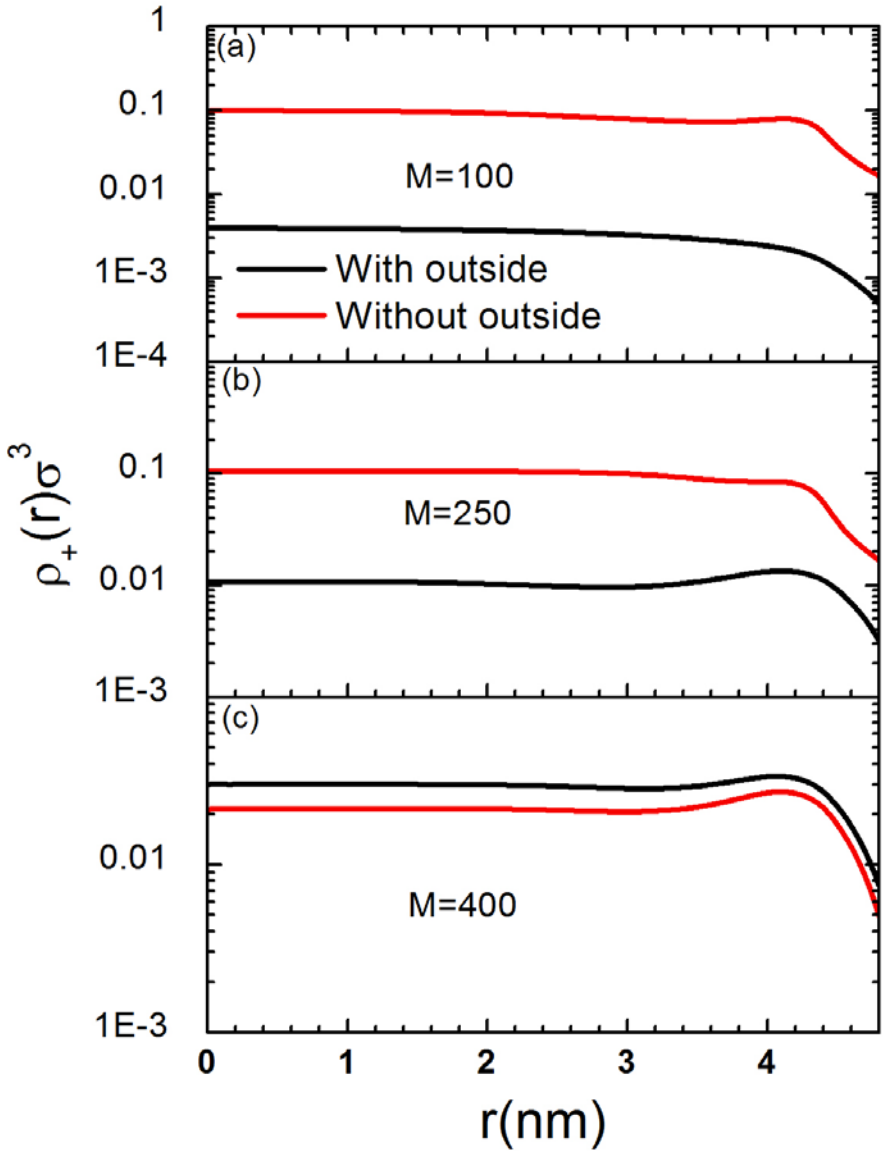

Figure 4-14 The DFT prediction on the net charge of capsid complex versus polyelectrolyte chain length at various salt concentrations. The capsid charge is $Q_c = +252$, the cell radius is $R_{cell} = 56.5\,\text{nm}$, the valences of cation and anion are $Z_+ = +1$ and $Z_- = -1$. The red line depicts bulk salt concentration $C_{salt} = 11\,\text{mM}$, the green line presents bulk salt concentration $C_{salt} = 110\,\text{mM}$, and the blue line is for bulk salt concentration $C_{salt} = 550\,\text{mM}$, respectively.

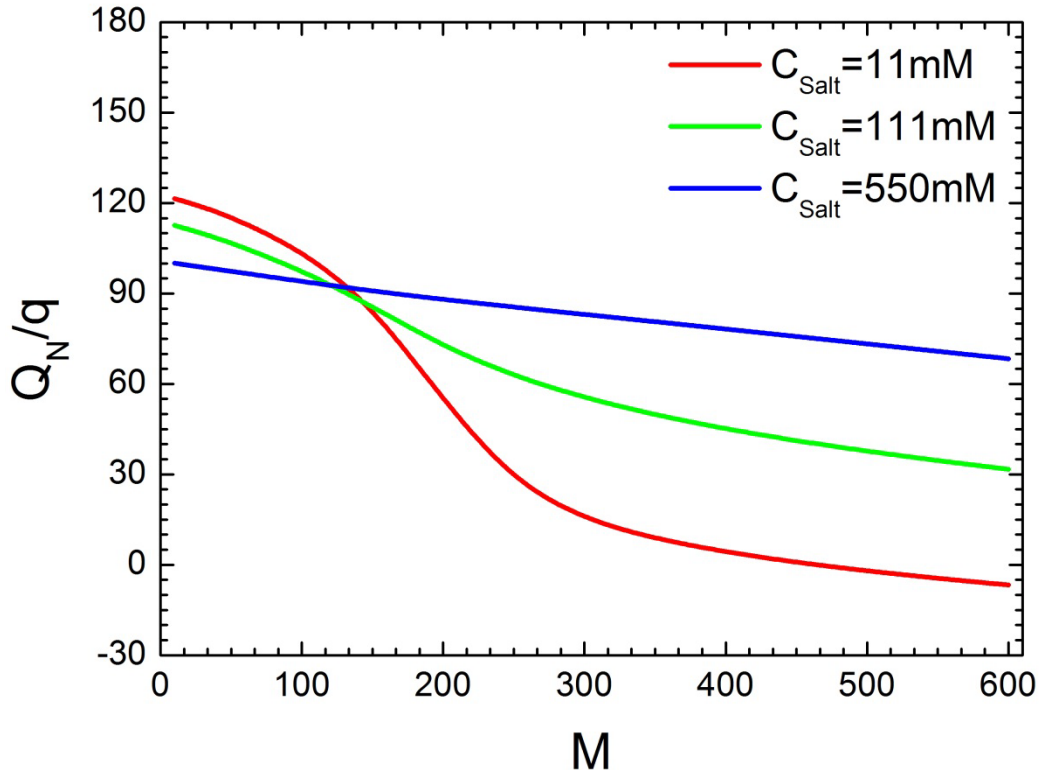

Figure 4-15 The DFT prediction on the net charge of capsid complex versus polyelectrolyte chain length at various cation valences. The capsid charge is $Q_c = +252$, the cell radius is $R_{cell} = 56.5\,\text{nm}$, the valence of anion is $Z_- = -1$, and bulk salt concentration $C_{salt} = 110\,\text{mM}$. The red solid line depicts cation valence $Z_+ = +1$, the green solid line presents cation valence $Z_+ = +2$, and blue solid line is cation valence $Z_+ = +3$, respectively.

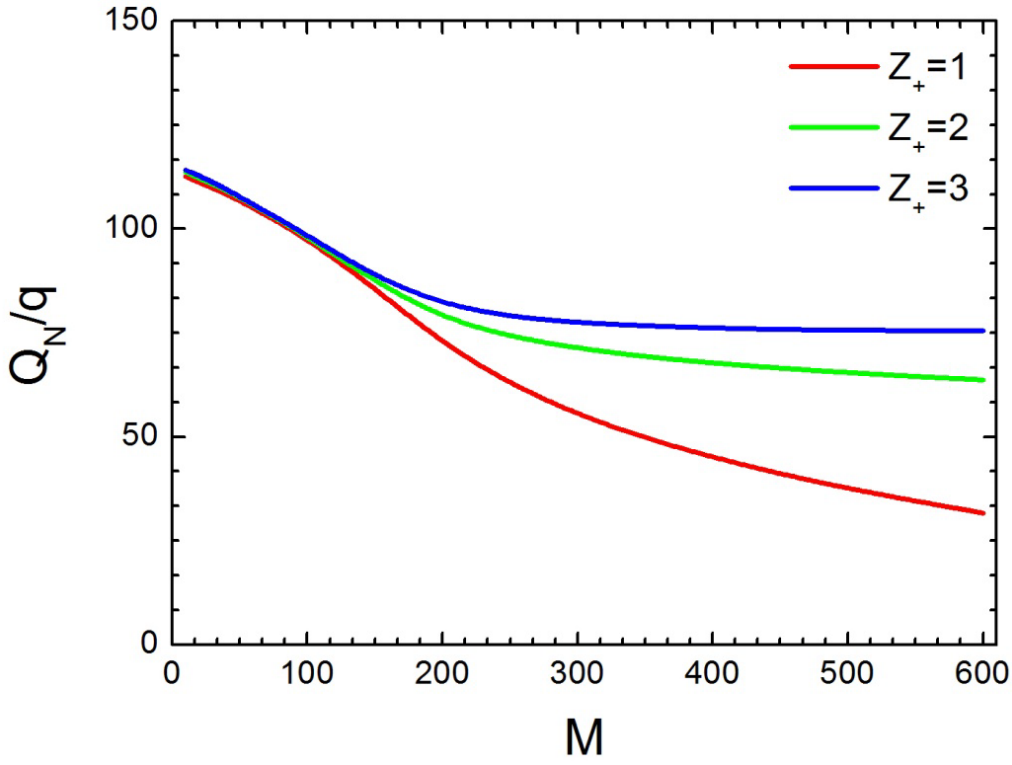

Figure 4-16 (a) The density distribution of polyelectrolyte segments $\rho_p(r)$ as a function of radial distance r for a flexible polyelectrolyte with chain length $M=100$ in a viral capsid with a total charge of $Q_c=+250$. The cell radius is $R_{cell}=56.5\,\text{nm}$, the valences of cations and anions are $Z_+=+1$ and $Z_-=-1$, respectively, and the bulk salt concentration $C_{salt}=110\,\text{mM}$. The black line is the density profile with capsid dielectric constant $\varepsilon_c=78.4$ and the red line depicts that with the capsid dielectric constant $\varepsilon_c=4$. (b) The same as (a) except for $M=250$. (c) The same as except for $M=600$.

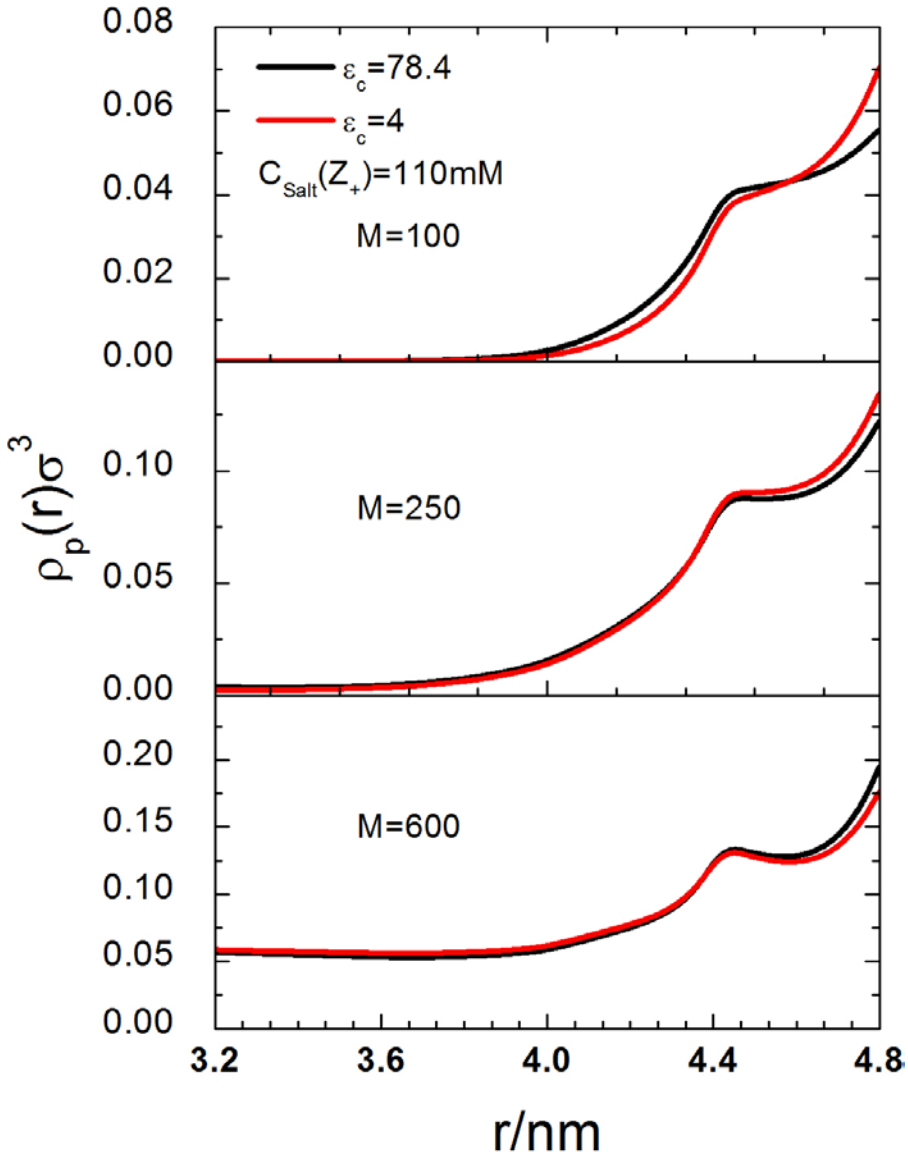

Figure 4-17 The same as Fig. 4-16 but for the density distributions of monomeric anions.

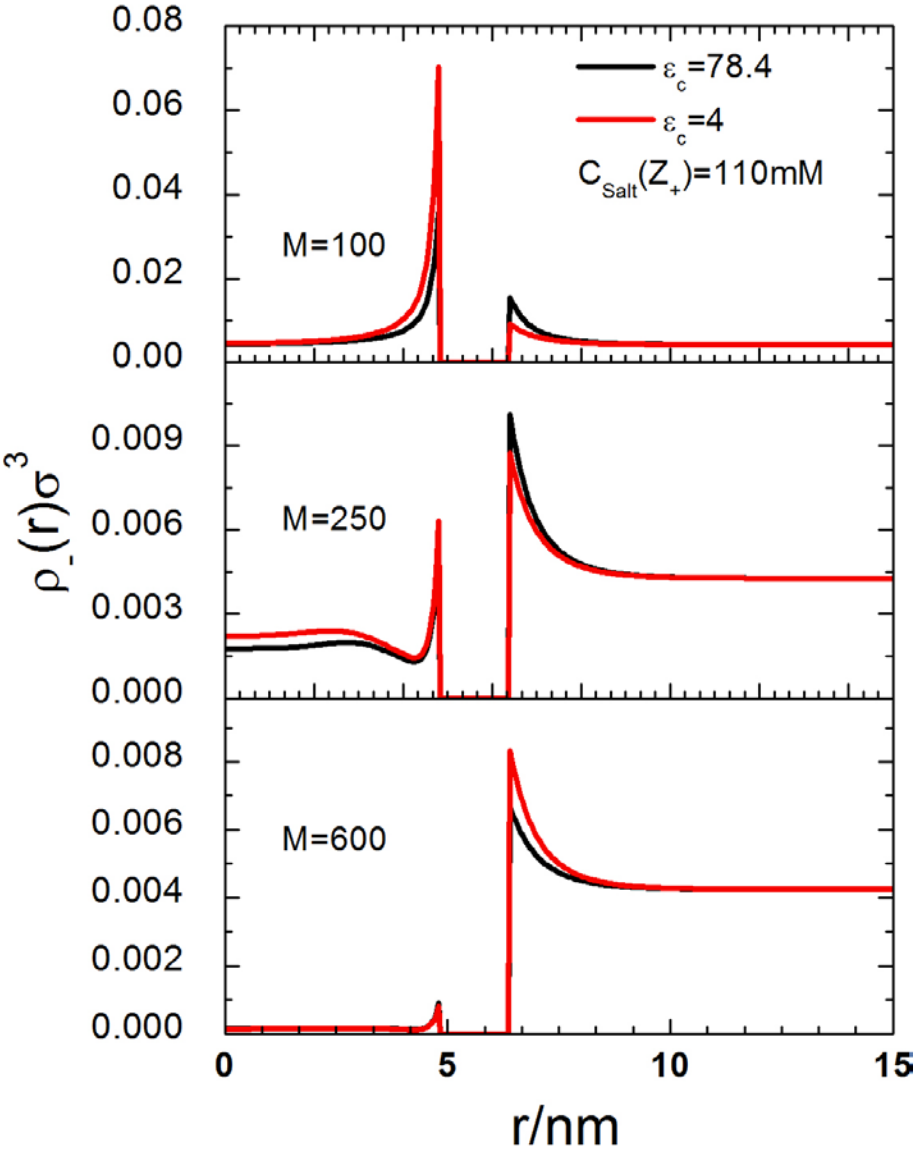

Figure 4-18 The same as Fig. 4-16 but for the density distributions of monomeric cations.

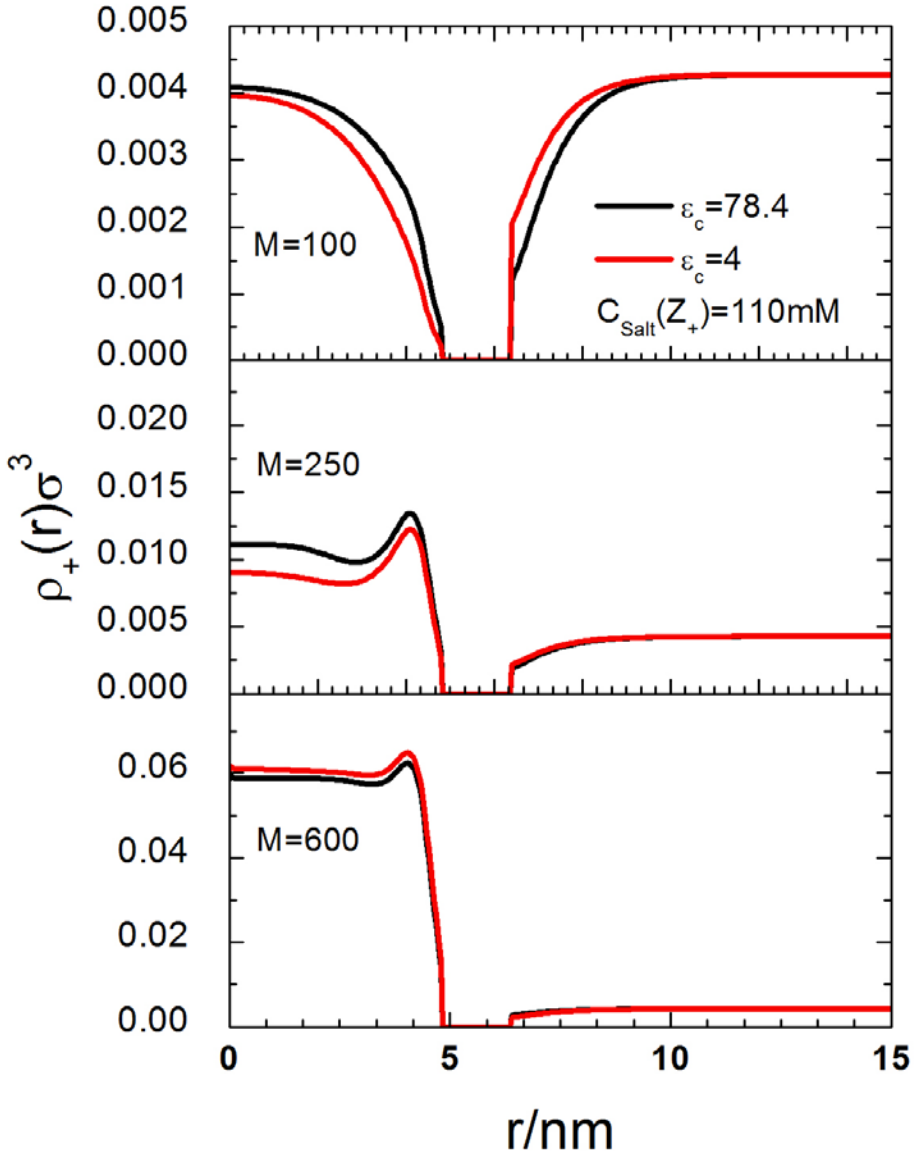

Chapter 5 Hybrid MC-DFT Method for Studying Multi-dimensional Entropic Forces

Abstract

Entropic force has been the focus of many recent theoretical studies because of its fundamental importance in solution thermodynamics and its close relevance to a broad range of practical applications. Whereas previous investigations are mostly concerned with the potential energy as a one-dimensional function of the separation, here we propose a hybrid method for studying multi-dimensional systems by combining Monte Carlo simulation for the microscopic configurations and the density functional theory for the free energy. We demonstrate that the hybrid method predicts the potential of mean force between a test particle and various concave objects in a hard-sphere solvent in excellent agreement with the results from alternative but more expensive computational methods. In particular, the hybrid method captures the entropic force between asymmetric particles and its dependence on the particle size and shape that underlies "lock and key" interactions. Because a single molecular model is used for both the theory and the simulation, we expect that the hybrid method provides a new avenue to predicting entropic forces in complex molecular systems.

5. 1 Introduction

An entropic force arises in a solution or a colloidal dispersion when the local distribution of solvent (or co-solvent) molecules is disrupted due to the presence of the solute. Because it is affiliated with the solvent configuration rather than a specific microscopic energy, the microscopic origin of an entropic force appears obscure and sometimes it is misinterpreted. Even in its simplest form induced by the excluded-volume effects, current understanding is mostly limited to interaction between colloidal particles in the presence of polymer chains dissolved in a good solvent. The first attempt to quantify such interaction was made by Asakura and Oosawa (AO) [148] who treated colloidal particles as non-penetrable spheres and polymer chains as “ideal-gas” molecules that are depleted from the particle surface due to the polymer excluded volume. According to the AO theory, two colloidal particles experience an entropic attraction when the polymer depletion layers overlap. The attraction is introduced by an increase of the system entropy or accessible volume for the polymer. Despite its simplicity, the AO theory captures the polymer-mediated entropic force at low and intermediate polymer concentrations semi-quantitatively. However, its performance is unsatisfactory at high polymer concentration when the inter-chain interactions become non-negligible. Besides, the AO theory is inadequate if the size of the colloidal particles is smaller or comparable to the radius gyration of the polymer chains [149]. Towards an improvement of the AO theory, many theoretical investigations and molecular simulations had been reported over the past decades. Common computational methods include the hyper-netted-chain (HNC) equation [150], the polymer self-consistent-field theory [151], the classical density

functional theory (DFT) [68, 152], and various forms of computer simulations [153, 154]. These investigations are mostly focused on the entropic potential between two spherical particles, or a spherical particle and a hard wall, in the presence of hard-sphere-like solvent.

Whereas existing theoretical methods are adequate to quantify entropic force in colloidal systems with relatively simple geometry, their extension to multi-dimensional interactions such as those important for biological systems is computationally challenging. On the one hand, simulation of the entropic potential entails free-energy calculations that are computationally demanding. The power of analytical methods, on the other hand, is often compromised by the numerical solution of multi-dimensional density distribution functions. Unlike a typical colloidal potential, interaction between biomacromolecules often depends on the center-to-center distance as well as the molecular geometry and orientation. While in general the entropic force is closely affiliated with the self-organization of water molecules around the solute, the geometry or shape of biomacromolecules plays a key role in receptor-ligand or “lock and key” interactions and its contribution to the overall potential is often manifested through the exclude-volume effects of the surrounding water molecules [150, 155, 156]. Recently, colloidal “lock and key” systems have been developed to mimic the geometry affinity of bio-interactions [11, 12, 157-160]. Such model systems have generated extensive interests not only because they resemble interactions in biological processes, including protein folding [161] and recognition between drug compounds [162], but because the affinity force empowers a precise control of the microscopic structure during colloidal self-assembly [11]. These

model systems have also inspired a number of theoretical and simulation works. For example, Kinoshita [22] used a three-dimensional HNC equation to examine interactions between a substrate with a hemi-sphere cavity and a testing spherical particle in a hard-sphere solvent. Konig and coworkers [155] used the White Bear [88] version of fundamental measure theory (FMT) [83] and a curvature expansion technique [163] to study the depletion potential between a smooth substrate and a biaxial elliptical testing particle. On the simulation side, Odriozola and coworkers [164] investigated the effective interaction between a sphere with an open cavity using Monte Carlo (MC) simulation.

In this work, we propose a hybrid method for computation of entropy forces by using MC simulation to predict the density distributions of solvent molecules and the fundamental measure theory for free-energy calculations. Whereas the DFT is formulated in terms of the density profiles, direct minimization of the free energy functional with respect to a three-dimensional density is unrealistic for most anisotropic systems. This is because the DFT calculation often entails lengthy iterations and requires an extremely small grid (~0.002 molecular diameter). On the other hand, simulation of the solvation free energy is in general very time-consuming but simulation of the solvent density at a fixed solute configuration is not a computationally demanding task. For calculating the solvent density, simulation on the time scale comparable to that corresponding to fast the relaxation dynamics is often sufficient. Besides, the simulation is not limited by the dimensionality and much larger grids (~0.1 molecular diameter) can be used to sample the solvent density profile. While extension of molecular simulation for simple colloidal systems to those with solutes of more complicated shape requires essentially no increase

of the computational cost, DFT provides an efficient link between the microscopic structure and thermodynamic potentials. A combination of simulation and DFT takes advantages of the good features of both methods.

With an analytical expression from DFT for the free-energy as a functional of the solute and solvent density profiles, we can calculate the entropic force by using the potential distribution theorem (PDT) [165]. This method has been previously used to calculate the colloidal force between two big particle and particle-wall interactions [68, 152] in the presence of a hard-sphere solvent or polymers [68]. Alternatively, entropic force can be calculated from the free energy of the solvent with the colloidal particles treated as an external potential. In comparison with PDT, computation of the free energy at explicit colloidal configurations is more time consuming but the latter method is useful when an accurate expression for the free energy functional of the solute-solvent mixture is not attainable.

The remainder of this article is organized as follows. In section 2, introduce the molecular theory and simulation methods. In section 3, we define the thermodynamic system and molecular models studied in this work and validate the proposed methods by comparing with previous computer simulations and theoretical investigations on the colloidal force for the targeted systems. In section 4, we summarize the key conclusions and discuss further implications of newly implemented methods.

5. 2 Theoretical Approaches

The main idea behind our new method for calculating the entropic force in multidimensional systems is as the following: First, we use MC simulation to generate 3-

dimensional density profiles required in analytical calculations. Then, we use the DFT calculate the free energy and subsequently the entropic forces. The hybrid method can be implemented either by explicit consideration of the colloidal configuration or by using the potential distribution theorem (PDT). The first procedure is referred to as the MC-DFT and the second as MC-PDT. Because PDT requires only the density profile of the solvent molecules around a single solute, the numerical advantage of MC-PDT is self-evident. However, MC-PDT hinges on a free energy functional that is accurate for the solute-solvent mixture, and the numerical efficiency is often compromised by approximations introduced in the DFT. In this work, we will validate both procedures by considering entropic forces (1) between two spherical particles, (2) between a spherical particle and a planar hard wall, (3) between a spherical particle and a substrate with a hemispherical cavity mimicking the "lock and key" system, and (4) between a hard rod and a hard wall. In all cases, the molecular excluded volume effect is represented by using a hard-sphere solvent, and the theoretical predictions will be validated with results from direct simulations of the colloidal forces.

5. 2. 1 MC-DFT

In MC-DFT, the density profile of solvent molecules is simulated at each solute configuration. For interaction between two colloidal particles in a hard-sphere solvent, the potential of mean force corresponds to the reversible work to separate them apart or the difference in the free energy when the system is at a given colloidal configuration and that when the particles are infinitely apart. If both particles are spherical, the potential of

mean force depends only on the center-to center distance r. In that case, the potential of mean force $W(r)$ can be calculated from

$$W(r) = \Omega(r) - \Omega(\infty), \tag{5.1}$$

where $\Omega(r)$ stands for the grand potential of the system when the particles are separated and $\Omega(\infty)$ for the grand potential of the same system but when the particles are "far" apart, i.e., $r \to \infty$: Eq. (5.1) can be directly extended to many-body interactions and multi-dimensional systems by augmenting r with the orientation angles and/or solute configurations.

In a one-component hard-sphere system, the grand potential can be related to the intrinsic Helmholtz energy functional $F[\rho(\mathbf{r})]$ via the Legendre transform:

$$\Omega[\rho(\mathbf{r})] = F[\rho(\mathbf{r})] + \int [V(\mathbf{r}) - \mu]\rho(\mathbf{r})\, d\mathbf{r}, \tag{5.2}$$

In Eq. (5.2), $d\mathbf{r}$ denotes a differential volume, $\rho(\mathbf{r})$ is the density distribution of hard spheres, μ is the chemical potential, and $V(\mathbf{r})$ stands for the external potential. Here $V(\mathbf{r})$ refers to the potential due to the colloidal particles. The intrinsic Helmholtz free energy functional can be further divided into two parts: an ideal-gas term and an excess free energy. The former is exactly known:

$$F^{id}[\rho(\mathbf{r})] = k_B T \int \rho(\mathbf{r}) \left\{ \ln[\rho(\mathbf{r})\lambda^3] - 1 \right\} d\mathbf{r}, \tag{5.3}$$

where k_B is Boltzmann's constant, T is the thermal temperature, and λ is the thermal wavelength. For hard-sphere systems, the excess Helmholtz free energy functional can be accurately represented by the modified fundamental measure theory [85, 88]

$$F^{ex} = k_B T \int \Phi\left[n_\alpha(\mathbf{r})\right] d\mathbf{r}, \tag{5.4}$$

where $\Phi(\mathbf{r})$ is the reduced excess Helmholtz free energy density

$$\begin{aligned}\Phi\left[n_\alpha(\mathbf{r})\right] = &-n_0 \ln(1-n_3) + \frac{n_1 n_2 - \mathbf{n_{V1}}\mathbf{n_{V2}}}{1-n_3} \\ &+ \frac{1}{36\pi}\left[n_3 \ln(1-n_3) + \frac{n_3^2}{(1-n_3)^2}\right] \times \frac{n_2^3 - 3n_2 \mathbf{n_{V2}}\mathbf{n_{V2}}}{n_3^3}\end{aligned}. \tag{5.5}$$

In Eqs. (5.4) and (5.5), $n_\alpha(\mathbf{r})$, $\alpha = 0,1,2,3,V1$ and $V2$ are weighted densities [83]. The expression for $n_\alpha(\mathbf{r})$ are given in previous publications [85].

In contrast to typical DFT calculations, in this work the three dimensional (3D) density profiles are not calculated from minimization of the grand potential but from grand-canonical Monte Carlo simulations. The two procedures are equivalent if the free-energy functional is exact. While minimization of the grand potential is numerically efficient if the density profile varies only in a single dimension, its extension to higher dimensional becomes numerically cumbersome. To implement the hybrid method, we first simulate hard-sphere systems in the presence of two colloidal particles within the grand canonical (μVT) ensemble. The number of hard spheres simulated varies with the colloidal separation. The colloidal particles are fixed along the X-axis of the simulation box and the periodic boundary conditions are used in all directions. In each MC cycle, a trial random displacement is applied to all solvent spheres (but not colloidal particles)

and a solvent particle is randomly removed from or inserted into the simulation box at approximately equal probability. The MC moves are implemented by using the Metropolis algorithm [166]. The simulation consists of 1 million MC cycles for equilibrium and 5 million MC cycles for sampling the 3-dimensional density profiles.

5. 2. 2 MC-PDT

In the MC-PDT method, the potential of mean force is obtained from the one-body direct correlation function. For example, the solvent-mediated potential between two spherical particles is related to the solvent density profile around a single particle and the one-body direct correlation of the second particle in the presence of the solvent [68]

$$\beta W\left(r\right)=c^{(1)}\left(\infty\right)-c^{(1)}\left(r\right), \tag{5.6}$$

where $\beta=1/\left(k_{B}T\right)$. The one-body direct correlation function of the second particle $c^{(1)}\left(r\right)$ is obtained from the excess intrinsic Helmholtz free energy F^{ex} for the particle and solvent mixture in the limit of zero particle concentration $\rho_{p}\left(r\right)\to 0$

$$c^{(1)}\left(r\right)=-\left.\frac{\delta\beta F^{ex}}{\delta\rho_{p}\left(r\right)}\right|_{\rho_{p}(r)\to 0}. \tag{5.7}$$

When two particles are far apart, $c^{(1)}\left(\infty\right)$ is related to the reduced excess chemical potential of the particle in the bulk solvent, i.e.,

$$c^{(1)}\left(\infty\right)=-\beta\mu_{p}^{ex}. \tag{5.8}$$

With the density profile of the solvent molecules around a single particle obtained from MC simulation, PDT allows us to calculate the potential of mean force between two particles at all colloidal separations. Like MC-DFT, MC-PDT can also be extended to

multi-dimensional systems. The key difference between the MC-DFT and the MC-PDT is whether simulation includes a single particle or two particles at different separations. For some relatively simple systems, we may derive the density profile of the solvent by direct minimization of the grand potential and use the PDT to calculate the PMF. The results calculated from this method are labeled as DFT-PDT.

5. 3 Results and Discussions

For calibration of the proposed computational procedures, we consider four model systems where the entropic potentials have been studied before and the physics is relatively well understood. The potential between two identical spheres or between a hard-sphere and a planar surface depends only on the surface-to-surface separation. On the other hand, the interaction in a colloidal key and lock system or between a hard rod and a hard wall depends on both the separation and orientation. We will compare the numerical performances of MC-DFT and MC-PDT with exact full simulation results or with alternative analytical methods. Table 5-1 lists different methods discussed in this work.

5. 3. 1 Two Identical Spheres

Entropic interaction between two identical spherical particles immersed in a sea of small hard spheres is affiliated with the particle-hard sphere interaction

$$\varphi_{SB}(r)=\begin{cases}\infty, r<(\sigma+D_B)/2\\ 0, r\geq(\sigma+D_B)/2\end{cases}, \tag{5.9}$$

and the pair interaction among small hard spheres

$$\varphi_{SS}(r)=\begin{cases}\infty, r<\sigma\\ 0, r\geq\sigma\end{cases}. \tag{5.10}$$

In Eqs. (5.9) and (5.10), σ stands for the diameter of the solvent hard spheres, D_B is the diameter of colloidal particle, and r is the center-to-center distance. For comparison with results from direct simulation [154], we set $D_B=5\sigma$. In our MC-DFT calculations, two colloidal particles were placed at $(x,y,z)=\left(-\frac{D_B+H}{2},0,0\right)$ and $(x,y,z)=\left(\frac{D_B+H}{2},0,0\right)$, respectively, where H represents the contact distance between two colloidal spheres. The simulation box is a rectangular prism with side $L_x=22\sigma$ and $L_y=L_z=14\sigma$. In MC-PDT calculations, a single particle is placed at the center of a simulation with dimensions $L_x=20\sigma$ and $L_y=L_z=16\sigma$.

Figure 5-1 presents the depletion potentials calculated from direct MC simulations and from three different semi-analytical methods. Figure 5-2 shows the contour plots of the density profiles of the hard sphere solvent at different colloidal separations. Here $\eta=\pi\rho_0\sigma^3/6$ stands for the packing fraction of the hard-sphere solvent in the bulk and ρ_0 is the bulk density. In the DFT-PDT calculations [68], the density profile of the solvent molecules near a single particle is calculated from minimization of the grand potential. At low density ($\eta=0.116$), all methods give virtually the same results. Noticeable differences are observed, however, at high density ($\eta=0.229$). The DFT-PDT method over-predicts the repulsive barrier regardless whether the density profile is

from the DFT or from simulation. On the other hand, MC-DFT provides good agreement with the simulation results [154].

As mentioned before, the attraction between colloidal particles arises from an overlap of the solvent depletion layers (see Fig 5-2). The depletion potential is most significant when the colloidal particles are at contact. Because the two particles are aligned in X-axis ($y=0$, $z=0$), the solvent density profiles are in cylindrically symmetric and can be represented in terms of $\rho(x,r)$ where $r=\left(y^2+z^2\right)^{1/2}$. Whereas all DFT–based methods are able to capture the simulation results quantitatively, the numerical performance of the AO theory is unsatisfactory. While it captures the surface depletion, the AO theory fails to describe accumulation of the solvent molecules at the interstice of colloidal spheres (as seen in Figure 5-2a) that is responsible for the repulsive barrier.

5. 3. 2 A Sphere near A Hard Wall

We now consider the PMF between a spherical particle and a hard wall in a hard-sphere solvent. The system can be understood as the limit of the interactions between two asymmetric hard spheres. Similar to the case of two identical spheres, we again use MC-DFT and MC-PDT to calculate the entropic forces. In MC simulations, the wall is placed at $x=0$ of the simulation box, and a spherical particle of diameter $D_B=5\sigma$ is placed at $\left(H+\frac{D_B}{2},0,0\right)$ where H stands for the surface-to-surface distance between the hard wall and the colloidal particle. The dimensions of the simulation box are set as $L_x=24\sigma$

and $L_y = L_z = 14\sigma$ for MC-DFT calculations and $L_x = 16\sigma$ and $L_y = L_z = 14\sigma$ in MC-PDT calculations. To apply the periodic boundary conditions to all three directions, we place the flat wall in the center of the simulation box and the boundaries are selected such that the solvent density approaches to that corresponding to the bulk.

Figure 5-3 shows the depletion potential again at two representative solvent packing fractions. In this case, both MC-DFT and MC-PDT agree well with the simulation results. At both solvent densities, the entropic potential shows a global minimum at the contact point and a repulsive barrier at intermediate separation, similar to the interaction between identical spheres. In comparison to Fig. 5-1, the performance of MC-PDT is slightly improved mainly because numerical integrations in 3D Cartesian grid is more easily formulated near the flat wall comparing to that between spherical surfaces.

5. 3. 3 Colloidal Lock and Key Interactions

We now investigate a model "lock and key" interaction where the lock is represented by a planar substrate with a hemispherical cavity and the key is represented by a spherical testing particle. The system is immersed in a sea of hard spheres. In contrast to the simple systems discussed earlier, the PMF for the lock-and-key interaction depends on the three-dimensional distribution of the solvent molecules.

To facilitate numerical comparison between simulation and DFT calculations, we consider a symmetric configuration of the lock and key system as shown in Fig. 5-4. In our MC simulations, the center of the hemispherical cavity is placed at $(x_0, 0, 0)$ of the

simulation box with $x_0 = 3\sigma$ and the center of the key is located at $(x, 0, 0)$ with varying x. The radius of the cavity is fixed at $R_{lock} = 2.5\sigma$. We examine the depletion potential $W(x - x_0)$ for various key particles with radius R_{key} along the symmetric axis. At all situations, the dimensions of the simulation box are $L_y = L_z = 14\sigma$ and $L_x = 30\sigma$. The MC-DFT and MC-PDT calculations utilize the three-dimensional density profiles of the solvent molecules, with and without the key particles, respectively. Besides, we also use a direct sampling method originally proposed by Wu et al. [167] to obtain the entropic force $f(x - x_0)$ at different lock and key separations. The potential of mean force can be derived from the integration of the mean force [168].

Figure 5-5 presents the entropic potentials corresponding to a cavity lock and three different spherical keys. Again both MC-DFT and MC-PDT methods are in quantitative agreement with the direct sampling method. They all faithfully predict that the lock and key interaction is highly specific at short separations. When the key is either too small or too large, the entropic potential resembles that between two identical spheres or that between a spherical particle and a hard wall. In those cases, the entropic potential oscillates with separation and exhibits a maximum attraction at the contact. When the key geometry matches that of the substrate, the contact potential is drastically magnified and less intuitively, the repulsion barrier disappears. For comparison, also shown in Figure 5-5 are predictions from the 3-dimensional HNC [22] and from the DFT and curvature expansion method [155]. While the HNC overestimates the maximum attraction between the lock and a perfectly matched key, the opposite is true for the results from the

curvature expansion method. Furthermore, application of the curvature expansion is ambiguous for concave objects, especially for systems with a discontinuous curvature [155, 169].

Similar to interactions between two identical spheres, the attraction between the lock and key is also related to the local distributions of small particles. Figure 5-6 shows the solvent density distributions obtained from MC simulation. When the size of the testing particle (key) matches perfectly that of the cavity at the substrate (lock), the system reaches the maximum entropy when the key fits into the lock. In this case, the solvent molecules have the maximum accessible volume. Figure 5-6d indicates that the solvent accessible volume and the lock-key potential decrease monotonically as separation between the key and the lock increases. When the separation between the lock and key is sufficiently large, we expect that the distributions of the solvent molecules around on the lock and key become independent and the entropic potential diminishes.

Figure 5-7 shows similar solvent density profiles when the lock and key are not in perfect match. When the key is too small, the solvent enters into the unfilled hemi-spherical pocket compromising the attraction at contact. Furthermore, at certain lock-key separation, the solvent is highly concentrated in the pocket (Figure 5-7b). The high local concentration results in the maximum repulsion in the lock-key interaction. The dependence of the PMF on separation for the oversized key is similar to that for the case of the perfect match case (Figure 5-5), and thus it is not shown here.

5. 3. 4 Angle-Dependent Entropic Potential

To test the applicability of the proposed method for non-spherical systems, we study also the angle-dependence of the entropic potential between a spherocylinder and a hard wall. Because the modified fundamental measure theory (MFMT) is not directly applicable to rod-sphere mixtures, we calculate the depletion potential only from MC-DFT and compare the results with simulation data and with predictions of an analytical method by Roth et al. [170]. Whereas the MC-PDT method requires the free energy functional of the mixture, the MC-DFT method requires only the free energy of the solvent, which makes it more generic for complicated multi-dimensional systems.

Figure 5-8 shows a schematic representation of the cylinder-wall system. In simulation of the density profile of solvent molecules at a given rod configuration, we consider a hard wall placed at $x = 0$ and a hard spherocylinder of diameter σ and cylinder length $L = 10\sigma$ with its center placed at distance x from the wall. The orientation of the spherocylinder, relative to the direction perpendicular to the wall, varies from $\theta \in [0, \pi/2]$. The simulation box is filled with a hard sphere solvent and the periodic boundary conditions are applied to the y and z directions [170]. Because the focus here is on the orientation dependence of the entropic potential, the rod center is either fixed at the smallest distance from the wall (i.e., with one end in contact with the surface, $x_{\min}(\theta) = \left(\sigma + L\left|\cos\theta\right|\right)/2$) or at $x = 5.5\sigma$. For all cases, the lengths of the simulation box are $L_y = L_z = 20\sigma$ and $L_x = 16\sigma$.

Figure 5-9 presents the reduced depletion potential $\beta W\left(x_{\min}, \theta\right)$ as a function of θ. The agreement between MC-DFT and the DFT calculation by Roth et al is excellent

[170]. When the rod is parallel to the wall, i.e., $\theta = \pi / 2$, the DFT calculations yield a contact potential significantly greater than that from the AO theory. The trend is consistent with their performance for the sphere-sphere and sphere-wall interactions[154]. The AO theory underestimates the contact potential primarily due to its negligence of the solvent-solvent interactions. Such depletion effect is due to the solvent density distribution which is shown in Figure 5-10.

Because of the inhomogeneity of the depletion potential on the rod surface, the entropic force introduces a torque $\mathbf{M}(x,\theta)$ that varies with the rod position and angle θ [170]. From the depletion potential $W(x,\theta)$, we can obtain the torque $\mathbf{M}(x,\theta)$ around an axis passing through the center of the rod and parallel to the wall [170]

$$\mathbf{M}(x,\theta) = -\frac{\partial W(x,\theta)}{\partial \theta}\mathbf{n}_\theta, \tag{5.11}$$

where $\mathbf{n}_\theta$ is the unit vector normal to the symmetry plane shown in Fig. 5-8. Figure 5-11 shows the dependence of torque on orientation when the rod center is fixed at $x = 5.5\sigma$. The line denotes the results from the MC-DFT and the symbols are from molecular dynamics simulations [170]. The hybrid method and simulation agree well.

5. 4 Conclusions

We introduced two complementary methods for studying the entropic forces in hard-sphere solvents by combination of Monte Carlo (MC) simulation and the density functional theory (DFT). In the first method (MC-DFT), MC simulation is used to sample the solvent density profiles at different colloidal configurations, and the entropic force is obtained from the difference in the grand potential. In the second method (MC-PDT),

MC simulation is used to calculate the solvent density around a single particle, and the potential of mean force is obtained by using the potential distribution theorem (PDT). For hard-sphere systems, the free energy functional has been calibrated in a number of previous publications [85, 88] and has been broadly used by others [171]. Because the fundamental measure theory provides an extremely accurate prediction of the free-energy functional, the density profile obtained from minimization of the free energy is expected similar to that from simulation; thus, the latter can be used as an input for the DFT calculations. We have tested the performance of the hybrid MC-DFT method by comparing with results from direct MC/MD simulations for the potential of mean force between a pair of hard spheres, between a hard sphere and a hard-wall, in colloidal "lock and key" system, and between a hard rod and a hard surface. In addition, comparison was made between the hybrid method and direct DFT calculations. The theoretical predictions are all in good agreement with results from full simulations. Because MC-DFT requires only an accurate DFT for the solvent, its performance is in general superior to MC-PDT, which relies on the density profile of the solvent near a single particle and a free energy function for the solute-solvent mixture. Nevertheless, MC-PDT avoids simulation at different colloidal configurations and therefore it is numerically much more efficient. In comparison with alternative methods, both MC-DFT and MC-PDT take the advantages of simulation and analytical calculations for multi-dimensional structure and thermodynamic properties, and both are computationally more efficient than direct simulations.

Whereas for numerical calibration this work is focused on relatively simple systems, we expect that, with a good expression of the free-energy functional to account for various components of intermolecular interactions and correlation effects, a similar procedure can be extended to more realistic systems including to those underlying biological and physical processes of direct interest for practical applications.

Figure 5-1 Depletion potential between two large particles in a solvent of small particles at different densities. The size ratio between the big and small particles is $s = 5$. The symbols are MC simulation results by Dickman [154], the red lines are from the MC-DFT calculations, the green lines are from MC-PDT , and the blue lines are from DFT-PDT calculations [68, 152]. The solid lines are bulk solvent packing density $\eta = 0.116$ and dashed lines are bulk solvent packing density $\eta = 0.229$.

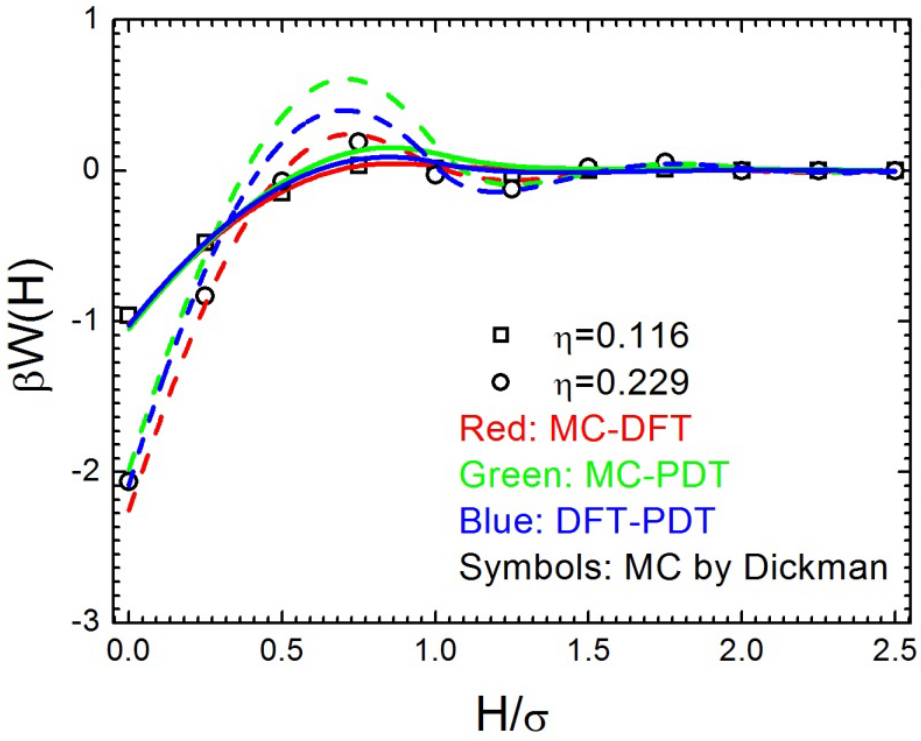

Figure 5-2 (a) Contour plots of the solvent density near two big spheres at contact ($H = 0$). Here the packing density of small spheres is $\eta = 0.116$. The centers of two big particles are placed along the x-axis ($y = 0$, $z = 0$). (b) $H = 1.5\sigma$. (c) $H = 2.5\sigma$.

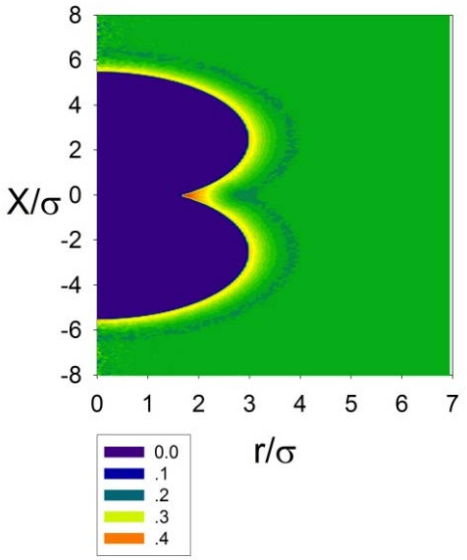

(a)

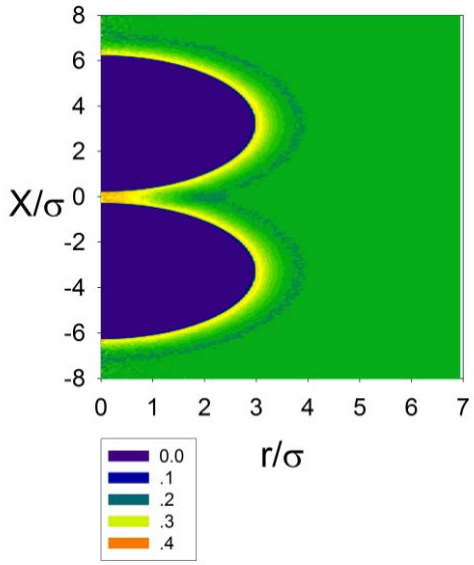

(b)

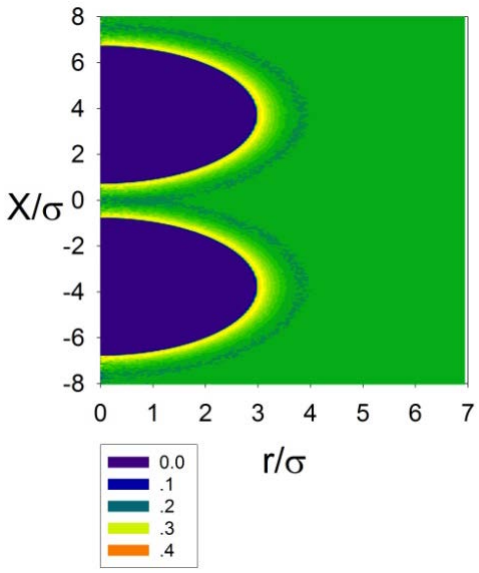

(c)

Figure 5-3 Depletion potentials between a big sphere ($s = 5$) and a flat hard wall immersed in a sea of small hard spheres at different bulk densities. The symbols are MC simulation results by Dickman [154], the red lines are from the MC-DFT calculations, and the green lines are from the MC-PDT predictions. The solid lines are bulk solvent packing density $\eta = 0.1$ and dashed lines are bulk solvent packing density $\eta = 0.2$.

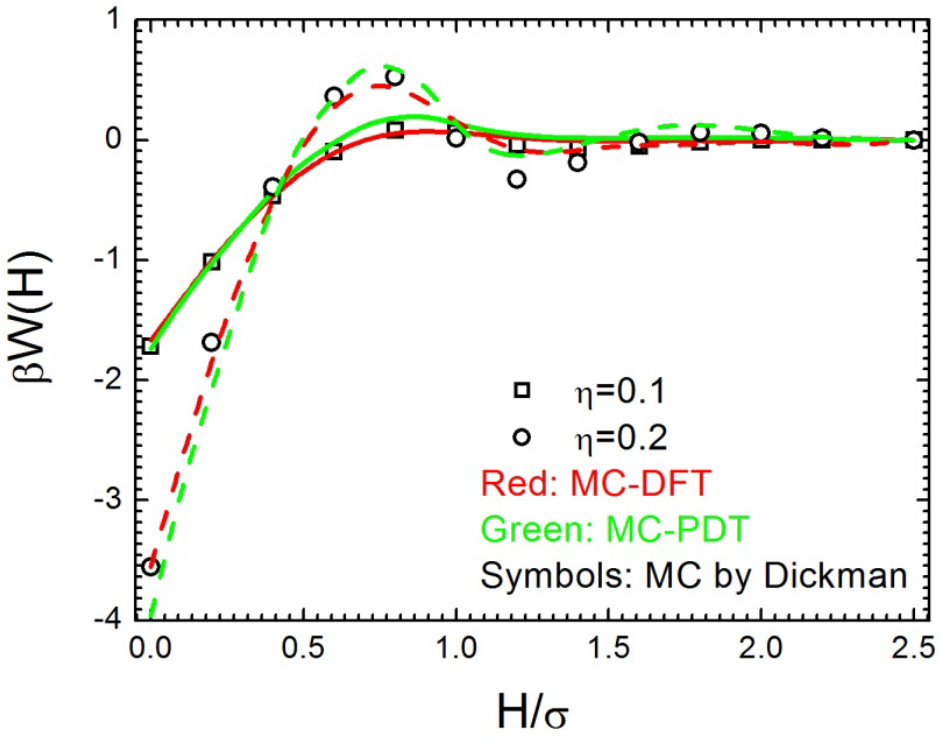

Figure 5-4 The geometry of the key and lock system ($y = 0$ plane cut). The key is a big spherical particle with diameter D_{key} and the lock is a substrate with a hemispherical pocket with diameter D_{lock}. The separation between key and lock is represented by the distance between the centers of key placing at $(x, 0, 0)$ and lock at $(x_0, 0, 0)$.

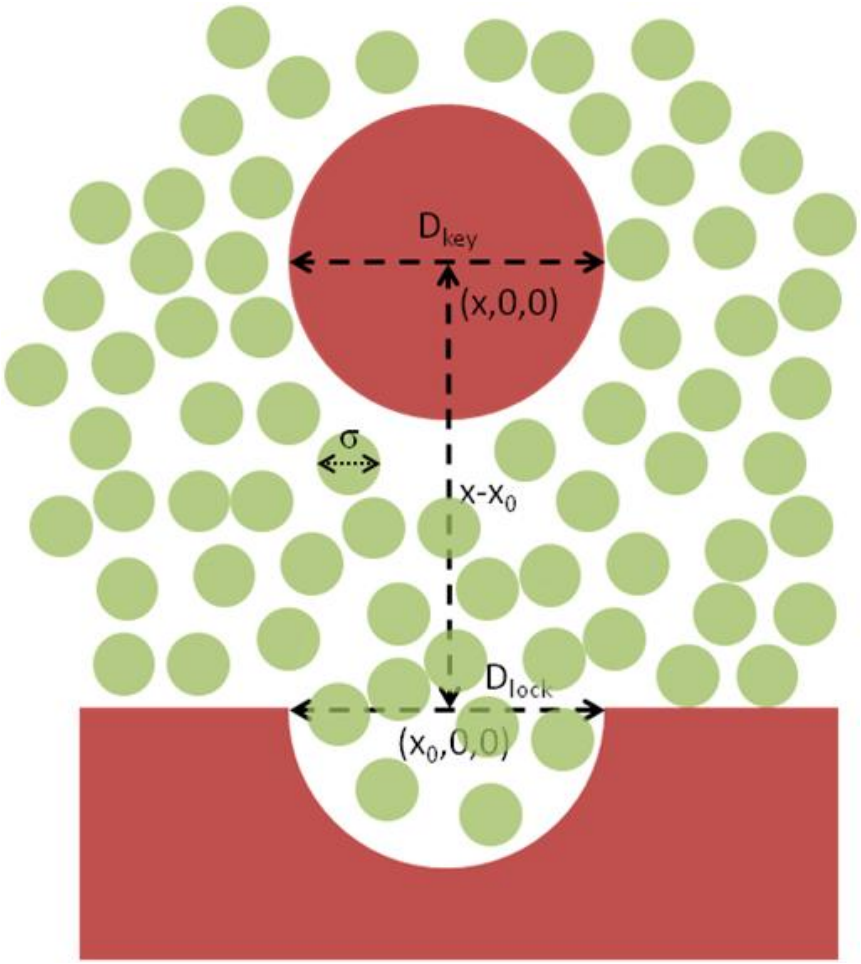

Figure 5-5 (a) Depletion potential between a hard spherical key with key diameter $D_{key} = 4\sigma$ and a hard hemi-spherical lock substrate with lock diameter $D_{lock} = 5\sigma$ in a hard- sphere solvent at bulk packing fraction $\eta = 0.367$. We compare the MC-PDT (blue line) and MC-DFT (magenta line) methods with the simulation data (symbols), HNC results (red line) from Kinoshita [22] and DFT results (green line) from P.M. Konig [155]. (b) The same to Fig. 5-5 (a) except with key diameter $D_{key} = 5\sigma$. (c) The same to Fig. 5-5 (a) except with key diameter $D_{key} = 6\sigma$.

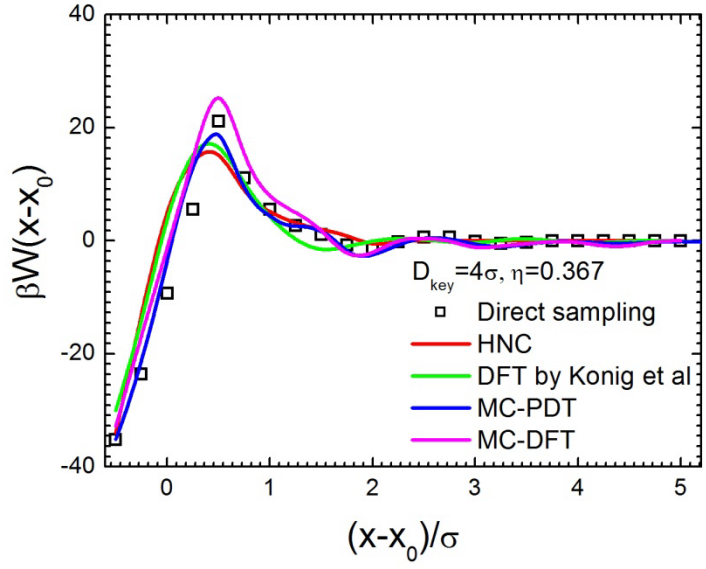

(a)

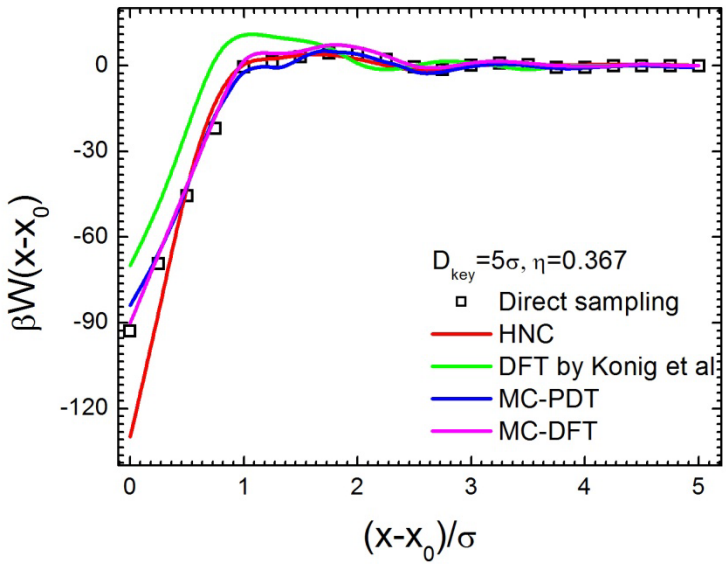

(b)

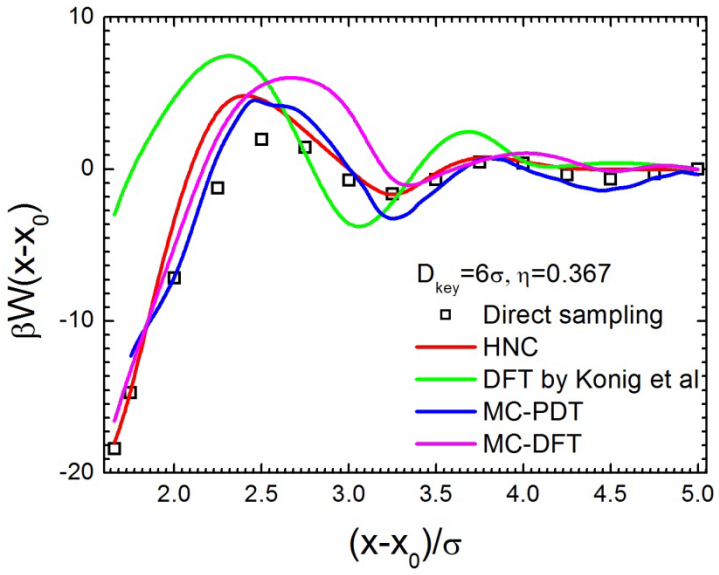
10
0
-10
-20
2.0
2.5
3.0
3.5
4.0
4.5
5.0
βW(x-x0)
(x-x0)/σ
Dkey=6σ, η=0.367
Direct sampling
HNC
DFT by Konig et al
MC-PDT
MC-DFT

(c)

Figure 5-6 Contour plots for the solvent density near a "key-lock" system. The key diameter is $D_{key} = 5\sigma$, and the hemi-spherical lock has a cavity of diameter $D_{lock} = 5\sigma$. The packaging fraction of hard spheres in the bulk is $\eta = 0.367$. The centers of the key and lock are aligned in the x-direction and the figure is plotted in a way similar to that in Fig. 5-2. (a) $x - x_0 = 0$, (b) $x - x_0 = 2\sigma$, and (c) $x - x_0 = 4\sigma$. (d) The excluded volume difference $\Delta V_{ex}(x - x_0) = V_{ex}(x - x_0) - V_{ex}(\infty)$ for different separation between lock and key particle. $V_{ex}(x - x_0)$ is the excluded volume due to lock substrate and key particle. The solvent available volume is negatively proportional to the excluded volume.

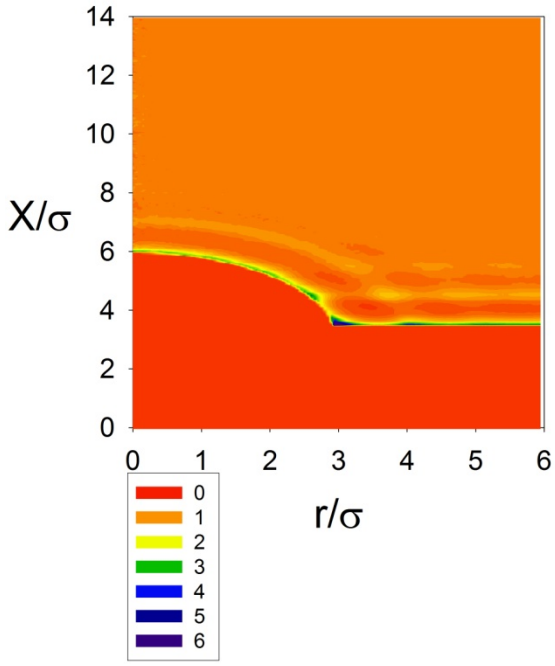

(a)

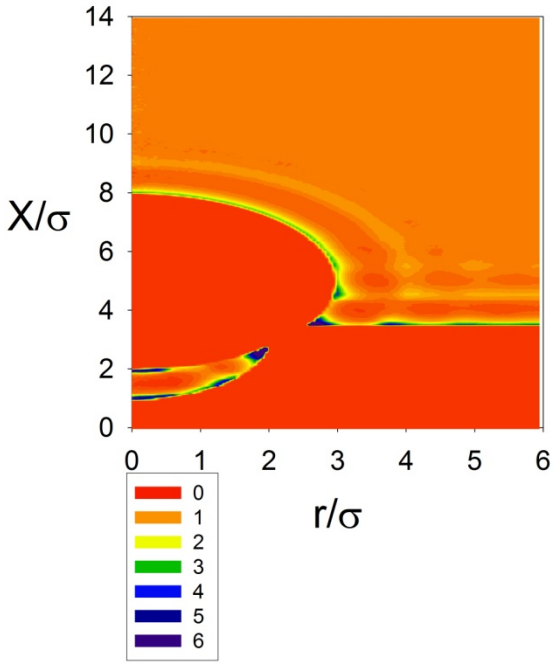
14
12
10
8
6
4
2
0
X/σ
0 1 2 3 4 5 6
r/σ
0
1
2
3
4
5
6

(b)

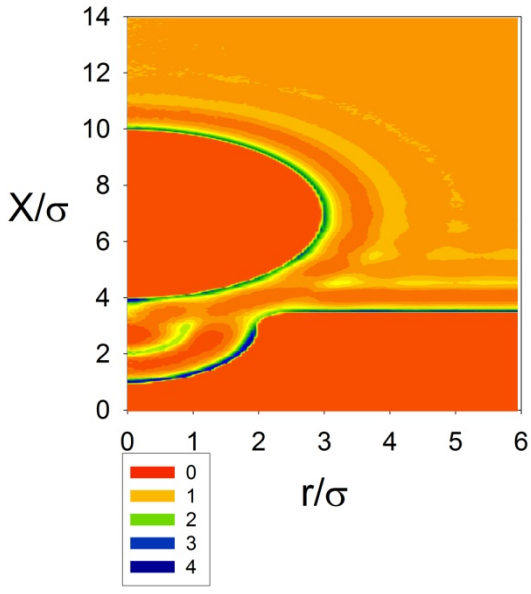
14
12
10
8
6
4
2
0
X/σ
0 1 2 3 4 5 6
r/σ
0
1
2
3
4

(c)

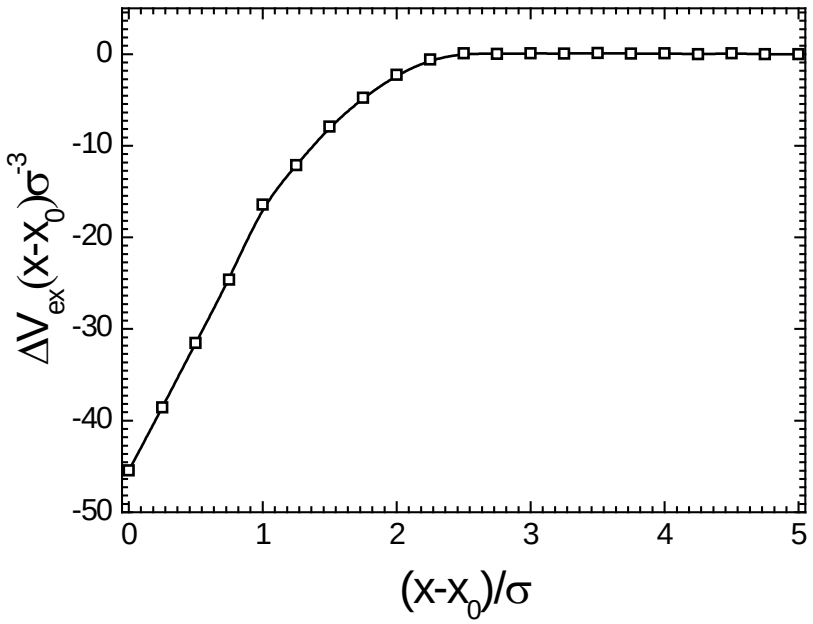

(d)

Figure 5-7 The same as Fig. 5-6 except that the key diameter $D_{key} = 4\sigma$ and (a) $x - x_0 = -0.5\sigma$.

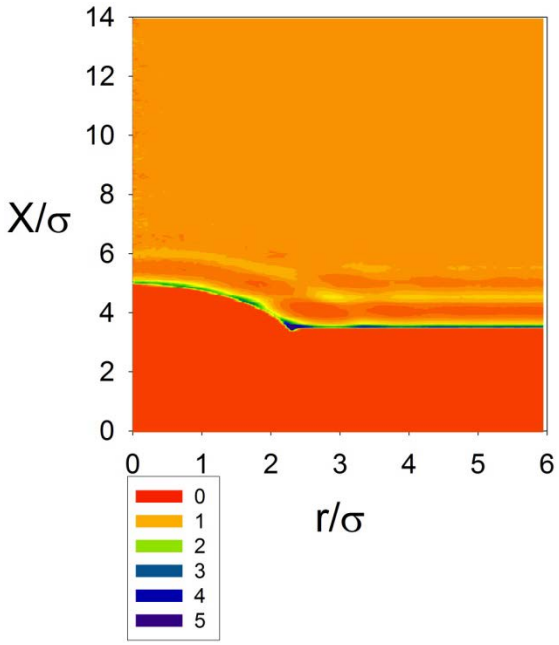

(a)

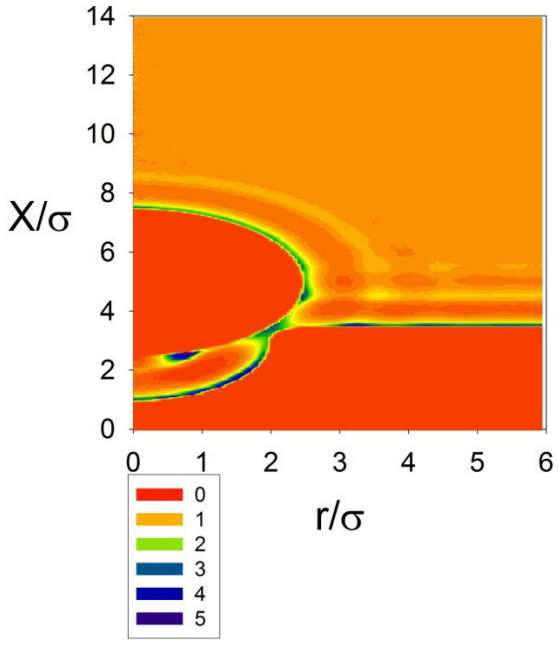

(b)

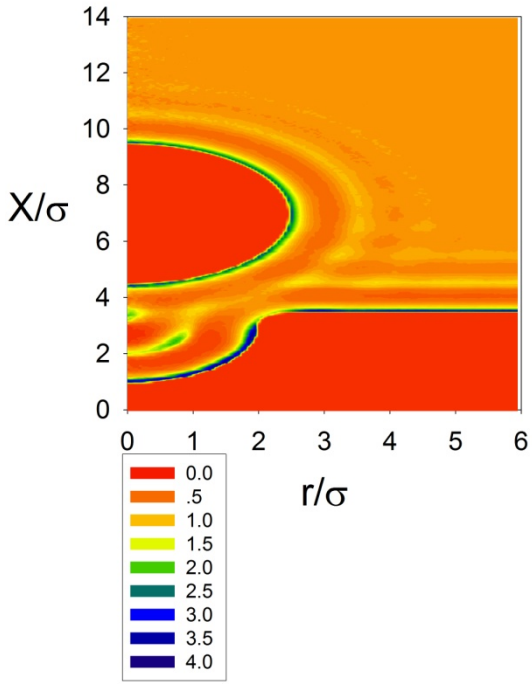

(c)

Figure 5-8 Schematic of a hard rod near a wall ($y = 0$ plane cut) in a hard-sphere solvent. The spherocylinder is placed at $(x, 0, 0)$ while the wall is at $x = 0$. The closet distance between them is $x_{\min}(\theta) = (\sigma + L|\cos\theta|)/2$.

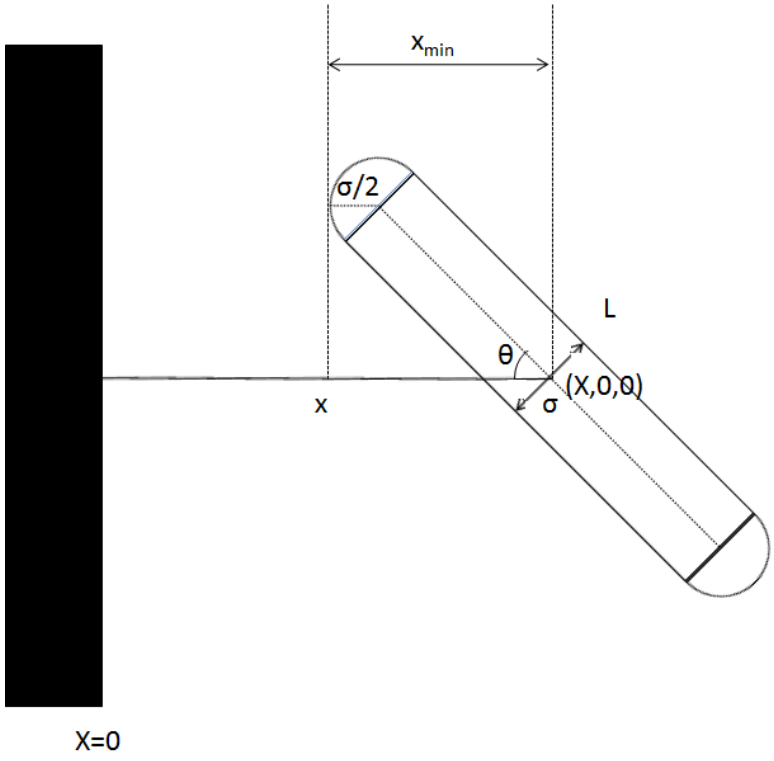

Figure 5-9 The contact potential $\beta W\left(x_{\min},\theta\right)$ as a function of angle θ between a hard spherocylinder and a flat wall. The length of the hard spherocylinder is $L=10\sigma$ and the packing fraction for the hard spheres in the bulk is $\eta=0.2239$. The solid line is from DFT by R. Roth [170], the dashed line is from AO theory, and symbols represent the MC-DFT results.

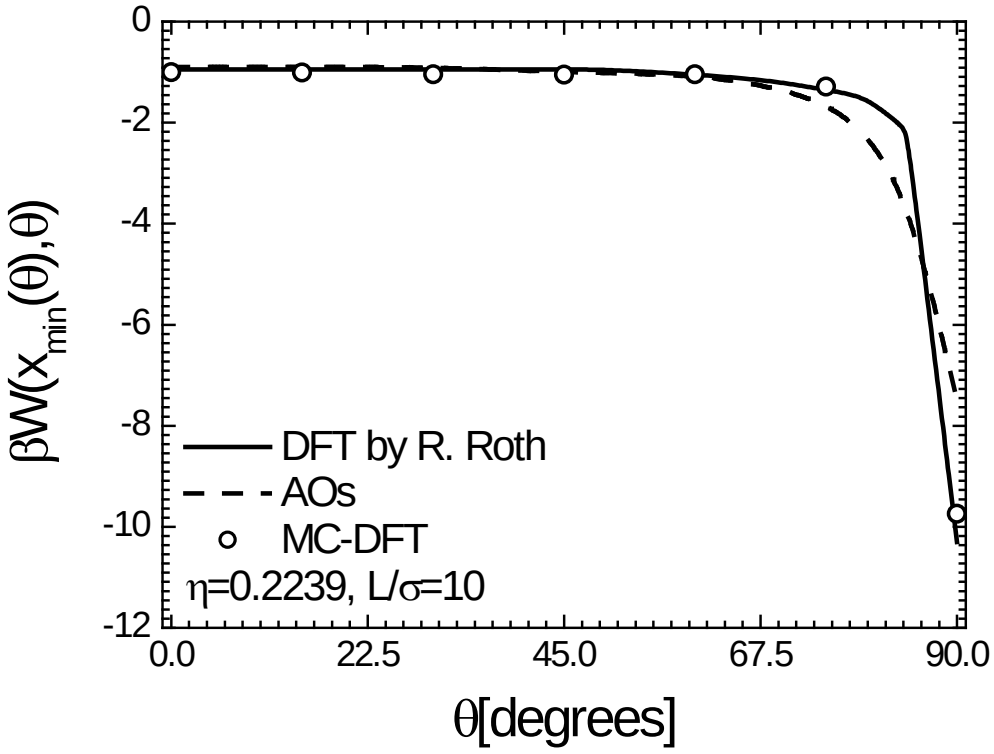

Figure 5-10 Contour plots ($y = 0$ plane) for density distribution of small hard spheres in the presence of a hard rod at $(5.5\sigma, 0, 0)$ and a flat wall at $x = 0$. The packaging fraction of the bulk state is $\eta = 0.2239$. (a) $\theta = 0^{\circ}$, (b) $\theta = 30^{\circ}$, and (c) $\theta = 90^{\circ}$.

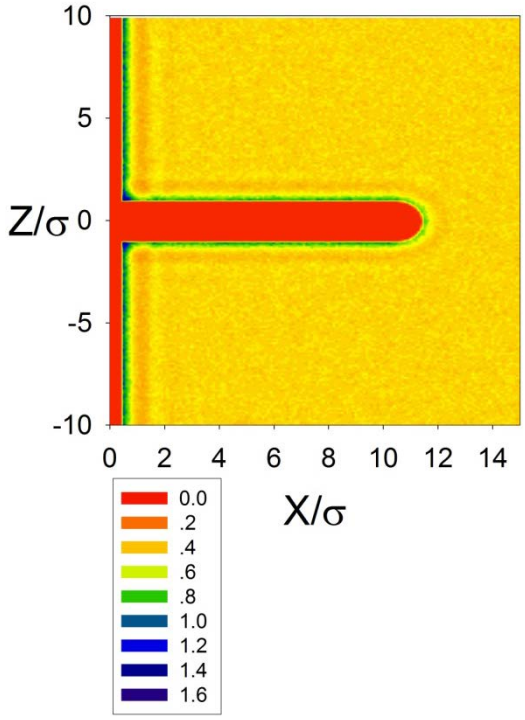

(a)

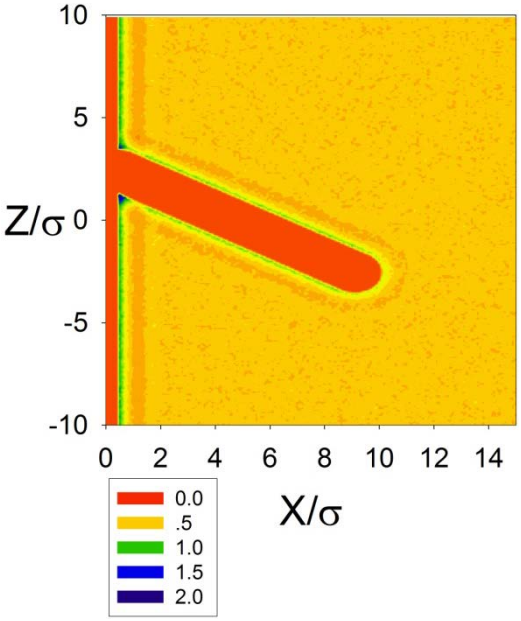
10
5
Z/σ 0
-5
-10
0 2 4 6 8 10 12 14
X/σ
0.0
.5
1.0
1.5
2.0

(b)

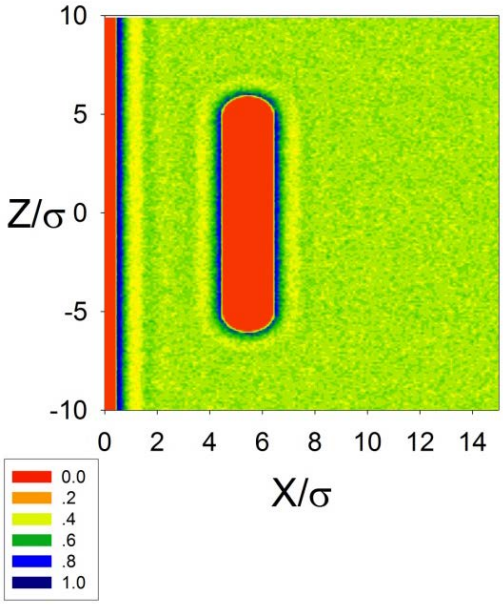
10
5
Z/σ 0
-5
-10
0 2 4 6 8 10 12 14
X/σ
0.0
.2
.4
.6
.8
1.0

(c)

Figure 5-11 The torque $\beta M(x,\theta)$ between a hard rod and a flat wall in a hard-sphere solvent. Here $x = 5.5\sigma$, the length of the hard spherocylinder is $L = 10\sigma$, and the packaging fraction of the bulk state is $\eta = 0.2239$. The solid line is our MC-DFT calculation and symbols are from MD.

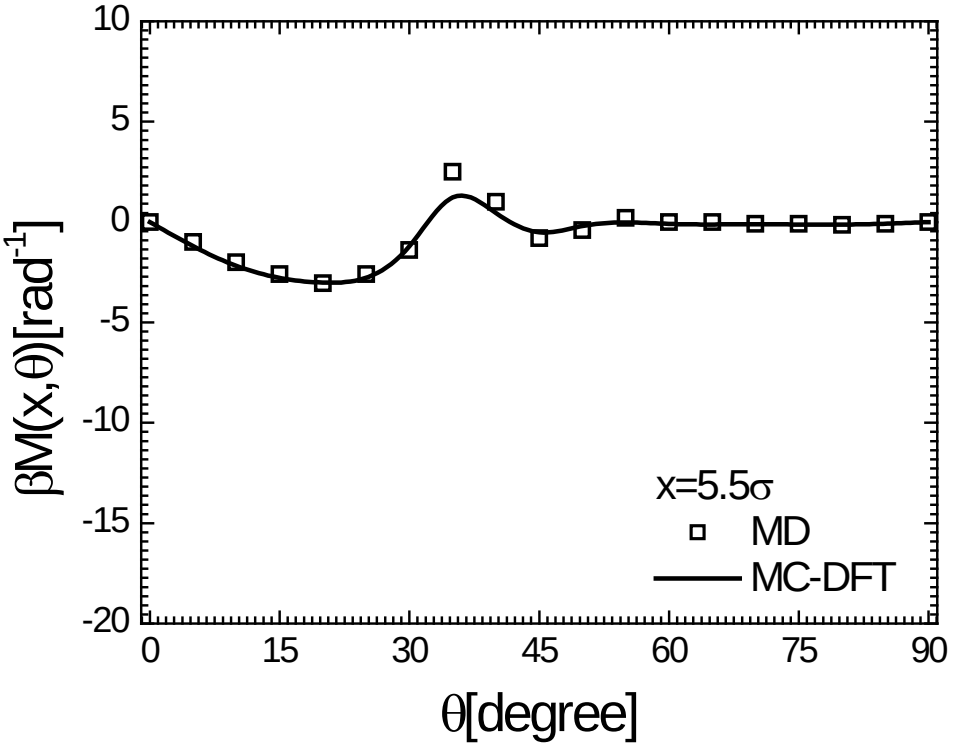

Table 5-1 Different methods for calculation of the potential of mean force (PMF).

Methods	MC-DFT	MC-PDT	DFT-PDT	MC
Density profile	**MC**	**MC**	**DFT**	**Direct sampling**
Free energy calculation	**DFT**	**PDT**	**PDT**	**Integration of the mean force**

Chapter 6 A New Theoretical Method for Rapid Prediction of Solvation Free Energy in Water

Abstract

We present a new theoretical method for rapid calculation of the solvation free energy in water by combining molecular simulation and the classical density functional theory (DFT). The DFT calculation is based on an accurate free-energy functional for water that incorporates the simulation results for long-range correlations and the fundamental measure theory for the molecular excluded-volume effects. The numerical performance of the theoretical method has been validated with simulation results and experimental data for the solvation free energies of halide (F^-, Cl^-, Br^- and I^-) and alkali (Li^+, Na^+, K^+, Rb^+ and Cs^+) ions in water at ambient conditions. Because simulation is applied only to the particular thermodynamic condition of interest, the hybrid method is computationally much more efficient than conventional ways of solvation free energy calculations.

6. 1 Introduction

Understanding dissolution of various chemical species in water has been an eternal pursuit of solution chemistry [172-175]. While the literature is vast, recent interest has been mostly focused on the microscopic details of solute-water interactions and the

effect of the local water structure on the chemical and biochemical affinities of dissolved species [4, 176]. Such information is indispensible for studying chemical/biochemical processes in aqueous systems including relaxation dynamics, stability of biomacromolecules, and "lock-key" interactions for rational drug design [15, 177]. Whereas traditional thermodynamic methods and the semi-empirical theories of solvation (e.g., the Born model and the Langevin-Debye theory) treat water as an "inert" dielectric medium [178-181], recent theoretical and experimental investigations highlight the importance of the surrounding water molecules as an active component of the chemical and biochemical interactions [15, 177]. Despite significant progress in recent years toward a comprehensive understanding of solvation in water, quantification of the water structure at atomistic length scales and, more importantly, connection of the local water structure to the properties of dissolved species remain a daunting scientific challenge.

Current theoretical investigation of water structure at very small length scales is mostly based on molecular simulations [182, 183]. Given a semi-empirical force field or an efficient first-principle algorithm for the solute-solvent interactions, computer simulation provides atomistic details of solvation in water including those pertinent to biological systems. While molecular simulation yields microscopic structure complementary to experimental measurements of the thermodynamic properties, lengthy calculation is often required to establish the structure-property relationships [184]. Besides, approximation of the intermolecular interactions (or first-principle calculations) necessitates certain discrepancy between simulation and experiment [185]. Alternatively, solvation in water may be studied with a number of analytical methods such as the

integral-equation theories [186-189], the classical density functional theory [190-192], the scaled-particle theory [8], and modified Born models [193]. These analytical methods are computationally efficient in comparison to molecular simulation and provide direct information on thermodynamic properties or/and explicit structure-property relationships. Regrettably, the numerical performance of conventional analytical methods is often limited not only by the semi-empirical nature of the intermolecular potential and but also by approximations for various multi-body correlation effects.

In this work, we propose a new theoretical procedure to predict the solvation free energy in water by combining the merits of molecular dynamics (MD) simulation and the classical density functional theory (DFT). We use MD to calculate the microscopic structure up to atomic details and then the DFT to link the microscopic structure with thermodynamic properties. For efficient DFT calculations, the solute degrees of freedom are decoupled from those of the solvent molecules. The DFT free-energy functional incorporates the microscopic structure of water obtained from the simulation, the modified fundamental measure theory (FMT) [83, 85, 88] for molecular excluded volume effects, and a bridge functional for long-range correlations. The new computational procedure has been validated with simulation and experimental data for the solvation free energies of halide (F^-, Cl^-, Br^- and I^-) and alkali (Li^+, Na^+, K^+, Rb^+ and Cs^+) ions in water [194].

6. 2 Theory

We consider solvation of individual monovalent ions in water at ambient conditions. As being extensively studied before, water molecules are represented by the

SPC/E model [194] and water-ion interactions are represented by the Lennard-Jones potential plus Coulomb forces [195]. While we use relatively simple models for calibration of the new theoretical method, a similar procedure can be extended to systems where both the solute and solvent molecules are more complicated.

The solvation free energy is defined as the reversible work to transfer a solute molecule from a hypothetical ideal-gas state into the pure solvent at a fixed temperature and the solvent chemical potential (or equivalently, the solvent temperature and pressure). To transfer a single solute molecule (or ion) from vacuum to a solvent of constant temperature, volume and chemical potential, the solvation free energy corresponds to the change in the grand potential, i.e.,

$$F\left[\rho(\mathbf{x});\mu,V,T\right]=\Omega\left[\rho(\mathbf{x});\mu,V,T\right]-\Omega\left[\rho_0;\mu,V,T\right], \tag{6.1}$$

where $\rho(\mathbf{x})$ stands for the density profile of water molecules near the solute; composite vector $\mathbf{x}=(\mathbf{r},\Theta)$ specifies the position and orientation of a water molecule, ρ_0 and μ are, respectively, the average density and the chemical potential of water molecules in the bulk, and T stands for the absolute temperature. For bulk water, $\rho(\mathbf{x})=\rho_0=n_0/\int d\Theta$ where n_0 is the number density of water molecules in the bulk. Because the solvation free energy is an intensive thermodynamic quantity independent of the system size, numerical implementation of Eq. (6.1) requires that the system volume V must be sufficiently large such that the properties of water remote from the solute are the same as those corresponding to the bulk.

With a molecular model for water and water-solute interactions, it is straightforward to calculate the local density profile of water molecules by molecular simulation. Direct simulation of the solvation free energy, however, would entail an imaginary thermodynamic pathway to transfer a solute molecule from the ideal-gas state into bulk water. Because a large number of thermodynamic states must be used to represent the reversible process, the free-energy calculation is computationally demanding [196, 197]. Application of the DFT alleviates such numerical burden because it provides a direct connection between the microscopic structure and thermodynamic properties.

Water molecules around a single solute consist of an inhomogeneous system of *pure* water in the presence of an effective external field defined by the solute-solvent interactions. The grand potential is given by [65]

$$\begin{aligned}\Omega\left[\rho(\mathbf{x});\mu,V,T\right] = k_B T \int d\mathbf{x}\rho(\mathbf{x})\left\{\ln\left[\rho(\mathbf{x})\Lambda^3\right]-1\right\} \\ + \int d\mathbf{x}\left[V_{ext}(\mathbf{x})-\mu\right]\rho(\mathbf{x}) + F^{ex}\left[\rho(\mathbf{x})\right]\end{aligned}, \tag{6.2}$$

where k_B stands for the Boltzmann constant, Λ is an effective thermal wavelength for water molecules, and $V_{ext}(\mathbf{x})$ represents the external potential (here the solute-solvent interaction). $F^{ex}\left[\rho(\mathbf{x})\right]$ denotes the excess *intrinsic* Helmholtz energy, i.e., deviation of the free energy from that of an ideal-gas state due to intermolecular interactions. Here intrinsic means that the property depends only on the pair potential and the microscopic distribution of water molecules, not directly related to the water-solute interaction. In other words, the free energy functional is universally applicable to water at arbitrary

inhomogeneous conditions. As described in Appendix C, Eq. (6.2) can also be used to calculate the self-solvation free energy (or excess chemical potential) of pure water by tagging one water molecule in the bulk.

Formally, the excess intrinsic Helmholtz energy may be expressed relative to that of the bulk water at the same temperature and chemical potential [77, 198]

$$F^{ex}\left[\rho(\mathbf{x})\right] = F^{ex}\left[\rho_0\right] + \mu_0^{ex}\int d\mathbf{x}\Delta\rho(\mathbf{x}) - \frac{k_BT}{2}\int d\mathbf{x}_1\int d\mathbf{x}_2\Delta\rho(\mathbf{x}_1)\Delta\rho(\mathbf{x}_2)c(\mathbf{x}_1,\mathbf{x}_2;\rho_0) + F_B\left[\rho(\mathbf{x})\right], \tag{6.3}$$

where $\Delta\rho(\mathbf{x}) = \rho(\mathbf{x}) - \rho_0$, μ_0^{ex} and $c(\mathbf{x}_1,\mathbf{x}_2;\rho_0)$ stand for, respectively, the excess chemical potential and the two-body direct correlation function for the pure water, and $F_B\left[\rho(\mathbf{x})\right]$ is a bridge functional that accounts for thermodynamic non-ideality beyond the two-body correlations. Without the bridge functional, Eq. (6.3) becomes equivalent to the hypernetted chain (HNC) approximation [21], which has been used extensively for the solvation research (see for example [199]). As detailed in Appendix C, $\rho(\mathbf{x})$ and $c(\mathbf{x},\mathbf{x}';\rho_0)$ can be calculated from molecular simulation of bulk water.

We divide the bridge functional $F_B\left[\rho(\mathbf{x})\right]$ into a contribution due to the short-range (SL) molecular excluded-volume effects and that due to longer-ranged (LR) van der Waals and electrostatic interactions:

$$F_B\left[\rho(\mathbf{x})\right] = F_B^{SR}\left[\rho(\mathbf{x})\right] + F_B^{LR}\left[\rho(\mathbf{x})\right]. \tag{6.4}$$

The total bridge functional $F_B\left[\rho(\mathbf{x})\right]$ must satisfy the Euler-Lagrange equation:

$$\delta\beta F_B\left[\rho(\mathbf{x})\right]/\delta\rho(\mathbf{x}) = \ln y(\mathbf{x}) - \int d\mathbf{x}'c(\mathbf{x},\mathbf{x}';\rho_0)\Delta\rho(\mathbf{x}'), \tag{6.5}$$

where $y(\mathbf{x}) \equiv \rho(\mathbf{x}) \exp\left[\beta V_{ext}(\mathbf{x})\right] / \rho_0$ denotes the solute-solvent cavity correlation function. Eq. (6.5) is obtained by minimization of the grand potential (Eq. (6.2)) with respect to $\rho(\mathbf{x})$. With the local density $\rho(\mathbf{x})$ obtained from molecular simulation, we can calculate $B(\mathbf{x}) \equiv \delta F_B\left[\rho(\mathbf{x})\right] / \delta\rho(\mathbf{x})$ from Eq. (6.5) over the region accessible to water molecules. Within the solute core, the density profile vanishes but the solute-solvent cavity correlation function remains finite. In this region, the bridge functional is closely related to the molecular excluded-volume effects. Whereas there is no *a priori* knowledge for the SR bridge functional, the excluded-volume contribution arises mainly from the physical size of water molecules. In this work, we assume that the short-range component of the bridge functional can be approximated by that of a hard-sphere system with the density profile identical to that of oxygen atoms in water, i.e.,

$$F_B^{SR}\left[\rho(\mathbf{x})\right] \approx F_B^{HS}\left[n(\mathbf{r})\right], \tag{6.6}$$

where $n(\mathbf{r}) = \int \rho(\mathbf{r}, \Theta)\, d\Theta$. Because of the *universality* of intrinsic Helmholtz energy for water, the hard-sphere diameter d can be determined self-consistently by considering the excess chemical potential of pure water, i.e., by application of the same theoretical procedure to calculating the self-solvation free energy of a water molecule in bulk water (As detailed in Appendix C, we obtain $d = 2.85$ Å for the SPC/E water considered in this work [200, 201]). For the hard-sphere reference system, the bridge functional is given by

$$\begin{aligned} F_B^{HS}\left[n(\mathbf{r})\right] = {} & F_{HS}^{ex}\left[n(\mathbf{r})\right] - F_{HS}^{ex}(n_0) - \mu_{0,HS}^{ex} \int d\mathbf{r} \Delta n(\mathbf{r}) \\ & + \frac{k_B T}{2} \int d\mathbf{r}_1 \int d\mathbf{r}_2 \Delta n(\mathbf{r}_1) \Delta n(\mathbf{r}_2)\, c_{HS}^{(2)}\left(|\mathbf{r}_1 - \mathbf{r}_2|\right) \end{aligned}, \tag{6.7}$$

where $\Delta n(\mathbf{r}) = n(\mathbf{r}) - n_0$, and $\mu_{0,HS}^{ex}$ and $c_{HS}^{(2)}\left(|\mathbf{r}_1 - \mathbf{r}_2|\right)$ are, respectively, the excess chemical potential and the direct correlation function of bulk hard spheres. Accurate equations are available for predicting the structural and thermodynamic properties of both uniform and inhomogeneous hard-sphere systems [171]. In this work, the properties of the reference hard spheres are calculated from the modified fundmanetal measure theory (MFMT) [85, 88].

Because for a system with uniform density the excess intrinsic Helmholtz energy reduces to that of the bulk system, both the SR and LR components of the bridge functional disappears as $\Delta\rho(\mathbf{x}) = 0$. Besides, it is known from previous work that the bridge functional is dominated by the short-range interactions [202-204]. As a result, we expect that the LR component of the bridge functional is relatively small and it may be approximated by a linear functional integration:

$$F_B^{LR}\left[\rho(\mathbf{x})\right] \approx -k_B T \int d\mathbf{x} \Delta\rho(\mathbf{x}) B^{LR}(\mathbf{x}), \tag{6.8}$$

where

$$B^{LR}(\mathbf{x}) = \begin{cases} \ln y(\mathbf{x}) - \int d\mathbf{x}' c(\mathbf{x}, \mathbf{x}'; \rho_0) \Delta\rho(\mathbf{x}') & \rho(\mathbf{x})/\rho_0 \geq \delta \\ 0 & \text{otherwise} \end{cases}. \tag{6.9}$$

In Eq. (6.9), parameter δ defines the solvent accessibility: the space is solvent accessible if $\rho(\mathbf{x})/\rho_0 \geq \delta$ and inaccessible otherwise. Apparently, δ is intimately related to the hard-sphere diameter of the reference system. For calculations in this work, we use $\delta = 10^{-6}$. We find that the theoretical results are not sensitive to small variations of δ .

Once we have explicit expressions for the SR and LR components of the bridge functional (Eqs. (6.6) and (6.8)), we can finally derive the solvation free energy from Eq. (6.1), which, after some algebra, becomes

$$F\left[\rho(\mathbf{x})\right] = k_B T \int d\mathbf{x}\left\{\rho(\mathbf{x})\ln y(\mathbf{x}) - \rho(\mathbf{x}) + \rho_0\right\} - k_B T \int d\mathbf{x}\Delta\rho(\mathbf{x}) B^{LR}(\mathbf{x}) - \frac{k_B T}{2}\int d\mathbf{x}_1 \int d\mathbf{x}_2 \Delta\rho(\mathbf{x}_1)\Delta\rho(\mathbf{x}_2) c(\mathbf{x}_1, \mathbf{x}_2; \rho_0) + F_B^{SR}\left[\rho(\mathbf{x})\right] \quad (6.10)$$

As expected, the solvation free-energy is immaterial to the effective thermal wave length of water molecules. Without the terms related to the bridge functional, Eq. (6.10) would yield a solvation free energy identical to that from the HNC approximation.

6. 3 Results

We first use MD simulation to obtain the direct correlation function of bulk water and the local density profile of water molecules around individual ions (see Appendix C for details). From the local density and bulk correlation functions, we then calculate the solvation free energies by numerical integrations of Eq. (6.10). In the region not accessible to solvent molecules ($\rho(\mathbf{x})/\rho_0 < \delta$), the cavity correlation function and the long-range component of the bridge functional make no contribution to the solvation free energy. In this region, the solvation free energy is determined by that of a hard-sphere reference system using MFMT [85].

Table 6-1 summarizes the theoretical results for the solvation free energies of alkali ions (Li^+, Na^+, K^+, Rb^+, Cs^+) and halide ions (F^-, Cl^-, Br^-, I^-) in water at 300K and mass density 0.996 g/cm^3. These monomeric ions are considered in this work because extensive experimental, simulation, and theoretical results are readily available from

previous studies thus the published results for these simple systems provide ideal benchmark data for calibration of the proposed computational procedure. For comparison, Table 6-1 also includes some representative results from previous theoretical investigations.

As well documented [205, 206], the solvation free energies of individual ions are not accessible to direct experimental measurements. As a result, the conventional values are often tabulated relative to the solvation free energy of proton that cannot be directly used for compassion with theoretical predictions. The two sets of experimental data shown in Table 6-1 correspond to the "absolute" values obtained from different estimations of the proton solvation free energy. The data from Schmidt et al. used the proton solvation free energy (-251.4 kcal/mol at 298 K) estimated from thermodynamic measurements r dissociation of water [207]. The much cited values tabulated by Marcus involve a so-called "extra thermodynamic assumption", i.e., a large cation and a large anion of equal size and equally low electric charge have the same solvation free energy (as predicted by Born model) [208]. Based on the extra thermodynamic assumption and the Gibbs energy of solvation for tetraphenylarsonium tetraphenylborate (TABA), Marcus deduced a proton solvation free energy (-252.4 kcal/mol at 298 K) remarkably close to that given by Schmidt et al. (even though they differ much in both the enthalpy and entropy of the solvation). Besides the difference in the reference solvation free energy, additional discrepancies between the two sets of experimental data, in particular for the solvation free energy of anions, are probably due to different sources of experimental measurements. Table 6-1 also includes two sets of simulation data which

differ slightly in terms of the Lennard-Jones parameters for ion-water interactions [195]. The simulation results were obtained without evoking a hypothetical vacuum-water interface, i.e., the solvation free energies calculated do not include the phase or surface potential arising from anisotropic distribution of water molecules at the interface [209].

Table 6-1 shows that, with the same parameters for water-water and ion-water interactions, our theoretical predictions for the ion solvation free energy agree well with those from a recent simulation by Joung and Cheatham [195]. In comparison with the experiment data, the solvation free energies predicted from this work are comparable to the simulation results: while for alkali ion (Li^+, Na^+, K^+, Rb^+, Cs^+) the simulation results appear closer to experimental data, the opposite is true for halide ion (F^-, Cl^-, Br^-, I^-). From a practical point of view, the difference between the theory and simulation is insignificant, in particular if we refer to another set of simulation data predicted with a slightly different set of parameters for the Lennard-Jones potential between ion and water reported by Jensen and Jorgensen [210].

We have also compared the solvation free energies predicted from this work with those from the Born solvation model and from the mean-spherical approximation (MSA) [211]. The well-known Born model accounts for the self-electrostatic energy for ionization of a neutral particle in a continuous dielectric medium. According to this model, the solvation free energy depends only on the particle size and the bulk dielectric constant of the solvent. Because the local dielectric property of the solvent near an ion can be quite different from that in the bulk and because an appropriate selection of the ionic radius is often questionable, the Born model is not very reliable and has been much

criticized. In comparison to the Born model, the MSA predictions are much closer to the experimental results. However, representation of water molecules in terms of hard spheres each with a point dipole is an oversimplification from a microscopic point of view. Besides, the numerical performance of MSA is not reliable even within the highly idealized model.

Finally, we compare the solvation free energies predicted from Eq. (6.10) with those from the HNC approximation. These two methods differ only in terms of the bridge functional, i.e., contributions to the intrinsic Helmholtz energy beyond the quadratic terms. Table 6-1 shows that the agreement between the HNC predictions and the experimental results barely matches those from the Born model, indicating that a quadratic approximation is insufficient to capture the solvation free energy quantitatively.

6. 4 Conclusions

We present a new theoretical method for calculating the solvation free energies of ions in water using molecular dynamics (MD) simulation and the classical density functional theory (DFT). An accurate intrinsic Helmholtz energy functional for water has been developed by decomposing the intermolecular potential into a short-range (SR) repulsion and longer-ranged (LR) van der Waal and electrostatic interactions. The free energy due to the SR repulsion is accounted for by using an inhomogeneous hard-sphere reference system and that due to the LR interactions are calculated from a linear approximation of the bridge functional. With the local density distribution of water molecules obtained from MD simulation, the DFT predicts the solvation free energies of halide and alkali ions in excellent agreement with simulation results. In comparison to

conventional simulation methods, the new theoretical approach is computationally very efficient because it avoids simulation along a hypothetical thermodynamic pathway to connect the initial and final states of the solvation process.

We should point out that the new computational method is not limited to any particular force field for water or ion-water interactions. Indeed, the same procedure can be applied to any semi-empirical models that entail a pairwise additive intermolecular potential for water. While combination of the DFT with MD simulation greatly reduces the computational cost for free energy calculations, our method is intrinsically limited by the applicability of MD simulation concerning the system size (e.g., solvation of large proteins) and by the reliability of the semi-empirical force field (e.g., molecular model for water and water-transition ion interactions).

Table 6-1 Solvation free energies of cations and anions in SPC/E water obtained from different methods. All values are negative and in the units of kcal/mol. The temperature is 300K and mass density of SPC/E water is 0.996 g/cm^3.

	Experiment		Simulation		Theory			
					This work			
	Schmid et al [207]	Marcus [208]	Joung-Cheatham [195]	Jensen-Jorgensen [210]	total	HNC	MSA [211]	Born [211]
Li^+	113.8	113.5	113.3	105.6	111.9	178.7	115.5	186.2
Na^+	88.7	87.2	88.4	76.4	88.4	153.2	96.4	141.3
K^+	71.2	70.5	71	59.5	69.5	127.3	79.6	107.8
Rb^+	66.0	65.7	65.6	54.5	64.2	118.7	75.6	100.6
Cs^+	60.5	59.8	60.5	48.6	60.3	110.3	68.9	89.2
F^-	119.7	111.1	119.8	119.6	118	153.4	94.7	137.7
Cl^-	89.1	81.3	89.3	91	86.5	107.7	74.1	90.6
Br^-	82.7	75.3	82.7	85.8	81.5	97.6	69.6	90.1
I^-	74.3	65.7	74.4	77.5	72.9	82.2	63.1	79.6

Chapter 7 A Perturbative Density Functional Theory for Square-Well Fluids

Abstract

We report a perturbative density functional theory for quantitative description of the structural and thermodynamic properties of square-well fluids in the bulk or at inhomogeneous conditions. The free-energy functional combines a modified fundamental measure theory to account for the short-range repulsion and a quadratic density expansion for the long-range attraction. The long-correlation effects are taken into account by using analytical expressions of the direct correlation functions of bulk fluids recently obtained from the first-order mean-spherical approximation. The density functional theory has been calibrated by extensive comparison with simulation data from this work and from the literature. The theory yields good agreement with simulation results for the radial distribution function of bulk systems and for the density profiles of square-well fluids near the surfaces of spherical cavities or in slit pores over a broad range of the parameter space and thermodynamic conditions.

7. 1 Introduction

Understanding the equilibrium structure and thermodynamic properties of complex fluids such as colloids, protein solutions and micelles often relies on model

systems where drastically simplified potentials are used to describe the solvent-mediated potential of mean force [212-216]. Among such model systems, the square-well (SW) potential is a popular choice because it provides succinct description of the molecular excluded-volume effects as well as the strength and the range of solvent-mediated colloidal interactions. Despite its simplicity, accurate prediction of the properties of the SW fluids remains a theoretical challenge for systems with long-range attractions and/or at inhomogeneous conditions.

Statistical-mechanical study of the equilibrium properties of SW fluids was originated in the late 1960s concomitant with development of the integral-equation and perturbation liquid-state theories [217]. In particular, the perturbation theory of Barker and Henderson provides the groundwork for much of later theoretical descriptions of the bulk thermodynamic properties [218-222]. The first attempt to derive an analytical expression for the equilibrium structure of SW fluids was reported by Baxter using the Percus-Yevick (PY) approximation [223]. Explicit expressions were also given for the equation of state and the internal energy of SW fluids in the limit such that the range of attraction vanishes and the well depth approaches infinite (i.e., in the "sticky" hard-sphere limit). Baxter's theoretical procedure was later extended by Nezbeda to systems with a non-zero but very short-range attraction [224]. Another extension of Baxter's theory was proposed by Yuste and Santos based on statistical-mechanics sum rules and the low-density expansion of the radial distribution function [225]. These extensions are most accurate when the attraction range is extremely narrow, typically within about 5% of the hard-sphere diameter. The sticky-hard-sphere model was also used by Malijevsky

et al. as a reference for effective representation of short-range attraction in SW fluids [226]. Similar to other extensions of Baxter's integral-equation theory, the mapping method is reliable only when the range of attraction is much smaller than the hard-sphere diameter.

The properties of bulk SW fluids can be predicted by numerical solutions of the integral-equation theories incuding the hypernetted-chain (HNC) approximation [227, 228], the mean-spherical approximation (MSA) [229], the self-consistent HMSA closure (i.e. an empirical superposition of the mean-spherical and the hypernetted-chain approximation) [230, 231], and more recently the self-consistent Ornstein-Zernike approximation (SCOZA) [232]. With the condition of thermodynamic self-consistency imposed at each equilibrium state, the SCOZA gives excellent predictions of the structural and thermodynamic properties of bulk SW fluids including the critical temperature and pressure. In addition to integral-equation theories, a simple expression was derived by Sharma and Sharma [233] for calculating the static structure factor of SW fluids. The closed form was obtained from the random phase approximation (RPA), i.e., the direct correlation function is assumed the same as that of the hard-sphere fluid within the hard core and the long-range component follows MSA. While the analytical expression is convenient for practical applications, the numerical performance can be much improved by using the optimized RPA (ORPA) of Andersen and Chandler[234] that imposes the exact constraint due to the hard-core exclusion. Recently, Lang and coworkers analyzed systematically the performance of ORPA, along with several integral-equation methods including the Rogers–Young (RY) integral-equation method,

for representing the structural and thermodynamic properties of bulk SW fluids by extensive comparison with Monte Carlo simulation data [235]. At intermediate and high temperatures, ORPA agrees well with the simulation results but its performance deteriorates at low temperature or as the range of attraction increases. For systems with narrow-range attractions, the RY method yields excellent results but numerical difficulties emerge as the range of the attractive potential increases. Another avenue to improve the RPA theory was proposed by Tang and Lu [236] by using the first-order MSA (FMSA) closure. Recently, Tang [100] derived an analytical expression for the direct correlation function of bulk SW fluids and the derivation was extended by Hlushak et al. for systems with longer-range interactions [104]. Although FMSA does not impose thermodynamic self-consistency *per se*, it offers analytical expressions for both the equation of state and various correlation functions of SW fluids that are convenient for practical applications.

Whereas statistical-mechanical research on uniform SW fluids is now well advanced, relatively few theoretical developments have been devoted to SW fluids at inhomogeneous conditions [65, 69, 237-241]. Previous investigations of inhomogeneous SW systems often hinge on various forms of weighted-density or/and mean-field approximations that ignore nonlocal packaging effects and long-range correlations. Although the weighted density approximation (WDA) works well for inhomogeneous hard-sphere systems in comparison with exact results from molecular simulations, its combination with the mean-field approximation is mostly insufficient to capture the attractive potential quantitatively [242, 243].

The purpose of this work is to extend a perturbative density functional theory (PDFT) proposed by Tang and Wu [101] to SW fluids and tests its performance by comparing with molecular simulations. The PDFT combines a modified fundamental measure theory (MFMT) for the hard-sphere excluded-volume effects [85, 88] and the first-order mean spherical approximation (FMSA) for the bulk direct correlation functions [244]. The non-mean-field method has been successfully applied to a number of inhomogeneous systems including Lennard-Jones fluids [245], systems with multiple Yukawa potentials [246, 247], and Sutherland fluids [248]. While MFMT is directly applicable to systems with hard-core interactions, analytical expressions for the direct correlation function of uniform SW fluids were derived only recently by Tang [100] for the width of square-well attraction smaller than one particle diameter and by Hlushak et al. [104] for up to two particle diameters. These correlation functions have been proved numerically reliable in comparison with simulation results for bulk systems. However, no work has yet been reported to test the applicability of these direct correlation functions for inhomogeneous SW systems.

The remainder of this article is organized as follows. Section 2 describes the perturbative density theory (PDFT) and simulation details. Calibration of the theoretical method is presented in Section 3. Specifically, we will validate the proposed theory by extensive comparison with simulation results for the radial distribution functions of bulk SW fluids with long-range attractions, and with simulation results for the inhomogeneous density profiles of SW fluids near spherical cavities and in slit pores. In Section 4, we discuss the strength and pitfall of the PDFT and summarize the key conclusions.

7. 2 Theory and Simulation Details

In a SW fluid, the intermolecular interaction is represented by a pairwise additive potential that includes a hard-sphere repulsion and a fixed attractive energy of finite distance (i.e., "square well") right beyond the hard core. For one-component systems, the pair potential is given by

$$u(r)=\begin{cases}\infty & r<\sigma \\ -\varepsilon & \sigma \le r<\lambda \\ 0 & r\ge \lambda\end{cases}, \tag{7.1}$$

where r designates the center-to-center distance between two spherical particles, σ stands for the hard-core diameter, λ denotes the range of attraction, and $\varepsilon > 0$ represents an attractive energy or the well depth. For typical colloids, spherical micelles or globular proteins in an aqueous environment, the solvent-mediated van der Waals attraction is most significant within a range about 10% of the particle diameter (i.e., $\lambda \sim 1.1\sigma$) [214, 215]. However, the range of attraction can be much extended for systems with electrostatic or polymer-mediated interactions.

We use the classical density functional theory (DFT) to describe the equilibrium structure and thermodynamic properties of SW fluids [64, 77, 198]. While DFT provides an exact mathematical framework for describing the equilibrium properties of both uniform and inhomogeneous systems, its application requires formulation of the grand potential as a functional of the density profile. For systems containing spherical particles, the grand potential can be expressed in terms of intrinsic Helmholtz energy functional $F\left[\rho(\mathbf{r})\right]$ and one-body external potential $V_{ext}(\mathbf{r})$:

$$\Omega\left[\rho(\mathbf{r})\right] = F\left[\rho(\mathbf{r})\right] + \int [V_{ext}(\mathbf{r}) - \mu]\rho(\mathbf{r})\, d\mathbf{r}\,, \tag{7.2}$$

where $d\mathbf{r}$ denotes a differential volume, $\rho(\mathbf{r})$ stands for the local number density or the density profile, and μ is the chemical potential. In general, the intrinsic Helmholtz free energy can be further decomposed into that corresponding to an ideal-gas system with the same microscopic structure and an excess due to the intermolecular potential,

$$F\left[\rho(\mathbf{r})\right] = F^{id}\left[\rho(\mathbf{r})\right] + F^{ex}\left[\rho(\mathbf{r})\right]. \tag{7.3}$$

In Eq. (7.3), the ideal-gas term is known exactly

$$F^{id} = k_B T \int d\mathbf{r}\rho(\mathbf{r})\left[\ln \Lambda^3 \rho(\mathbf{r}) - 1\right], \tag{7.4}$$

where k_B denotes the Boltzmann constant, T is absolute temperature, and Λ is the thermal de Broglie wavelength. With an appropriate expression for excess Helmholtz energy $F^{ex}\left[\rho(\mathbf{r})\right]$, minimization of the grand potential yields the Euler-Lagrange equation

$$\rho(\mathbf{r}) = \frac{1}{\Lambda^3} \ln\left[\delta\beta F^{ex} / \delta\rho(\mathbf{r}) - \beta\mu\right]. \tag{7.5}$$

The numerical details for solving the Euler-Lagrange equation are given in previous publications (see, e.g., reference [101]). Once we have the density profile, all thermodynamic properties and correlation functions of the system can be subsequently derived from the analytical expression of the grand potential functional.

Whereas there is no *a prior* knowledge on the excess Helmholtz energy for most systems of practical interest, reasonable approximations can be developed by following a number of standard statistical-mechanical procedures [77]. For SW fluids, the

thermodynamic non-ideality due to short-range interactions arises mainly from the molecular packaging effect, and long-range interactions are closely related to the density fluctuations. Because of the different origins of thermodynamic non-ideality, separate strategies are typically used to deal with the short- and long-range contributions to the excess Helmholtz free energy.

In perturbative DFT, we adopt the fundamental measure theory of Rosenfeld [83] for hard-sphere repulsion and a perturbative density expansion of the Helmholtz energy for the SW attraction [101]. Specifically, we divide the total excess Helmholtz energy into contributions due to the hard-sphere repulsion and the square-well attraction:

$$F^{ex}\left[\rho(\mathbf{r})\right] = F_{hs}^{ex}\left[\rho(\mathbf{r})\right] + F_{att}^{ex}\left[\rho(\mathbf{r})\right], \tag{7.6}$$

where $F_{hs}^{ex}\left[\rho(\mathbf{r})\right]$ represents the excess Helmholtz energy of a hard-sphere reference system, and $F_{att}^{ex}\left[\rho(\mathbf{r})\right]$ is the contribution due to the perturbative attraction. As in applications of the DFT to Lennard-Jones and Yukawa systems [101, 244], the modified fundamental measure theory provides an accurate description of the excess Helmholtz free energy due to the hard-sphere repulsion [85, 88]

$$\begin{aligned}\beta F_{hs}^{ex} = \int & -n_0 \ln(1-n_3) + \frac{n_1 n_2 - \mathbf{n_{V1}}\cdot\mathbf{n_{V2}}}{1-n_3} \\ & + \frac{1}{36\pi}\left[n_3 \ln(1-n_3) + \frac{n_3^2}{(1-n_3)^2}\right]\frac{\left(n_2^3 - 3n_2\mathbf{n_{V2}}\cdot\mathbf{n_{V2}}\right)}{n_3^3} d\mathbf{r}\end{aligned}, \tag{7.7}$$

where $\beta = 1/(k_B T)$. The detailed expressions for the scalar and vector weighted densities, n_α, $\alpha = 0,1,2,3,\mathbf{V1},\mathbf{V2}$ can be retrieved from previous publications [85, 88]. On the other hand, the excess Helmholtz free energy due to the attraction is formulated by a

quadratic density expansion with respect to that of a bulk system with the same chemical potential but uniform density ρ_b:

$$\begin{aligned}\beta F_{att}^{ex} &= \beta F_{att}^{ex}\left(\rho_b\right) + \beta\mu_b^{att}\int d\mathbf{r}\left[\rho(\mathbf{r})-\rho_b\right] \\ &\quad -\frac{1}{2}\int\int d\mathbf{r}d\mathbf{r}' C_b^{att}\left(|\mathbf{r}-\mathbf{r}'|\right)\left[\rho(\mathbf{r})-\rho_b\right]\left[\rho(\mathbf{r}')-\rho_b\right]\end{aligned}, \tag{7.8}$$

where $F_{att}^{ex}\left(\rho_b\right)$ and μ_b^{att} are the attractive parts of the bulk excess Helmholtz energy and the bulk chemical potential, respectively, and $C_b^{att}(r)$ stands for the attractive part of the bulk direct correlation function (DCF). While in principle the DCF can be calculated from Fourier transform of the radial distribution function obtained from molecular simulation, here we use analytical expressions of $C_b^{att}(r)$ by Tang [100] for $\sigma < \lambda \le 2\sigma$ and by Hlushak et al. [104] for $2\sigma < \lambda \le 3\sigma$. For comparison, we also consider the mean-field representation of the attractive Helmholtz energy

$$\beta F_{att}^{MF} = \frac{1}{2}\int\int d\mathbf{r}d\mathbf{r}' u_{att}\left(|\mathbf{r}-\mathbf{r}'|\right)\rho(\mathbf{r})\rho(\mathbf{r}'), \tag{7.9}$$

where the attractive potential is $u_{att}(r) = -\varepsilon$ for $r < \lambda$. Similar to the optimized random phase approximation (ORPA), the mean-field method ignores all long-range correlations. To calibrate the above Helmholtz-energy equations (Eqs. (7.8) and (7.9)), we have compared the DFT predictions with results from Monte Carlo (MC) simulation for the microscopic structures of bulk and inhomogeneous SW fluids. MC simulation for bulk fluids was carried out using the canonical ensemble (*NVT*) and that for inhomogeneous systems using the grand canonical ensemble (μVT). In both cases, we used a cubic simulation box with periodic boundary conditions. Typically the simulation box contains

about 750 particles for bulk systems, around 5000 particles for SW fluids near a cavity, and around 600 particles in slit pores. The MC moves were implemented using the Metropolis algorithms with 0.1 million cycles per particle for equilibrium and another 0.1 million cycles per particle for sampling [166].

7. 3 Results and Discussions

In the following we examine the numerical performance of the PDFT by direct comparison with MC simulation data for the radial distribution functions of bulk fluids and the density profiles of SW fluids near hard spheres (i.e., cavities) or in slit pores. Representative system parameters and thermodynamic conditions are selected to ensure a systematic test of the analytical methods. To distinguish the two versions of DFT discussed above, we designate combination of MFMT for hard-sphere repulsion with the FMSA for square-well attraction as "MFMT+FMSA" and that of MFMT with the mean-field approximation as "MFMT+MFT".

7. 3. 1 Radial Distribution Functions of Bulk SW Fluids ($\lambda > 2\sigma$)

The radial distribution function (RDF) of a bulk SW fluid can be calculated from the density profile around a "test particle" fixed at the origin such that the interaction between the test particle and any other particle in the system is the same as the pair potential, i.e., $V_{ext}(r) = u(r)$. In this case, the density profile in the pseudo-inhomogeneous system is directly related to RDF, i.e.,

$$g(r) = \frac{\rho(r)}{\rho_b}. \tag{7.10}$$

The test-particle method was used before to predict the RDFs of bulk SW fluids with the range of attraction less than two particle diameters [249]. Figure 7-1, 7-2, and 7-3 show further comparisons of the theoretical results with simulation data for systems with long-ranged attractions. We first consider the RDF of a density fluid ($\rho_b^* \equiv \rho_b \sigma^3 = 0.75$) at a reduced temperature $T^* \equiv k_B T / \varepsilon = 5.0$. The system can be a stable liquid or a supercritical fluid depending on the range of the SW attraction. Figure 7-1 shows, as for systems with short-range attractions, the predictions from MFMT+FMSA agree excellently with the simulation results. As expected, the RDF exhibits discontinuity at the boundaries of the SW potential. Unlike that for systems with short-range attractions ($\lambda < 2\sigma$), hard-sphere packaging leads to a second peak in the RDF around $r = 2\sigma$ when the range of attraction exceeds two particle diameter. Because of the discontinuity in the SW potential, the second peak may be truncated at the boundary of the attraction (e.g. $\lambda = 2.2\sigma$). Because the RDF of a dense fluid is mainly determined by hard-sphere repulsion [249], the results from the MFMT+MFT (not shown) are virtually identical to those from the MFMT+FMSA.

Figure 7-2 shows a similar comparison between the theoretical results and simulation data for SW fluids close the vapor side of the vapor-liquid coexistence. Here we consider RDF at different temperatures and ranges of attraction with the density fixed at $\rho_b^* \equiv \rho_b \sigma^3 = 0.01$. In all cases, the predictions from the MFMT+FMSA agree well with the simulation results. Unlike that for a dense fluid, the RDF at low density is mainly determined by the pair interaction potential. As expected, the RDF of the vapor phase is close to a constant within the range of the SW interaction and it approaches to unity.

Figure 7-3 shows further comparisons for the SW fluid near the liquid-side of the coexistence curve at different combinations of temperature and range of attraction. In all cases, the agreement between MFMT+FMSA and MC simulation is excellent.

7. 3. 2 Distribution of SW Fluids near Spherical Cavities

Understanding solvent distribution around a spherical cavity provides useful information for studying solvation thermodynamics, wetting/drying transitions, and the curvature effects of interfacial phenomena [250]. Because of its broad relevance, the model system is used here for calibrating the numerical performance of the PDFT for inhomogeneous SW fluids. For a SW fluid near a hard-sphere or spherical cavity, the one-body external potential is given by

$$V_{ext}(r) = \begin{cases} \infty, & r < R \\ 0, & r \geq R \end{cases}, \tag{7.11}$$

where R denotes the cavity radius, i.e., the maximum distance that prohibits the accessibility of the centers of SW particles.

We first consider the distributions of SW fluids near a small cavity ($R = \sigma$) at different temperatures, different bulk densities, and different ranges of attraction. Figure 7-4 compares the density profiles predicted by the PDFT and by MC simulation for a SW fluid with $\lambda = 1.5\sigma$ at reduced temperature $T^* = 1.0$ and several bulk densities. For comparison, this figure shows the PDFT results both from MFMT+FMSA and from MFMT+MFT. As explained before, the simulation was performed in μVT ensemble with the cavity fixed at the origin. The simulation box is sufficiently large such that far from the spherical cavity the solvent density reduces to that of the bulk fluid. Figure 7-4

shows that, near a small cavity, both the MFMT+FMSA and the MFMT+MFT predictions agree well with the simulation data. Here the good performance of the MFMT+MFT is mainly because, as the RDF of a dense liquid, the inhomogeneous structure near a small cavity is primarily determined by the hard-sphere repulsions. A closer comparison between the MFMT+FMSA and the simulation results reveals some small discrepancy as the bulk density decreases ($\rho^* = 0.677$).This discrepancy arises primarily from the quadratic approximation in the density expansion (Eq. (7.8)), which becomes less reliable as the fluid is significantly depleted from the surface. While MFMT+FMSA slightly underestimates the contact value at low densities, opposite predictions are given by MFMT+MFT. At low fluid densities, the discrepancy of MFMT+MFT from the simulation is probably due to the fact that the mean-field theory gives a phase diagram quite different from that from MC simulation (The coexistence density of liquid phase from MC is $\rho_l^* = 0.647$ [251], while MFT gives $\rho_l^* = 0.602$). At high packing densities, the numerical performance of MFMT+FMSA is excellent while MFMT+MFT still underestimates the contact density.

Figure 7-5 presents the density profiles of the same SW fluid near the small cavity ($R = \sigma$) but at a higher temperature ($T^* = 1.2$). As the temperature approaches to the vapor-liquid critical point, discrepancy between the mean-field theory and simulation results become more significant. In that case, we expect that MFMT+FMSA will be much more accurate than MFMT+MFT. As shown in Fig. 7-5, the MFMT+FMSA predictions agree well with MC simulation at all conditions. However, the performance of the MFMT+MFT noticeably deteriorates as the temperature increases approaching to

vapor-liquid critical point. Besides, the discrepancy between MFMT+MFT and MC simulation magnifies as the particle density decreases.

To test the effect of the attraction range, we show in Figure 7-6 the density distributions of SW fluids with a longer-well width ($\lambda = 1.7\sigma$) near the spherical cavity of radius $R = \sigma$. Here we did not include results from MFMT+MFT predictions because, according to the mean-field theory, the system would be unstable in the bulk at certain densities. While the inter-particle attraction enhances with the range of attraction, the numerical performance of the MFMT+FMSA remains very robust.

We now consider the performance of the PDFT for SW fluids near a larger hard sphere or cavity. Figure 7-7 shows the results for the same SW fluids as depicted in Fig. 7-4 but near a spherical cavity of larger radius ($R = 5\sigma$).Unlike that near the small cavity, the particles are depleted from the hard surface as the bulk density decreases. Because of the quadratic expansion of the excess Helmholtz energy for the SW attraction, MFMT+FMSA overestimates the simulation results at low bulk density. Nevertheless, it faithfully captures the transition from depletion to accumulation as the bulk density increases. In all cases the performance of MFMT+FMSA is significantly superior to that of MFMT+MFT.

Figure 7-8 shows the density profiles of the SW fluid near the same spherical cavity but at a higher temperature ($T^* = 1.2$), slightly below the vapor-liquid critical point of the bulk fluid ($T^*_{c,FMSA} = 1.31$). Despite that MFMT+FMSA is not able to capture the dewetting transition near a macroscopic hard surface, it yields a density profile in reasonably agreement with the simulation result. Interestingly, the numerical

performance of MFMT+MFT remains inferior to that of MFMT+FMSA even though in principle the mean-field theory is able to describe the dewetting transition. Figure 7-9 shows the density profiles of a SW fluid with a longer interaction range ($\lambda = 1.7\sigma$) near the same spherical cavity. As mentioned above, the MFMT+MFT results are not included because, according to the mean-field theory, the systems would be unstable at some bulk conditions. While in general the numerical performance of the MFMT+FMSA is insensitive to the range of attraction, near a slightly dewetting surface it overestimates the local density for systems with short-range attraction (Fig. 7-8) but the trend is opposite for systems with a longer-ranged attraction (Fig. 7-9).

7. 3. 3 Density Profiles of SW Fluids in Slit Pores

We finally consider the numerical performance of the PDFT for SW fluids near extended surfaces. Because the simulation is not directly applicable to systems with a single wall, here the comparison is focused on the density profiles of SW fluids in slit pores of different thicknesses and surface energies. For convenience, we assume that the two confining walls are identical and that the surface-fluid interaction can also be represented by the square-well potential, i.e.,

$$V_{ext}(z) = \begin{cases} \infty & \sigma/2 > z \quad \text{or} \quad z > H - \sigma/2 \\ -\varepsilon_{AW} & \lambda_W \geq z \geq \sigma/2 \ \text{or} \ H - \sigma/2 \geq z \geq H - \lambda_W \\ 0 & H - \sigma > z > \lambda_W \end{cases}, \tag{7.12}$$

where H stands for the pore width, ε_{AW} and λ_W designate the strength and the range of the surface energy. For SW fluids confined between hard walls (i.e., $\varepsilon_{AW} = 0$ in Eq. (7.12)), such system has been thoroughly studied by Henderson and van Swol [252] and

their simulation results are used directly for calibration of the PDFT. When the confining walls are attractive, we carried out some additional MC simulations using the *NVT* ensemble. In our MC simulation, the slit pore is represented by a rectangular prism with periodic boundary conditions in the planar directions. The cross section area of the rectangular prism is fixed at $A = 100\sigma^2$ and the height is $H = 10\sigma$. MC simulations were performed for SW fluids at different temperatures and different average densities (or different numbers of particles) inside the slit pore. Figure 7-10 presents the density profiles of SW fluids of different densities near a hard wall. Here the simulation results are from Ref. [252]; the MC simulation was carried out with the averaged density inside the slit pore fixed at $\rho_{ave}^{*} = 0.568$, 0.672 and 0.746, respectively. In all cases, the range of attraction between SW particles is fixed at $\lambda = 1.5\sigma$, and the reduced temperature is $T^{*} = 1.0$. In the PDFT calculations, the density profiles were calculated from the average density instead of the bulk chemical potential:

$$\rho_{av} = \frac{1}{H}\int_0^H \rho(z)\,dz\,. \tag{7.13}$$

Figure 7-10 shows that, similar to what we have discussed above, the MFMT+FMSA predictions are much more accurate than those from MFMT+MFT at all conditions. When $\rho_{ave}^{*} = 0.568$, the fluid density in the middle of the slit pore is very close to that of the saturated liquid in the bulk ($\rho_{ave}^{*} = 0.669$). The excellent performance of MFMT+FMSA near dewetting transition is rather unexpected.

Figures 7-11, 7-12, and 7-13 present the density distributions of SW fluids inside an attractive slit pore. In all cases, the reduced surface energy is fixed at $\beta\varepsilon_{AW} = 1.5$ and

the range of the surface attraction is $\lambda_w = \sigma$. The results from MFMT+FMSA calculation are compared systematically with MC simulation as well as those from MFMT+MFT by varying the system temperature, the range of attraction between SW particles, and the average density inside the slit pore. While at large interaction range some noticeable discrepancy exists near the surface, overall the agreement between MFMT+FMSA and MC simulation is rather satisfactory, in particular, for systems with short-range attractions. MFMT+FMSA faithfully captured the curve-up shape in density profiles near the attractive surface, which is missed by MFMT+MFT when the interaction range is relatively short (Fig. 7-11 and 7-12). For SW fluids with short-range interactions, MFMT+MFT overestimates the contact densities at low packing densities but the trend is opposite at high packing densities. Similar to that shown in Figs. 7-6 and 7-9, MFMT+MFT is not included for comparison because the mean-field approximation predicts that the system is unstable in this region. In contrast to Figs. 7-11 and 7-12, Figure 7-13 reveals that inside the attractive well from the surface, MFMT+FMSA becomes less accurate as the interaction range increases.

7. 4 Conclusions

In this work, we have examined the numerical performance of a perturbative density functional theory for quantitative representation of the equilibrium structure of square-well fluids in the bulk and at inhomogeneous conditions. The PDFT incorporates the modified fundamental measure theory (MFMT) to account for the excess Helmholtz energy functional due to the hard-sphere repulsion and the first-order mean-spherical approximation (FMSA) for perturbative representation of the square-well attraction. For

bulk fluids, the thermodynamic properties predicted by the PDFT are fully consistent with those from the FMSA, which have been calibrated with simulation results in previous publications [100, 236, 249]. The focus of the present work is calibration of the PDFT with MC simulation data for the radial distribution functions of bulk SW fluids, the density profiles of SW fluids near spherical cavities, and the density profiles of SW fluids in slit pores. The PDFT predictions are also compared with results from combination of the MFMT with a mean-field representation of the attractive energy (MFT).

As reported in an earlier work for SW fluids with relatively short-range attractions [249], the PDFT predicts the radial distribution functions of bulk SW fluids with long-range attractions in excellent agreement with MC data. To test the PDFT performance for SW fluids at inhomogeneous conditions, we consider two representative systems, i.e., SW fluids near individual hard spheres (i.e., cavities) or in slit pores. We find that for both bulk and inhomogeneous systems the numerical performance of the PDFT is in excellent agreement with simulation data for several different temperatures and interaction ranges. By contrast, the mean-field predictions are much less reliable, in particular at conditions where the system temperature is close to the critical point. Because the thermodynamic properties of an equilibrium system are fully determined by the one-body density profile or equivalently the microscopic structure, the good agreement between theory and MC simulation results for the structural properties ensures that the theory will also be reliable for thermodynamic properties. Indeed, the DFT

reduces to an equation of state for bulk systems that yields an accurate phase diagram in comparison with simulation data [100, 236, 244].

While a quadratic density expansion for the attractive part of the Helmholtz energy functional is probably insufficient to capture long-range density correlations as occurred in wetting/drying transitions, the local density profiles predicted by the PDFT are all in reasonable agreement with simulation results even very close to the saturation point. Near wetting/drying transitions, the caveat may be removed by an alternative formulation of the intrinsic Helmholtz energy functional that also utilizes MFMT and FMSA:

$$\begin{aligned} F^{ex}\left[\rho(\mathbf{r})\right] &= F^{MFMT}\left[\rho(\mathbf{r})\right] + \int d\mathbf{r} f_A^{FMSA}\left[\rho(\mathbf{r})\right] \\ &\quad + \frac{k_B T}{4}\iint d\mathbf{r}_1 d\mathbf{r}_2 \left[\rho(\mathbf{r}_1) - \rho(\mathbf{r}_2)\right]^2 c_A^{FMSA}\left(\bar{\rho}, |\mathbf{r}_1 - \mathbf{r}_2|\right), \end{aligned} \tag{7.14}$$

where f_A^{FMSA} represents the attractive part of the Helmholtz energy density for a bulk system at the local density, and $c_A^{FMSA}\left(\bar{\rho}, |\mathbf{r}_1 - \mathbf{r}_2|\right)$ is the attractive part of the bulk direct correlation function at average local density $\bar{\rho} = \left[\rho(\mathbf{r}_1) + \rho(\mathbf{r}_2)\right]/2$. A similar formulism was used before for predicting wetting transition near attractive surfaces [253].

Figure 7-1 (a) The radial distribution function of a bulk SW fluid with range of attraction $\lambda = 2.2\sigma$ at reduced temperature $T^* = k_B T / \varepsilon = 5.0$ and reduced bulk density $\rho_b^* = \rho_b \sigma^3 = 0.75$. The solid line is from MFMT+FMSA and the symbols denote *NVT* MC simulation data. (b) The same as (a) but for $\lambda = 2.4\sigma$. (c) The same as (a) but for $\lambda = 2.6\sigma$. (d) The same as (a) but for $\lambda = 2.8\sigma$.

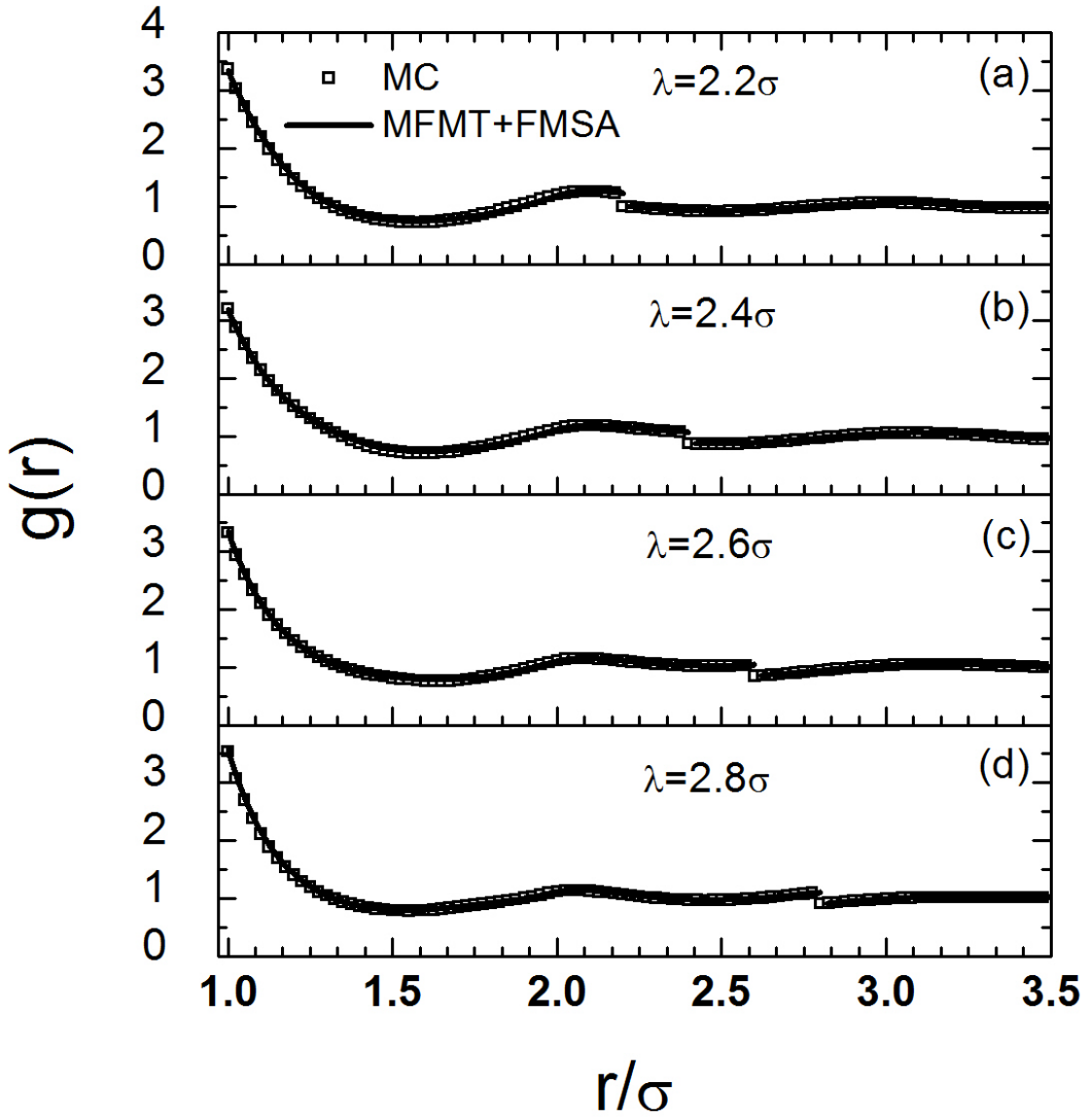

Figure 7-2 (a) The radial distribution function of a bulk SW fluid with range of attraction $\lambda = 2.3\sigma$ at reduced temperature $T^* = k_B T / \varepsilon = 3.1$ and reduced bulk density $\rho_b^* = \rho_b \sigma^3 = 0.01$. The solid line is from MFMT+FMSA and the symbols denote data from *NVT* MC simulation. (b) The same as (a) but for $\lambda = 2.5\sigma$, $T^* = 3.9$. (c) The same as (a) but for $\lambda = 2.7\sigma$, $T^* = 4.9$. (d) The same as (a) but for $\lambda = 3.0\sigma$, $T^* = 6.7$.

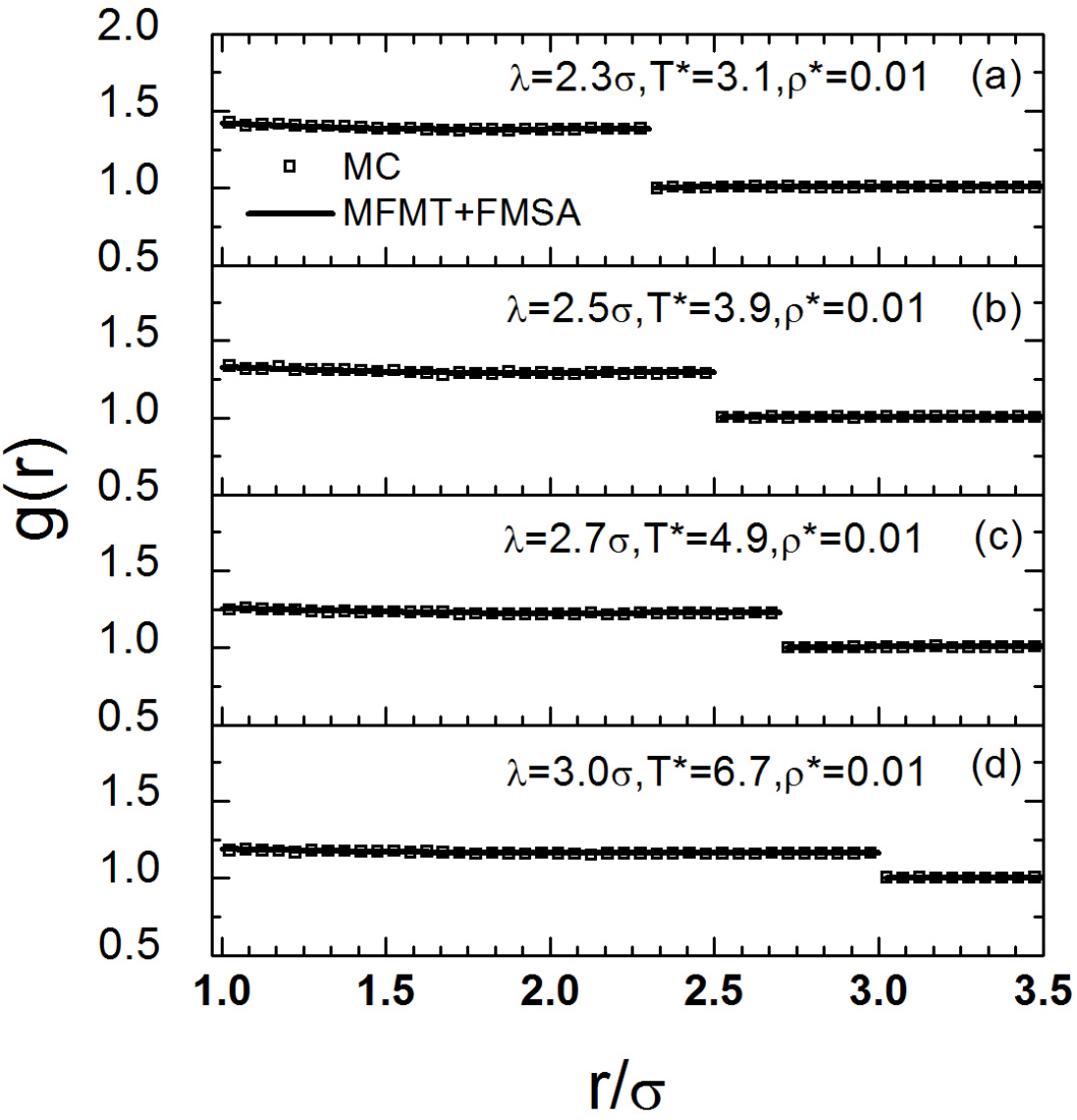

Figure 7-3 (a) The same as Fig. 7-2(a) but at reduced bulk density $\rho_b^* = 0.77$. (b) The same as Fig. 7-2(b) but at reduced bulk density $\rho_b^* = 0.72$. (c) The same as Fig. 7-2(c) but at reduced bulk density $\rho_b^* = 0.7$. (d) The same as Fig. 7-2(d) but at reduced bulk density $\rho_b^* = 0.72$.

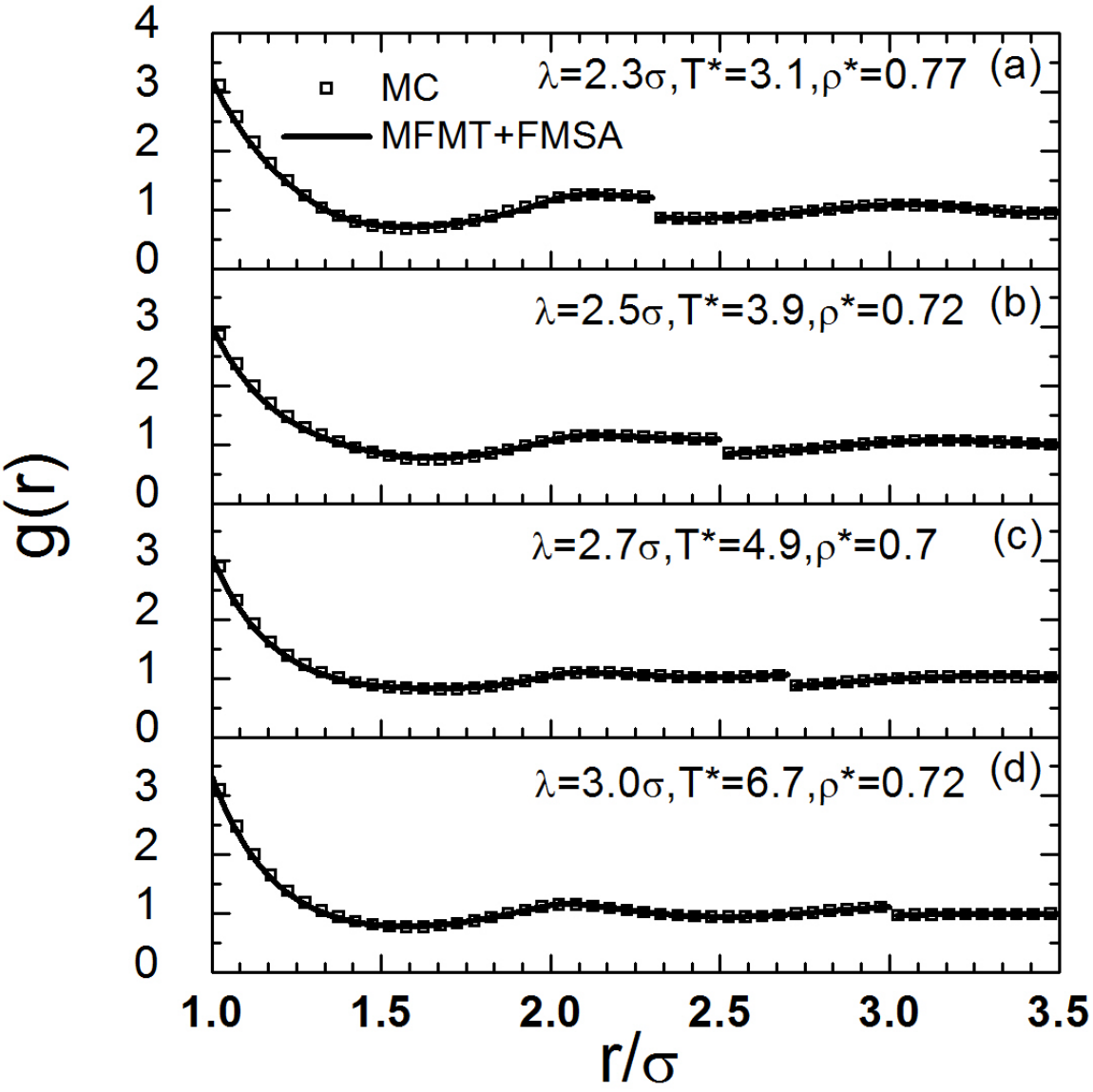

Figure 7-4 (a) The density distribution of a SW fluid around a hard cavity of radius $R = \sigma$. The range of attraction is $\lambda = 1.5\sigma$, and the reduced temperature and density are $T^* = 1.0$ and $\rho_b^* = 0.677$, respectively. The solid line represents prediction of MFMT+FMSA, the dashed line is from MFMT+MFT, and symbols are from μVT MC simulation. (b) The same as (a) but $\rho_b^* = 0.685$. (c) The same as (a) but $\rho_b^* = 0.706$. (d) The same as (a) but $\rho_b^* = 0.733$. (e) The same as (a) but $\rho_b^* = 0.775$.

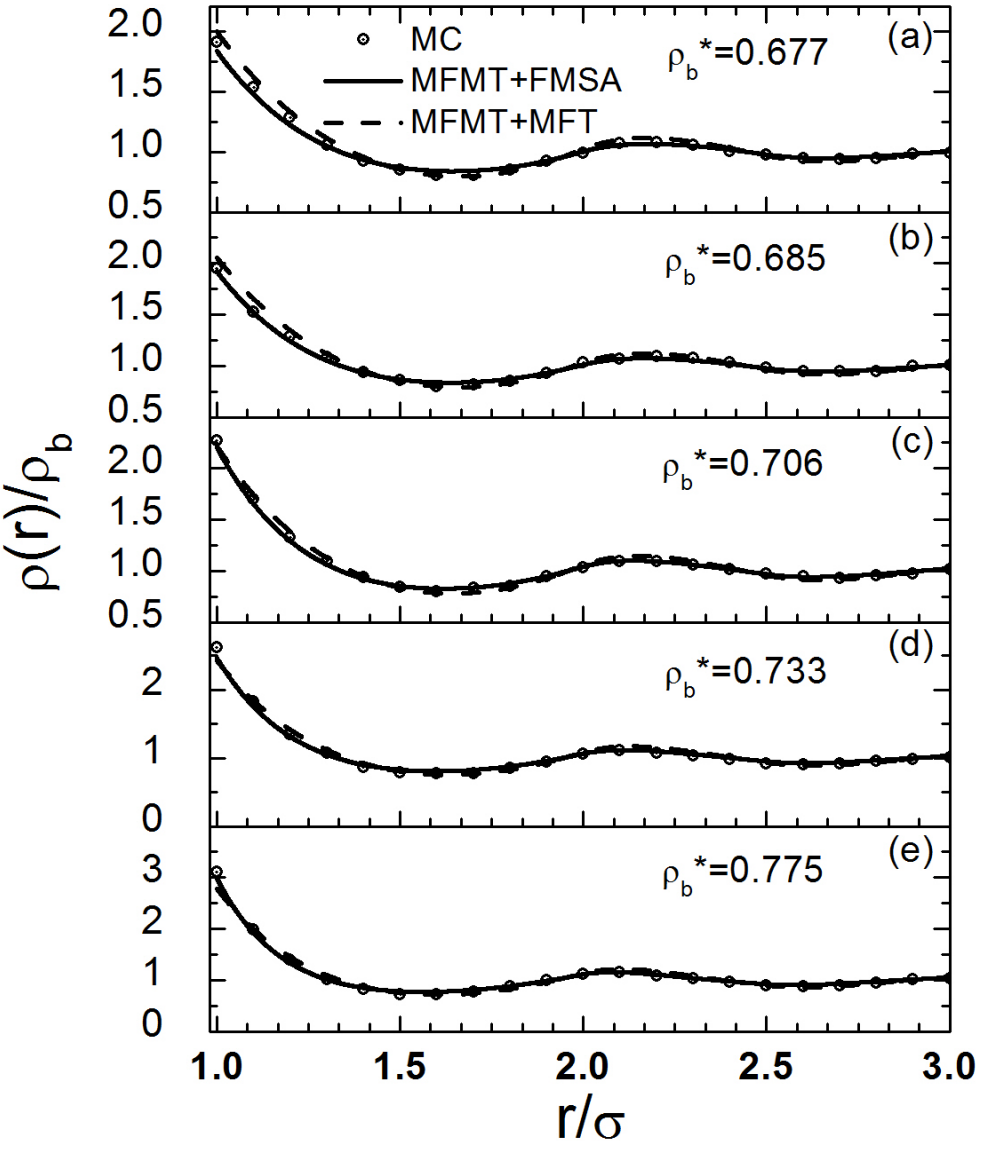

Figure 7-5 (a) The density distribution of a SW fluid around a hard cavity of radius $R = \sigma$. The range of attraction is $\lambda = 1.5\sigma$, and the reduced temperature and density are $T^* = 1.2$ and $\rho_b^* = 0.586$, respectively. The solid line represents prediction of MFMT+FMSA, the dashed line is from MFMT+MFT, and symbols are from μVT MC simulation. (b) The same as (a) but $\rho_b^* = 0.602$. (c) The same as (a) but $\rho_b^* = 0.638$. (d) The same as (a) but $\rho_b^* = 0.679$. (e) The same as (a) but $\rho_b^* = 0.735$.

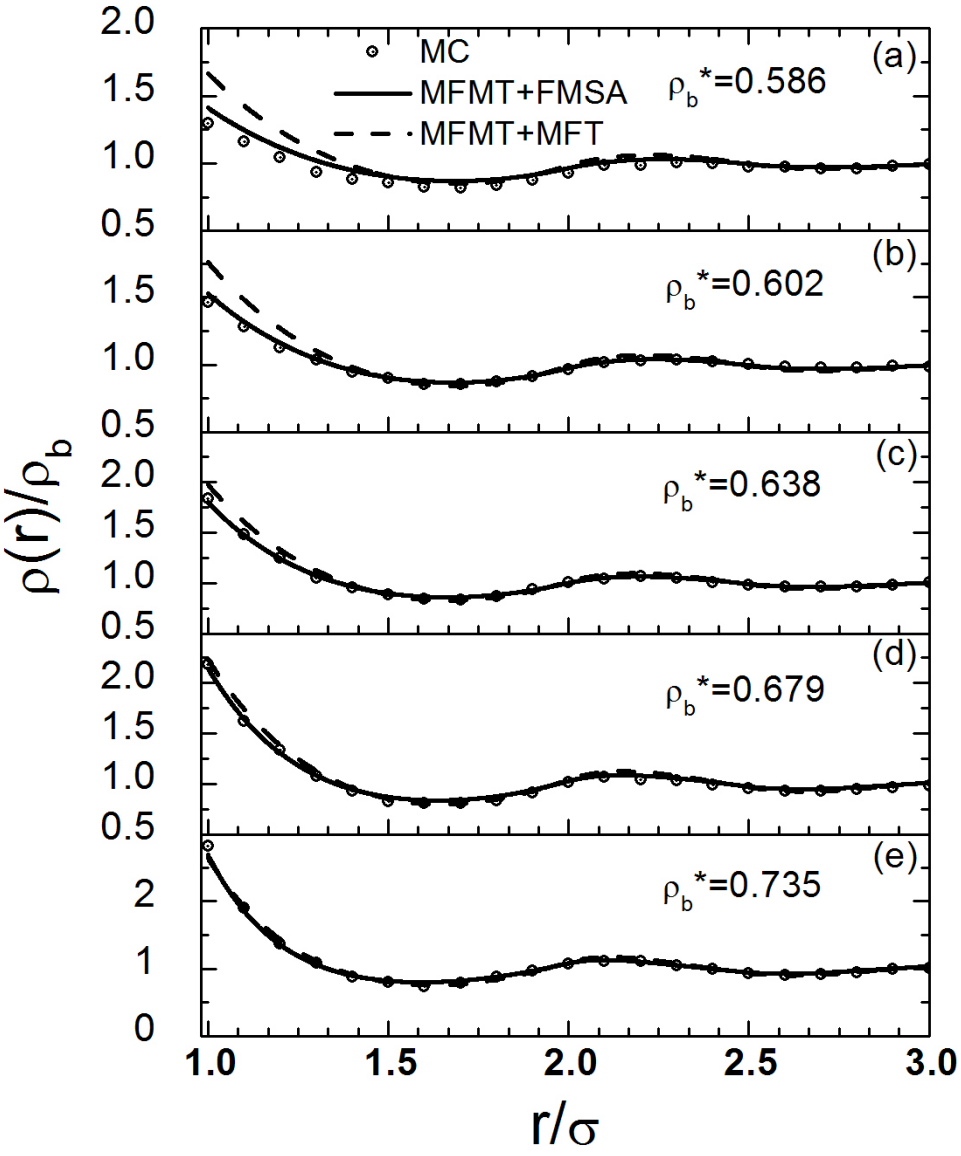

Figure 7-6 (a) The density distribution of a SW fluid around a cavity of radius $R=\sigma$. The range of attraction is $\lambda=1.7\sigma$, and the reduced temperature and density are $T^*=1.0$ and $\rho_b^*=0.711$, respectively. The solid line represents prediction of MFMT+FMSA and symbols are from μVT MC simulation. (b) The same as (a) but $\rho_b^*=0.716$. (c) The same as (a) but $\rho_b^*=0.731$. (d) The same as (a) but $\rho_b^*=0.755$. (e) The same as (a) but $\rho_b^*=0.794$.

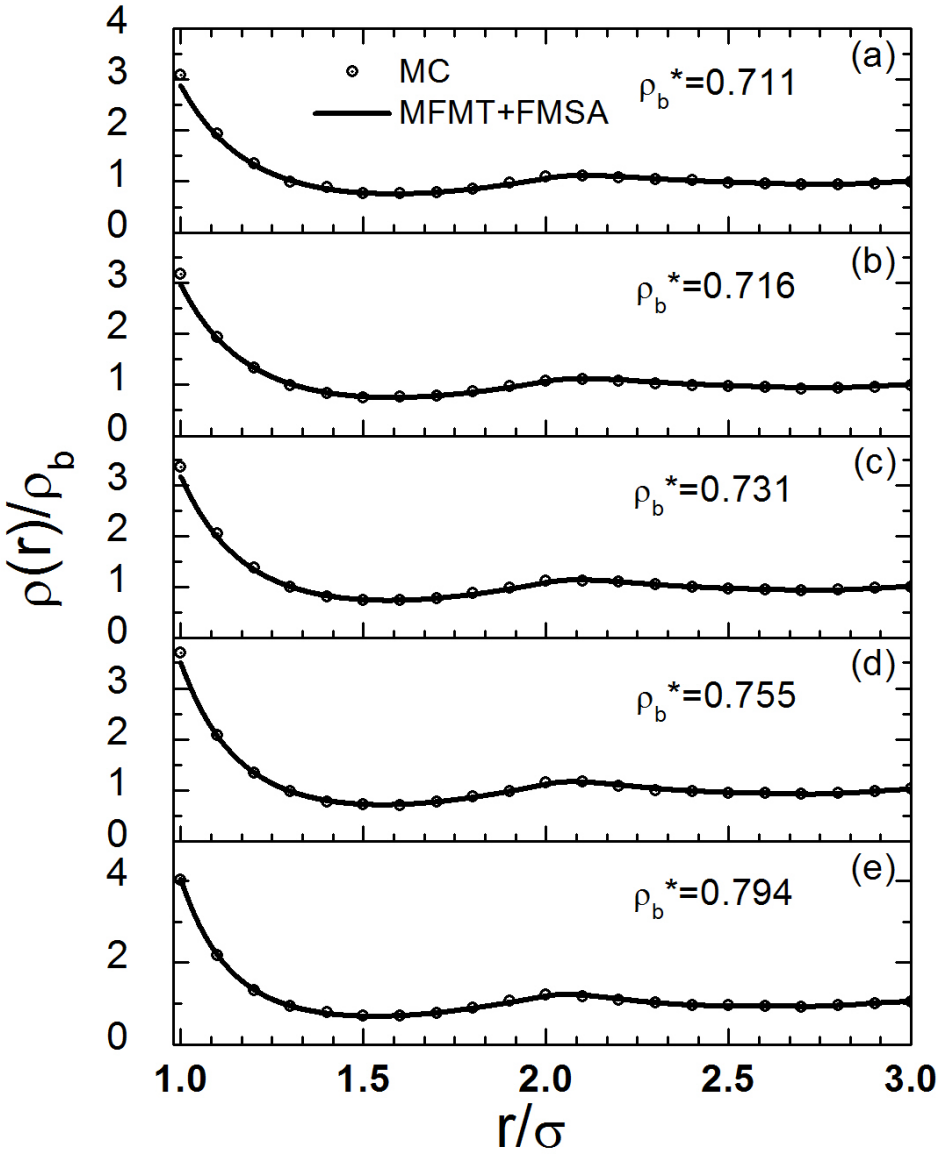

Figure 7-7 The same as Figure 7-4 but $R = 5\sigma$.

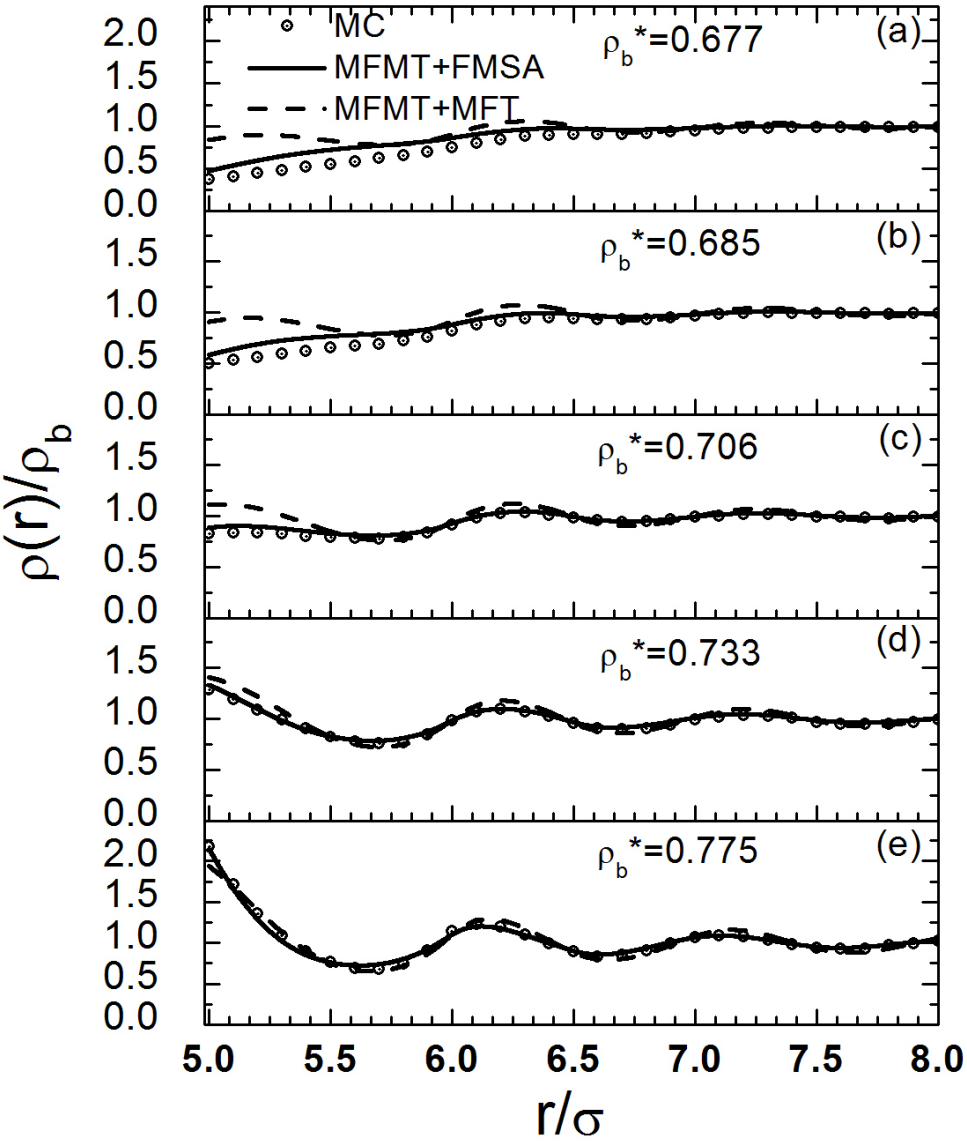

Figure 7-8 The same as Figure 7-5 but $R = 5\sigma$.

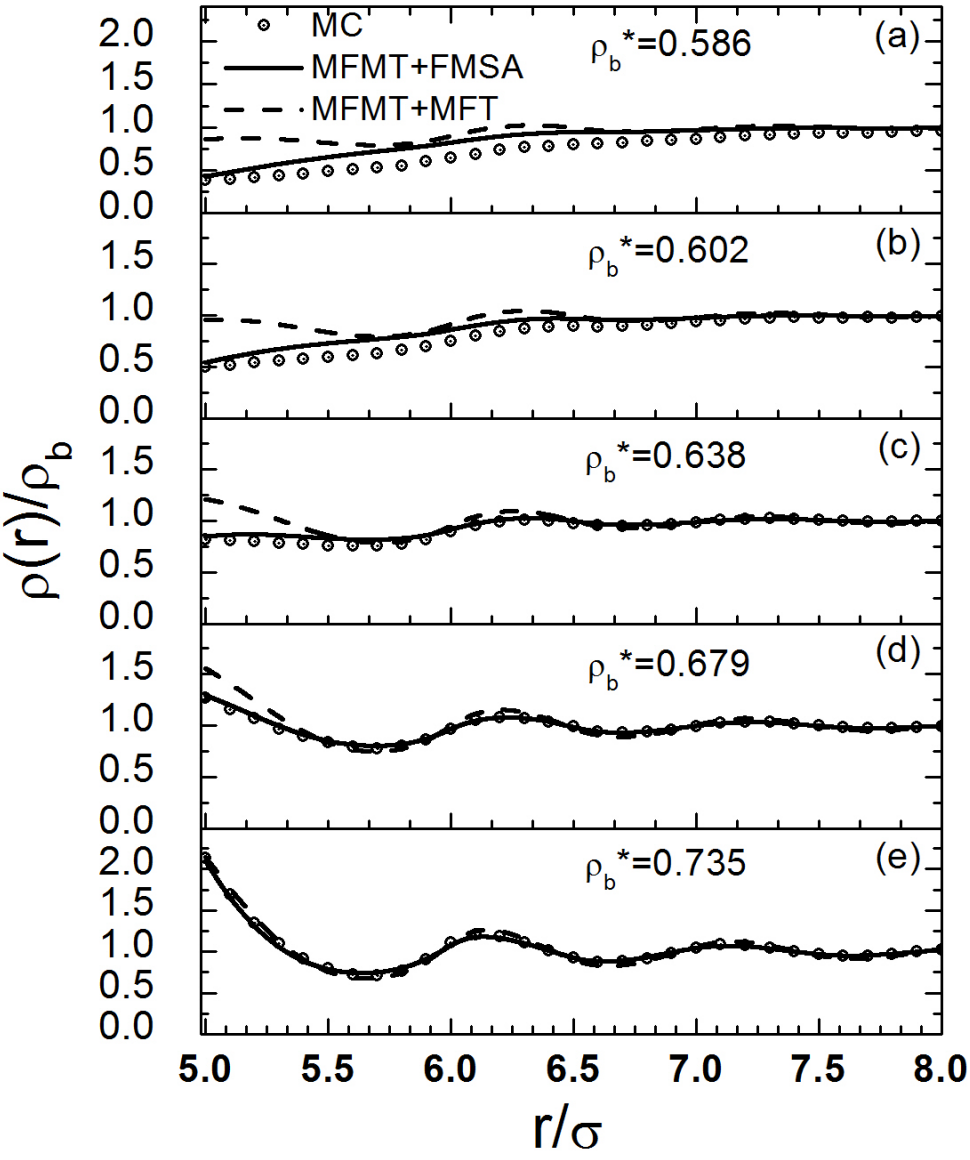

Figure 7-9 The same as Figure 7-6 but $R = 5\sigma$.

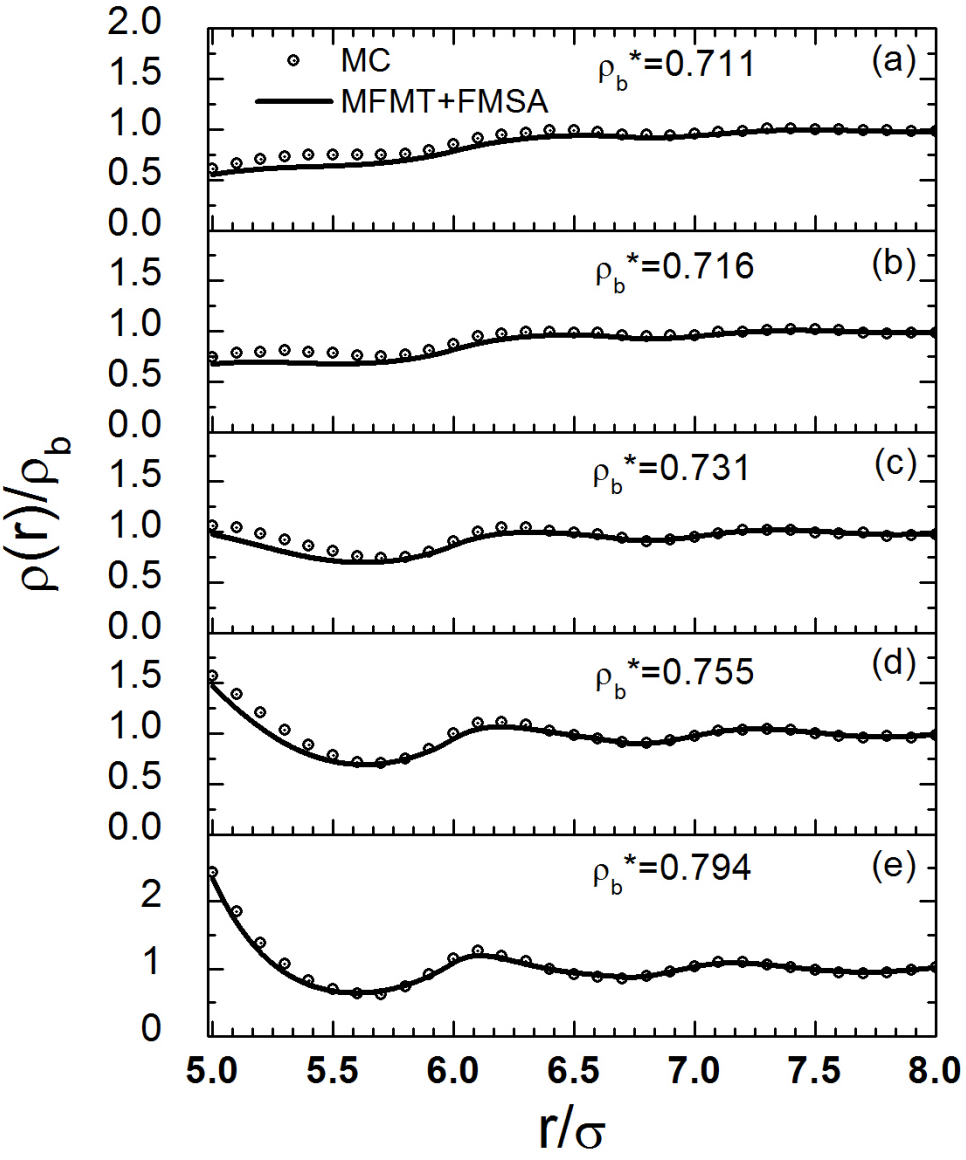

Figure 7-10 (a) The density profiles of a SW fluid near a hard wall. Here the range of attraction is $\lambda = 1.5\sigma$, the reduced temperature is $T^* = 1.0$. The surface area and the height of the simulation box are $A = 31.22\sigma^2$ and $H = 21.18\sigma$, respectively. The solid line represents prediction of MFMT+FMSA, the dashed line is from MFMT+MFT, and the symbols are MC simulation data [253]. (b) The same as (a) but the simulation condition was changed to surface area $A = 27.82\sigma^2$ and height $H = 11.55\sigma$. (c) The same to (a) but for $A = 25.89\sigma^2$ and $H = 11.18\sigma$.

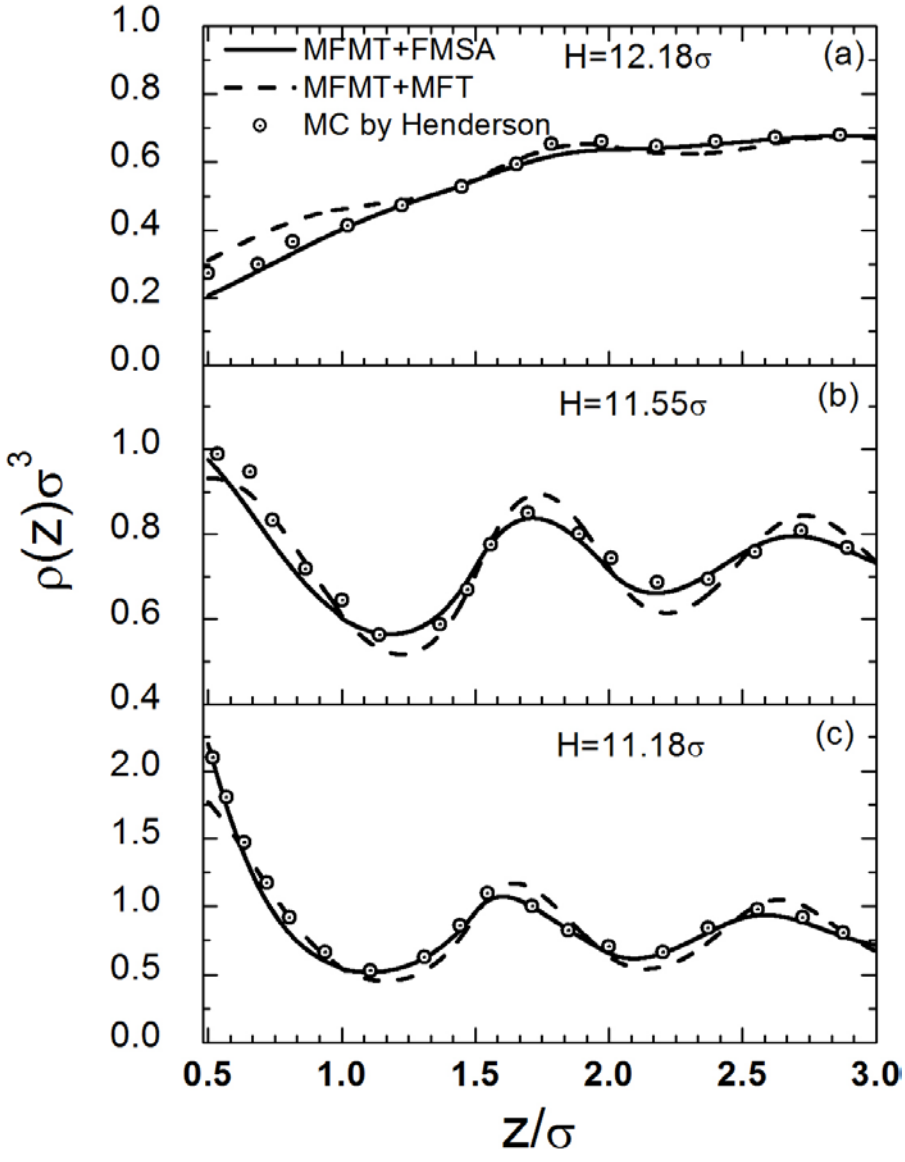

Figure 7-11 (a) The density distribution of a SW fluid near an attractive wall. Here the range of attraction is $\lambda = 1.5\sigma$, the reduced temperature is $T^* = 1.0$. The solid line represents prediction of MFMT+FMSA, the dashed line denotes MFMT+MFT result, and the symbols are MC simulation data. The MC simulation was carried out within a rectangular prism with cross section area $A = 100\sigma^2$ and height $H = 10\sigma$ containing $N = 620$ SW particles. (b) The same as (a) but for particle number $N = 654$. (c) The same as (a) but for particle number $N = 730$.

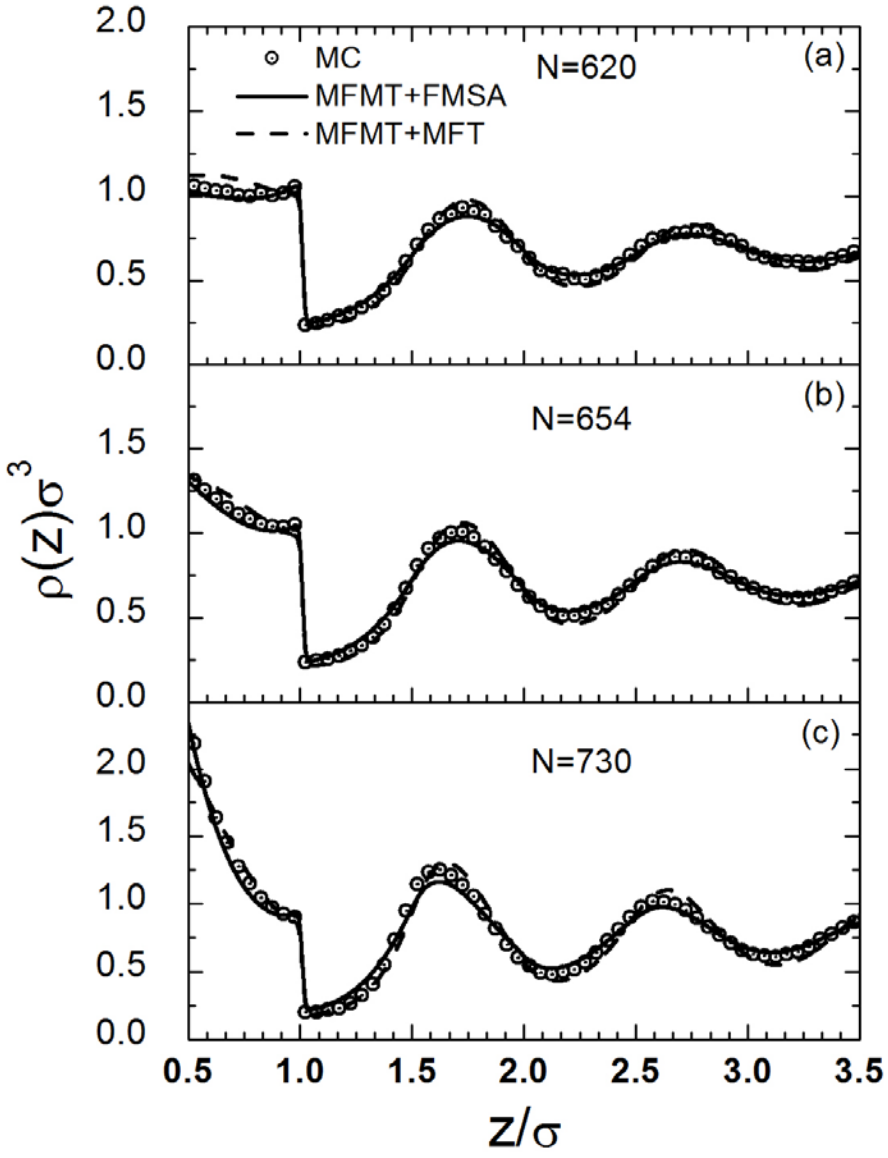

Figure 7-12 The same as Fig. 7-11 but at higher temperatures. (a) $T^* = 1.2$, $N = 545$. (b) The same to (a) but $N = 600$. (c) The same as (a) but $N = 700$.

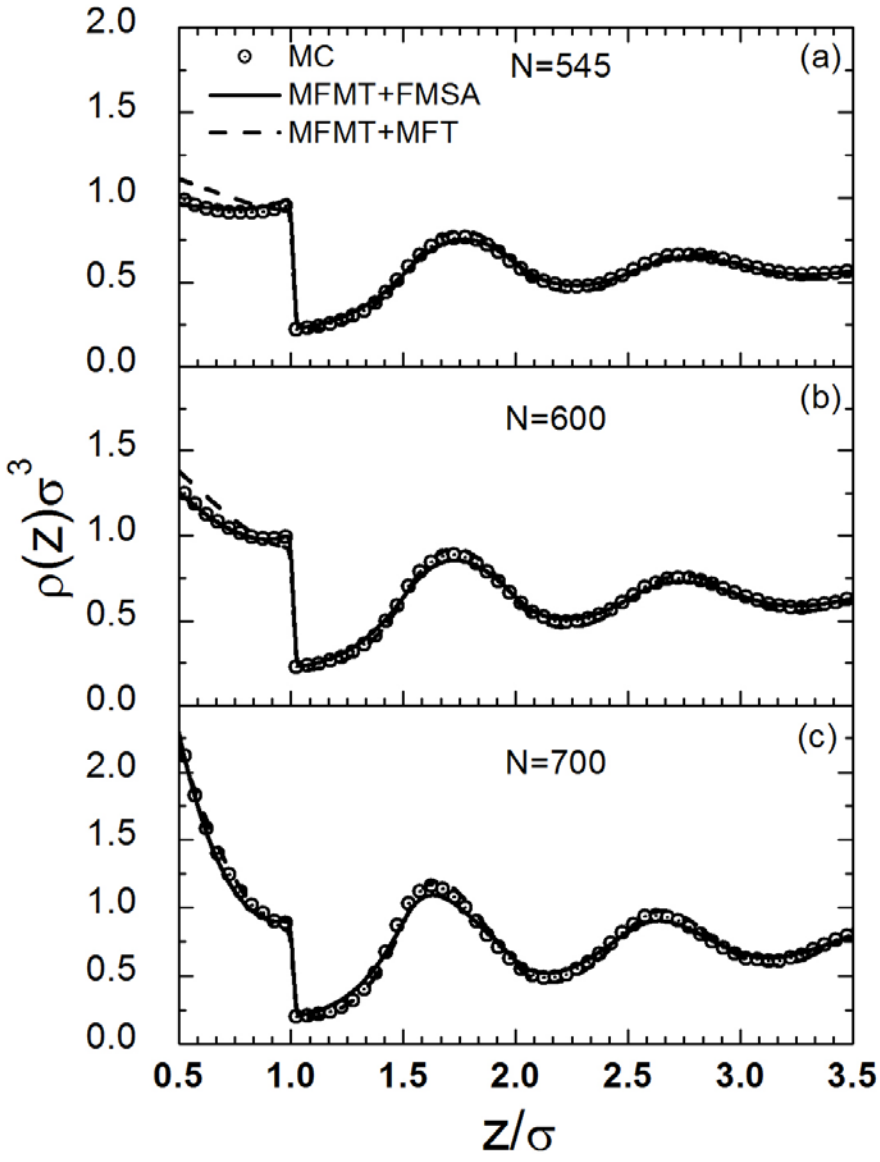

Figure 7-13 (a) The density distribution of a SW fluid near an attractive wall. Here the range of attraction is $\lambda = 1.7\sigma$, the reduced temperature is $T^* = 1.0$. The solid line represents prediction of MFMT+FMSA, and the symbols are MC simulation data. The MC simulation was carried out within a rectangular prism with cross section area $A = 100\sigma^2$ and height $H = 10\sigma$ containing $N = 615$ SW particles. (b) The same as (a) but for particle number $N = 648$. (c) The same as (a) but for particle number $N = 730$.

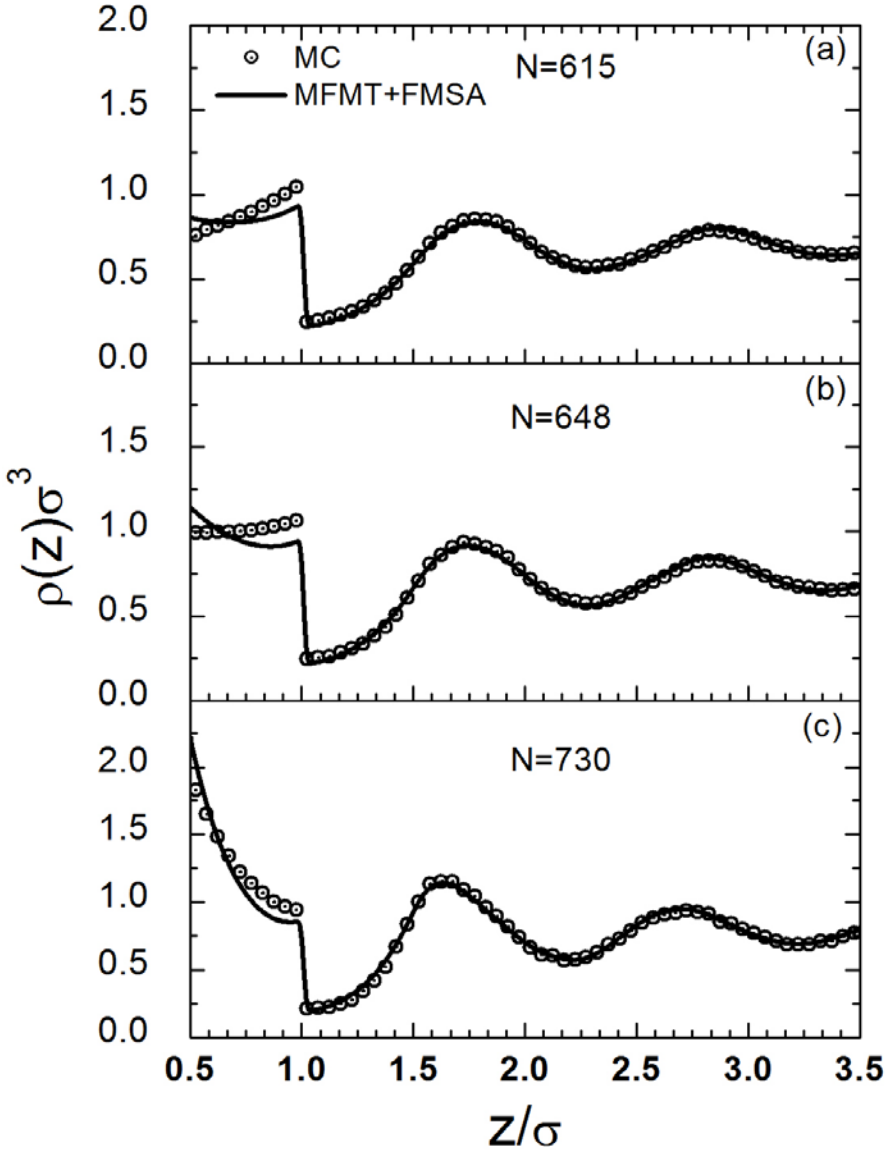

Chapter 8 Drying Transition at A Non-Attractive Surface: Continuous or Precipitous?

Abstract

Solvent depletion from a non-attractive surface has been extensively studied in recent years for its intimate connection to hydrophobic phenomena and superhydrophobicity of patterned materials. While such effect is well understood near microscopic substrates, prediction of the solvent behavior near an extended surface is more complicated and the nature of drying transition has been a long controversy. In this work, we use a perturbative density functional theory (DFT) to examine the receding of a saturated solvent from a spherical cavity as the radius varies from micro to macro length scales. The DFT calculations show that the solvent inhomogeneity remains microscopic when the cavity radius approaches the macroscopic limit and thus give a strong evidence of a first-order drying transition at non-attractive substrates.

8. 1 Introduction

Solvent distribution near macroscopic substrates is pertinent to materials performance in solutions and a broad range of biological, chemical and physical processes [1-4]. Whereas current knowledge has been well advanced, quantification of the microscopic structure of the solvent near an extended surface remains a daunting theoretical challenge. Computational predictions are difficult in particular when solvation is competing with a surface phase transition or occurs near a surface with chemical or topological heterogeneity at a length scale much larger than the size of the solvent

molecules [254]. The problem is imperative for understanding hydrophobic phenomena near macroscopic substrates [8] and for rational design and fabrication of superhydrophobic materials [9]. Despite much recent progress, a satisfactory solution is not yet attainable by microscopic theories or by molecular simulations. Interpretation of experimental results often hinges on phenomenological methods or mean-field approximations. In this work, we will study one aspect of this problem by considering depletion of a near saturated liquid from a non-attractive substrate when its size changes from microscopic to macroscopic scales. To capture the essential physics, our work is focused on a model system that consists of a spherical cavity submerged in a square-well liquid close to saturation. Whereas the simple model is not intended to represent any specific system of practical concern, we expect that, qualitatively, the results are relevant to the solvent behavior in realistic systems.

For a non-attractive substrate immersed in a liquid that is thermodynamically stable, the liquid density can be significantly depressed near the substrate surface, leading to the formation of a vapor-like layer [239, 242]. The depletion layer thickness depends on the substrate size and surface energy as well as the closeness of the liquid to the saturation point. The so-called drying effect has been affirmed by molecular simulations for simple liquids near hard surfaces [255-258] and likewise for solvation of nanometer objects in water [175, 259, 260]. Similar results can be obtained by using the classical density functional theory (DFT) [91, 252, 261]. Because the microscopic methods are not directly applicable to large systems [262, 263], it is not immediately obvious whether the solvent inhomogeneity near a non-attractive surface remains microscopic or extends to

macroscopic scales as the surface curvature vanishes and the liquid approaches the saturation [264-266]. A recent study by Evans and coworkers on drying at curved substrates predicts that in a saturated liquid the vapor-layer thickness grows continuously with the substrate size and diverges at the planar limit [240, 250, 267]. The complete drying transition leads to non-analytical curvature effects on the interfacial free energy and the solvent density profile near the substrate, including the solvent contact density, that cannot be captured by conventional theory of solvation including various versions of the scaled particle theory (SPT) [16, 19, 268]. While such non-analytical behavior is not directly testable with experiments or molecular simulations, it appears consistent with predictions of microscopic theories and statistical-mechanical sum rules. However, a number of simulation results for saturated Lennard-Jones liquids near spherical cavities or confined in slit pores suggest that the film thickness does not grow indefinitely [257, 258, 264, 266]. Several recent simulation and DFT calculations suggest that drying at a non-attractive surface is a first-order phase transition such that the vapor-layer thickness grows discontinuously at the transition point [269, 270].

A cornerstone in the theoretical analysis by Evans *et al* is a phenomenological interface model that evokes the sharp-kink approximation for the solvent inhomogeneity and a repulsive disjoining potential between the liquid and the substrate [271]. For a spherical cavity of radius R immerged in a near-saturated liquid, the solvent density profile is represented by a step function along the radial direction, reflecting the spherical cavity, a vapor-like depletion layer, and the bulk liquid:

$$\rho(r) = \begin{cases} 0 & r < R \\ \rho_g^+ & R \le r < R + L \\ \rho_b & r \le R + L \end{cases}, \tag{8.1}$$

where r stands for the radial distance from the cavity center, ρ_b is the number density of the liquid in the bulk, ρ_g^+ is the number density of a metastable vapor with the temperature and the chemical potential identical to those corresponding to the bulk liquid, and L denotes the vapor layer thickness. According to this interface model, the solvation free energy depends on: 1) the difference between the grand potential of the metastable vapor phase and that of the bulk liquid of the same volume, 2) the solid-vapor and the vapor-liquid interface tensions, and 3) a repulsive disjoining potential or "binding potential" that describes the surface interaction between the substrate and the liquid. Given an explicit expression for the disjoining potential, the vapor layer thickness can be analytically determined by minimization of the solvation free energy. For cavity solvation in a square-well fluid, the equilibrium vapor-layer thickness is given by [240]

$$L_{eq} = \xi \ln\left(\frac{a}{\Delta\rho\delta\mu + 2\gamma_{gl}^{\infty} / R} \right), \tag{8.2}$$

where ξ denotes the correlation length of the vapor phase in the bulk, a stands for an energy parameter depending on temperature. In Eq. (8.2), $\Delta\rho \equiv \rho_l^{co} - \rho_g^{co}$ is the difference between the coexisting liquid and vapor densities at the system temperature, $\delta\mu = \mu_b - \mu_{co}$ where μ_{co} is the chemical potential at the gas-liquid coexistence point and μ_b is that for the bulk liquid, and γ_{gl}^{∞} is the surface tension of the gas-liquid interface at the planar limit.

Eq. (8.2) indicates that when the liquid approaches saturation ($\delta\mu \to 0$), the equilibrium thickness of the vapor-like film scales as $L_{eq} \sim \ln R$ and diverges as the cavity size approaches infinity. On the other hand, near a planar hard wall ($R \to \infty$), the film thickness varies with the liquid chemical potential according to $L_{eq} \sim -\ln \delta\mu$ and diverges at the saturation point. For a large cavity in a near saturated liquid, the interface behavior can be divided into two regimes by using a critical cavity radius R_c [240],

$$R_c \equiv \frac{2\gamma_{gl}^{\infty}}{\Delta\rho\delta\mu}. \tag{8.3}$$

The film thickness is mainly determined by the cavity size for the regime $R << R_c$ and by the liquid chemical potential or closeness of the liquid to saturation otherwise:

$$L_{eq} \to \begin{cases} \xi \ln\left(\frac{aR}{2\gamma_{gl}^{\infty}}\right), R << R_c \\ \xi \ln\left(\frac{a}{\Delta\rho\delta\mu}\right), R >> R_c \end{cases}. \tag{8.4}$$

The depletion layer thickness predicted by the phenomenological theory agrees well with the density functional calculations within the mean-field approximation for the attractive potential [240, 250, 267]. Whereas the mean-field approximation conforms the contact value theorem and the Gibbs adsorption theorem [267], it has been shown that neglect of the fluctuation effects may result in continuous variation of the vapor-layer thickness and thus yield a second-order drying transition [264]. In addition, it is well documented that quantitatively the mean-field method is not accurate in comparison with simulation results [101, 272, 273]. While most comparisons were made under conditions

away from the liquid-vapor coexistence, there is no reason that its numerical performance improves at the saturation point. In particular, the mean-field approximation overpredicts the contact density of a liquid near a hard wall [239, 242, 272]. On the other hand, the simulation results can be quantitatively reproduced by the DFT if it incorporates the correlation effect [67, 85, 101]. While non-mean-field DFT calculations are now well advanced [63, 64, 77], the effect of density correlation on drying effect has not been studied before. In this work, we use a perturbative DFT to re-examine the depletion of a near saturated square-well liquid from a spherical cavity and compare the DFT calculations with the results from the phenomenological theory. For convenience, the perturbative DFT is designated as "FMT+FMSA" because it incorporates the fundamental measure theory (FMT) of Rosenfeld [83] for the molecular excluded volume effects and the direct correlation function of the bulk fluid from the first-order mean spherical approximation (FMSA) [100, 103]. The DFT results will be compared with those based on FMT and the mean-field theory (MFT) for the attractive energy (designated as "FMT+MFT").

The remainder of this article is organized as follows. Section 2 introduces the molecular model and the DFT equations. In section 3, we compare the DFT predictions for the liquid density profiles around a spherical cavity and near a hard wall close to the drying transition. The vapor-layer thicknesses from FMT+FMSA and FMT+MFT will be compared with those from the sharp-kink approximation. In section 4, we summarize the key conclusions.

8. 2 Molecular Model and DFT Equation

The intermolecular energy in a square-well (SW) fluid is represented by a pairwise additive potential that includes a hard-core repulsion and a short-ranged attraction:

$$u(r)=\begin{cases}\infty, & r<1\\ -\varepsilon, & 1\le r<\lambda\\ 0, & r\ge\lambda\end{cases}. \tag{8.5}$$

Throughout this work, the hard-core diameter σ is taken as the unit length, r represents the center-to-center distance, λ provides a measure of the range of attraction, and $\varepsilon>0$ characterizes the strength of the intermolecular attraction. A spherical cavity is imposed by application of a hard-sphere-like repulsion to each SW particle:

$$V(r)=\begin{cases}\infty, & r<R\\ 0, & r\ge R\end{cases}. \tag{8.6}$$

Apparently, the presence of a spherical cavity of radius R in a SW fluid is equivalent to solvation of a hard sphere of radius $R-1/2$. For a SW liquid near a hard wall, the external potential is given by

$$V(z)=\begin{cases}\infty, & z<1/2\\ 0, & z\ge 1/2\end{cases}. \tag{8.7}$$

where z represents the perpendicular distance between a particle center and the hard-wall surface.

In the DFT calculations, the number density of a SW fluid near a cavity or a hard wall, $\rho(\mathbf{r})$, is obtained by minimization of the grand potential:

$$\Omega=k_BT\int d\mathbf{r}\rho(\mathbf{r})\left\{\ln\left[\rho(\mathbf{r})\Lambda^3\right]-1\right\}+F^{ex}+\int d\mathbf{r}\left[V(\mathbf{r})-\mu_b\right]\rho(\mathbf{r}). \tag{8.8}$$

In Eq. (8.8), k_B is the Boltzmann constant, T is absolute temperature, Λ represents the thermal wavelength, and F^{ex} is the intrinsic excess Helmholtz energy functional. In the FMT+FMSA version of DFT [101, 103], the excess Helmholtz energy functional is divided into two parts: the excess Helmholtz energy due to the hard-sphere repulsion F_{hs}^{ex} and that due to attraction F_{att}^{ex}. The former is represented by the modified fundamental measure theory (MFMT) [85, 88],

$$\beta F_{hs}^{ex} = \int \Phi^{hs}\left[n_\alpha(\mathbf{r})\right] d\mathbf{r}, \tag{8.9}$$

where $\beta = \left(k_B T\right)^{-1}$, Φ^{hs} represents the reduced excess energy density, and, $\alpha = 0,1,2,3,V_1,V_2$, are weighted densities. The detail expressions for Φ^{hs} and $n_\alpha(\mathbf{r})$ can be found in previous publications [85, 88]. The excess Helmholtz free energy due to the SW attraction is represented by a quadratic expansion with respect to that of a bulk fluid with density ρ_b [103]:

$$\begin{aligned} F_{att}^{ex} &= F_{att}^{ex}\left(\rho_b\right) + \mu^{att}\int d\mathbf{r}\left[\rho(\mathbf{r}) - \rho_b\right] \\ &\quad - \frac{k_B T}{2}\int\int d\mathbf{r}d\mathbf{r}' C^{att}\left(|\mathbf{r}-\mathbf{r}'|\right)\left[\rho(\mathbf{r}) - \rho_b\right]\left[\rho(\mathbf{r}') - \rho_b\right], \end{aligned} \tag{8.10}$$

where $C^{att}(r)$ stands for the direct correlation function (DCF) due to the attractive component of the SW potential for the uniform system, and $F_{att}^{ex}\left(\rho_b\right)$ and μ^{att} represent the corresponding excess Helmholtz energy and chemical potential, respectively. Accurate expressions for the DCF of SW fluids have been derived by Tang [100] and by Hlushak *et al* [104]. In In the FMT+MFT version of DFT, the hard-sphere free energy is

the same as that in FMT+FMSA but the attractive component is given by the mean-field approximation [103]

$$F_{att}^{ex} = \frac{k_B T}{2} \int\int d\mathbf{r} d\mathbf{r}' \phi_{att}\left(|\mathbf{r}-\mathbf{r}'|\right) \rho(\mathbf{r}) \rho(\mathbf{r}'). \tag{8.11}$$

where the attractive potential is $\phi_{att}(r) = -\varepsilon$ for $1 \le r < \lambda$ and zero otherwise.

At a given external potential and the bulk thermodynamic condition, we obtain the equilibrium density profile by using the conventional Picard iteration method [250]. From the density distribution of the solvent particles obtained from the DFT, the vapor-layer thickness is calculated from [250],

$$L_{eq} \equiv -\frac{\int_R^\infty r^2 \left[\rho(r) - \rho_b\right] dr}{R^2\left(\rho_l^{co} - \rho_g^{co}\right)}. \tag{8.12}$$

Because FMSA and MFT yield different equations of state, the DFT calculations are not performed at identical thermodynamic conditions but close to their corresponding vapor-liquid coexistence curves.

8. 3 Results and Discussions

Drying at a non-attractive surface occurs only when the liquid approaches saturation, which is different according to different theoretical methods. Figure 8-1 shows the phase diagrams of a square-well (SW) fluid with interaction range $\lambda = 1.5$ predicted by the first-order mean-spherical approximation (FMSA) and by the mean-field theory (MFT). In comparison with the simulation results, the phase diagram from the FMSA is more accurate than that from MFT [244]. The difference is mainly because MFT ignores the density-density correlation due to the attractive potential. At high temperature, the

FMSA yields a saturation density on the liquid side larger than that from the MFT, while the opposite is true at low temperature. Throughout this work, we consider the SW fluid at reduced temperature $T^* = k_B T / \varepsilon = 1.0$. At this particular temperature, the reduced vapor and liquid densities at the coexistence are $\rho^{co}_{g,MFT}\sigma^3 = 0.03699$ and $\rho^{co}_{l,MFT}\sigma^3 = 0.601662$, respectively according to MFT; and the coexisting densities are $\rho^{co}_{g,FMSA}\sigma^3 = 0.027326$ and $\rho^{co}_{l,FMSA}\sigma^3 = 0.668755$ from the FMSA.

Figure 8-2 shows the DFT predictions for the contact densities of the SW liquids near a spherical cavity as the radius varies from one half of the solvent diameter to infinity. The contact density is exactly known at both small and large limits of the cavity size [263]. When the cavity is small ($R \le 1/2$), the contact density $\rho(R)$ is given by [16]

$$\rho(R) = \rho_b \left(1 - \frac{4}{3}\pi R^3 \rho_b\right)^{-1}. \tag{8.13}$$

When the cavity radius approaches infinity, on the other hand, the contact density can be obtained from the bulk pressure through the contact value theorem [274]

$$\lim_{R\to\infty} \rho(R) = \beta P_b, \tag{8.14}$$

where P_b is the bulk pressure. Fig. 8-2 indicates that both FMT+FMSA and FMT+MFT reproduce their corresponding limiting contact densities reasonably well. Both theories predict that the contact density exhibits a maximum at an intermediate cavity radius ($1/R \approx 1.4$). The non-monotonic behavior of the contact density reflects a balance of the surface depletion due to the inter-particle attraction and adsorption due to the solute excluded-volume effects.

The sharp-kink approximation predicts that for a spherical cavity of radius R in a saturated liquid, the drying layer thickness is identical to that of the same liquid near a planar hard wall with the bulk chemical potential shifted by $\delta\mu = 2\gamma_{gl}^{\infty} / \left[R\left(\rho_{l}^{co} - \rho_{g}^{co} \right) \right]$. Moreover, previous FMT+MFT calculations suggest that these two systems would yield *virtually identical* density profiles [267]. Apparently, the density profiles cannot be *exactly* identical because the bulk densities are different: one corresponds to that at the saturation and the other is for the compressed liquid. Nevertheless, recent simulations indicate that the two systems indeed have almost the same reduced density profile [258]. To examine whether such similarity is also reproduced with FMT+FMSA, we present in Figure 8-3 the DFT predictions for the density profiles of the SW fluid near curved surfaces at the saturation condition and those for the compressed liquids near a flat wall with the bulk chemical potential shifted. When the cavity is small (Fig. 7-3a), both MFT and FMSA predict that the planar and curved walls result in quite different reduced density profiles. In this case, the sharp-kink approximation is not valid because the gas film is nonexistent near the cavity or the flat surface. As the cavity size increases (Fig. 7-3b-e), however, both theories predict that the two reduced density profiles are converging. Because FMSA utilizes the direct correlation function in the bulk, it accounts for at least in part the density fluctuation effects and the cavity-particle correlations. On the other hand, such correlations are ignored in the MFT. As a result, the FMSA yields density profiles systematically closer to the surface in comparison to the MFT results. Whereas MFT predicts that the liquid becomes more depleted form the surface as it approaches

saturation or as the cavity size increases, the FMSA results suggest that depletion layer is saturating rather than emerging into a macroscopic vapor phase.

In general a drying transition can be introduced by changing the thermodynamic state of the liquid or the properties of the substrate such as size or surface energy. To explore these two different approaches, we consider the variation of the vapor-layer thickness for a cavity in a saturate liquid as the cavity size increases and for a liquid in contact with a hard wall as the chemical potential approaches the saturation point. The asymptotic behavior obtained from the DFT calculations provides a direct test of the sharp-kink approximation and may shed light on the order of the drying transition. Figure 8-4 shows that for a non-saturated liquid near a planar hard wall ($R = +\infty$), the sharp-kink approximation provides a reasonable representation of the vapor-layer thickness predicted by the DFT. Correlation of the film thickness L_{eq} calculated from FMT+MFT with the second line in Eq. (8.4) yields $\xi_{MFT} / \sigma = 0.43962$ and $a_{MFT}\sigma^3 / k_B T = 0.667383$, which are in good agreement with Ref. [240]. The bulk correlation length and surface energy are $\xi_{FMSA} / \sigma = 0.24534$ and $a_{FMSA}\sigma^3 / k_B T = 1.08202$ if we fit the sharp-kink approximation to the results from FMT+FMSA. While both versions of DFT agree well with phenomenological approximation when $\Delta\mu$ is large, neither FMT+FMSA nor FMT+MFT predicts the film thickness diverges as $\Delta\mu \to 0$. In comparison to FMT+FMSA, FMT+MFT shows better agreement with the sharp-kink approximation but it shows no sign of divergence when $\Delta\mu = 0$. The first-order drying transition predicted

by the DFT appears in good agreement with the simulation results in the early literature [264, 266].

Drying transition has been carefully examined by simulations but to our knowledge there is still no consensus on whether it belongs to first or second order. For example, Henderson and van Swol suggested that drying is a “fluctuation-induced” first-order phase transition that cannot be represented by a mean-field method [264]. However, Nijmeijer and coworkers indicated that simulations are limited by finite size effect that results in a “quasi-first-order” transition [265, 275]. Drying transition becomes “continuous-like” with increasing the substrate area. Probably the controversy can be resolved by considering an Ising model for vapor-liquid transition where the molecules are placed on a lattice with vacancies. According to molecule-spin isomorphism [276], the occupied and unoccupied sites as well as the vapor-liquid phase diagram are perfectly symmetric. Similarly, phase transition of the system near a surface consisting of occupied sites (i.e. wetting) is symmetric with that of the same system near a surface of unoccupied lattice sites (i.e., drying). Such symmetry implies that for a system with short-range fluid-substrate interactions, both wetting and drying are first order phase transitions as long as the fluid is away from the critical point [277]. In that case, the first-order transition is not intrinsically affiliated with fluctuations and can be described by a mean-field theory [269]. Besides, the drying transition may be preceded by a pre-drying parallel to pre-wetting in first order wetting transitions [270].

The first-order drying transition is also evident from the DFT predictions for the vapor-layer thickness near a spherical cavity in a saturated SW liquid. Figure 8-5 shows

that at the microscopic scales, L_{eq} increases with the cavity radius in good agreement with the sharp-kink approximation. The vapor-liquid surface tension ($\gamma^{\infty}_{gl,MFT}\sigma^3 / k_B T = 0.18055$) obtained from the mean-field approximation agrees well with that reported in Ref. [240]. Fitting of the sharp-kink approximation to the FMT+FMSA results yields a slightly larger surface tension ($\gamma^{\infty}_{gl,FMSA}\sigma^3 / k_B T = 0.29535$). A comparison of Figs 8-4 and 8-5 suggests that, as indicated in Ref. [240], the effect of surface curvature on the vapor-layer thickness is equivalent to that due to the change in the bulk chemical potential. While the vapor layer thickness predicted by the mean-field theory is significantly larger than that from the perturbation theory, the DFT calculations give similar asymptotical behavior signaling a first-order phase transition in the planar limit.

In addition to extreme limits ($R = +\infty$ and $\Delta\mu = 0$), we have considered the depletion layer thickness for cavity solvation in near saturated SW liquids. Figure 8-6 compares the DFT results with the phenomenological surface model, which predicts that the vapor-layer thickness is determined by parameter (Eq. (8.2)):

$$\mathrm{x} = \xi \ln\left[a / \left(\Delta\rho\delta\mu + 2\gamma^{\infty}_{gl} / R \right) \right]. \tag{8.15}$$

When the system is away from drying transition (large $\delta\mu$ and small cavity radius), the mean-field theory shows excellent agreement with the sharp-kink approximation. Near drying transition, however, the discrepancy increases (see Fig. 8-6a). Such discrepancy was not identified in the previous mean-field DFT calculations probably due to small computation range [240]. While the results from FMT+MFT show good agreement with

the sharp-kink approximation over a wide range of the cavity size and the solvent chemical potential, the asymptotic behavior near drying transition is noticeably different. Such difference becomes more apparent in Fig. 8-6(b) that compares the sharp-kink approximation with FMT+FMSA calculations. Although the mean-field approximation ignores long-range correlation effect, it does not predict a second-order drying transition.

8. 4 Conclusions

We used two versions of classical density functional theory (DFT), one is based on the mean filed approximation (FMT+MFT) and the other incorporates the correlation effects (FMT+FMSA), to investigate the growth of a vapor-like layer near a non-attractive substrate submerged in a near saturated liquid. We demonstrated unequivocally that drying near a nano-attractive surface belongs to first-order phase transition, similar to wetting near an attractive surface. By applying the Ising isomorphism, we argue that the drying transition may be preceded by a pre-drying that involves two coexisting vapor-like layers. Although the calculations were based on square-well fluids near a spherical cavity of varying size, we believe that the conclusions hold qualitatively for realistic systems.

Whereas we were able to reproduce some of the numerical results reported in a previous work that also used the mean-field version of the DFT[240], our calculations agree with the sharp-kink approximation only at conditions remote from drying transition. Unlike prediction of the phenomenological surface model, both versions of DFT predict a finite vapor-layer thickness near a non-attractive surface as the solvent approaches saturation or the cavity size increases to infinity. While the numerical results are sensitive to formulation of the free-energy functional, introduction of the correlation effect in the

DFT does not render the qualitative behavior. Because drying occurs as a first-order phase transition, we expect that the interfacial properties exhibit no non-analytic behavior except at the critical point. The lack of non-analytic terms probably explains excellent the description of the cavity solvation free energy in a saturated Lennard-Jones liquid by the scaled-particle theory [257].

Figure 8-1 Vapor-liquid coexistence curves for a square-well fluid with interaction range $\lambda = 1.5\sigma$. The solid line is calculated from FMSA, and the dashed line is from the mean-field approximation. The horizontal dotted line identifies the corresponding liquid densities at the temperature used in this work ($T^* = k_B T / \varepsilon = 1.0$).

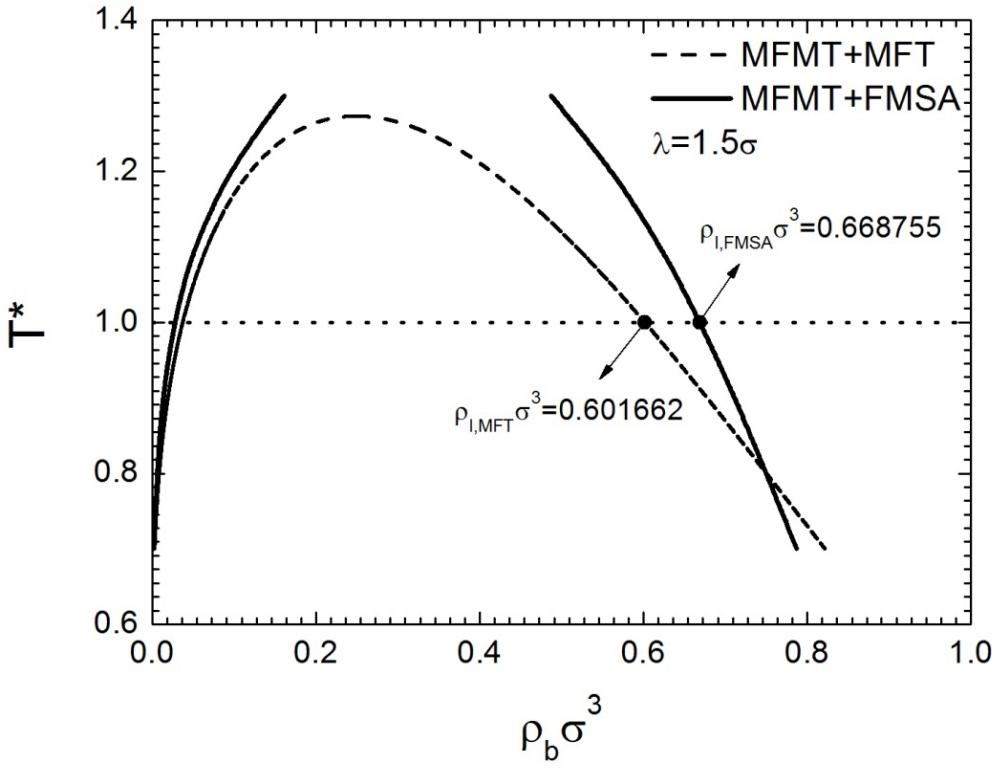

Figure 8-2 The influence of curvature (σ / R) on the contact density for a spherical cavity in a saturated square-well liquid. The blue line is predicted by FMT+FMSA at reduced solvent density $\rho_{FMSA}\sigma^3 = 0.668755$; and the red line is from FMT+MFT at $\rho_{MFT}\sigma^3 = 0.601662$. The symbols represent exact values according to Eqs. (8.13) and (8.14).

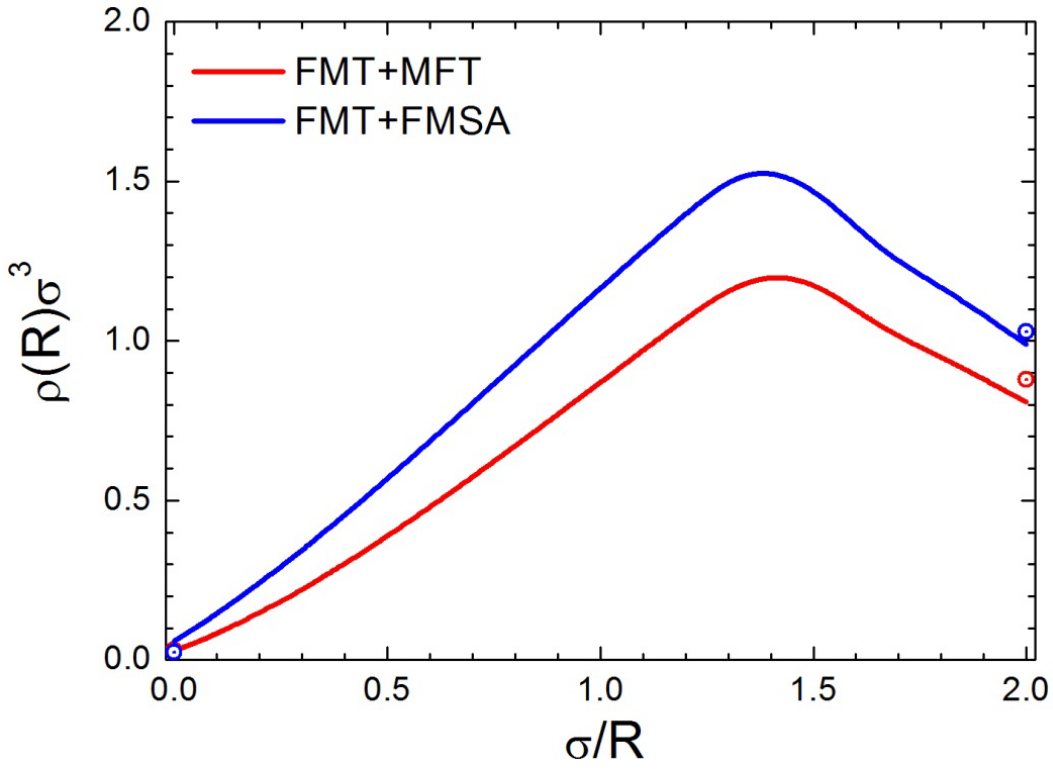

Figure 8-3 Comparison of the density profile of a near-saturated liquid in contact with a hard wall (symbols) with that of a saturated liquid near a spherical cavity (lines). (a) $R/\sigma = 1$; (b) $R/\sigma = 10$; (c) $R/\sigma = 100$; (d) $R/\sigma = 10^3$; (e) $R/\sigma = 10^4$. In all panels, $h = r - R$ for the spherical cavity case and $h = z - \sigma/2$ for the flat wall; $\delta\mu = 2\gamma_{gl}^{\infty}/(\Delta\rho R)$. The results from FMT+FMSA are colored blue and those from FMT+MFT are red.

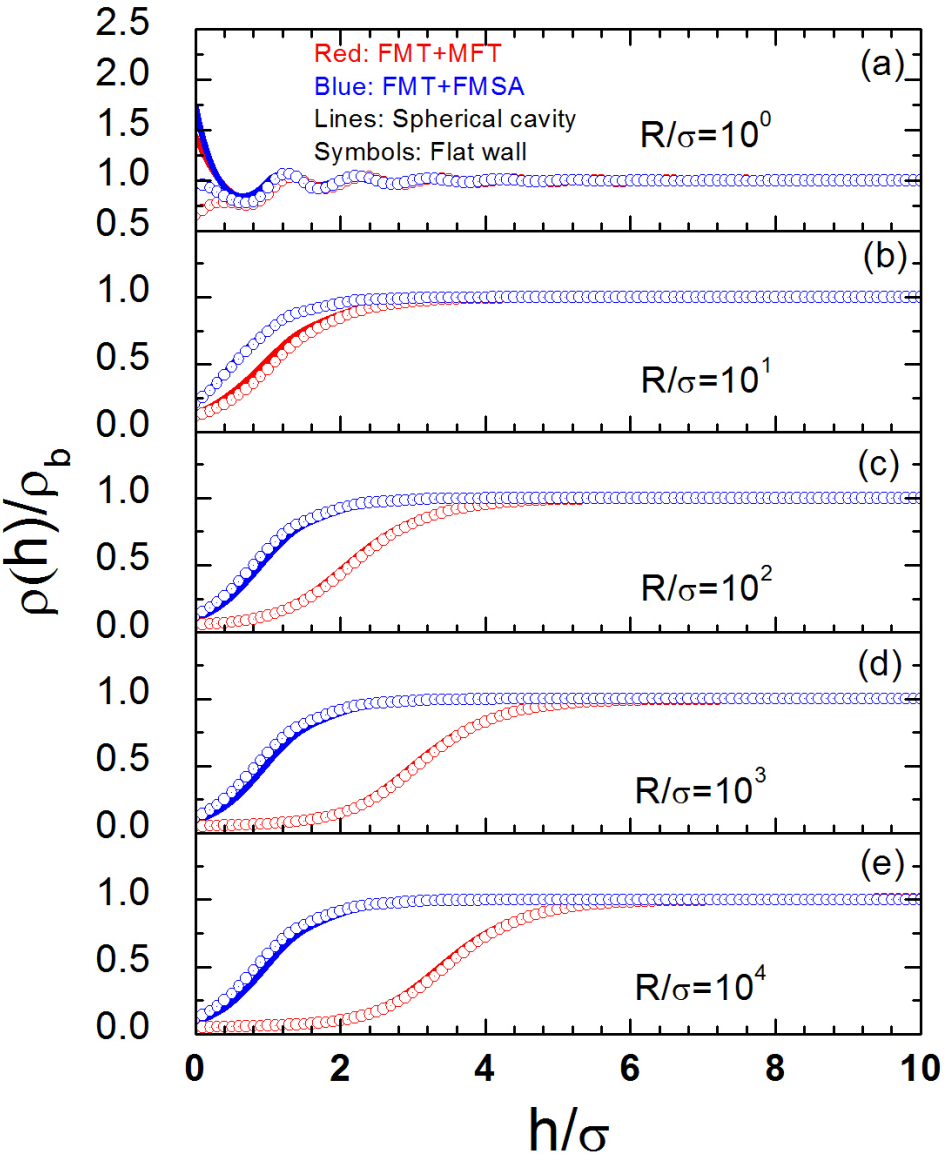

Figure 8-4 The thickness of a vapor-like layer (L_{eq}) for a square-well liquid near a hard wall with the solvent chemical potentials approaching saturation. The symbols are obtained from DFT calculations and the dashed lines are correlations according to Eq. (8.4).

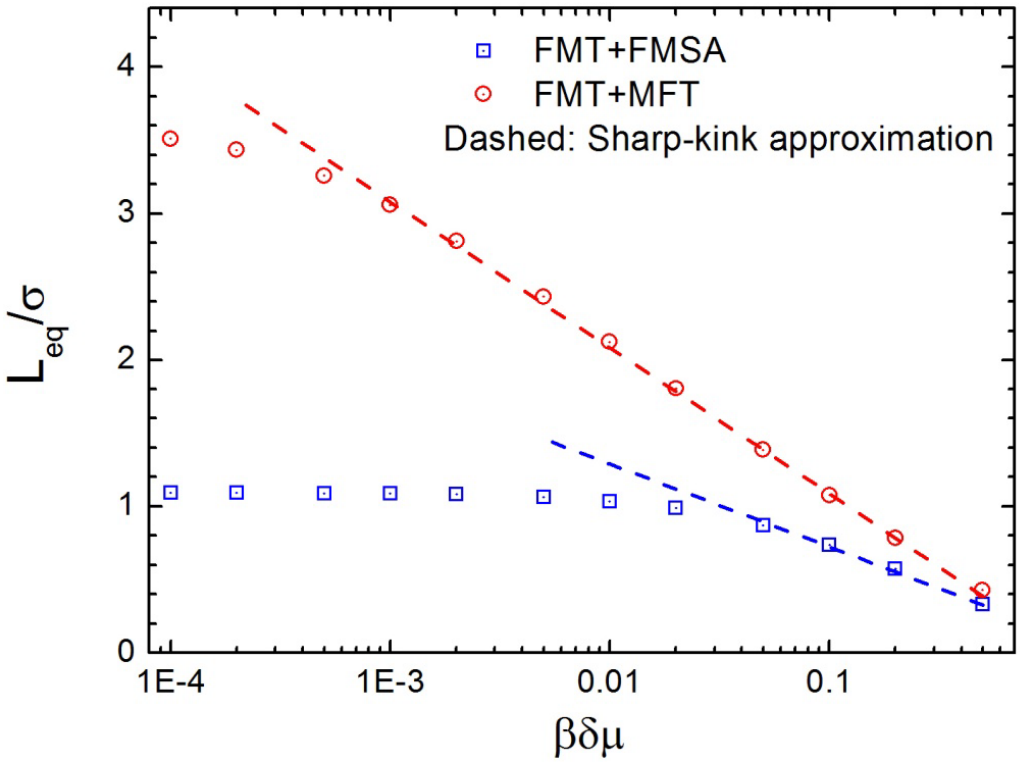

Figure 8-5 The thickness of a vapor-like layer near a spherical cavity in a saturated square-well liquid obtained from FMT+MFT and FMT+FMSA.

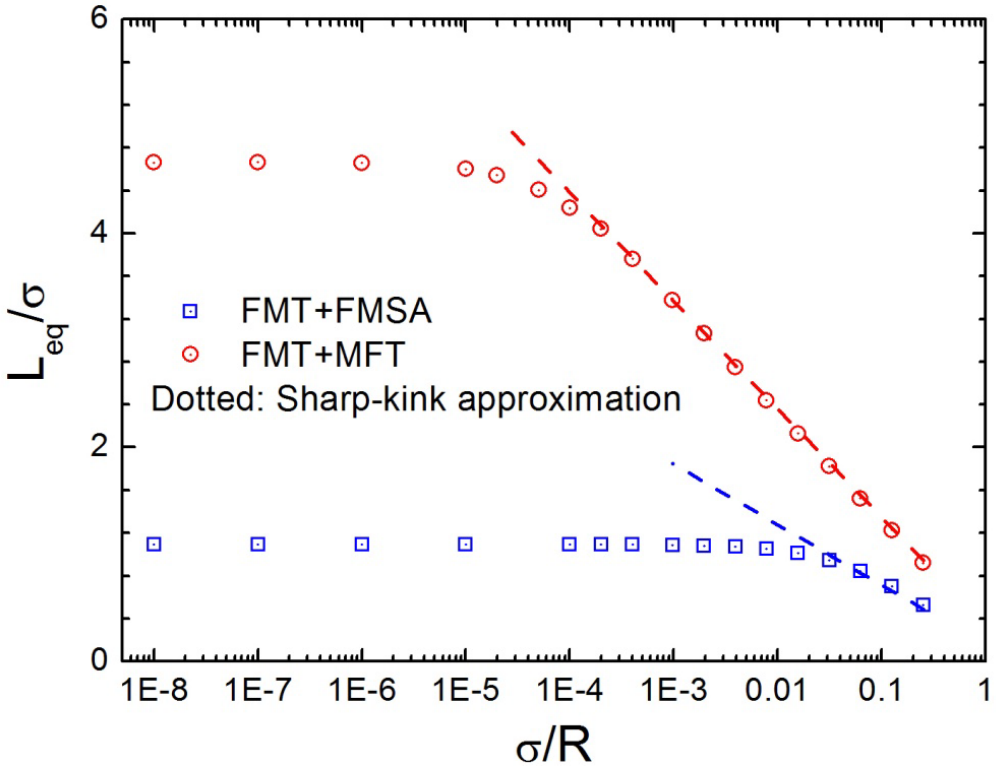

Figure 8-6 (a) Vapor-layer thickness L_{eq} versus $\mathrm{x} = \xi \ln\left[a/\left(\Delta\rho\delta\mu + 2\gamma_{gl}^{\infty}/R\right)\right]$ calculated from FMT+MFT at $\beta\Delta\mu = 0.01$, $\beta\Delta\mu = 0.001$, $\beta\Delta\mu = 0.0001$, and $\beta\Delta\mu = 0$. The dashed line is obtained from the sharp-kink approximation $L_{eq} = x$. (b) The same as Fig. 8-6a except from FMT+FMSA.

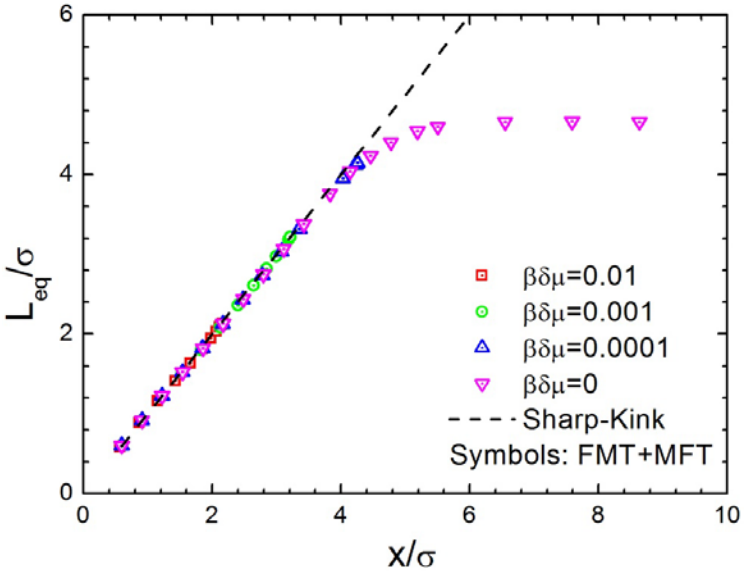

(a)

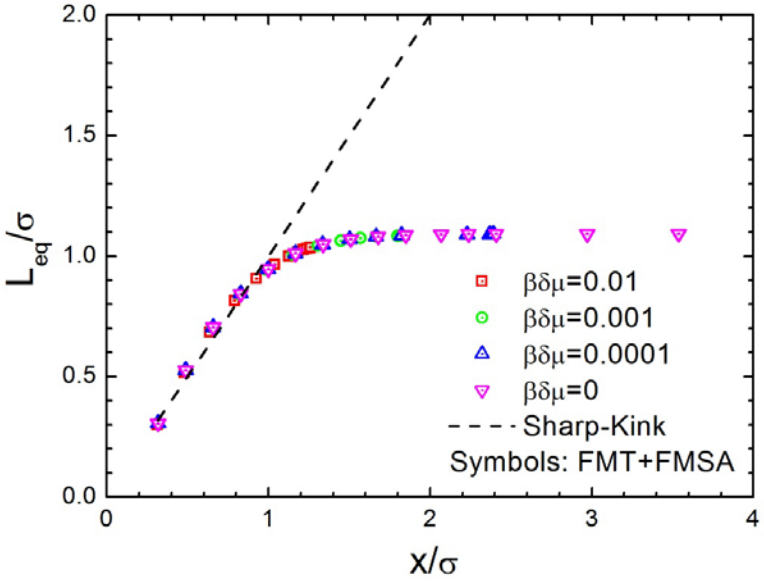

(b)

Chapter 9 The Shape Effect on Nanoparticle Solvation: A Comparison of Morphometric Thermodynamics and Microscopic Theories

Abstract

A conventional wisdom for controlling nanoparticle size and shape during the synthesis is that particle growth favors the direction of a facet with the highest surface energy. However, the particle solvation free energy, which dictates the particle stability and growth, depends not only on the surface area/free energy but also on other geometric measures such as the solvent excluded volume and the surface curvatures and their affiliated thermodynamic properties. In this work, we study the geometrical effects on the solvation free energies of non-spherical nanoparticles using morphometric thermodynamics and density functional theories. For idealized systems that account for only molecular excluded-volume interactions, morphometric thermodynamics yields a reliable solvation free energy when the particle size is significantly larger than the solvent correlation length. However, noticeable deviations can be identified in comparison with the microscopic theories for predicting the solvation free energies of small nanoparticles. The conclusion holds also for predicting the potential of mean force underlying the colloidal “key and lock” interactions. In comparison with the microscopic theories, morphometric thermodynamics requires negligible computational cost and thereby is very appealing for broad practical applications.

9. 1 Introduction

Characterization of the local distribution of solvent molecules and the solvation free energy often serves as a starting point to understand the solution behavior of nanoparticles including stability and self-assembly. In particular, the solvation free energy is instrumental for controlling the size and shape of nanoparticles during the synthesis and the particle geometry is inextricably related to their unique properties and utilities [5, 278, 279]. From a broader perspective, nanoparticle solvation is also important for understanding colloidal forces and the microscopic mechanisms underlying biological processes including protein folding [13] and structure-based rational drug design [14, 15]. For a given nanoparticle or a specific conformation of a biomolecule, modern instrumentation or computational methods are now well advanced that enable quantification of the solvation free energy and the local solvent structure up to atomistic details. But these methods are often labor intensive or computationally demanding thereby cumbersome for many practical applications. For practical purposes, one often seeks fast yet reliable methods that require little effort or computational cost. Theoretically, a new thrust toward that direction is provided by morphological thermodynamics that prescribes the solvation free energy in terms of various geometric measures of the solute-solvent interface and the affiliated thermodynamic variables. The geometrical measurements characterize the volume, surface area, integrated mean and Gaussian curvatures of the space occupied of the solute and their affiliated thermodynamic quantities are independent of the solute size and shape [280]. Proposed by Mecke, Roth and coworkers over the past few years [23, 280, 281], the thermo-

geometric method has been successfully applied to a wide variety of systems including solvation of proteins [22, 88, 150, 152, 282-285].

A cornerstone of morphometric thermodynamics is the Hadwiger theorem from integral geometry concerning the valuations of convex bodies [286, 287]. This mathematical theorem asserts that for a functional defined on the set of bodies B in space $\mathbf{R}$ that satisfies motion invariance, conditional continuity, and additivity, the functional can be presented by a bilinear combination of the intrinsic volume of B in different dimensions [288, 289]. The Hadwiger theorem implies that the solvation free energy of a rigid particle is a bilinear function of four geometrical measures (*viz*, the solute volume, surface area, and integral mean and Gaussian curvatures) and the corresponding thermodynamic coefficients (*viz*, pressure, surface tension, and bending rigidities, respectively). Although the Hadwiger theorem is not strictly valid if the solute-solvent interaction consists of a long-ranged potential [280], or if the solute size is comparable to the solvent correlation length, or if the solute is in a concave shape [288], it has been shown that the morphometric method predicts the solvation free energy in good agreement with the results from the three-dimensional hyper-netted-chain (HNC) equation [23] or from the classical density functional theory (DFT) [283]. Recently, the morphological method has been applied to the study of solvation in water [285] and to proteins in multi-component solvents [284].

The objectives of this paper are twofold. First we use morphological thermodynamics to examine the shape effects on the solvation free energies of nanoparticles that are ignored in conventional interfacial thermodynamics. Because the

macroscopic approach is not strictly valid at microscopic length scales, a comparison of the solvation free energies from different theoretical predictions provides insights into the strengths and limits of morphological thermodynamics. In addition, we test the performance of the morphological method for predicting colloidal lock-and-key interactions. Specifically, we use the morphometric method to investigate the solvation free energies of four types of idealized non-spherical particles and the depletion potentials in colloidal "lock and key" systems. Unlike that for a spherical particle, the solvation free energy of a non-spherical object depends on the size as well as the solute-solvent surface geometry. In particular, the edges and vertexes of the non-spherical particles make additional contributions to the solvation free energy and such effects have not been investigated before. The particle shape also plays an important role in colloidal "lock and key" interactions that entail colloidal spheres (keys) interacting with spherical cavities (locks) [11].

As in previous applications of the morphometric method [10, 22, 155, 163], we consider solvation of hard particles in a hard-sphere solvent. In other words, we are concerned only with the molecular excluded-volume effects of the solute-solvent interactions. While clearly the hard-sphere model is an oversimplification for any realistic solvent, the system is ideal for testing the numerical performance of the morphometric method and for studying the shape effects of particle solvation. The hard-sphere model captures at least in part the solvent depletion or the excluded volume effects in realistic systems. For comparison with predictions from microscopic methods, we conduct in parallel theoretical investigations based on the DFT and Monte Carlo (MC) simulations.

The DFT methods are selected for comparison because they are numerically accurate in comparison to mean-field theories and provide potential alternatives to simulation methods for rapid prediction of the solvation free energies [24]. We expect that a comparison of the solvation free energies and the depletion potentials from different theoretical methods may shed light into future development of analytical solvation models toward large-scale practical applications.

9. 2 Theoretical Methods

9. 2. 1 Morphometric Thermodynamics

As in many previous applications of the morphometric method [10, 22, 155, 163], we consider solvation of non-spherical nanoparticles in a solvent of uniform hard spheres. The athermal system provides a simple yet non-trivial representation of the solvent excluded volume or depletion effects that are relevant to molecular solvation as well as colloidal self-assembly. Throughout this work, the free energy of solvation is defined as the reversible work to insert a nanoparticle from *a fixed position* in vacuum into *a fixed position* in the bulk solvent.

Based on Hadwiger theorem, the morphometric thermodynamics [23, 286] asserts that the solvation free energy F_{sol} of a nanoparticle, here designated a continuous convex body designated as $\mathbf{B}$, can be expressed in terms of a bilinear function of four geometrical (Minkowski) measurements and the corresponding thermodynamic coefficients:

$$F_{sol} = PV + \sigma A + \kappa C + \bar{\kappa} X \,, \tag{9.1}$$

where $V(\mathbf{B})$ stands for the excluded volume of the solute particle, $A(\mathbf{B})$ for the total solute-solvent interfacial area, $C(\mathbf{B})$ and $X(\mathbf{B})$ are the integral mean and Gaussian curvatures of the solute-solvent interface, respectively. Here the integral curvatures are defined by surface integrations of the local principal curvatures (χ_1 and χ_2) at the solute-solvent interface:

$$C(\mathbf{B}) = \int_{\partial \mathbf{B}} \frac{1}{2}(\chi_1 + \chi_2)\, dA, \tag{9.2}$$

$$X(\mathbf{B}) = \int_{\partial \mathbf{B}} \chi_1 \chi_2 dA. \tag{9.3}$$

The coefficients on the right side of Eq. (9.1) are familiar thermodynamic variables: solvent bulk pressure P, solute-solvent interfacial tension σ at the planar limit, and the surface bending rigidities κ and $\bar{\kappa}$ of the solute-solvent interface. These coefficients are defined by the properties of the pure solvent and by the solute-solvent interactions but independent of the particle size and geometry (body $\mathbf{B}$) [280].

Eq. (9.1) is exact if the solvation free energy satisfies motion invariance, continuity, and additivity as required by Hadwiger theorem. While motion invariance and continuity are automatically satisfied for the solvation free energy, additivity holds exactly only in the thermodynamic limit, i.e., when both the solute and its embedding thermodynamic system are infinitely large. Nevertheless, additivity remains a good approximation if the solute has a convex shape and its size is much larger than the solvent correlation length. For a solute particle represented by a rigid convex body, the four geometrical measures can be calculated from *Steiner's formula* [290].

The thermodynamic coefficients affiliated with the geometric measures can be obtained from experimental/simulation/theoretical results for the solvation free energies of solutes with relatively simple geometry (e.g., spherical particles of different diameters) [23]. Although no thermodynamic coefficients are explicitly related to the solute edges and corners, their effect on the solvation free energy is integrated within the curvature and the corresponding bending energy as shown in the last two terms of Eq. (9.1).

For hard particles in a hard-sphere solvent, analytical expressions for the thermodynamic coefficients have been derived on the basis of the White-Bear version II (WBII) of the fundamental measure theory (FMT) [288, 291]:

$$\frac{\beta P}{\rho_b} = \frac{1+\eta+\eta^2-\eta^3}{(1-\eta)^3}, \tag{9.4}$$

$$\frac{\beta\sigma}{\rho_b(d/2)} = -\frac{1+2\eta+8\eta^2-5\eta^3}{3(1-\eta)^3} - \frac{\ln(1-\eta)}{3\eta}, \tag{9.5}$$

$$\frac{\beta\kappa}{\rho_b(d/2)^2} = \frac{4-10\eta+20\eta^2-8\eta^3}{3(1-\eta)^3} + \frac{4\ln(1-\eta)}{3\eta}, \tag{9.6}$$

$$\frac{\beta\overline{\kappa}}{\rho_b(d/2)^3} = -\frac{4-11\eta+13\eta^2-4\eta^3}{3(1-\eta)^3} - \frac{4\ln(1-\eta)}{3\eta}, \tag{9.7}$$

where d is the diameter of a solvent hard sphere, ρ_b is the number density of the hard-sphere solvent in the bulk, and $\eta = \pi\rho_b d^3/6$ is the solvent packing fraction. As usual, $\beta = 1/(k_B T)$, k_B is the Boltzmann constant, and T is the absolute temperature. For uniform systems, the modified FMT free energy reduced to that from the Carnahan-Staling equation of state [292]. Like the bulk equation of state, FMT [85, 88] has been

proven to be the most accurate theory for the structural and thermodynamic properties of inhomogeneous hard-sphere fluids.

Whereas the morphometric method has been used before to study protein solvation and interactions between spherical particles [288], we are unaware of previous work on its application to nanoparticles of non-spherical geometries. To study the effects of particle shape on the solvation free energy, we consider the solvation of four idealized particles: cubes, cylinders, cones, and equilateral triangular prisms (see Fig. 9-1). Different from spherical particles, these nanoparticles have sharp edges and vertexes and their contributions to the interfacial properties are not well defined by conventional methods. To validate the predictions of morphometric thermodynamics, we will compare the results with predictions from microscopic approaches including simulation and DFT calculations. Furthermore, we will test the performance of the morphometric method for predicting the colloidal lock-and-key interactions.

9. 2. 2 Density Functional Theory

As an alternative to molecular simulations, DFT provides a generic computational framework to predict the microscopic structure and thermodynamic properties of macroscopic systems on the basis of the molecular constituents [68, 198]. Because DFT is focused on density profiles instead of microstates and provides analytical expressions for thermodynamic variables of interest, it is computationally more efficient than simulation methods. For hard particles in a hard-sphere solvent, the free energies of solvation can be calculated either from the potential distribution theorem [293] or by direct evaluation of the grand potential [152]. Because the former requires an accurate

free-energy functional for the solute-solvent mixture that is not readily available, the latter method is used in this work.

The free energy of solvation predicted by Eq. (9.1) can be tested with that from the three-dimensional (3D)-DFT or from the MC-DFT calculations [10]. Here MC-DFT refers to a combination of MC simulation for acquiring the three-dimensional density profiles of the solvent with the DFT equations for solvation free-energy calculations. While MC simulation is readily applicable to calculating the microscopic structure of complex multi-dimensional system, simulation of thermodynamic quantities such as the solvation free energy is extremely time-consuming. On the other hand, DFT provides analytical relation between microscopic structure and thermodynamic properties but computation of three-dimensional structures is computationally challenging. MC-DFT combines the merits of simulation and DFT methods but avoids the limitations. In both DFT-based methods, the solvation free energy is calculated from the difference between the grand potential $\Omega(\mathbf{B})$ of hard body **B** in a hard-sphere solvent and that of a bulk system of hard spheres with the same volume and the solvent chemical potential:

$$F_{sol} = \Omega(\mathbf{B}) - \Omega_b . \tag{9.8}$$

The grand potential of the inhomogeneous system is calculated from a modified FMT [85, 88] and that for the bulk hard-sphere system (Ω_b) from the Carnahan-Starling equation of state [292]. The two DFT-based methods differ in the way how we obtain the 3D density distributions of the solvent hard spheres near the nanoparticle solute. In 3D-DFT, the density profiles are calculated by minimization of the grand potential. At

equilibrium, the functional derivative of $\Omega\left[\rho(\mathbf{r})\right]$ with respect to $\rho(\mathbf{r})$ vanishes leading to the Euler-Lagrange equation

$$\rho(\mathbf{r}) = \exp\left\{\beta\mu - \frac{\partial\beta F_{ex}}{\partial\rho(\mathbf{r})} - \beta V(\mathbf{r})\right\}, \tag{9.9}$$

where μ is the chemical potential of the bulk hard-sphere system, F_{ex} represents the intrinsic excess Helmholtz energy. For the athermal system, the external potential ,$V(\mathbf{r})$, is given by

$$V(\mathbf{r}) = \begin{cases} \infty, & \mathbf{r} \in \partial\mathbf{B} \\ 0, & otherwise \end{cases}. \tag{9.10}$$

The Picard-type iterative method [85] was used to solve Eq. (9.9). The functional minimization is performed in a cubic box with the nanoparticle placed at the center and with the 3D density profile expressed in Cartesian coordinates.

In MC-DFT, the density profiles of the solvent hard spheres are obtained from grand-canonical Monte Carlo (μVT) simulations. Because FMT is very accurate for inhomogeneous hard-sphere systems, we expect that these two procedures yield similar results. However, it is not immediate obvious whether the MC calculation or the 3D minimization has better in terms of the numerical efficiency. As in functional minimization, we use a cubic simulation box with the regular periodic boundary conditions and the nanoparticle is fixed at the center of simulation box. The number of solvent hard spheres in MC simulation varies with the shape and the size of the nanoparticle such that the boundary effects can be neglected. In each MC simulation, we

run 1 million MC cycles for equilibration and 5 million cycles for sampling the solvent density profiles.

9. 3 Results and Discussions

We studied the effects of nanoparticle shape on the solvation free energy based on four types of non-spherical particles (see Fig. 9-1) in hard-sphere solvents at different packing fractions. The solvation free energy of each particle depends on the particle size, the shape as well as the solvent bulk density. We compare the numerical performances of morphometric method with 3D-DFT and MC-DFT calculations. In addition, we apply the morphometric approach to a colloidal lock-and-key system and compare the colloidal forces with results from microscopic methods.

9. 3. 1 Cubic Particles

The solvation free energy of a cube in a hard-sphere solvent depends only on the edge length (a) and the solvent packing fraction. According to *Steiner's formula* [290], the geometric measures of the cube are given by:

$$\begin{cases} V = a^3 \\ A = 6a^2 \\ C = 3\pi a \\ X = 4\pi \end{cases}. \tag{9.11}$$

In the 3D-DFT and MC-DFT calculations, the mass center of the cube is placed at the origin $(x, y, z) = (0, 0, 0)$ and the simulation box is also cubic with sides $L_x = L_y = L_z = 12d$ such that the boundary effect can be neglected.

Figure 9-2 presents the solvation free energy versus edge length *a* at different solvent densities. The solid line is predicted by morphometric thermodynamics and symbols are from 3D-DFT and MC-DFT. At a given solvent density, the solvation free energy increases monotonically with the particle size due to the fact that it takes more work to insert a larger nanoparticle. The solvation free energy also rises with the solvent density. As expected, the results from 3D-DFT and MC-DFT are almost indistinguishable. For solvation of cubic particles, the agreement between the morphometric and DFT methods is very good in all cases. The excellent agreement among different methods is in part due to the use of Cartesian coordinates that match perfectly with the edges of cubic particles. In other words, for this particular system we can calculate the 3D density profiles and subsequently the solvation free energy in 3D-DFT and MC-DFT very accurately. While the computational cost for the morphometric method is negligible, it takes several hours or even days to obtain the density profiles from 3D-DFT or MC-DFT (on single core of AMD 'Budapest' 2.3 GHz processor computer at National Energy Research Scientific Computing Center). In particular, MC simulation becomes very time consuming at high solvent densities.

9. 3. 2 Cylindrical Particles

For a cylinder particle of height h and base radius r, the four geometric measures are given by:

$$\begin{cases} V = \pi r^2 h \\ A = 2\pi r^2 + 2\pi r h \\ C = \pi h + \pi^2 r \\ X = 4\pi \end{cases}. \tag{9.12}$$

To minimize the number of parameters, we fix the cylinder height at $h = 2d$ for simplicity. As for the cubic case, the mass center of the cylinder is placed at $(x, y, z) = (0, 0, 0)$, and the simulation box is cubic with sides $L_x = L_y = L_z = 12d$ in both MC simulation and DFT calculations.

Figure 9-3 shows the solvation free energy of a cylindrical particle versus base radius r. Similar to that for a cubic particle, the solvation free energy rises monotonically with the radius at a given solvent density. Overall the results from the morphometric method are in good agreement with those from the DFT calculations. Because the solvent densities are highly localized near the edges of a cylindrical particle, we attribute the increased discrepancy for large particles dissolved at high solvent density to the Cartesian coordinates used in the DFT calculations. The particle geometry also does not perfectly match the grids for MC sampling of the solvent density profiles.

9. 3. 3 Cones

The four geometric measures of a right circular cone are given by

$$\begin{cases} V = \dfrac{\pi}{3} r^2 h \\ A = \pi r^2 \left(1 + \dfrac{\sqrt{h^2 + r^2}}{r} \right) \\ C = \pi r \left[\dfrac{\pi}{2} + \arctan\left(\dfrac{r}{h} \right) + \dfrac{h}{r} \right] \\ X = 4\pi \end{cases}, \tag{9.13}$$

where r is the base radius and h stands for the height. As for a cylinder, we fix the height at $h = 2d$. In 3D-DFT and MC-DFT calculations, the origin of the coordinates

$(x, y, z) = (0, 0, 0)$ is placed at the middle height of the cone. The simulation box is again cubic with sides $L_x = L_y = L_z = 12d$.

Figure 9-4 presents the size dependence of the solvation free energies of hard cones dissolved in a hard-sphere solvent at different solvent densities. Similar to other nanoparticles, in most cases the solvation free energy predicted by the morphometric method agrees well with 3D-DFT and MC-DFT. However, at high solvent density ($\rho\sigma^3 = 0.7$), the morphometric method predicts that the solvation free energy exhibits a minimum for a cone of moderate size, while both the 3D-DFT and MC-DFT predictions show a monotonic increase of the free energy as the particle grows. The discrepancy at small particle size is probably due to the correlation effect that becomes stronger and longer-ranged at higher solvent density. In other words, the performance of the morphometric method deteriorates when the cone size is comparable to the correlation length. In contrast to the case for cylindrical nanoparticles, the agreement between the DFT and morphometric method improves as the particle base radius increases.

9. 3. 4 Equilateral Triangle Prisms

We now consider the solvation of equilateral triangle prisms in a hard-sphere solvent. For simplicity, the prism height is fixed at $h = 2d$, while a stands for the triangular side length. The four geometric measurements of an equilateral triangle prism are given by

$$\begin{cases} V = \dfrac{\sqrt{3}}{4} a^2 h \\ A = \dfrac{\sqrt{3}}{2} a^2 + 3ah \\ C = \pi h + \dfrac{3}{2} \pi a \\ X = 4\pi \end{cases}. \tag{9.14}$$

In 3D-DFT and MC-DFT calculations, the mass center of the equilateral triangle prism is placed at $(x, y, z) = (0, 0, 0)$ and the box is cubic with sides $L_x = L_y = L_z = 12d$.

Figure 9-5 shows the solvation free energies calculated from the morphometric method and DFT. Here the 3D-DFT and MC-DFT results were depicted together for easy comparison. Similar to the cylinder case, there is a discrepancy between morphometric approach and the DFT methods for large prisms dissolved in a high density solvent. The discrepancy grows as the bulk solvent density increases. Meanwhile, the results from 3D-DFT and MC-DFT are slightly different because the grids of Cartesian coordinates cannot match a perfect triangle prism. At high bulk solvent density, the morphometric method erroneously predicts that the solvation free energy is negative when the side length *a* is small, which contradicts the results from the 3D-DFT and MC-DFT. The negative solvation energy indicates that the morphometric approach breaks down as the solvent correlation length is comparable to the particle size.

9. 3. 5 Comparison between Particles of Different Geometries

A study of nanoparticles with the same volume and surface area but different geometries allows us to examine the effects of particle shape on the solvation free energy. For convex nanoparticles, the integral Gaussian curvature is invariant with the particle

geometry. As a result, when the particle volume and surface area are fixed, the shape effect is manifested exclusively in terms of the contribution from the integral mean curvature to the total solvation free energy.

Figure 9-6(a) compares the solvation free energies of cylinders relative to that of a cube of the same solvent excluded volume V and surface area A. For a given cube of edge length a, there are two types of cylinders that give the same V and A: Type 1 has radius $r/a = 0.401$ and height $h/a = 1.982$; Type 2 has radius $r/a = 0.713$ and height $h/a = 0.626$. The difference in the solvation free energy is reflected in the curvature contribution:

$$\kappa \Delta C(a) = \kappa \left[C^{solute}(a) - C^{cubic}(a) \right]. \tag{9.15}$$

The cone and equilateral triangle prism are not compared here because particles of these shapes cannot have the volume and surface area the same as those of a cube. Fig. 9-6 (a) indicates that the integral mean curvature contributions in cylinder type 1 and 2 are quite different. While the relative solvation free energy of type 1 cylinder (longer and thinner) is positive, the opposite is true for type 2 cylinder (shorter and thicker). In other words, the solvation free energy is decreased when the radius and height of the cylinder are close to each other. It should be noted that the surface of a cube is not curved according to conventional interfacial thermodynamics but because of the edge effect, its solvation energy can be either larger or smaller than that of a cylinder depending on the aspect ratio.

For comparison, Fig. 9-6 (a) also shows the relative solvation free energy of a sphere with the same V or A as that of the cube. In both cases, the solvation free energy of a sphere is lower than that of either cylinder 1 or 2. In comparison to that for a cube of

either the same V or the same A, the relative curvature contribution is always negative. At the same V, a sphere has less surface area than that of cube ($A_{sphere} / A_{cube} = 0.81$), while at the same A, a sphere has larger volume ($V_{sphere} / V_{cube} = 1.38$). In contrast to the case of the same volume, a sphere of the same area has larger solvation free energy due to a stronger contribution from the excluded volume effect. In both cases, the effect of the curvature on the solvation free energy is relatively insignificant.

Figure 9-6 (b) presents the solvation free energies of a cylinder and an equilateral triangle prism relative to that of a cone with equal radius and height ($h_0 = r_0$). Similar to Fig. 9-6 (a), these particles have the same solvent excluded volume and surface area. For a given cone dimension, there are two types of cylinders and two types of equilateral triangle prisms that give identical volume and surface area: Cylinder type 1 has radius $r / r_0 = 0.298$ and height $h / h_0 = 3.751$; cylinder type 2 has radius $r / r_0 = 0.919$ and height $h / h_0 = 0.395$; Equilateral triangle prism type 1 has edge length $a / r_0 = 2.24$, height $h / h_0 = 0.482$, equilateral triangle prism type 2 has edge length $a / r_0 = 1.115$ and height $h / h_0 = 1.946$. While both equilateral triangle prisms have a higher solvation free energy in comparison with the cone, cylinder type 2 has a lower solvation free energy and the opposite is true for cylinder type 1. The comparison between prism and cone insists that more sharp edges may have higher solvation free energy. As depicted in Fig. 9-6 (a), the shorter and thicker cylinder (type 2) has a smaller solvation free energy. In other words, a reduction of the size disparity between radius/edge and height lowers the solvation free energy for both cylinder and equilateral triangle prism.

9. 3. 6 Lock-and-Key in A Hard-Sphere Solvent

The colloidal "Lock and Key" system considered in this work consists of a planar lock with a hemispherical cavity and a key represented by a spherical particle. Both the lock and the key are immersed in a hard-sphere solvent. The colloidal "lock-and-key" system has been studied before with 3-D integral-equation theory [22], curvature expansion method [155], hybrid MC-DFT method [10], level-set method with variational implicit solvent model [159, 160], and computer simulations [164]. Here we re-examine the potential of mean force (PMF) for the lock-and-key interactions using the morphological thermodynamics.

As discussed in Ref. [10], we consider only perpendicular alignment of the lock and key particles. Figure 9-7 shows a schematic representation of the lock and key system. The center of the hemispherical cavity is placed at $(x_0, 0, 0)$ and the center of the key is located at $(x, 0, 0)$ with varying x. The radius of the cavity is fixed at $R_{lock} = 2.5d$. We examine the depletion potential $W(x - x_0)$ for various key particles with radius R_{key} along the symmetric axis.

When the key and lock particles are aligned, the PMF depends only on the center-to-center distance r between the hemispherical cavity and the spherical key:

$$W(r) = \Omega(r) - \Omega(\infty), \tag{9.16}$$

where $\Omega(r)$ is the grand potential of system with lock and key separated by distance r and $\Omega(\infty)$ is that of the same system with particles are "far" apart, i.e., $r \to \infty$. Substituting Eq. (9.8) into Eq. (9.16) gives

$$W(r) = F_{sol}(r) - F_{sol}(\infty), \tag{9.17}$$

where $F_{sol}(r)$ is the solvation free energy of the entire lock-and-key system when the particles are separated by distance r, and $F_{sol}(\infty)$ is that of the same system with particles are "far" apart. When the lock and key are far apart, the lock and key particles are not correlated. As a result, $F_{sol}(\infty)$ can be separated into the solvation free energies of lock F_{sol}^{lock} and that of key F_{sol}^{key}:

$$F_{sol}(\infty) = F_{sol}^{lock} + F_{sol}^{key}. \tag{9.18}$$

As for solvation of nanoparticles, both the morphometric and DFT methods are used to study the solvation free energies of the lock, the key, and the lock-and-key complexes.

The geometric measurements of the spherical key particle are known exactly,

$$\begin{cases} V = \frac{4}{3}\pi\left(R_{key} + \frac{d}{2}\right)^3 \\ A = 4\pi\left(R_{key} + \frac{d}{2}\right)^2 \\ C = 4\pi\left(R_{key} + \frac{d}{2}\right) \\ X = 4\pi \end{cases}. \tag{9.19}$$

On the other hand, the geometric measurements of the substrate are given by

$$\begin{cases} V = \frac{\pi d}{2}\left(R_T{}^2 - R_{lock}{}^2\right) + \pi R_{lock}{}^2 d - \frac{\pi}{2} R_{lock} d^2 + \frac{\pi^2}{8} R_{lock} d^2 + \pi R_T{}^2 h - \frac{2\pi}{3} R_{lock}{}^3 \\ A = 2\pi R_{lock}{}^2 - 2\pi R_{lock} d + \pi\left(R_T{}^2 - R_{lock}{}^2\right) + \frac{\pi^2}{2} R_{lock} d + \pi R_T{}^2 \\ C = -2\pi R_{lock} + \frac{\pi^2}{2} R_{lock} \\ X = 0 \end{cases}. \tag{9.20}$$

To obtain the four geometric measurements of the entire Lock-and-Key system, we create a contour parallel to the solvent-accessible surface of the solute with distance u. Figure 9-8 shows the effective shapes of the lock, the key, and the lock-and-key complexes. At given key and lock separation, we calculate numerically the volume $V(u)$ enclosed by such surfaces and subsequently surface area $A(u)$, integral mean curvature $C(u)$ and integral Gaussian curvature $X(u)$ from [283]

$$\begin{aligned} A(u) &= -\partial_u V(u) \\ C(u) &= -\frac{1}{2}\partial_u A(u) \\ X(u) &= -\partial_u C(u) \end{aligned} . \tag{9.21}$$

The desired geometric measurements of lock-key complex are obtained in the limit of $u \to 0$ by solving $V(u)$ numerically.

Figures 9-9a and 9-9b present, respectively, the depletion potential between the lock and key particles when the key is slightly smaller than the lock cavity and when there is a perfect match of the lock size. The results calculated from morphological thermodynamics are compared with the two DFT-based methods and with direct MC simulations [10]. Because an analytical expression is available the free energy functional of hard-sphere mixture, we may obtain the potential of mean force from the potential distribution theorem (PDT) [165]. In this method, we first obtain the solvent density profile near the lock particle and the lock-key potential is calculated from the local excess chemical potential of the key particle. The solvent density profile can be obtained either from MC simulation or from DFT. The former is referred to as MC-PDT and the latter is

referred to as DFT-PDT. More details about the PDT calculations can be given in Ref. [10]. Alternatively, the potential of mean force can also be obtained from the integration of mean force which is directly sampled from MC simulation from two particles far apart to a certain separation.

In comparison with MC simulations, the morphometric method is not as accurate as the MC-DFT and MC-PDT for predicting the depletion potential [10]. And when the separation x is larger than one diameter of hard-sphere solvent, a cavity appears in the interior of lock-key complex. In this case, Hadwiger theorem is not valid. So morphological thermodynamics shows a curve-up shape for smaller key ($R_{key} = 2\sigma$) case and a sudden jump is identified for perfect match case ($R_{key} = 2.5\sigma$) near $x = 2.15\sigma$. Such unphysical jump due to the contribution from mean integral curvature of line has appeared in sphere-sphere interactions [283]. Furthermore, when the excluded-volumes of key and lock are completely separated, morphological thermodynamics predicts that these two particles do not affect each other, because of additivity of Hadwiger theorem. However, it is well known that even though they are separated, they do experience solvent-mediated interactions. Therefore, when Hadwiger theorem is not valid, morphological thermodynamics predicts qualitatively inaccurate potential of mean force in comparison with MC simulation and DFT calculations. Nevertheless, it captures at least semi-quantitatively the potential of mean force for both cases when x is less than one diameter of hard-sphere solvent. The numerical deficiency is probably because the size of concave container is comparable to the correlation length of the solvent. If the concave size is much larger than the correlation length, we expect that the morphological

thermodynamics will agree better with simulation results [280]. Indeed, morphological approach shows satisfactory agreement with simulation even when the concave size is comparable to the correlation length.

9. 4 Summary

In this work, we used morphometric thermodynamics to study the solvation free energies of non-spherical nanoparticles and colloidal “lock and key” interactions in a hard-sphere solvent. In comparison to molecular simulation and microscopic methods such as the classical density functional theory DFT, the morphological method does not require the configurations of the solvent molecules thus it drastically reduces the computational cost. While the statistical-mechanical methods perform best at small length scales, morphological thermodynamics does not scale with the system size and it becomes most accurate at large scales. As a result, the two approaches are complementary to each other and a combination of both can be most profitable for practical applications.

Ideas similar to the morphometric method have being deployed in extension of the scaled-particle theory to studying hydrophobic solvation [8]. In application of the morphometric method to particle solvation in realistic solvents (e.g., Lennard-Jones fluid or water), the thermodynamic coefficients can be obtained from the solvation free energy of spherical particles. Because the thermodynamic properties of the solvent and the solute-solvent interactions are independent of the particle shape, the same coefficients are applicable to particles of arbitrary geometry. The solvation of hard particles in a realistic solvent may induce drying at the surface when the solvent is in the proximity of

saturation. In that case, the additivity condition required by the Hadwiger theorem breakdowns and the morphometric thermodynamics becomes inaccurate. The additivity also breaks down at small scales and at conditions where there exist significant long-range correlations and fluctuation effects. Another drawback of the macroscopic approach is that it is not able to account for surface heterogeneity or defects that do not simply scale with system size. Under those conditions, we must use molecular simulation or microscopic theories. Because morphometric thermodynamics divorces the solute geometry from thermodynamic properties, this method is powerful in particular for calculation of the interfacial free energy of continuous systems that adopt different sizes and shapes.

The morphometric thermodynamics compares well with DFT for predicting the solvation free energies of non-spherical particles, *viz.*, cube, cylinder, cone and equilateral prism in a hard- sphere solvent of varying bulk densities. While the conventional wisdom is that the stability or solvation free energy of a nanoparticle is determined by the excluded-volume and surface area, morphological thermodynamics accounts for additional effects due to the surface curvature. For particles with different geometries but the same excluded-volume and surface area, morphological thermodynamics predicts that a reduction of the ratio between radius/edge and height of the particle lowers the solvation free energy. The DFT calculations also indicate that the solute curvature can have significant effects on the solvent behavior near solute and subsequently the solvation free energy. In morphometric thermodynamics, the edge and

corner effects are taken into account through the integrated curvatures, which make additional contributions to the solvation free energy [294].

We further applied morphological thermodynamics to the study of more complicated Lock-and-Key model system which includes complex convex and concave geometry. Although Hadwiger theorem breaks down for solute particles with concave regions which introduce confinement effect on solvent, the prediction from morphological thermodynamics is generally good comparing to alternative analytical methods and computer simulations. As the concave size increases and confinement effect becomes less significant, the morphometric approach should have better agreement with computer simulation, while it virtually costs no extra time. One very attractive feature of the morphometric approach is that it can be easily altered to study solvation in different solvents, because the properties of solvent are only presented by four thermodynamic coefficients [283].

Figure 9-1 Schematic representation of **B** with different geometry considered in this work: (a) Cube; (b) Cylinder; (c) Cone; (d) Equilateral triangle prism.

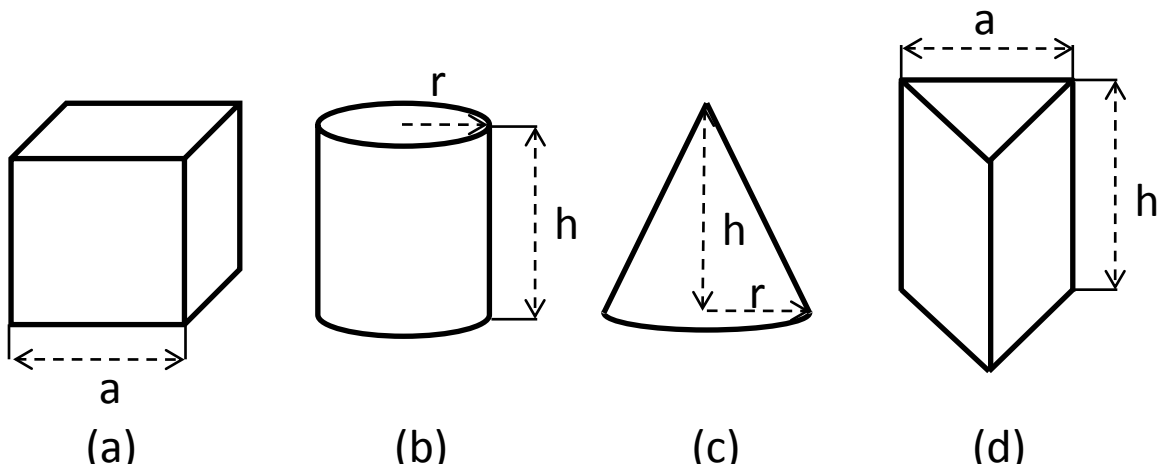

Figure 9-2 (a) The solvation free energy of a cubic **B** versus length *a* in a hard sphere solution with solvent density $\rho\sigma^3 = 0.1$. (b) The same as Fig. 9-2(a), except $\rho\sigma^3 = 0.3$. (c) The same as Fig. 9-2(a), except $\rho\sigma^3 = 0.5$. (d) The same as Fig. 9-2(a), except $\rho\sigma^3 = 0.7$.

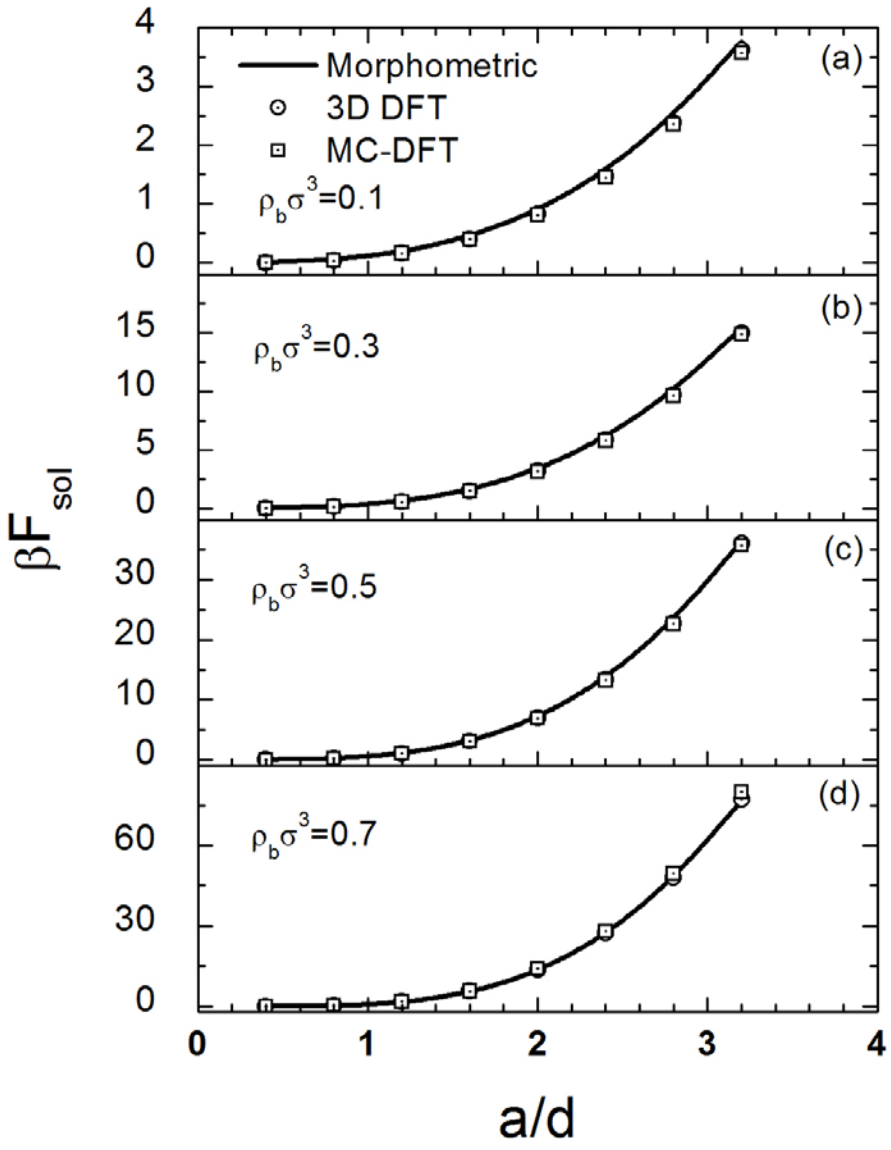

Figure 9-3 (a) The solvation free energy of a cylindrical **B** of height $h = 2d$ versus radius r in a hard sphere solution with solvent density $\rho\sigma^3 = 0.1$. (b) The same as Fig. 9-3(a), except $\rho\sigma^3 = 0.3$. (c) The same as Fig. 9-3(a), except $\rho\sigma^3 = 0.5$. (d) The same as Fig. 9-3(a), except $\rho\sigma^3 = 0.7$.

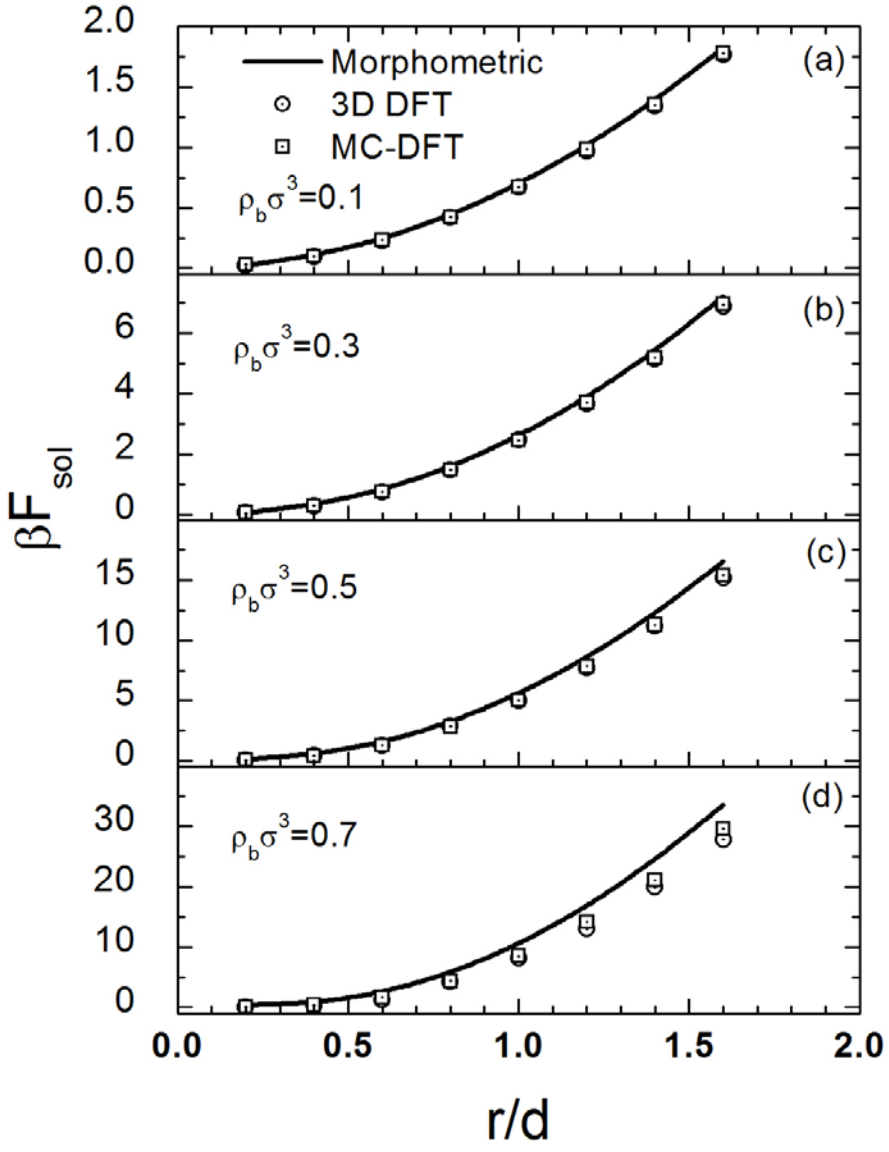

Figure 9-4 (a) The solvation free energy of a cone **B** of height $h = 2d$ versus radius r in a hard sphere solution with solvent density $\rho\sigma^3 = 0.1$. (b) The same as Fig. 9-4(a), except $\rho\sigma^3 = 0.3$. (c) The same as Fig. 9-4(a), except $\rho\sigma^3 = 0.5$. (d) The same as Fig. 9-4(a), except $\rho\sigma^3 = 0.7$.

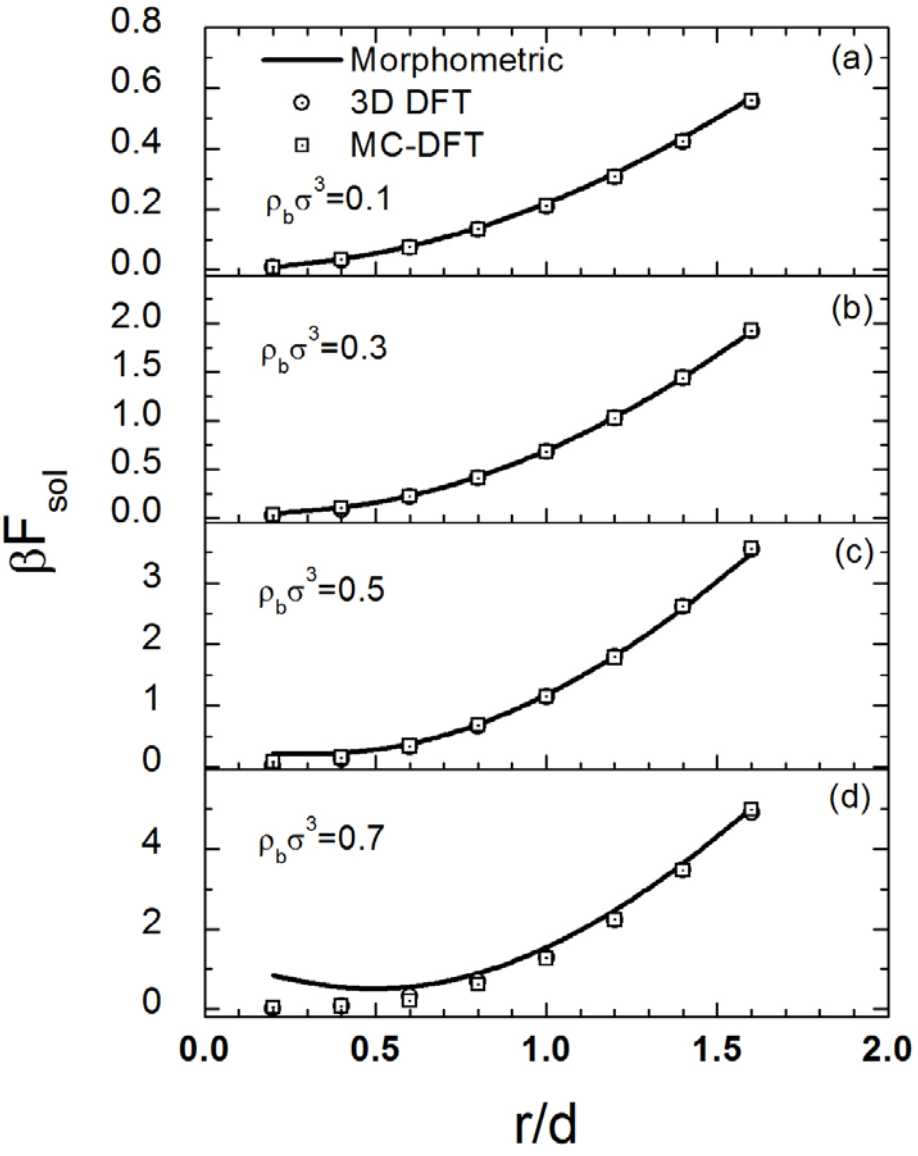

Figure 9-5 (a) The solvation free energy of an equilateral triangular prism **B** of height $h = 2d$ in a hard sphere solution with solvent density $\rho\sigma^3 = 0.1$. (b) The same as Fig. 9-5(a), except $\rho\sigma^3 = 0.3$. (c) The same as Fig. 9-5(a), except $\rho\sigma^3 = 0.5$. (d) The same as Fig. 9-5(a), except $\rho\sigma^3 = 0.7$.

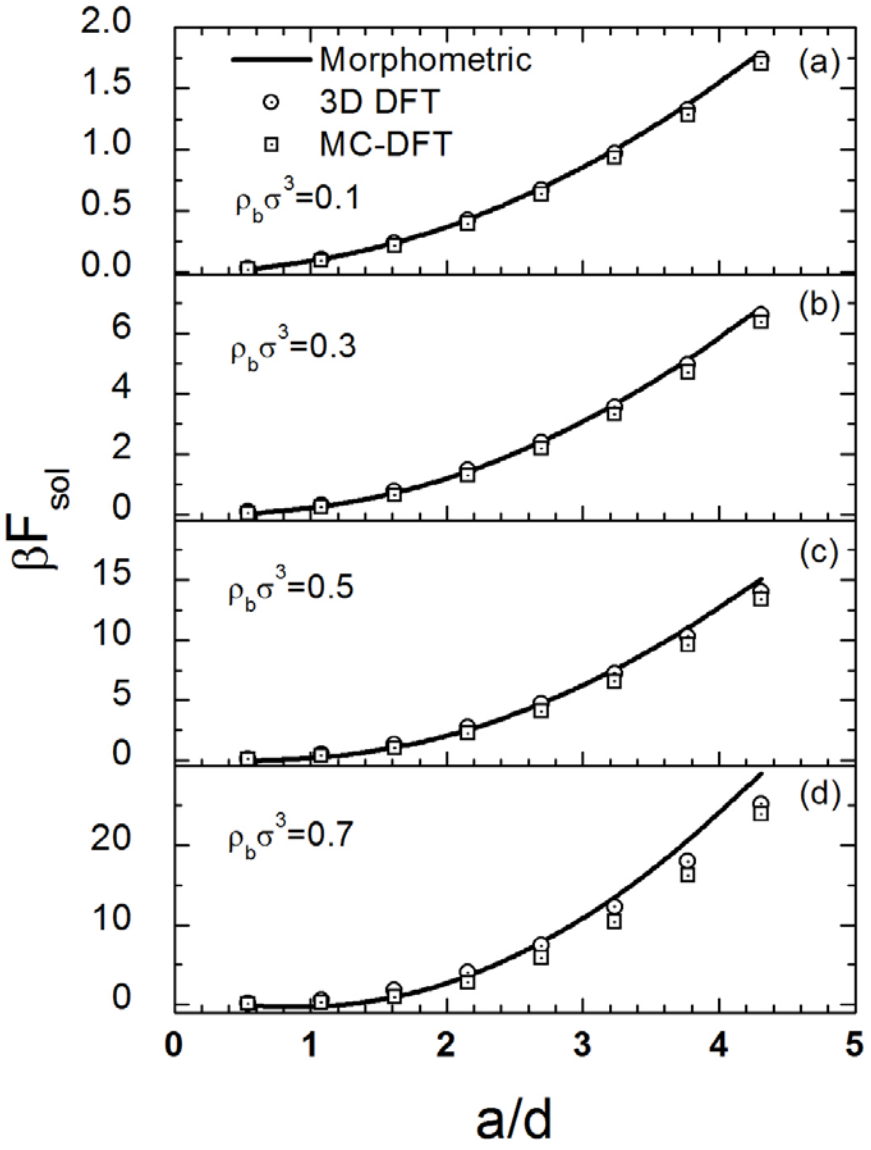

Figure 9-6 (a) The relative curvature contribution with respect to a cube with edge length a, $\kappa\Delta C(a)=\kappa\left[C^{solute}(a)-C^{cubic}(a)\right]$ of cylinders with the same volume and surface areas as that of the same cube immersed in a hard sphere solution with bulk density $\rho\sigma^3=0.7$. The red line indicates cylinder type 1 with radius $r/a=0.401$, height $h/a=1.982$ and blue line indicates cylinder type 2 with radius $r/a=0.713$ and height $h/a=0.626$. The green line presents the relative curvature contribution of spheres with the same volume as the cube with edge length a and the magenta line depicts that of the sphere with the same surface areas as cube with edge length a. The radius of sphere is $r/a=0.62$ for the same V and $r/a=0.69$ for the same A. (b) The relative curvature contribution with respect to a cone with radius r_0 and height $h_0=r_0$, $\kappa\Delta C(r_0)=\kappa\left[C^{solute}(r_0)-C^{cone}(r_0)\right]$ of cylinder and equilateral triangle prism with the same volume and surface area as that of the same cone immersed in a hard sphere solution with bulk density $\rho\sigma^3=0.7$. The red line indicates cylinder type 1 with radius $r/r_0=0.298$ and height $h/h_0=3.751$, blue line indicates cylinder type 2 with radius $r/r_0=0.919$, height $h/h_0=0.395$, the green line presents equilateral triangle prism type 1 with edge length $a/r_0=2.24$, height $h/h_0=0.482$, blue line indicates equilateral triangle prism type 2 with edge length $a/r_0=1.115$ and height $h/h_0=1.946$.

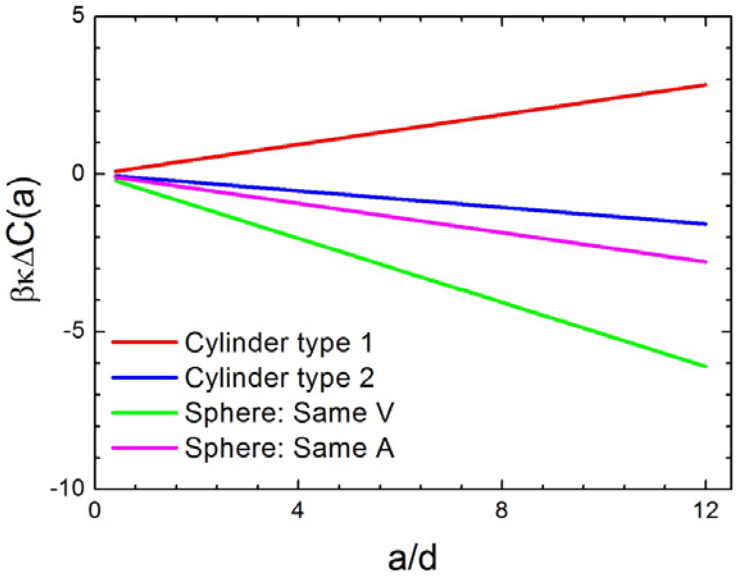

(a)

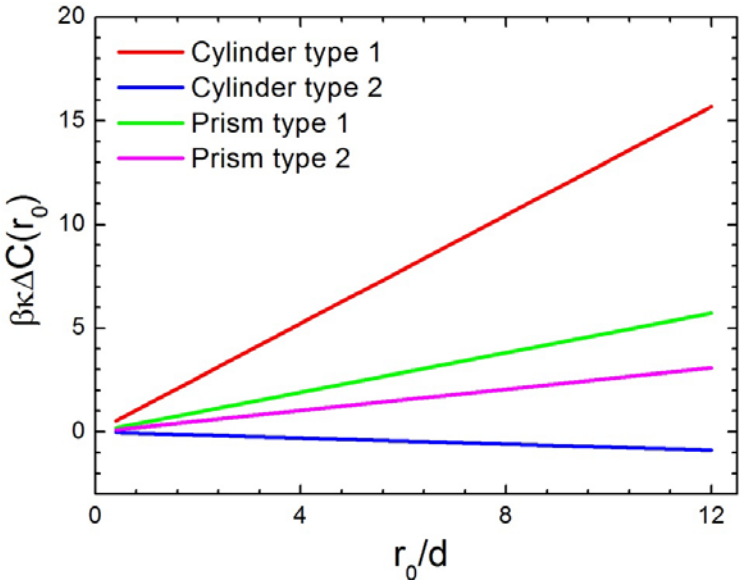
Cylinder type 1
Cylinder type 2
Prism type 1
Prism type 2
βκΔC(r0)
r0/d
20
15
10
5
0
0
4
8
12

(b)

Figure 9-7 The schematic representation of the lock and key system. The key is a big spherical particle with diameter D_{key} and the lock is a substrate with a hemispherical pocket with diameter D_{lock}. The separation between key and lock is represented by the distance between the centers of key placing at $(x,0,0)$ and lock at $(x_0,0,0)$.

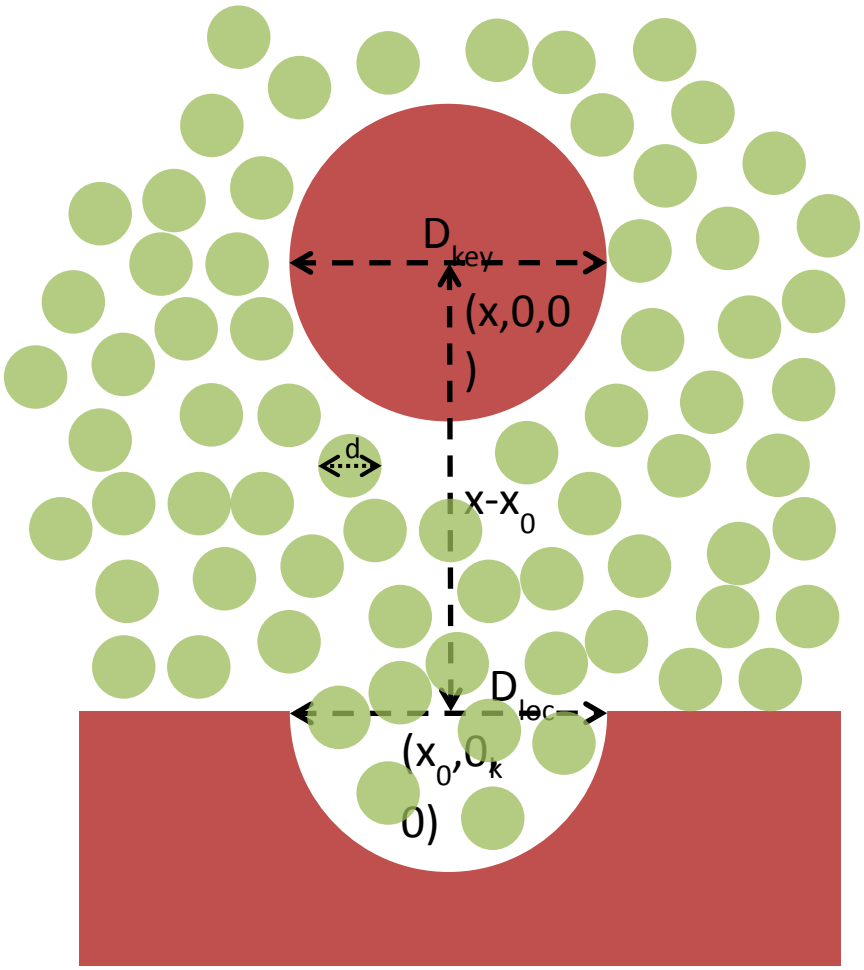

Figure 9-8 (a) The schematic representation of the key particle of radius R_{key}. The dash line shows the solvent-accessible surface enclosing excluded-volume by the key particle. (b) The same as Fig. 9-8 (a), except the lock particle. (c) The same as Fig. 9-8 (a), except the lock and key complex for radius of key particle $R_{key} = R_{lock}$ located at $(x_0, 0, 0)$ and dotted line represents a surface parallel to the solvent-accessible surface with distance u.(d) The same as Fig. 9-8 (c), except the lock and key complex for radius of key particle $R_{key} = R_{lock}$ located at $(x, 0, 0)$.

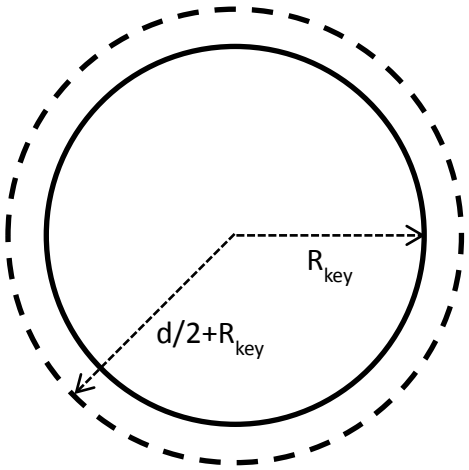

(a)

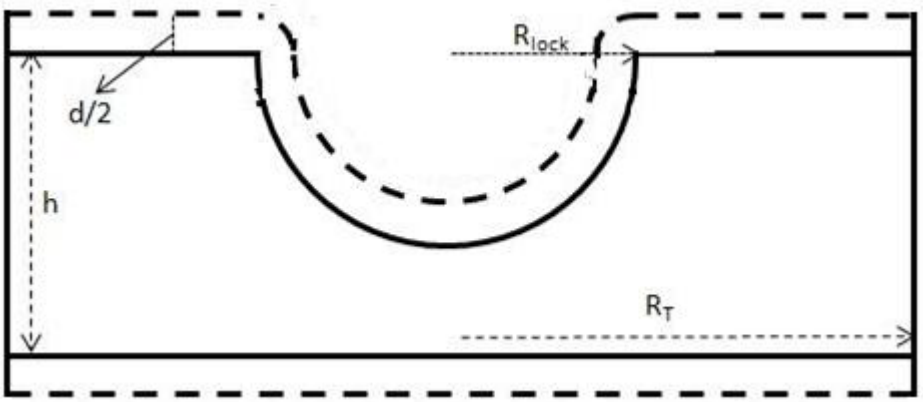

(b)

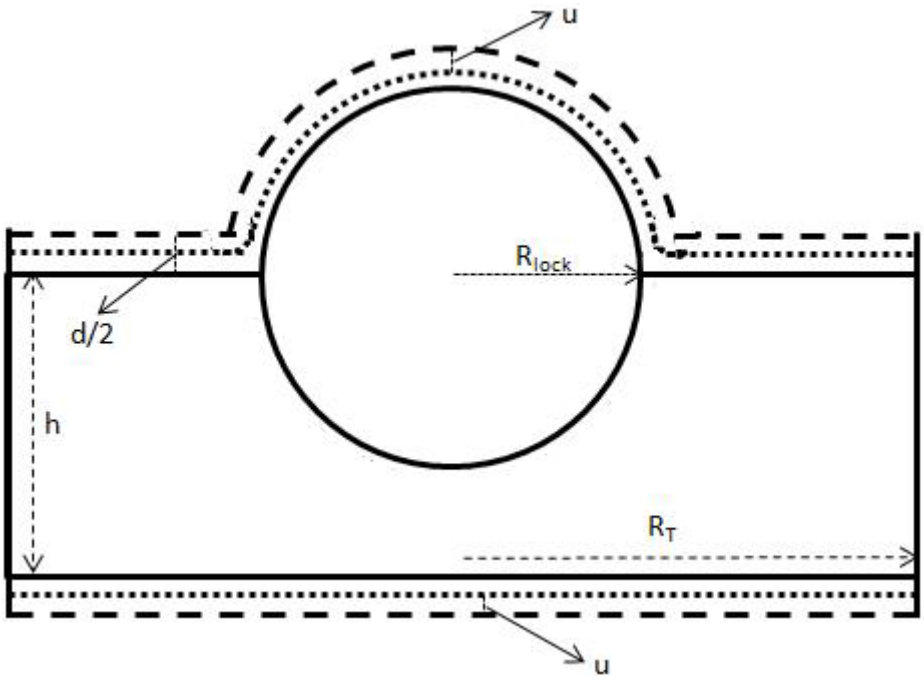

(c)

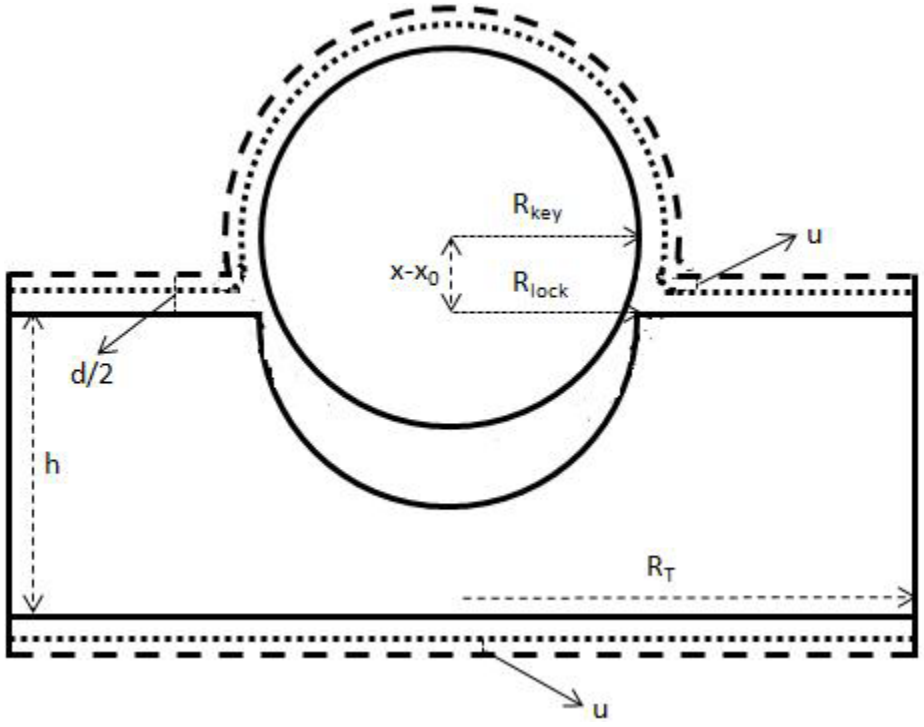

(d)

Figure 9-9 (a) Depletion potential between a hard spherical key with key diameter $D_{key} = 4\sigma$ and a hard hemi-spherical lock substrate with lock diameter $D_{lock} = 5\sigma$ in a hard- sphere solvent at bulk packing fraction $\eta = 0.367$. We compare the morphological thermodynamics (red line) with MC-DFT (green line) and MC-PDT (blue line) methods and simulation data (symbols) reported in Ref. [10]. (b) The same to Fig. 9-9 (a) except with key diameter $D_{key} = 5\sigma$.

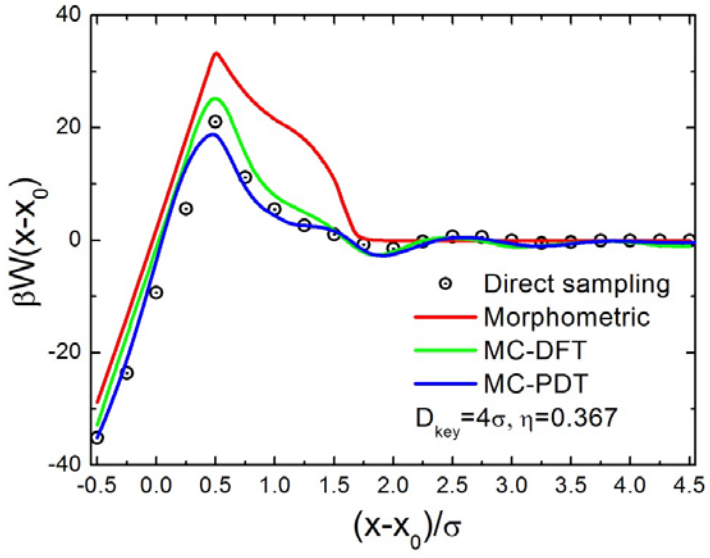

(a)

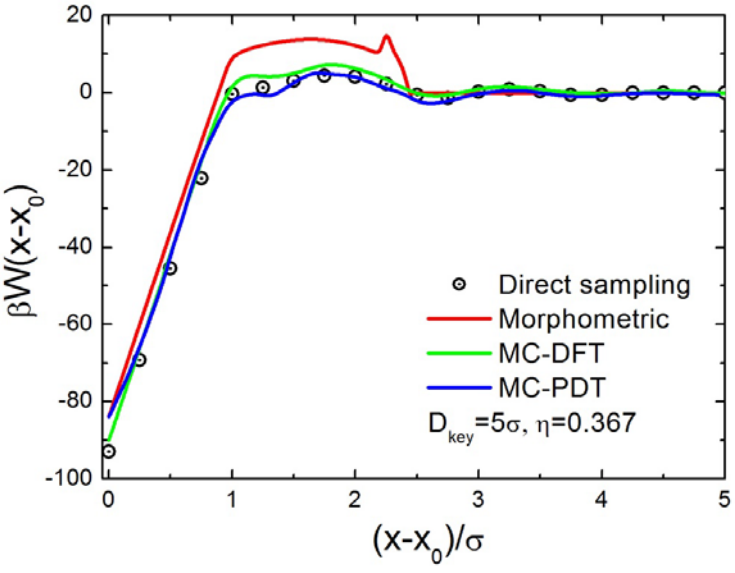

(b)

Chapter 10 Conclusions

A key contribution of this thesis is development of a hybrid density functional theory (DFT) and its application for studying solvation of flexible and rigid molecules, surface wetting/drying transitions and colloidal forces. Flexible molecules studied in this work include polymers, block copolymers, and polyelectrolytes that are important in polymer engineering and biological systems. The research on solvation of rigid molecules is pertinent to hydrophobic interactions, drying transitions, and fabrications of nanoparticles. In the first place, I studied the structural and thermodynamic properties of polymers and polyelectrolytes in confined geometry as of interest in polymer separations by chromatography and in viral packaging and gene delivery. The numerical performance of the polymer density functional theory has been tested by extensive comparison with computer simulations and scaling analysis. Second, I creatively combined molecular simulations and density functional theory to study the colloidal interactions between rigid molecules and potential of mean force underlying "Lock-and-Key" interactions in an idealized solvent and for ion solvation in liquid water. The hybrid DFT method is able to describe the structural and thermodynamic properties of multi-dimensional complex systems with modest computational costs. Third, I studied the solvent distributions and thermodynamic properties near a rigid solute ranging from microscopic to macroscopic scales and illustrated the discontinuous nature of drying transition. Lastly, I applied morphological thermodynamics to study the solvation free energy of nanoparticles. Most results included in this thesis have been published in the leading journals.

Chapter 2 outlines the theoretical framework of DFT used in this thesis, especially on the formalism of excess Helmholtz free energy arising from the thermodynamic non-ideality due to segmental-level inter-molecular and intra-molecular interactions. Within classical DFT, the excess Helmholtz free energy is a functional of the one-body density distribution and can be decomposed into several different contributions based on the origins of molecular interactions. Moreover, derivations of one-body effective potential field (i.e., excess chemical potential) are provided in details.

In Chapter 3, I studied the structural and thermodynamic properties of single chain polymer under confinement. The microscopic distributions predicted from DFT are in excellent agreement with MC simulations. The confinement free energy and osmotic pressure of single chain presented a good agreement with the slope of scaling analysis when concentration is moderate and agreed well with simulation and experimental data for concentrated regime. While the theoretical calculations discussed in this work are only concerned with athermal systems where the confinement free energy is solely determined by the entropic effects, we expect that the theoretical framework can be extended to realistic polymeric systems with an explicit consideration of the solvent effects.

In Chapter 4, DFT was used to the study of microscopic distributions of flexible and semi-flexible polyelectrolytes and ions confined in a spherical cavity mimicking a viral capsid. Unlike previous publications, the outside environment is explicitly considered and the charge neutrality is imposed to a system including a polyelectrolyte containing capsid and a bulk salt solution. The density profiles of polymer segments and

small ions from DFT were compared with MC simulation data from the literature. Similar to the MC simulation work, our DFT calculation reveals that the net charge of polyelectrolyte and capsid complex is non-neutral in good agreement with experimental data. Although such coarse-grained model ignores the local solvent distribution and is not used to simulate a real virus model, we hope that an extended primitive model that takes into account the hydrophobic interactions and ionic polarizability can be applied to the studies of structural and thermodynamic properties of real genome encapsidation processes.

In Chapter 5, I proposed a hybrid method for studying the entropic forces in hard-sphere solvents by combination of MC simulation and the DFT. In this work, we tested the performance of the hybrid MC/DFT method by comparing with results from direct MC/MD simulations for the potential of mean force between a pair of hard solutes with various different shapes and a colloidal "Lock-and-Key" system. The theoretical predictions are all in good agreement with results from full simulations. Whereas for numerical calibration this work is focused on relatively simple systems, we expect that, with a good expression of the free-energy functional to account for various components of intermolecular interactions and correlation effects, a similar procedure can be extended to more realistic systems including to those underlying biological and physical processes of direct interest for practical applications.

In Chapter 6, the hybrid method is extended to investigating the solvation free energies of ions in water by combining MD simulation and the DFT. An accurate free energy functional for water has been developed by accounting the short-range repulsion

and longer-ranged van der waals and electrostatic interactions. With the local density distribution of water molecules obtained from MD simulation, the DFT predicts the solvation free energies of small cations and anions in excellent agreement with simulation results. In comparison to conventional simulation methods, the new theoretical approach is computationally very efficient because it avoids simulation along a hypothetical thermodynamic pathway to connect the initial and final states of the solvation process.

In Chapter 7, I applied a perturbative DFT to study the microscopic structure of the square-well fluids in the bulk and at inhomogeneous conditions. The DFT predicts the radial distribution functions of bulk SW fluids and structural properties of SW fluids at different inhomogeneous conditions in excellent agreement with MC data for several different temperatures and ranges of inter-particle interactions. Because the thermodynamic properties of an equilibrium system are fully determined by the one-body density profile or equivalently the microscopic structure, the good agreement between theory and MC simulation results for the structural properties ensures a good performance of the theory for thermodynamic properties of uniform as well as inhomogeneous systems.

In Chapter 8, I used two versions of classical density functional theory to investigate the growth of a vapor-like layer near a non-attractive substrate submerged in a near saturated liquid. Whereas we were able to reproduce some of the numerical results reported in a previous work that also used the mean-field version of the DFT, our calculations agree with the phenomenological method only at conditions remote from drying transition. Unlike prediction of the phenomenological surface model, both

versions of DFT predict a finite vapor-layer thickness near a non-attractive surface as the solvent approaches saturation or the cavity size increases to infinity. We demonstrated unequivocally that drying near a nano-attractive surface belongs to first-order phase transition, similar to wetting near an attractive surface. By applying the Ising isomorphism, we argue that the drying transition may be preceded by a pre-drying that involves two coexisting vapor-like layers. Although the calculations were based on square-well fluids near a spherical cavity of varying size, we believe that the conclusions hold qualitatively for realistic systems.

In Chapter 9, I used morphometric thermodynamics to study the solvation free energies of non-spherical nanoparticles and colloidal "lock and key" interactions in a hard-sphere solvent. In comparison to molecular simulation and microscopic theories such as DFT, the morphological method does not require the configurations of the solvent molecules thus it drastically reduces the computational cost. The numerical performance of the morphometric thermodynamics shows good agreement with alternative theoretical calculations for predicting the solvation free energies of non-spherical particles in a hard sphere solution of varying bulk densities. In addition, the dependence of the curvature of solute on the solvation free energy of nanoparticles was studied by the comparison between different geometries with the same excluded-volume and surface area. Because morphometric thermodynamics divorces the solute geometry from thermodynamic properties, this method is powerful in particular for calculation of the interfacial free energy of continuous systems that adopt different sizes and shapes.

In summary, DFT is proved to be unifying theoretical tool for describing the structural and thermodynamic properties of flexible and rigid molecules in a complicated thermodynamic environment. The theoretical framework established in this thesis provides a foundation for future applications to presenting the properties of polymeric fluids and colloidal dispersions of practical concern. With the proper molecular modeling, the DFT framework and the hybrid method presented in this work will provide insight into synthetic plastics and fibers in polymer engineering, biopolymers such as nucleic acids, genome and proteins in many biological systems and the synthesis of nanoparticles and the control of the shape and properties of nanocrystals.

Appendices

Appendix A: Excess Chemical Potential Due to Chain Connectivity of A Mixture of Block Copolymers and Monomers

The total free energy density due to chain connectivity of a mixture of block copolymers and monomers is given as:

$$\Phi_{ch}^{ex} = \sum_{k=1}^{m_p} \Phi_{ch,k}^{ex} \,. \tag{A.1}$$

The excess chemical potential $\mu_{ch,t}^{ex}$ is given as

$$\beta\mu_{ch,t}^{ex}\left(\mathbf{r}\right) = \frac{\delta\beta F_{ch}^{ex}}{\delta\rho_t\left(\mathbf{r}\right)} = \sum_{\alpha}\int d\mathbf{r}' \frac{\partial\Phi_{ch}^{ex}}{\partial n_{\alpha,t}\left(\mathbf{r}'\right)}\omega_t^{(\alpha)}\left(\mathbf{r}'-\mathbf{r}\right), \tag{A.2}$$

where t applies to all species of block copolymer segments and monomers. Because t includes both block copolymer segments and monomers, we separate t into two species: block copolymers and monomers.

Each functional derivative of free energy density due to chain connectivity for m-th block copolymer segment type s is given as

$$\begin{aligned}\frac{\partial\Phi_{ch}^{ex}}{\partial n_{0,s}^{m}\left(\mathbf{r}\right)} = &-\frac{\zeta^m}{\sum_{i=1}^{p_m} M_i^{\,m}}\left[\sum_{i=1}^{p_m}\left(M_i^{\,m}-1\right)\ln y_{i,i}^{m} + \sum_{i=1}^{p_m-1}\ln y_{i,i+1}^{m}\right] \\ &-\sum_{k=1}^{m_p}\frac{n_0^k\zeta^k}{\sum_{i=1}^{p_k} M_i^{\,k}}\left[\sum_{i=1}^{p_k}\left(M_i^{k}-1\right)\frac{\delta\ln y_{i,i}^{k}}{\delta n_{0,s}^{m}} + \sum_{i=1}^{p_k-1}\frac{\delta\ln y_{i,i+1}^{k}}{\delta n_{0,s}^{m}}\right],\end{aligned} \tag{A.3}$$

$$\frac{\partial \Phi_{ch}^{ex}}{\partial n_{1,s}^{m}(\mathbf{r})} = -\sum_{k=1}^{m_p} \frac{n_0^k \zeta^k}{\sum_{i=1}^{p_k} M_i^k} \left[\sum_{i=1}^{p_k} \left(M_i^k - 1 \right) \frac{\delta \ln y_{i,i}^k}{\delta n_{1,s}^m} + \sum_{i=1}^{p_k - 1} \frac{\delta \ln y_{i,i+1}^k}{\delta n_{1,s}^m} \right], \tag{A.4}$$

$$\begin{aligned} \frac{\partial \Phi_{ch}^{ex}}{\partial n_{2,s}^{m}(\mathbf{r})} = & -n_0^m \frac{2\vec{\mathbf{n}}_{V2}^{m} \cdot \vec{\mathbf{n}}_{V2}^{m}}{\left(n_2^m\right)^3 \sum_{i=1}^{p_m} M_i^m} \left[\sum_{i=1}^{p_m} \left(M_i^m - 1 \right) \ln y_{i,i}^m + \sum_{i=1}^{p_m - 1} \ln y_{i,i+1}^m \right] \\ & - \sum_{k=1}^{m_p} \frac{n_0^k \zeta^k}{\sum_{i=1}^{p_k} M_i^k} \left[\sum_{i=1}^{p_k} \left(M_i^k - 1 \right) \frac{\delta \ln y_{i,i}^k}{\delta n_{2,s}^m} + \sum_{i=1}^{p_k - 1} \frac{\delta \ln y_{i,i+1}^k}{\delta n_{2,s}^m} \right] \end{aligned}, \tag{A.5}$$

$$\frac{\partial \Phi_{ch}^{ex}}{\partial n_{3,s}^{m}(\mathbf{r})} = -\sum_{k=1}^{m_p} \frac{n_0^k \zeta^k}{\sum_{i=1}^{p_k} M_i^k} \left[\sum_{i=1}^{p_k} \left(M_i^k - 1 \right) \frac{\delta \ln y_{i,i}^k}{\delta n_{3,s}^m} + \sum_{i=1}^{p_k - 1} \frac{\delta \ln y_{i,i+1}^k}{\delta n_{3,s}^m} \right] \tag{A.6}$$

$$\frac{\partial \Phi_{ch}^{ex}}{\partial \vec{\mathbf{n}}_{V1,s}^{m}(\mathbf{r})} = 0, \tag{A.7}$$

$$\begin{aligned} \frac{\partial \Phi_{ch}^{ex}}{\partial \vec{\mathbf{n}}_{V2,s}^{m}(\mathbf{r})} = & n_0^m \frac{2\vec{\mathbf{n}}_{V2}^{m}}{\left(n_2^m\right)^2 \sum_{i=1}^{p_m} M_i^m} \left[\sum_{i=1}^{p_m} \left(M_i^m - 1 \right) \ln y_{i,i}^m + \sum_{i=1}^{p_m - 1} \ln y_{i,i+1}^m \right] \\ & - \sum_{k=1}^{m_p} \frac{n_0^k \zeta^k}{\sum_{i=1}^{p_k} M_i^k} \left[\sum_{i=1}^{p_k} \left(M_i^k - 1 \right) \frac{\delta \ln y_{i,i}^k}{\delta \vec{\mathbf{n}}_{V2,s}^{m}} + \sum_{i=1}^{p_k - 1} \frac{\delta \ln y_{i,i+1}^k}{\delta \vec{\mathbf{n}}_{V2,s}^{m}} \right] \end{aligned}, \tag{A.8}$$

where

$$\frac{\delta \ln y_{i,j}^k}{\delta n_{0,s}^m} = -\frac{1}{4\pi \sigma_{i,j}^k l_B} \left(2\Gamma a_i^k a_j^k \frac{\delta \Gamma}{\delta n_{0,s}^m} + \Gamma^2 a_i^k \frac{\delta a_j^k}{\delta n_{0,s}^m} + \Gamma^2 a_j^k \frac{\delta a_i^k}{\delta n_{0,s}^m} \right), \tag{A.9}$$

$$\frac{\delta \ln y_{i,j}^k}{\delta n_{1,s}^m} = -\frac{1}{4\pi \sigma_{i,j}^k l_B} \left(2\Gamma a_i^k a_j^k \frac{\delta \Gamma}{\delta n_{1,s}^m} + \Gamma^2 a_i^k \frac{\delta a_j^k}{\delta n_{1,s}^m} + \Gamma^2 a_j^k \frac{\delta a_i^k}{\delta n_{1,s}^m} \right), \tag{A.10}$$

$$\frac{\delta \ln y_{i,j}^k}{\delta n_{2,s}^m} = \frac{1+\vec{\mathbf{n}}_{V2}\cdot\vec{\mathbf{n}}_{V2}/{n_2}^2}{\frac{4(1-n_3)\sigma_{i,j}^k}{\sigma_i^k\sigma_j^k}+n_2\left(1-\vec{\mathbf{n}}_{V2}\cdot\vec{\mathbf{n}}_{V2}/{n_2}^2\right)}, \tag{A.11}$$

$$\frac{\delta \ln y_{i,j}^k}{\delta n_{3,s}^m} = \frac{4\sigma_{i,j}^k+\frac{2n_2\sigma_i^k\sigma_j^k\left(1-\vec{\mathbf{n}}_{V2}\cdot\vec{\mathbf{n}}_{V2}/{n_2}^2\right)}{1-n_3}}{4(1-n_3)\sigma_{i,j}^k+n_2\sigma_i^k\sigma_j^k\left(1-\vec{\mathbf{n}}_{V2}\cdot\vec{\mathbf{n}}_{V2}/{n_2}^2\right)} \tag{A.12}$$
$$-\frac{1}{4\pi\sigma_{i,j}^k l_B}\left(2\Gamma a_i^k a_j^k\frac{\delta\Gamma}{\delta n_{3,s}^m}+\Gamma^2 a_i^k\frac{\delta a_j^k}{\delta n_{3,s}^m}+\Gamma^2 a_j^k\frac{\delta a_i^k}{\delta n_{3,s}^m}\right),$$

$$\frac{\delta \ln y_{i,j}^k}{\delta \vec{\mathbf{n}}_{V1,s}^m} = 0, \tag{A.13}$$

$$\frac{\delta \ln y_{i,j}^k}{\delta \vec{\mathbf{n}}_{V2,s}^m} = -\frac{2\vec{\mathbf{n}}_{V2}/n_2}{\frac{4(1-n_3)\sigma_{i,j}^k}{\sigma_i^k\sigma_j^k}+n_2\left(1-\vec{\mathbf{n}}_{V2}\cdot\vec{\mathbf{n}}_{V2}/{n_2}^2\right)}. \tag{A.14}$$

The functional derivative of $\delta\Gamma/\delta n_{\alpha,s}^m$ and $\delta a_i^k/\delta n_{\alpha,s}^m$ is given as

$$\frac{\delta\Gamma}{\delta n_{\alpha,s}^m} = \frac{\frac{\partial f}{\partial P_n}\frac{\delta P_n}{\delta n_{\alpha,s}^m}+\frac{\partial f}{\partial n_{\alpha,s}^m}}{2\Gamma-\frac{\partial f}{\partial\Gamma}-\frac{\partial f}{\partial P_n}\frac{\delta P_n}{\delta\Gamma}}, \tag{A.15}$$

$$\frac{\delta a_i^k}{\delta n_{\alpha,s}^m} = \frac{\partial a_i^k}{\partial\Gamma}\frac{\delta\Gamma}{\delta n_{\alpha,s}^m}+\frac{\partial a_i^k}{\partial P_n}\frac{\delta P_n}{\delta n_{\alpha,s}^m}+\frac{\partial a_i^k}{\partial n_{\alpha,s}^m}, \tag{A.16}$$

where

$$f=\Gamma^2=\pi l_B\sum_t n_{0t}\left(\frac{1}{1+\Gamma\sigma_t}\right)^2\left(Z_t-\frac{\pi P_n{\sigma_t}^2}{2(1-n_3)}\right)^2, \tag{A.17}$$

$$\frac{\partial f}{\partial P_n}=\pi l_B\sum_t n_{0t}\left(\frac{1}{1+\Gamma\sigma_t}\right)^2\left(Z_t-\frac{\pi P_n{\sigma_t}^2}{2(1-n_3)}\right)\left(-\frac{\pi{\sigma_t}^2}{1-n_3}\right), \tag{A.18}$$

$$\frac{\partial f}{\partial n_{0,s}^m} = \pi l_B \left(\frac{1}{1+\Gamma\sigma_t} \right)^2 \left(Z_t - \frac{\pi P_n \sigma_t^{\,2}}{2(1-n_3)} \right)^2, \tag{A.19}$$

$$\frac{\partial f}{\partial n_{3,s}^m} = -\frac{\pi^2 l_B P_n \sigma_t^{\,2}}{(1-n_3)^2} \sum_t n_{0t} \left(\frac{1}{1+\Gamma\sigma_t} \right)^2 \left(Z_t - \frac{\pi P_n \sigma_t^{\,2}}{2(1-n_3)} \right), \tag{A.20}$$

$$\frac{\partial f}{\partial n_{\alpha,s}^m} = 0, \quad \alpha = 1, 2, V1, V2, \tag{A.21}$$

$$\frac{\partial f}{\partial \Gamma} = -\pi l_B \sum_t n_{0t} \frac{2\sigma_t}{(1+\Gamma\sigma_t)^3} \left(Z_t - \frac{\pi P_n \sigma_t^{\,2}}{2(1-n_3)} \right)^2, \tag{A.22}$$

$$\frac{\partial a_i^k}{\partial \Gamma} = -2\pi l_B \left(Z_i^k - \frac{\pi P_n \left(\sigma_i^k\right)^2}{2(1-n_3)} \right) \frac{1+2\Gamma\sigma_i^k}{\Gamma^2 \left(1+\Gamma\sigma_i^k\right)^2}, \tag{A.23}$$

$$\frac{\partial a_i^k}{\partial P_n} = -\frac{\pi^2 l_B \left(\sigma_i^k\right)^2}{(1-n_3)\Gamma\left(1+\Gamma\sigma_i^k\right)}, \tag{A.24}$$

$$\frac{\partial a_i^k}{\partial n_{3,s}^m} = -\frac{\pi^2 l_B P_n \left(\sigma_i^k\right)^2}{\Gamma\left(1+\Gamma\sigma_i^k\right)(1-n_3)^2}, \tag{A.25}$$

$$\frac{\partial a_i^k}{\partial n_{\alpha,s}^m} = 0, \quad \alpha = 0, 1, 2, V1, V2, \tag{A.26}$$

$$\frac{\delta P_n}{\delta n_{\alpha,s}^m} = \frac{\partial P_n}{\partial \Gamma} \frac{\delta \Gamma}{\delta n_{\alpha,s}^m} + \frac{\partial P_n}{\partial n_{\alpha,s}^m}, \tag{A.27}$$

$$\frac{\partial P_n}{\partial \Gamma} = \frac{-\sum_t \frac{2n_{1t}Z_t\sigma_t}{(1+\Gamma\sigma_t)^2}}{1+\frac{3}{1-n_3}\sum_t \frac{n_{3t}}{1+\Gamma\sigma_t}} + \frac{\sum_t \frac{2n_{1t}Z_t}{1+\Gamma\sigma_t}}{\left(1+\frac{3}{1-n_3}\sum_t \frac{n_{3t}}{1+\Gamma\sigma_t}\right)^2} \frac{3}{1-n_3} \sum_t \frac{n_{3t}\sigma_t}{(1+\Gamma\sigma_t)^2}, \tag{A.28}$$

$$\frac{\partial P_n}{\partial n_{1,s}^m} = \frac{\dfrac{2Z_{1,s}^m}{1+\Gamma\sigma_{1,s}^m}}{1+\dfrac{3}{1-n_3}\displaystyle\sum_t \frac{n_{3t}}{1+\Gamma\sigma_t}}, \tag{A.29}$$

$$\frac{\partial P_n}{\partial n_{3,s}^m} = -\frac{\displaystyle\sum_t \frac{2n_{1t}Z_t}{1+\Gamma\sigma_t}}{\left(1+\dfrac{3}{1-n_3}\displaystyle\sum_t \frac{n_{3t}}{1+\Gamma\sigma_t}\right)^2}\left(\sum_t \frac{3n_{3t}}{(1-n_3)^2(1+\Gamma\sigma_t)} + \frac{3}{(1-n_3)(1+\Gamma\sigma_s^m)}\right), \tag{A.30}$$

$$\frac{\partial P_n}{\partial n_{\alpha,s}^m} = 0, \quad \alpha = 0,2,V1,V2\,. \tag{A.31}$$

On the other hand, each functional derivative of free energy density due to chain connectivity for monomer type u is given as

$$\frac{\partial \Phi_{ch}^{ex}}{\partial n_{\alpha,u}(\mathbf{r})} = -\sum_{k=1}^{m_p} \frac{n_0^k \zeta^k}{\displaystyle\sum_{i=1}^{p_k} M_i^k}\left[\sum_{i=1}^{p_k}\left(M_i^k - 1\right)\frac{\delta \ln y_{i,i}^k}{\delta n_{\alpha,u}^m} + \sum_{i=1}^{p_k-1}\frac{\delta \ln y_{i,i+1}^k}{\delta n_{\alpha,u}^m}\right], \tag{A.32}$$

where $\alpha = 0,1,2,3,V1,V2$.

Appendix B: Solution of One-Dimensional Poisson Equation

If the density profiles are spherically symmetric, the density distributions of polyelectrolyte segment and small ions are only r dependent and the Poisson equation can be reduced to:

$$\frac{1}{r^2}\frac{d}{dr}\left(r^2\frac{d\psi(r)}{dr}\right)=-\frac{4\pi e}{\varepsilon}\rho_c(r). \tag{B.1}$$

To solve Eq. (B.1), two boundary conditions are necessary and both boundary conditions can be specified depending on the system. For simplicity, we choose

$$\left.\frac{d\psi(r)}{dr}\right|_{r=r_c}=0, \tag{B.2}$$

$$\left.\psi(r)\right|_{r=r_c}=0, \tag{B.3}$$

where r_c means the calculation range beyond which the electrolyte solution already reaches bulk properties. To solve Eq. (B.1), we do integration on both sizes of Eq. (B.1),

$$\int_r^{r_c} d\left(r_1^2\frac{d\psi(r_1)}{dr_1}\right)=-\frac{4\pi e}{\varepsilon}\int_r^{r_c} r_1^2\rho_c(r_1)dr_1. \tag{B.4}$$

By applying one boundary condition given in Eq. (B.2), we have

$$r^2\frac{d\psi(r)}{dr}=\frac{4\pi e}{\varepsilon}\int_r^{r_c} r_1^2\rho_c(r_1)dr_1. \tag{B.5}$$

Similar to Eq. (B.4), we do integration on both sides of Eq. (B.5) and applies another boundary condition specified in Eq. (B.3),

$$\begin{aligned}\psi(r) &= -\frac{4\pi e}{\varepsilon}\int_r^{r_c}\frac{1}{r_2^{\,2}}dr_2\int_{r_2}^{r_c} r_1^{\,2}\rho_c(r_1)\,dr_1 \\ &= \frac{4\pi e}{\varepsilon}\int_r^{r_c}\left(r_1-\frac{r_1^{\,2}}{r}\right)\rho_c(r_1)\,dr_1\end{aligned}. \tag{B.6}$$

For the case of slab, the density profile and electrostatic potential is only z dependent and the Poisson equation can be simplified as

$$\frac{d}{dz}\left(\frac{d\psi(z)}{dz}\right) = -\frac{4\pi e}{\varepsilon}\rho_c(z). \tag{B.7}$$

Similar to spherical geometry case, two boundary conditions are needed to solve Eq. (B.7) depending on the specific system. For simplicity, we choose:

$$\left.\frac{d\psi(z)}{dz}\right|_{z=z_c} = 0, \tag{B.8}$$

$$\left.\psi(z)\right|_{z=z_c} = 0, \tag{B.9}$$

where z_c means the calculation range beyond which the electrolyte solution already reaches bulk properties. Similar to Eq. (B.4), we do integration on both sizes of Eq. (B.7) and apply one boundary condition given in Eq. (B.8):

$$\frac{d\psi(z)}{dz} = \frac{4\pi e}{\varepsilon}\int_z^{z_c}\rho_c(z_1)\,dz_1. \tag{B.10}$$

After another integration on both sides of Eq. (B.10) with Eq. (B.9) as a boundary condition, we have

$$\begin{aligned}\psi(z) &= -\frac{4\pi e}{\varepsilon}\int_z^{z_c} dz_2\int_{z_2}^{z_c}\rho_c(z_1)\,dz_1 \\ &= \frac{4\pi e}{\varepsilon}\int_z^{z_c}(z-z_1)\,\rho_c(z_1)\,dz_1\end{aligned}. \tag{B.11}$$

Appendix C: Theoretical Method for Rapid Prediction of Solvation Free Energy in Water: Computational Details for MD Simulation and DFT Calculations

In the following we describe the computational procedure to obtain the direct correlation function of SPC/E water in the bulk and the local distribution of water molecules around individual halide (F^-, Cl^-, Br^- and I^-) and alkali (Li^+, Na^+, K^+, Rb^+ and Cs^+) ions. In addition, we give the detail equation for calculation of the excess chemical potential of SPC/E water in the bulk and that for the ionic solvation free energy.

C. 1 MD Simulation

We combine molecular dynamics (MD) simulation and the molecular Orenstein-Zernike (OZ) equation [295, 296] to calculate the direct correction function of SPC/E water in the bulk. Namely, the direct correction function is solved from the OZ equation with the total correlation function extracted from MD simulation as the input. The MD simulation was carried out with package Moldy [297] within the NVT ensemble. The system temperature is set at T=300 K using the Nose-Hoover method. The number of water molecules simulated is N=4096, and the simulation box has a dimension of 49.738 × 49.738 × 49.738 $Å^3$. The periodic boundary condition is applied to all three directions.

As depicted in Fig. C-1(a), the relative conformation for a pair of SPC/E water molecules can be described by the center-to-center distance between the oxygen atoms (r) and by the Euler angles of each water molecule $\Theta_{i=1,2} = (\theta_i, \varphi_i, \psi_i)_{i=1,2}$. Using the intermolecular frame with the z-axis coinciding the vector connecting the center of one

oxygen atom to the other [296, 298], we may express the pair distribution function in terms of the oxygen-oxygen distance plus four angular variables:

$$g^{(2)}\left(\mathbf{x}_1,\mathbf{x}_2\right)=g\left(r,\cos\theta_1,\cos\theta_2,\varphi_{12},\psi_1,\psi_2\right), \tag{C.1}$$

where $\varphi_{12}=\varphi_1-\varphi_2$. The usage of a relative frame greatly reduces the matrix size to describe the pair correlation function.

Because the intermolecular potential depends weakly on ψ_1 and ψ_2 (the rotational angles along the dipolar axes), we assume that the pair distribution function can be effectively represented in terms of the dipole-dipole orientation, i.e.,

$$g\left(r,\cos\theta_1,\cos\theta_2,\varphi_{12}\right)=\left\langle g\left(r,\cos\theta_1,\cos\theta_2,\varphi_{12},\psi_1,\psi_2\right)\right\rangle_{\psi_1,\psi_2}. \tag{C.2}$$

We extract the pair correlation $g\left(r,\cos\theta_1,\cos\theta_2,\varphi_{12}\right)$ over 100,000 system configurations. In numerical implementation of the OZ equation, the radial distribution $g\left(r,\cos\theta_1,\cos\theta_2,\varphi_{12}\right)$ is discretized for $\cos\theta_1$ and $\cos\theta_2$ each by 10 equal intervals, φ_{12} by 20 equal intervals, and r by a step length of 0.1 Å.

Figure C-2 shows $g(r,\cos\theta_1,\cos\theta_2,\varphi_{12})$ calculated from the MD simulation for three representative sets of orientations between two water molecules. Whereas the position of the first peak is almost doubled when the relative dipolar orientations of two water molecules are changed from parallel (~2.5 Å in dash-dotted line) to anti-parallel (~5 Å in solid line), the magnitude of the pair distribution function varies only slightly with the molecular orientations. In sharp contrast to the pair interaction potential between two isolated water molecules, it appears that the magnitude of the potential of mean force

in bulk water, $-k_B T \ln g(r, \cos\theta_1, \cos\theta_2, \varphi_{12})$, is relatively insensitive to water orientations.

The Moldy program is also used to calculate the local distribution of water molecules around each ion. Simulation of alkali ions (Li^+, Na^+, K^+, Rb^+, Cs^+) and halide ions (F^-, Cl^-, Br^-, I^-) in SPC/E water was carried out with the NVT ensemble similar to that for pure water except that now an ion is placed at the center of the simulation box. The distribution of water molecules around the fixed ion is sampled within a spherical subsystem of diameter 40Å. This subsystem mimics an open system with the number of water molecules fluctuated and the chemical potential the same as that of the bulk. The Lennard-Jones parameters for the ions are the same as those reported by Joung and Cheatham [195]. The Lorentz-Berthelot combining rule is applied to the Lennard-Jones parameters between ion and water.

As shown in Fig. C-1(b), the orientation of each SPC/E molecule around a spherical ion is specified by three Euler angles θ, φ and ψ. Because of the spherical symmetry of the solute and the rotational symmetry of water molecules (φ angle), the solvent density depends only on distance r and two Euler angles (θ, ψ). Similar to water-water interactions, the water-ion interaction depends weakly on angle ψ and such dependence can be treated as an average over all water molecules. After the ensemble average, the density profile can be expressed as $\rho(r, \cos\theta) = \rho_0 g(r, \cos\theta)$ where ρ_0 is the bulk density, and $g(r, \cos\theta)$ represents the radial distribution function of water

molecules with respect to the solute. From each simulation, we sample the radial distribution function $g(r,\cos\theta)$ over 50,000 configurations.

As a representative example, Figure C-3 shows the reduced density profile of water molecules near a sodium ion and that near a chloride ion at three representative orientations. Near a cation surface, the orientation of water molecules is most favorable when its dipole aligns with the vector connecting the positions of the fixed ion and the oxygen atom. Interestingly, the most favorable orientation for a water molecule near an anion surface is not simply opposite to that near a cation surface. As shown in Fig. S3(b), near an anion surface the most favorable orientation corresponds to that when the anion center aligns with those of a hydrogen atom and the oxygen atom (instead of the charge center of two hydrogen sites). The asymmetry in the preferable orientations of water molecules near cations and anions is partially responsible for the difference in their solvation free energies. Such asymmetry cannot be captured by simple dipolar representation of water molecules.

C. 2 Direct Correlation Function

We calculate the direct correlation function (DCF) of bulk SPC/E water based on the intermolecular frame shown in Fig. C-1(a). In the Fourier space, the molecular Ornstein-Zernike (OZ) equation is given by [295, 296]

$$h(k,\cos\theta_1,\cos\theta_2,\varphi_1,\varphi_2) = c(k,\cos\theta_1,\cos\theta_2,\varphi_1,\varphi_2) + \frac{\rho_0}{(4\pi)^2}\int d\cos\theta_3 d\varphi_3 c(k,\cos\theta_1,\cos\theta_3,\varphi_1,\varphi_3) h(k,\cos\theta_3,\cos\theta_2,\varphi_3,\varphi_2), \quad \text{(C.3)}$$

where $c\left(k,\cos\theta_1,\cos\theta_2,\varphi_1,\varphi_2\right)$ are $h\left(k,\cos\theta_1,\cos\theta_2,\varphi_1,\varphi_2\right)$ Fourier transformations of the DCF and the total correlation function (TCF)

$$h\left(r,\cos\theta_1,\cos\theta_2,\varphi_{12}\right)=g\left(r,\cos\theta_1,\cos\theta_2,\varphi_{12}\right)-1. \tag{C.4}$$

With discretized representations of the orientational variables, the molecular OZ equation can be readily expressed as a multi-dimensional matrix equation at each k value [21].

Whereas the OZ equation is formally exact, direct evaluation of TCF is not reliable when Fourier variable k is small. To illustrate, Figure C-4(a) shows the total correlation function between oxygen atoms in the k space, i.e., $h_{OO}(k)$, obtained from Fourier transformation and that from direct simulation of the structure factor

$$S_{OO}(k)=\frac{1}{N}\left\langle\sum_{i=1}^{N}\sum_{j=1}^{N}\exp\left[-i\mathbf{k}\cdot\left(\mathbf{r}_i-\mathbf{r}_j\right)\right]\right\rangle, \tag{C.5}$$

where N stands for the number of water molecules, $\mathbf{r}$ denotes the position of an oxygen atom, and $\langle ... \rangle$ represents the ensemble average over all water configurations. The structure factor and total correlation function are related by [21]

$$S_{OO}\left(k\right)=1+n_O h_{OO}\left(k\right). \tag{C.6}$$

where n_O is the number density of oxygen atoms. In calculation of $h_{OO}(k)$ directly from simulation, we take vector $\mathbf{k}$ along the coordinate axis, and the step length as $2\pi/L$ with L the length of the cubic simulation box explained above. Figure C-4(a) indicates that the direct simulation and the Fourier transform method give identical results at large k. However, noticeable difference is observed when k approaches zero due to numerical uncertainty in transformation of the total correlation function from the real space to the

Fourier space. In this regime, the total correlation function may be represented by the asymptotic relation

$$h_{OO}(k) = h_{OO}^{(0)} + h_{OO}^{(2)} k^2 + \cdots. \tag{C.7}$$

Substituting Eq. (C.7) into the OZ equation

$$c_{OO}(k) = \frac{h_{OO}(k)}{1 + \rho_0 h_{OO}(k)}, \tag{C.8}$$

leads to

$$c_{OO}(k) = c_{OO}^{(0)} + c_{OO}^{(2)} k^2 + \cdots. \tag{C.9}$$

Because direct simulation of the structure factor for the entire range of k is numerically cumbersome, in particular when the structure factor depends also on molecular orientations, we use the asymptotic relation (Eq. (C.9)) in this work to correct the direct correlation function $c(k, \cos\theta_1, \cos\theta_2, \varphi_{12})$ at small k at each set of molecular orientations.

Figure C-4(b) shows the oxygen-oxygen direct correlation function after an average over all intermolecular orientations, i.e.,

$$c_{OO}(k) = \frac{1}{8\pi} \int_{-1}^{1} d\cos\theta_1 \int_{-1}^{1} d\cos\theta_2 \int_{0}^{2\pi} d\varphi_{12} c(k, \cos\theta_1, \cos\theta_2, \varphi_{12}). \tag{C.10}$$

For comparison, also shown in Fig. C-4(b) is the oxygen-oxygen direct correlation function obtained from Eq. (C.8) with the total correlation function obtained by Fourier transform for large k and by direct simulation of the structure factor for small k [21, 299]. As expected, the two methods yield virtually identical results. The direct correlation

function in Fourier space, $c\left(k,\cos\theta_1,\cos\theta_2,\varphi_{12}\right)$, is directly used for evaluation of the solvation free energy.

C. 3 Effective Hard-Sphere Diameter of Water Molecules

The effective hard-sphere diameter of water molecules is determined by considering the self-solvation of a water molecule in bulk water. According to the SPC/E model, the self-solvation free energy of a water molecule or the excess chemical potential of pure water is -23.01 kJ/mol at the temperature and the liquid density considered in this work (300K and 0.996 g/cm^3) [200, 201]. This value allows us to determine the reference hard-sphere diameter self-consistently.

In computation of the self-solvation free energy, we use a relative intermolecular frame as shown in Fig. C-1(a) such that both the position and the orientation of the tagged water molecule are fixed. The origin of the coordinate system coincides with the position of the oxygen atom of the tagged water molecule, the *z*-axis aligns with the electric dipole, and the x-axis is parallel to the vector connecting the centers of the two hydrogen atoms. The solvent density profile near the tagged water molecule, $\rho\left(\mathbf{x}\right)$, is related to the radial distribution function obtained from simulation of the bulk water [298]

$$\rho\left(\mathbf{x}\right)=\rho_0 g\left(r,\cos\theta_1,\cos\theta_2,\varphi_{12}\right). \tag{C.11}$$

The self-solvation free energy is calculated on a 3D cubic grid of size 30.0×30.0×30.0 Å^3. Such grid is discretized equally into 300×300×300 grid points while on each grid point the orientation space $\left(\cos\theta,\varphi\right)$ is discretized into 5 Gauss-Legendre angular grids and 10 equal intervals, respectively. In a relative frame with its origin at the

center of grid and three axes along the cubic grid box vectors, the density profile at each grid point, $\rho\left(x_i, y_j, z_k, \cos\theta_l, \varphi_m\right)$, is transferred from $\rho_0 g\left(r, \cos\theta_1, \cos\theta_2, \varphi_{12}\right)$ by linear interpolations. The self-solvation free energy is related to the solvent density profile $\rho\left(x_i, y_j, z_k, \cos\theta_l, \varphi_m\right)$ according to Eq. (C.10) of the main text except that, in calculation of the bridge function, the external potential (or the solute-solvent potential) is now replaced by the pair potential between water molecules

$$V_{ext}\left(\mathbf{x}\right) = \sum_{site\ \alpha}^{solute} \sum_{site\ \beta}^{solvent} \frac{q_\alpha q_\beta e^2}{r_{\alpha\beta}} + 4\varepsilon_{oo}\left[\left(\frac{\sigma_{oo}}{r_{oo}}\right)^{12} - \left(\frac{\sigma_{oo}}{r_{oo}}\right)^{6}\right]. \tag{C.12}$$

In Eq. (C.12), q_α and q_β ($\alpha, \beta = O, H_1, H_2$) are the electric valences, and e is elementary charge, $r_{\alpha\beta}$ is the ditance between those two sites, ε_{oo} and σ_{oo} are, respectively, the energy and the size parameters of the Lennard-Jones potential.

In calculation of the self-solvation free energy, the first term in Eq. (6.10) of the main text is rewritten as

$$F_1\left[\rho\left(\mathbf{x}\right)\right] = k_B T \int d\mathbf{x}\left\{\rho\left(\mathbf{x}\right)\ln y\left(\mathbf{x}\right) - \rho\left(\mathbf{x}\right) + \rho_0\right\}, \tag{C.13}$$

where the cavity function is related to the external potential $y\left(\mathbf{x}\right) \equiv \rho\left(\mathbf{x}\right)\exp\left[\beta V_{ext}\left(\mathbf{x}\right)\right]/\rho_0$. Although $y\left(\mathbf{x}\right)$ cannot be calculated directly within the solute core, $\rho\left(\mathbf{x}\right)\ln y\left(\mathbf{x}\right)$ disappears as $\rho\left(\mathbf{x}\right)$ approaches zero. In this work, the solvent accessibility is defined numerically by the reduced local density $\rho\left(\mathbf{x}\right)/\rho_0 < \delta = 10^{-6}$. The final value of the solvation free energy is not sensitive to the threshold density. Beyond

the solute core, integration over $\mathbf{x}=(\mathbf{r};\cos\theta,\varphi)$ is carried out by summation over the grid points for the position and by the Gauss-Legendre method for orientations.

To calculate the convolution between $\Delta\rho(\mathbf{x}_1)$ and $c^{(2)}(\mathbf{x}_1,\mathbf{x}_2;\rho_0)$ in the second term in Eq. (6.10) of the main text

$$F_2\left[\rho(\mathbf{x})\right]=-\frac{k_BT}{2}\int d\mathbf{x}_1\int d\mathbf{x}_2\Delta\rho(\mathbf{x}_1)\Delta\rho(\mathbf{x}_2)c(\mathbf{x}_1,\mathbf{x}_2;\rho_0). \tag{C.14}$$

We first define an effective intrinsic potential

$$V_{\text{int}}(\mathbf{x}_2)=-\frac{k_BT}{2}\int d\mathbf{x}_1\Delta\rho(\mathbf{x}_1)c(\mathbf{x}_1,\mathbf{x}_2), \tag{C.15}$$

with the direct correlation in Fourier space obtained from the OZ equation, Eq. (C.15) can be readily evaluated with the fast Fourier transform (FFT) method. From $V_{\text{int}}(\mathbf{x}_2)$, we can rewrite Eq. (C.14) as

$$F_2\left[\rho(\mathbf{x})\right]=\int d\mathbf{x}_2\Delta\rho(\mathbf{x}_2)V_{\text{int}}(\mathbf{x}_2). \tag{C.16}$$

In Eq. (C.16), the integral over $\mathbf{x}_2$ is carried out on the 3D grid similar to that for $F_1\left[\rho(\mathbf{x})\right]$, i.e., integration over $\mathbf{r}$ is via summation of $\Delta\rho(\mathbf{x}_2)V_{\text{int}}(\mathbf{x}_2)$ in each grid cell, and the integration over orientations is carried out using the Gauss-Legendre method.

Finally, we calculate the short-range (SR) and the long-range (LR) contributions of the bridge functional separately. As discussed in the main text, the short-range bridge functional $F_B^{SR}\left[\rho(\mathbf{x})\right]$ is equivalent to that of a reference hard-sphere system, i.e., $F_B^{HS}\left[n(\mathbf{r})\right]$ with $n(\mathbf{r})=\int\rho(\mathbf{r},\Theta)d\Theta$. Because $F_B^{HS}\left[n(\mathbf{r})\right]$ is independent of water orientations, Eq. (6.7) in the main text can be calculated on a 3D grid as detailed in our

previous work [85, 300]. According to the modified fundmanetal measure theory (MFMT) [85, 88], the free energy for the inhomogeneous hard sphere system is given by

$$F_{MFMT}^{ex}\left[n(\mathbf{r})\right]=k_BT\int\left[\Phi^{S(CS)}(\mathbf{r})+\Phi^{V(CS)}(\mathbf{r})\right]d\mathbf{r}\,, \tag{C.17}$$

with

$$\begin{aligned}\Phi^{S(CS)}(\mathbf{r})=&-n_0\ln(1-n_3)+\frac{n_1n_2}{1-n_3}\\&+\left[\frac{1}{36\pi n_3^2}\ln(1-n_3)+\frac{1}{36\pi n_3(1-n_3)^2}\right]n_2^3\end{aligned}, \tag{C.18}$$

and

$$\Phi^{V(CS)}(\mathbf{r})=-\frac{\mathbf{n}_{V1}\cdot\mathbf{n}_{V2}}{1-n_3}-\left[\frac{1}{12\pi n_3^2}\ln(1-n_3)+\frac{1}{12\pi n_3(1-n_3)^2}\right]n_2\mathbf{n}_{V2}\cdot\mathbf{n}_{V2}. \tag{C.19}$$

Weighted densities n_i ($i=0,1,2,3$) and $\mathbf{n}_{V1}$, $\mathbf{n}_{V2}$ are determined by $n(\mathbf{r})$ and the relations can be found in previous publications [85, 88]. For bulk hard-sphere system with a uniform density n_0, $F_{HS}^{ex}(n_0)$ reduces to the Helmholtz energy from the Carnahan-Starling (CS) equation of state [292]

$$F_{HS}^{ex}(n_0)=\frac{6Vk_BT}{\pi d^3}\frac{(4-3\eta)\eta^2}{(1-\eta)^2}, \tag{C.20}$$

where $\eta=\pi n_0d^3/6$ stands for the hard-sphere packing fraction. The excess chemical potential from the CS equation is given by

$$\mu_{0,HS}^{ex}=\frac{\eta(8-9\eta+3\eta^2)}{(1-\eta)^3}k_BT\,. \tag{C.21}$$

In Eq. (6.7) of the main text, integral $\int d\mathbf{r}\Delta n(\mathbf{r})$ is determined through $g(r,\cos\theta_1,\cos\theta_2,\varphi_{12})$, i.e.,

$$\int d\mathbf{r}\Delta n(\mathbf{r}) = \frac{n_0}{2}\int r^2 dr\left[g(r,\cos\theta_1,\cos\theta_2,\varphi_{12})-1\right]d\cos\theta_1 d\cos\theta_2 d\varphi_{12} = \overline{\Delta N}. \quad \text{(C.22)}$$

While for calculation of ionic solvation freee energy Eq. (C.22) must be evaluated numericlly on the 3D grid, the integral is exactly known for self-solvation, i.e., $\overline{\Delta N} = -1$ (because exactly only one water moelcule has been singled out). In evaluation of the last term of Eq. (6.7) in the main text, the direct correlation of the reference hard-sphere system, $c_{HS}^{(2)}(|\mathbf{r}_1-\mathbf{r}_2|)$, is calculated from MFMT [85, 88], and its convolution to $\Delta n(\mathbf{r}_1)$ and $\Delta n(\mathbf{r}_1)$ is implemented by FFT in a way similar to that for evaluation of $F_2[\rho(\mathbf{x})]$.

The long-range bridge term in Eq. (6.10) is calculated by substitution of Eq. (6.9) into Eq. (6.8) of the main text:

$$F_B^{LR}[\rho(\mathbf{x})] = -k_B T\int d\mathbf{x}\Delta\rho(\mathbf{x})\left\{\ln y(\mathbf{x}) - \int d\mathbf{x}' c(\mathbf{x},\mathbf{x}';\rho_0)\Delta\rho(\mathbf{x}')\right\}. \quad \text{(C.23)}$$

In Eq. (C.23), the integrals are applied only to the region accessible to water molecules, i.e., $\rho(\mathbf{x})/\rho_0 \geq \delta$. The integration procedure for $F_B^{LR}[\rho(\mathbf{x})]$ is similar to that for $F_1[\rho(\mathbf{x})]$ and $F_2[\rho(\mathbf{x})]$.

Finally the self-solvation free energy is obtained by adding up $F_1[\rho(\mathbf{x})]$, $F_2[\rho(\mathbf{x})]$ and the bridge contributions, i.e., $F_B^{LR}[\rho(\mathbf{x})]+F_B^{SR}[\rho(\mathbf{x})]$. Becasue the self-

solvation free energy is uniquely determined by the effective hard-sphere diameter d, we find that d =2.85Å yields the expected value of the self-solvation free energy.

C. 4 Ion Solvation Free Energy Computational procedure for the ion solvation free energy is similar to that for the self-solvation free energy of water. Because of the rotational symmetry of water molecules around a spherical solute, the calculation procedure can be slightly simplified. This simplification reduces the numerical error while improves the computational efficiency.

To calculate the solvation free energy for each ion, we rewrite the first term on the right side of Eq. (6.10) of the main text:

$$\begin{aligned} F_1\left[\rho(\mathbf{x})\right] &= k_B T \int d\mathbf{x}\left[\rho(\mathbf{x})\ln y(\mathbf{x}) - \rho(\mathbf{x}) + \rho_0\right] \\ &= 2\pi n_0 k_B T \int_0^\infty r^2 dr \int d\cos\theta \left\{ g(r,\cos\theta)\ln y(r,\cos\theta) - g(r,\cos\theta) + 1 \right\} \end{aligned}, \quad \text{(C.24)}$$

where $y(r,\cos\theta) \equiv g(r,\cos\theta)\exp\left[\beta V_{ext}(r,\cos\theta)\right]$, and the external potential $V_{ext}(r,\cos\theta)$ represents an average over angle ψ (see Fig. C-1b) for the solute-water interaction, i.e.,

$$\begin{aligned} V_{ext}(r,\cos\theta) &= \left\langle V_{ext}(r,\cos\theta,\psi)\right\rangle_\psi \\ &= -k_B T \ln\left\{ \frac{1}{\pi}\int_0^\pi \exp\left[-\beta V_{ext}(r,\cos\theta,\psi)\right] d\psi \right\} \end{aligned}, \quad \text{(C.25)}$$

Where

$$V_{ext}(r,\cos\theta,\psi) = \sum_{\text{site } \alpha}^{\text{on water}} \frac{q_s q_\alpha e^2}{r_{\alpha s}} + 4\varepsilon_{os}\left[\left(\frac{\sigma_{os}}{r}\right)^{12} - \left(\frac{\sigma_{os}}{r}\right)^{6}\right]. \quad \text{(C.26)}$$

In Eq. (C.26), q_s and q_α are the valences of the solute and α site (= O, H_1, H_2) of the water molecule, $r_{\alpha s}$ is the distance between solute and site α, ε_{os} and σ_{os} are, respectively, the energy parameter and size parameter of Lennard-Jones potential between oxygen site and solute [195]. The external potential is averaged over angle ψ from 0 to π because of the planar symmetry of the SPC/E model for water. In integration of Eq. (C.24), the integral is truncated at $r_m = 16$ Å, where the solvent density becomes uniform for all ions considered in this work.

For the hard-sphere reference system and an ion, the density profile $n(\mathbf{r})$ depends only on the radial distance. In that case, Eq. (C.17) simplifies [85]

$$F^{HS}\left[\rho(\mathbf{r})\right] = F^{HS}\left[g(r)\right], \tag{C.27}$$

with $g(r) = \int g(r,\cos) d\cos\theta / 2$. Calculation of the convolution term in Eq. (6.10) in the main text remains the same as that for self-solvation of water except that it entails on orientations.

From the water density profile obtained from MD, we can calculate the short- and long-range components of the bridge functional using Eqs. (6.7) and (6.8) in the main text, respectively. Figure C-5 shows representative results of $B^{LR}(r)$ and $B^{HS}(r)$ (after averaged over all water orientations) for solvation of cations and anions in water. As expected, the hard-sphere bridge function (in red) is most significant within the region not accessible to water molecules, and the zig-zag behavior near the solute surface is due to the average over all water orientations.

Figure C-1. Schematic diagrams for a pair of water molecules and for a water and an ion. (a) The intermolecular frame for two water molecules. The relative conformation can be determined by the center-to-center distance and by the Euler angles of both molecules, i.e., $(r,\theta_1,\varphi_1,\psi_1,\theta_2,\varphi_2,\psi_2)$ with r being the oxygen-oxygen distance and $(\theta_i,\varphi_i,\psi_i)_{i=1,2}$ the Euler angles of each water molecule. (b) The intermolecular frame for a spherical ion and a water molecule. The relative conformation is determined by (r,θ,φ,ψ) with r the ion-oxygen distance and (θ,φ,ψ) the Euler angles of the water molecule.

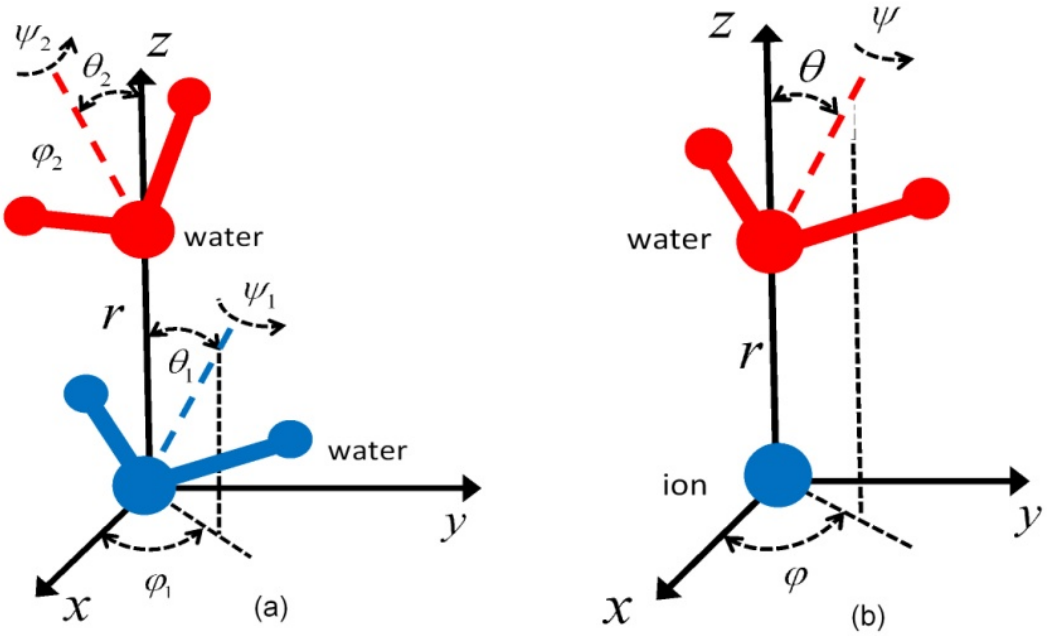

Figure C-2. The radial distribution function of bulk water $g\left(r,\cos\theta_1,\cos\theta_2,\varphi_{12}\right)$ at three representative orientations $\left(\cos\theta_1,\cos\theta_2,\varphi_{12}\right)$: (-0.9, 0.9, 0.95π), (-0.1, 0.9, 0.95π), and (0.9, 0.9, 0.95π).

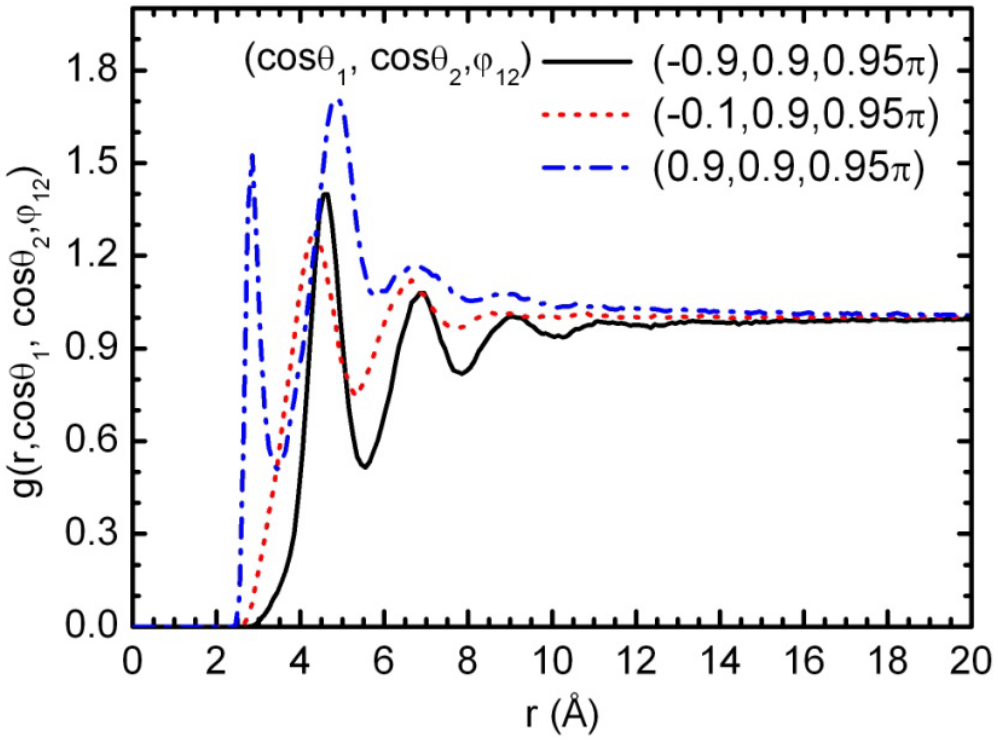

Figure C-3. The reduced density profile of water molecules, $g(r,\cos\theta) = \rho(r,\cos\theta)/\rho_0$ around (a) a sodium ion and (b) a chloride ion at various values of $\cos\theta$.

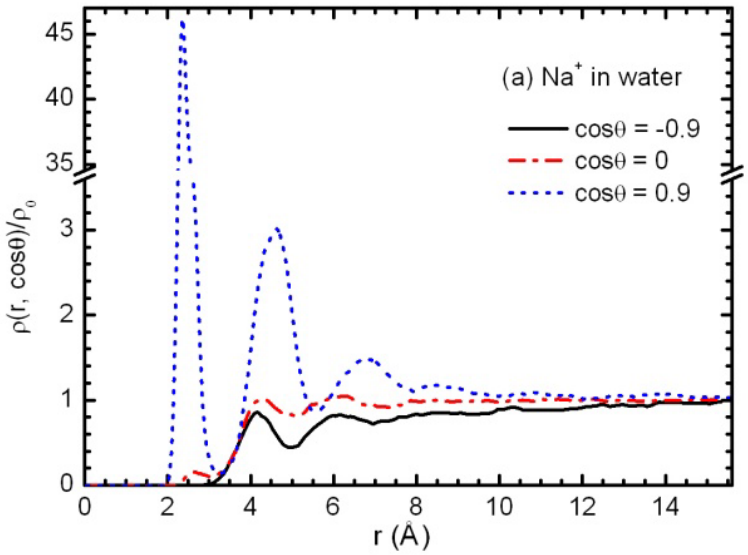

(a)

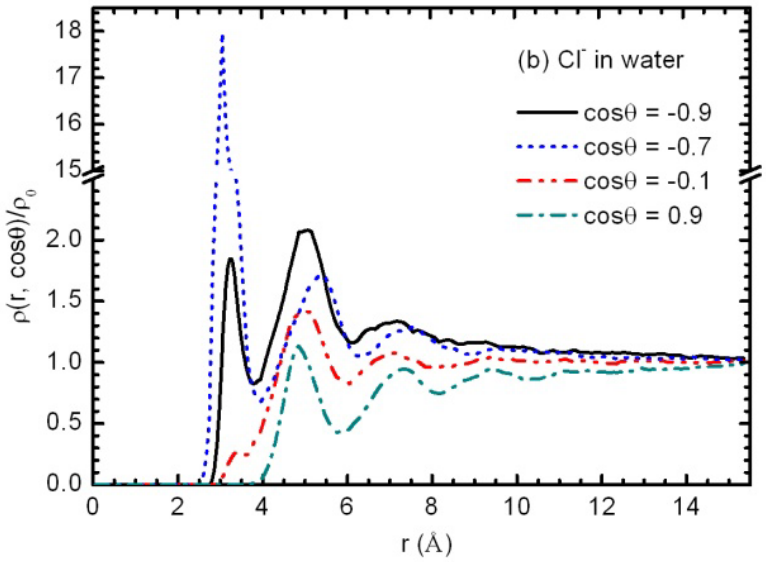

(b)

Figure C-4. The total and direct oxygen-oxygen correlation functions of SPC/E water in Fourier space. (a) The total oxygen-oxygen correlation functions calculated with Fourier transform (solid line) and with direct calculation of structure factor from simulation (circled dash line); (b) Direct oxygen-oxygen correlation function obtained by average of $c\left(k,\cos\theta_1,\cos\theta_2,\varphi_{12}\right)$ over orientations (circled line) and from total oxygen-oxygen correlation function (solid line).

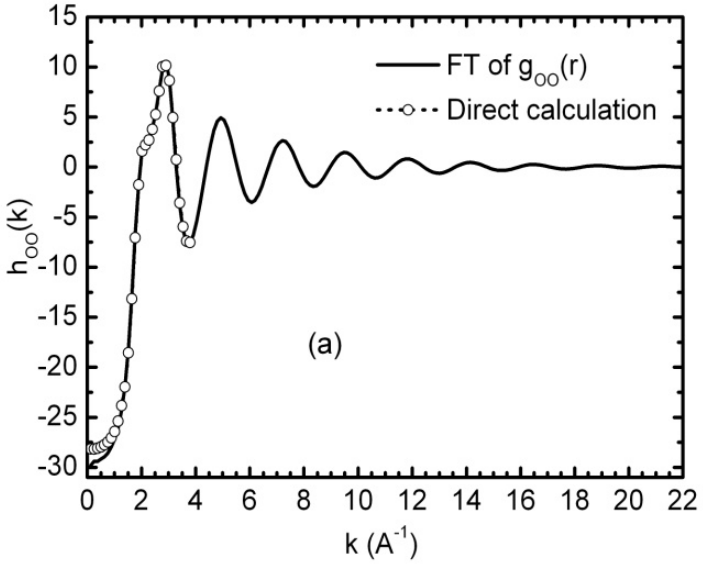

(a)

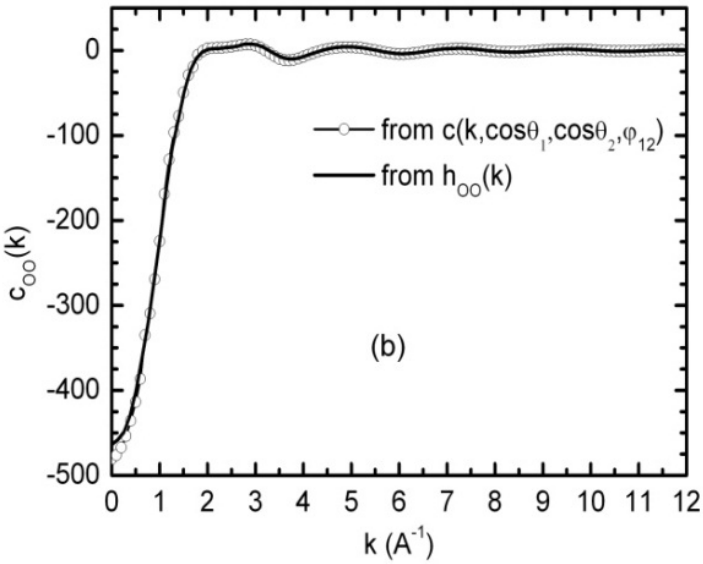

(b)

Figure C-5. The averaged LR bridge function over orientations of water (solid blank line) and bridge function of reference hard-sphere system (red line) for (a) Na^+ in water (b) Cl^- in water. The dashed lines are for a guide to the eye.

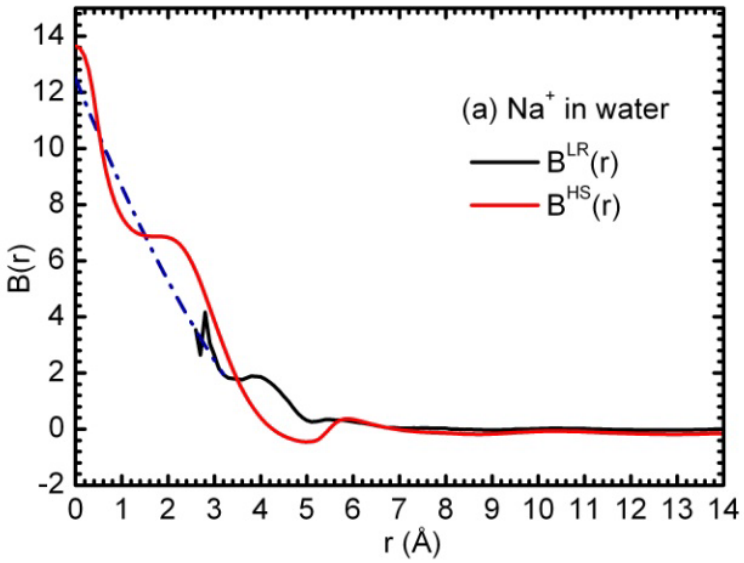

(a)

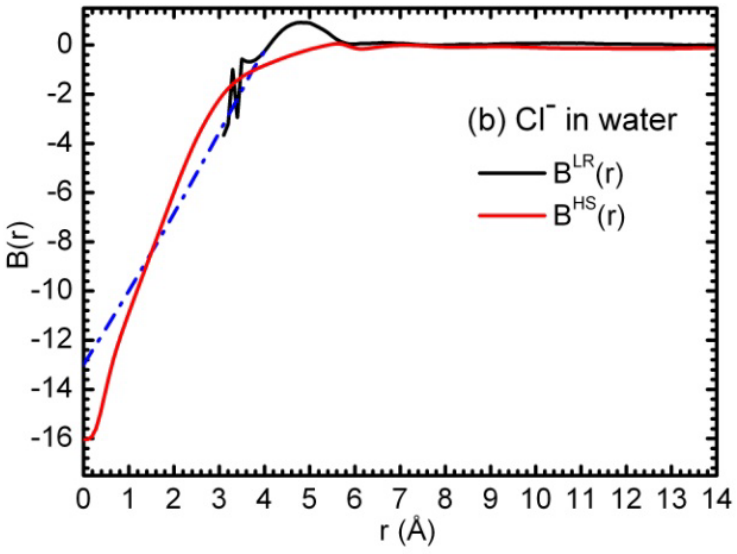

(b)

References

1. De Gennes, P.G., *Wetting - Statics and Dynamics.* Reviews of Modern Physics, 1985. **57**(3): p. 827-863.

2. Dietrich, S., *Phase Transitions and Critical Phenomena*, C. Domb and J.L. Lebowitz, Editors. 1988, Academic, New York.

3. Binder, K., *Modeling of wetting in restricted geometries.* Annual Review of Materials Research, 2008. **38**: p. 123-142.

4. Chandler, D., *Interfaces and the driving force of hydrophobic assembly.* Nature, 2005. **437**(7059): p. 640-647.

5. Chiu, C.Y., et al., *Platinum nanocrystals selectively shaped using facet-specific peptide sequences.* Nature Chemistry, 2011. **3**(5): p. 393-399.

6. Ye, X., et al., *Morphologically controlled synthesis of colloidal upconversion nanophosphors and their shape-directed self-assembly.* Proceedings of the National Academy of Sciences, 2010. **107**(52): p. 22430-22435.

7. Sun, Y. and Y. Xia, *Shape-Controlled Synthesis of Gold and Silver Nanoparticles.* Science, 2002. **298**(5601): p. 2176-2179.

8. Ashbaugh, H.S. and L.R. Pratt, *Colloquium: Scaled particle theory and the length scales of hydrophobicity.* Reviews of Modern Physics, 2006. **78**(1): p. 159-178.

9. Quere, D., *Wetting and roughness.* Annual Review of Materials Research, 2008. **38**: p. 71-99.

10. Jin, Z. and J. Wu, *Hybrid MC−DFT Method for Studying Multidimensional Entropic Forces.* Journal of Physical Chemistry B, 2011. **115**(6): p. 1450-1460.

11. Sacanna, S., et al., *Lock and key colloids.* Nature, 2010. **464**(7288): p. 575-578.

12. Solomon, M.J., *Materials science: Reconfigurable colloids.* Nature, 2010. **464**(7288): p. 496-498.

13. Eisenberg, D. and A.D. McLachlan, *Solvation energy in protein folding and binding.* Nature, 1986. **319**(6050): p. 199-203.

14. Terry P, L., *Ligand—protein docking and rational drug design.* Current Opinion in Structural Biology, 1995. **5**(2): p. 224-228.

15. Marcus, Y., *Effect of Ions on the Structure of Water: Structure Making and Breaking.* Chemical Reviews, 2009. **109**(3): p. 1346-1370.

16. Reiss, H., H.L. Frisch, and J.L. Lebowitz, *Statistical Mechanics of Rigid Spheres.* Journal of Chemical Physics, 1959. **31**(2): p. 369-380.

17. Helfand, E., et al., *Scaled Particle Theory of Fluids.* The Journal of Chemical Physics, 1960. **33**(5): p. 1379-1385.

18. Cotter, M.A., *Hard spherocylinders in an anisotropic mean field: A simple model for a nematic liquid crystal.* The Journal of Chemical Physics, 1977. **66**(3): p. 1098-1106.

19. Stillinger, F.H., *Structure in Aqueous Solutions of Nonpolar Solutes from the Standpoint of Scaled-Particle Theory.* Journal of Solution Chemistry, 1973. **2**(2-3): p. 141-158.

20. Ornstein, L.S. and F. Zernike, *Acculental deviations of density and opalescence at the critical point of a simple substance.* Proceedings of the Koninklijke Akademie Van Wetenschappen Te Amsterdam, 1914. **17**: p. 793-806.

21. Hansen, J.-P. and I.R. McDonald, *Theory of simple liquids*. Third ed. 2006, Amsterdam: Elsevier.

22. Kinoshita, M. and T. Oguni, *Depletion effects on the lock and key steric interactions between macromolecules.* Chemical Physics Letters, 2002. **351**(1-2): p. 79-84.

23. Roth, R., Y. Harano, and M. Kinoshita, *Morphometric Approach to the Solvation Free Energy of Complex Molecules.* Physical Review Letters, 2006. **97**(7): p. 078101.

24. Zhao, S., Z. Jin, and J. Wu, *New Theoretical Method for Rapid Prediction of Solvation Free Energy in Water.* Journal of Physical Chemistry B, 2011. **115**(21): p. 6971-6975.

25. Kelley, T.W., et al., *Recent Progress in Organic Electronics: Materials, Devices, and Processes.* Chemistry of Materials, 2004. **16**(23): p. 4413-4422.

26. McCrum, N.G., C.P. Buckley, and C.B. Bucknall, *Principles of polymer engineering*. 1997, New York: Oxford University Press.

27. Cacciuto, A. and E. Luijten, *Self-Avoiding Flexible Polymers under Spherical Confinement.* Nano Letters, 2006. **6**(5): p. 901-905.

28. Jun, S., A. Arnold, and B.-Y. Ha, *Confined Space and Effective Interactions of Multiple Self-Avoiding Chains.* Physical Review Letters, 2007. **98**(12): p. 128303-4.

29. Jin, Z., S. Zhao, and J. Wu, *Entropic forces of single-chain confinement in spherical cavities.* Physical Review E, 2010. **82**(4): p. 041805.

30. Li, Z., J. Wu, and Z.-G. Wang, *Osmotic Pressure and Packaging Structure of Caged DNA.* Biophysical Journal, 2008. **94**(3): p. 737-746.

31. Meng, D., et al., *A Theoretical Model for the Dynamic Structure of Hepatitis B Nucleocapsid.* Biophysical Journal, 2011. **101**(10): p. 2476-2484.

32. Ting, C.L., J. Wu, and Z.-G. Wang, *Thermodynamic basis for the genome to capsid charge relationship in viral encapsidation.* Proceedings of the National Academy of Sciences, 2011. **108**(41): p. 16986-16991.

33. Jiang, T., Z.-G. Wang, and J. Wu, *Electrostatic Regulation of Genome Packaging in Human Hepatitis B Virus.* Biophysical Journal, 2009. **96**(8): p. 3065-3073.

34. Likos, C.N., *Effective interactions in soft condensed matter physics.* Physics Reports-Review Section of Physics Letters, 2001. **348**(4-5): p. 267-439.

35. Theodorou, D.N., *Microscopic structure and thermodynamic properties of bulk copolymers and surface-active polymers at interfaces. 1. Theory.* Macromolecules, 1988. **21**(5): p. 1411-1421.

36. De Gennes, P.G., *Scaling Concepts in Polymer Physics*. 1979, Ithaca: Cornell University Press.

37. Daoud, M. and G. Jannink, *TEMPERATURE-CONCENTRATION DIAGRAM OF POLYMER-SOLUTIONS.* Journal De Physique, 1976. **37**(7-8): p. 973-979.

38. Daoud, M., et al., *SOLUTIONS OF FLEXIBLE POLYMERS - NEUTRON EXPERIMENTS AND INTERPRETATION.* Macromolecules, 1975. **8**(6): p. 804-818.

39. Degennes, P.G., *SCALING THEORY OF POLYMER ADSORPTION.* Journal De Physique, 1976. **37**(12): p. 1445-1452.

40. Andre, J.M., *SELF-CONSISTENT FIELD THEORY FOR ELECTRONIC STRUCTURE OF POLYMERS.* Journal of Chemical Physics, 1969. **50**(4): p. 1536-&.

41. Balazs, A.C., C. Singh, and E. Zhulina, *Modeling the interactions between polymers and clay surfaces through self-consistent field theory.* Macromolecules, 1998. **31**(23): p. 8370-8381.

42. Drolet, F. and G.H. Fredrickson, *Combinatorial screening of complex block copolymer assembly with self-consistent field theory.* Physical Review Letters, 1999. **83**(21): p. 4317-4320.

43. Schmid, F., *Self-consistent-field theories for complex fluids.* Journal of Physics-Condensed Matter, 1998. **10**(37): p. 8105-8138.

44. Baeurle, S.A., G.V. Efimov, and E.A. Nogovitsin, *Calculating field theories beyond the mean-field level.* Europhysics Letters, 2006. **75**(3): p. 378-384.

45. Bates, F.S. and G.H. Fredrickson, *Block Copolymers---Designer Soft Materials.* Physics Today, 1999. **52**(2): p. 32-38.

46. Blokhuis, E.M., K.I. Skau, and J.B. Avalos, *Free energy formalism for polymer adsorption: Self-consistent field theory for weak adsorption.* Journal of Chemical Physics, 2003. **119**(6): p. 3483-3494.

47. Wang, Q., T. Taniguchi, and G.H. Fredrickson, *Self-Consistent Field Theory of Polyelectrolyte Systems†*. Journal of Physical Chemistry B, 2004. **108**(21): p. 6733-6744.

48. Daoulas, K.C., et al., *Morphology of multi-component polymer systems: single chain in mean field simulation studies.* Soft Matter, 2006. **2**(7).

49. Chandler, D. and H.C. Andersen, *Optimized Cluster Expansions for Classical Fluids. II. Theory of Molecular Liquids.* Journal of Chemical Physics, 1972. **57**(5): p. 1930-1937.

50. Curro, J.G. and K.S. Schweizer, *THEORY OF POLYMER MELTS - AN INTEGRAL-EQUATION APPROACH.* Macromolecules, 1987. **20**(8): p. 1928-1934.

51. Schweizer, K.S. and J.G. Curro, *INTEGRAL-EQUATION THEORY OF THE STRUCTURE OF POLYMER MELTS.* Physical Review Letters, 1987. **58**(3): p. 246-249.

52. Schweizer, K.S. and J.G. Curro, *MICROPSCOPIC THEORY OF THE STRUCTURE, THERMODYNAMICS, AND APPARENT X-PARAMETER OF POLYMER BLENDS.* Physical Review Letters, 1988. **60**(9): p. 809-812.

53. Schweizer, K.S., K.G. Honnell, and J.G. Curro, *Reference interaction site model theory of polymeric liquids: Self-consistent formulation and nonideality effects in dense solutions and melts.* Journal of Chemical Physics, 1992. **96**(4): p. 3211-3225.

54. Rubinstein, M. and R.H. Colby, *Polymer Physics* 2003, Oxford: Oxford University Press.

55. Alder, B.J. and T.E. Wainwright, *Studies in Molecular Dynamics. I. General Method.* Journal of Chemical Physics, 1959. **31**(2): p. 459-466.

56. Frenkel, D., *Understanding molecular simulation: from algorithm to applications*. 2002, San Diego: Academic Press.

57. Allen, M. and D. Tildesley, *Computer Simulation of Liquids*. 1989, New York: Oxford University Press.

58. Care, C.M. and D.J. Cleaver, *Computer simulation of liquid crystals.* Reports on Progress in Physics, 2005. **68**(11): p. 2665.

59. Ruiz, R., et al., *Density Multiplication and Improved Lithography by Directed Block Copolymer Assembly.* Science, 2008. **321**(5891): p. 936-939.

60. Srinivas, G., D.E. Discher, and M.L. Klein, *Self-assembly and properties of diblock copolymers by coarse-grain molecular dynamics.* Nature Materials, 2004. **3**(9): p. 638-644.

61. Scheraga, H.A., M. Khalili, and A. Liwo, *Protein-Folding Dynamics: Overview of Molecular Simulation Techniques.* Annual Review of Physical Chemistry, 2007. **58**(1): p. 57-83.

62. Liao, Q., A.V. Dobrynin, and M. Rubinstein, *Molecular Dynamics Simulations of Polyelectrolyte Solutions: Osmotic Coefficient and Counterion Condensation.* Macromolecules, 2003. **36**(9): p. 3399-3410.

63. Wu, J. and Z. Li, *Density-Functional Theory for Complex Fluids.* Annual Review of Physical Chemistry, 2007. **58**(1): p. 85-112.

64. Wu, J., *Density functional theory for chemical engineering: From capillarity to soft materials.* AIChE Journal, 2006. **52**(3): p. 1169-1193.

65. Evans, R., *The nature of the liquid-vapour interface and other topics in the statistical mechanics of non-uniform, classical fluids.* Advances In Physics, 1979. **28**(2): p. 143-200.

66. Hohenberg, P. and W. Kohn, *Inhomogeneous Electron Gas.* Physical Review, 1964. **136**(3B): p. B864-B871.

67. Li, Z. and J. Wu, *Density Functional Theory for Polyelectrolytes near Oppositely Charged Surfaces.* Physical Review Letters, 2006. **96**(4): p. 048302.

68. Li, Z. and J. Wu, *Potential distribution theorem for the polymer-induced depletion between colloidal particles.* Journal of Chemical Physics, 2007. **126**(14): p. 144904.

69. Fu, D. and J. Wu *, *A self-consistent approach for modelling the interfacial properties and phase diagrams of Yukawa, Lennard-Jones and square-well fluids.* Molecular Physics, 2004. **102**(13): p. 1479-1488.

70. Jiang, D.-e., Z. Jin, and J. Wu, *Oscillation of Capacitance inside Nanopores.* Nano Letters, 2011. **11**(12): p. 5373-5377.

71. Cao, D. and J. Wu, *Theoretical Study of Cooperativity in Multivalent Polymers for Colloidal Stabilization.* Langmuir, 2005. **21**(21): p. 9786-9791.

72. Cao, D. and J. Wu, *Surface-induced phase transitions in ultrathin films of block copolymers.* Journal of Chemical Physics, 2005. **122**(19): p. 194703.

73. Cao, D. and J. Wu, *Microstructure of Block Copolymers near Selective Surfaces: Theoretical Predictions and Configurational-Bias Monte Carlo Simulation.* Macromolecules, 2005. **38**(3): p. 971-978.

74. Cao, D. and J. Wu, *Surface Forces between Telechelic Brushes Revisited: The Origin of a Weak Attraction.* Langmuir, 2006. **22**(6): p. 2712-2718.

75. Li, Z., D. Cao, and J. Wu, *Density-functional theory and Monte Carlo simulation for the surface structure and correlation functions of freely jointed Lennard-Jones polymeric fluids.* Journal of Chemical Physics, 2005. **122**(17): p. 174708.

76. Li, Z. and J. Wu, *Density Functional Theory for Planar Electric Double Layers: Closing the Gap between Simple and Polyelectrolytes.* Journal of Physical Chemistry B, 2006. **110**(14): p. 7473-7484.

77. Wu, J., *Molecular Thermodynamics of Complex Systems*, ed. X. Lu and Y. Hu. Vol. 131. 2009, Berlin: Springer. 1-73.

78. Rowlinson, J.S., *Translation of J. D. van der Waals' "The thermodynamik theory of capillarity under the hypothesis of a continuous variation of density"*. Journal of Statistical Physics, 1979. **20**(2): p. 197-200.

79. Yu, Y.-X. and J. Wu, *Density functional theory for inhomogeneous mixtures of polymeric fluids.* Journal of Chemical Physics, 2002. **117**(5): p. 2368-2376.

80. Wertheim, M.S., *Exact Solution of the Percus-Yevick Integral Equation for Hard Spheres.* Physical Review Letters, 1963. **10**(8): p. 321-323.

81. Kohn, W. and L.J. Sham, *Self-Consistent Equations Including Exchange and Correlation Effects.* Physical Review, 1965. **140**(4A): p. A1133-A1138.

82. Curtin, W.A. and N.W. Ashcroft, *Weighted-density-functional theory of inhomogeneous liquids and the freezing transition.* Physical Review A, 1985. **32**(5): p. 2909-2919.

83. Rosenfeld, Y., *Free-energy model for the inhomogeneous hard-sphere fluid mixture and density-functional theory of freezing.* Physical Review Letters, 1989. **63**(9): p. 980-983.

84. Rosenfeld, Y., D. Levesque, and J.-J. Weis, *Free-energy model for the inhomogeneous hard-sphere fluid mixture: Triplet and higher-order direct correlation functions in dense fluids.* Journal of Chemical Physics, 1990. **92**(11): p. 6818-6832.

85. Yu, Y.-X. and J. Wu, *Structures of hard-sphere fluids from a modified fundamental-measure theory.* Journal of Chemical Physics, 2002. **117**(22): p. 10156-10164.

86. Boublik, T., *Hard-Sphere Equation of State.* Journal of Chemical Physics, 1970. **53**(1): p. 471-472.

87. Mansoori, G.A., et al., *Equilibrium Thermodynamic Properties of the Mixture of Hard Spheres.* Journal of Chemical Physics, 1971. **54**(4): p. 1523-1525.

88. Roth, R., et al., *Fundamental measure theory for hard-sphere mixtures revisited: the White Bear version.* Journal of Physics: Condensed Matter, 2002. **14**(46): p. 12063.

89. Wertheim, M.S., *Fluids with highly directional attractive forces. I. Statistical thermodynamics.* Journal of Statistical Physics, 1984. **35**(1): p. 19-34.

90. Tildesley, D.J. and W.B. Streett, *An equation of state for hard dumbell fluids.* Molecular Physics, 1980. **41**(1): p. 85-94.

91. Yu, Y.-X. and J. Wu, *A fundamental-measure theory for inhomogeneous associating fluids.* Journal of Chemical Physics, 2002. **116**(16): p. 7094-7103.

92. Blum, L. and J.S. Hoye, *MEAN SPHERICAL MODEL FOR ASYMMETRIC ELECTROLYTES .2. THERMODYNAMIC PROPERTIES AND PAIR CORRELATION-FUNCTION.* Journal of Physical Chemistry, 1977. **81**(13): p. 1311-1317.

93. Blum, L., *MEAN SPHERICAL MODEL FOR ASYMMETRIC ELECTROLYTES .1. METHOD OF SOLUTION.* Molecular Physics, 1975. **30**(5): p. 1529-1535.

94. Blum, L., *Theoretical Chemistry: Advances and Perspectives*, ed. D. Henderson. Vol. 5. 1980, New York: Academic.

95. Jiang, J.W., et al., *A molecular-thermodynamic model for polyelectrolyte solutions.* Journal of Chemical Physics, 1998. **108**(2): p. 780-784.

96. Jiang, J.W., et al., *Thermodynamic properties and phase equilibria of charged hard sphere chain model for polyelectrolyte solutions.* Molecular Physics, 2001. **99**(13): p. 1121-1128.

97. Andersen, H.C. and D. Chandler, *OPTIMIZED CLUSTER EXPANSIONS FOR CLASSICAL FLUIDS .1. GENERAL THEORY AND VARIATIONAL FORMULATION OF MEAN SPHERICAL MODEL AND HARD-SPHERE PERCUS-YEVICK EQUATIONS.* Journal of Chemical Physics, 1972. **57**(5): p. 1918-+.

98. Andersen, H.C., D. Chandler, and J.D. Weeks, *OPTIMIZED CLUSTER EXPANSIONS FOR CLASSICAL FLUIDS .3. APPLICATIONS TO IONIC SOLUTIONS AND SIMPLE LIQUIDS.* Journal of Chemical Physics, 1972. **57**(7): p. 2626-+.

99. Hudson, S. and H.C. Andersen, *OPTIMIZED CLUSTER EXPANSIONS FOR CLASSICAL FLUIDS .4. PRIMITIVE MODEL ELECTROLYTE SOLUTIONS.* Journal of Chemical Physics, 1974. **60**(5): p. 2188-2188.

100. Tang, Y., *Direct correlation function for the square-well potential.* Journal of Chemical Physics, 2007. **127**(16): p. 164504.

101. Tang, Y.P. and J.Z. Wu, *Modeling inhomogeneous van der Waals fluids using an analytical direct correlation function.* Physical Review E, 2004. **70**(1).

102. Tang, Y.P., *On the first-order mean spherical approximation.* Journal of Chemical Physics, 2003. **118**(9): p. 4140-4148.

103. Jin, Z., Y. Tang, and J. Wu, *A perturbative density functional theory for square-well fluids.* Journal of Chemical Physics, 2011. **134**(17): p. 174702.

104. Hlushak, S., A. Trokhymchuk, and S. Sokolowski, *Direct correlation function of the square-well fluid with attractive well width up to two particle diameters.* Journal of Chemical Physics, 2009. **130**: p. 234511.

105. Tomasi, J. and M. Persico, *MOLECULAR-INTERACTIONS IN SOLUTION - AN OVERVIEW OF METHODS BASED ON CONTINUOUS DISTRIBUTIONS OF THE SOLVENT.* Chemical Reviews, 1994. **94**(7): p. 2027-2094.

106. Yu, Y.-X., J. Wu, and G.-H. Gao, *Density-functional theory of spherical electric double layers and zeta potentials of colloidal particles in restricted-primitive-model electrolyte solutions.* Journal of Chemical Physics, 2004. **120**(15): p. 7223-7233.

107. Hiroike, K., *SUPPLEMENT TO BLUMS THEORY FOR ASYMMETRIC ELECTROLYTES.* Molecular Physics, 1977. **33**(4): p. 1195-1198.

108. Fredrickson, G.H., *The Equilibrium Theory of Inhomogeneous Polymers*. 2006, New York: Oxford University Press.

109. Woodward, C.E. and J. Forsman, *Density functional theory for flexible and semiflexible polymers of infinite length.* Physical Review E, 2006. **74**(1).

110. Wertheim, M.S., *Thermodynamic perturbation theory of polymerization.* Journal of Chemical Physics, 1987. **87**(12): p. 7323-7331.

111. Kindt, J., et al., *DNA packaging and ejection forces in bacteriophage.* Proceedings of the National Academy of Sciences of the United States of America, 2001. **98**(24): p. 13671-13674.

112. Jun, S. and B. Mulder, *Entropy-driven spatial organization of highly confined polymers: Lessons for the bacterial chromosome.* Proceedings of the National Academy of Sciences, 2006. **103**(33): p. 12388-12393.

113. Grosberg, A.Y. and A.R. Khokhlov, *Statistical Physics of Macromolecules*. 1994, New York: American Institute of Physics.

114. Henderson, D., L. Blum, and J.L. Lebowitz, *An exact formula for the contact value of the density profile of a system of charged hard spheres near a charged wall.* Journal of Electroanalytical Chemistry and Interfacial Electrochemistry, 1979. **102**(3): p. 315-319.

115. Dautenhahn, J. and C.K. Hall, *Monte Carlo Simulation of Off-Lattice Polymer Chains: Effective Pair Potentials in Dilute Solution.* Macromolecules, 1994. **27**(19): p. 5399-5412.

116. Flory, P.J., *Principles of Polymer Chemistry*. 1953, Ithaca: Cornell University Press.

117. Kantor, Y. and M. Kardar, *Anomalous dynamics of forced translocation.* Physical Review E, 2004. **69**(2): p. 021806.

118. Purohit, P.K., et al., *Forces during bacteriophage DNA packaging and ejection.* Biophysical Journal, 2005. **88**(2): p. 851-866.

119. Sakaue, T. and E. Raphael, *Polymer Chains in Confined Spaces and Flow-Injection Problems: Some Remarks.* Macromolecules, 2006. **39**(7): p. 2621-2628.

120. Bezrukov, S.M., et al., *Dynamics and Free Energy of Polymers Partitioning into a Nanoscale Pore.* Macromolecules, 1996. **29**(26): p. 8517-8522.

121. Seeger, C. and W.S. Mason, *Hepatitis B Virus Biology.* Microbiology and Molecular Biology Reviews, 2000. **64**(1): p. 51-68.

122. De Guzman, R.N., et al., *Structure of the HIV-1 nucleocapsid protein bound to the SL3 Psi-RNA recognition element.* Science, 1998. **279**(5349): p. 384-388.

123. Melegari, M., P.P. Scaglioni, and J.R. Wands, *Hepatitis B virus mutants associated with 3TC and Famciclovir administration are replication defective.* Hepatology, 1998. **27**(2): p. 628-633.

124. Welsch, S., et al., *Composition and Three-Dimensional Architecture of the Dengue Virus Replication and Assembly Sites.* Cell Host & Microbe, 2009. **5**(4): p. 365-375.

125. Villordo, S.M. and A.V. Gamarnik, *Genome cyclization as strategy for flavivirus RNA replication.* Virus Research, 2009. **139**(2): p. 230-239.

126. Smith, D.E., et al., *The bacteriophage [phis]29 portal motor can package DNA against a large internal force.* Nature, 2001. **413**(6857): p. 748-752.

127. Zhang, D.Q., et al., *Electrostatic interaction between RNA and protein capsid in cowpea chlorotic mottle virus simulated by a coarse-grain RNA model and a Monte Carlo approach.* Biopolymers, 2004. **75**(4): p. 325-337.

128. Arsuaga, J., et al., *Knotting probability of DNA molecules confined in restricted volumes: DNA knotting in phage capsids.* Proceedings of the National Academy of Sciences of the United States of America, 2002. **99**(8): p. 5373-5377.

129. Marenduzzo, D. and C. Micheletti, *Thermodynamics of DNA packaging inside a viral capsid: The role of DNA intrinsic thickness.* Journal of Molecular Biology, 2003. **330**(3): p. 485-492.

130. Spakowitz, A.J. and Z.-G. Wang, *DNA Packaging in Bacteriophage: Is Twist Important?* Biophysical journal, 2005. **88**(6): p. 3912-3923.

131. Angelescu, D.G., R. Bruinsma, and P. Linse, *Monte Carlo simulations of polyelectrolytes inside viral capsids.* Physical Review E, 2006. **73**(4): p. 041921.

132. Angelescu, D.G., J. Stenhammar, and P. Linse, *Packaging of a Flexible Polyelectrolyte Inside a Viral Capsid: Effect of Salt Concentration and Salt Valence.* The Journal of Physical Chemistry B, 2007. **111**(29): p. 8477-8485.

133. Belyi, V.A. and M. Muthukumar, *Electrostatic origin of the genome packing in viruses.* Proceedings of the National Academy of Sciences of the United States of America, 2006. **103**(46): p. 17174-17178.

134. Kumar, R. and M. Muthukumar, *Confinement free energy of flexible polyelectrolytes in spherical cavities.* The Journal of Chemical Physics, 2008. **128**(18): p. 184902.

135. Forrey, C. and M. Muthukumar, *Electrostatics of capsid-induced viral RNA organization.* The Journal of Chemical Physics, 2009. **131**(10): p. 105101.

136. Butler, J.C., et al., *Ion Multivalence and Like-Charge Polyelectrolyte Attraction.* Physical Review Letters, 2003. **91**(2): p. 028301.

137. Ackermann, H.W. and M.S. Dubow, *Viruses of Prokaryotes*. 1987, Boca Raton, FL: CRC Press.

138. Qiao, R. and N.R. Aluru, *Charge Inversion and Flow Reversal in a Nanochannel Electro-osmotic Flow.* Physical Review Letters, 2004. **92**(19): p. 198301.

139. Boda, D., et al., *Computing induced charges in inhomogeneous dielectric media: Application in a Monte Carlo simulation of complex ionic systems.* Physical Review E, 2004. **69**(4): p. 046702.

140. Messina, R., *Image charges in spherical geometry: Application to colloidal systems.* Journal of Chemical Physics, 2002. **117**(24): p. 11062-11074.

141. Gillespie, D., *Free-Energy Density Functional of Ions at a Dielectric Interface.* The Journal of Physical Chemistry Letters, 2011. **2**(10): p. 1178-1182.

142. Lu, B.Z., et al., *Recent progress in numerical methods for the Poisson-Boltzmann equation in biophysical applications.* Communications in Computational Physics, 2008. **3**(5): p. 973-1009.

143. Johnson, J.M., et al., *Regulating Self-Assembly of Spherical Oligomers.* Nano Letters, 2005. **5**(4): p. 765-770.

144. Yethiraj, A. and C.E. Woodward, *Monte Carlo density functional theory of nonuniform polymer melts.* The Journal of Chemical Physics, 1995. **102**(13): p. 5499-5505.

145. Cao, D. and J. Wu, *Density functional theory for semiflexible and cyclic polyatomic fluids.* The Journal of Chemical Physics, 2004. **121**(9): p. 4210-4220.

146. Akesson, T., C. Woodward, and B. Jonsson, *Electric double layer forces in the presence of polyelectrolytes.* The Journal of Chemical Physics, 1989. **91**(4): p. 2461-2469.

147. Wang, K., Y.-X. Yu, and G.-H. Gao, *Density functional study on the structures and thermodynamic properties of small ions around polyanionic DNA.* Physical Review E, 2004. **70**(1): p. 011912.

148. Asakura, S. and F. Oosawa, *INTERACTION BETWEEN PARTICLES SUSPENDED IN SOLUTIONS OF MACROMOLECULES.* Journal of Polymer Science, 1958. **33**(126): p. 183-192.

149. Surve, M., V. Pryamitsyn, and V. Ganesan, *Depletion and pair interactions of proteins in polymer solutions.* Journal of Chemical Physics, 2005. **122**(15): p. 154901-16.

150. Kinoshita, M., *Spatial distribution of a depletion potential between a big solute of arbitrary geometry and a big sphere immersed in small spheres.* Journal of Chemical Physics, 2002. **116**(8): p. 3493-3501.

151. Kim, J.U. and M.W. Matsen, *Repulsion Exerted on a Spherical Particle by a Polymer Brush.* Macromolecules, 2007. **41**(1): p. 246-252.

152. Roth, R., R. Evans, and S. Dietrich, *Depletion potential in hard-sphere mixtures: Theory and applications.* Physical Review E, 2000. **62**(4): p. 5360-5377.

153. Striolo, A., et al., *The depletion attraction between pairs of colloid particles in polymer solution.* Molecular Simulation, 2004. **30**(7): p. 437-449.

154. Ronald, D., A. Phil, and S. Veronika, *Entropic forces in binary hard sphere mixtures: Theory and simulation.* Journal of Chemical Physics, 1997. **107**(1): p. 205-213.

155. Konig, P.M., R. Roth, and S. Dietrich, *Lock and key model system.* Europhysics Letters, 2008. **84**(6): p. 5.

156. Ellis, R.J., *Macromolecular crowding: obvious but underappreciated.* Trends in Biochemical Sciences, 2001. **26**(10): p. 597-604.

157. Jorgensen, W.L., *Rusting of the Lock and Key Model for Protein-Ligand Binding.* Science, 1991. **254**(5034): p. 954-955.

158. Piotr, S., *Water properties and potential of mean force for hydrophobic interactions of methane and nanoscopic pockets studied by computer simulations.* Journal of Chemical Physics, 2007. **127**(5): p. 054505.

159. Setny, P., et al., *Dewetting-Controlled Binding of Ligands to Hydrophobic Pockets.* Physical Review Letters, 2009. **103**(18): p. 187801.

160. Cheng, L.T., et al., *Interfaces and hydrophobic interactions in receptor-ligand systems: A level-set variational implicit solvent approach.* Journal of Chemical Physics, 2009. **131**(14): p. 144102.

161. Sui, H.X., et al., *Structural basis of water-specific transport through the AQP1 water channel.* Nature, 2001. **414**(6866): p. 872-878.

162. Young, T., et al., *Motifs for molecular recognition exploiting hydrophobic enclosure in protein-ligand binding.* Proceedings of the National Academy of Sciences of the United States of America, 2007. **104**(3): p. 808-813.

163. Konig, P.M., R. Roth, and S. Dietrich, *Depletion forces between nonspherical objects.* Physical Review E, 2006. **74**(4): p. 8.

164. Odriozola, G., F. Jimenez-Angeles, and M. Lozada-Cassou, *Entropy driven key-lock assembly.* Journal of Chemical Physics, 2008. **129**(11): p. 111101-4.

165. Widom, B., *Potential-distribution theory and the statistical mechanics of fluids.* Journal of Physical Chemistry, 1982. **86**(6): p. 869-872.

166. Metropolis, N., et al., *Equation of State Calculations by Fast Computing Machines.* Journal of Chemical Physics, 1953. **21**(6): p. 1087-1092.

167. Wu, J.Z., et al., *Monte Carlo simulation for the potential of mean force between ionic colloids in solutions of asymmetric salts.* Journal of Chemical Physics, 1999. **111**(15): p. 7084-7094.

168. Wu, J.Z., et al., *Interaction between oppositely charged micelles or globular proteins.* Physical Review E, 2000. **62**(4): p. 5273.

169. Konig, P.M., et al., *Curvature expansion of density profiles.* Europhysics Letters, 2005. **69**(5): p. 832-838.

170. Roth, R., et al., *Entropic Torque.* Physical Review Letters, 2002. **89**(8): p. 088301.

171. Roth, R., *Fundamental measure theory for hard-sphere mixtures: a review.* Journal of Physics-Condensed Matter, 2010. **22**(6): p. 063102.

172. Born, M., *Volumes and hydration warmth of ions.* Zeitschrift Fur Physik, 1920. **1**: p. 45-48.

173. Mayer, J.E., *THE THEORY OF IONIC SOLUTIONS.* Journal of Chemical Physics, 1950. **18**(11): p. 1426-1436.

174. Olivares, W. and D.A. McQuarrie, *THEORY OF IONIC-SOLUTIONS.* Biophysical Journal, 1975. **15**(2): p. 143-162.

175. Huang, D.M., P.L. Geissler, and D. Chandler, *Scaling of hydrophobic solvation free energies.* Journal of Physical Chemistry B, 2001. **105**(28): p. 6704-6709.

176. Hirata, F., *Molecular theory of solvation*. 2003, Boston: Kluwer Academic Publishers.

177. Ball, P., *Water as an active constituent in cell biology.* Chemical Reviews, 2008. **108**(1): p. 74-108.

178. Marenich, A.V., et al., *Self-consistent reaction field model for aqueous and nonaqueous solutions based on accurate polarized partial charges.* Journal of Chemical Theory and Computation, 2007. **3**(6): p. 2011-2033.

179. Mennucci, B. and R. Cammi, *Continuum solvation models in chemical physics: from theory to applications*. 2007, Chichester, England; Hoboken NJ: John Wiley & Sons.

180. Ben-Naim, A., *Solvation thermodynamics*. 1987, New York: Plenum Press.

181. Ben-Amotz, D. and R. Underwood, *Unraveling water's entropic mysteries: A unified view of nonpolar, polar, and ionic hydration.* Accounts of Chemical Research, 2008. **41**(8): p. 957-967.

182. Chandler, D., *Liquids: Condensed, disordered, and sometimes complex.* Proceedings of the National Academy of Sciences of the United States of America, 2009. **106**(36): p. 15111-15112.

183. Senn, H.M. and W. Thiel, *QM/MM Methods for Biological Systems*. Atomistic Approaches in Modern Biology, ed. M. Eriher. Vol. 268. 2007, Berlin Heidelberg: Springer-Verlag. 173-290.

184. Khavrutskii, I.V., et al., *Free Energy for the Permeation of Na+ and Cl- Ions and Their Ion-Pair through a Zwitterionic Dimyristoyl Phosphatidylcholine Lipid Bilayer by Umbrella Integration with Harmonic Fourier Beads.* Journal of the American Chemical Society, 2009. **131**(5): p. 1706-1716.

185. Kirchner, B., *Theory of complicated liquids - Investigation of liquids, solvents and solvent effects with modern theoretical methods.* Physics Reports-Review Section of Physics Letters, 2007. **440**(1-3): p. 1-111.

186. Schmidt, K.F. and S.M. Kast, *Hybrid integral equation/Monte Carlo approach to complexation thermodynamics.* Journal of Physical Chemistry B, 2002. **106**(24): p. 6289-6297.

187. Phongphanphanee, S., N. Yoshida, and F. Hirata, *On the proton exclusion of aquaporins: A statistical mechanics study.* Journal of the American Chemical Society, 2008. **130**(5): p. 1540-1541.

188. Chuev, G.N., et al., *Hydration of ionic species studied by the reference interaction site model with a repulsive bridge correction.* Journal of Computational Chemistry, 2008. **29**(14): p. 2406-2415.

189. Yoshida, N. and S. Kato, *Molecular Ornstein-Zernike approach to the solvent effects on solute electronic structures in solution.* Journal of Chemical Physics, 2000. **113**(12): p. 4974-4984.

190. Ramirez, R. and D. Borgis, *Density functional theory of solvation and its relation to implicit solvent models.* Journal of Physical Chemistry B, 2005. **109**(14): p. 6754-6763.

191. Yoshimori, A., *Time dependent density functional methods and their application to chemical physics.* Journal of Theoretical & Computational Chemistry, 2004. **3**(1): p. 117-143.

192. Lum, K., D. Chandler, and J.D. Weeks, *Hydrophobicity at small and large length scales.* Journal of Physical Chemistry B, 1999. **103**(22): p. 4570-4577.

193. Cramer, C.J. and D.G. Truhlar, *A universal approach to solvation modeling.* Accounts of Chemical Research, 2008. **41**(6): p. 760-768.

194. Berendsen, H.J.C., J.R. Grigera, and T.P. Straatsma, *THE MISSING TERM IN EFFECTIVE PAIR POTENTIALS.* Journal of Physical Chemistry, 1987. **91**(24): p. 6269-6271.

195. Joung, I.S. and T.E. Cheatham, *Determination of alkali and halide monovalent ion parameters for use in explicitly solvated biomolecular simulations.* Journal of Physical Chemistry B, 2008. **112**(30): p. 9020-9041.

196. Swanson, J.M.J., R.H. Henchman, and J.A. McCammon, *Revisiting free energy calculations: A theoretical connection to MM/PBSA and direct calculation of the association free energy.* Biophysical Journal, 2004. **86**(1): p. 67-74.

197. Leach, A.R., *Molecular modelling: principles and applications*. 2nd Edition ed. 2001, Harlow, England; New York: Prentice Hall.

198. Evans, R., *Fundamentals of Inhomogeneous Fluids*, ed. D. Henderson. 1992, New York: Marcel Dekker. 85-175.

199. Hirata, F., *Molecular Theory of Solvation*. 2003, Dordrecht; Boston: Kluwer Academic Publishers.

200. Ji, J., T. Cagin, and B.M. Pettitt, *DYNAMIC SIMULATIONS OF WATER AT CONSTANT CHEMICAL-POTENTIAL.* Journal of Chemical Physics, 1992. **96**(2): p. 1333-1342.

201. Hermans, J., A. Pathiaseril, and A. Anderson, *Excess free-energy of liquids from molecular-dynamics simulations-application to water models.* Journal of the American Chemical Society, 1988. **110**(18): p. 5982-5986.

202. Ratkova, E.L., et al., *An Accurate Prediction of Hydration Free Energies by Combination of Molecular Integral Equations Theory with Structural Descriptors.* Journal of Physical Chemistry B, 2010. **114**(37): p. 12068-12079.

203. Palmer, D.S., et al., *Towards a universal method for calculating hydration free energies: a 3D reference interaction site model with partial molar volume correction.* Journal of Physics-Condensed Matter, 2010. **22**(49): p. 492101.

204. Freedman, H., et al., *Improving the performance of the coupled reference interaction site model-hyper-netted chain (RISM-HNC)/Simulation method for free energy of solvation.* Journal of Physical Chemistry B, 2008. **112**(8): p. 2340-2348.

205. Pratt, L.R., *Contact Potentials of Solution Interfaces - Phase-Equilibrium and Interfacial Electric-Fields.* Journal of Physical Chemistry, 1992. **96**(1): p. 25-33.

206. Lamoureux, G. and B. Roux, *Absolute hydration free energy scale for alkali and halide ions established from simulations with a polarizable force field.* Journal of Physical Chemistry B, 2006. **110**(7): p. 3308-3322.

207. Schmid, R., A.M. Miah, and V.N. Sapunov, *A new table of the thermodynamic quantities of ionic hydration: values and some applications (enthalpy-entropy compensation and Born radii).* Physical Chemistry Chemical Physics, 2000. **2**(1): p. 97-102.

208. Marcus, Y., *A simple empirical-model describing the thermodynamics of hydration of ions of widely varying charges, sizes, and shapes.* Biophysical Chemistry, 1994. **51**(2-3): p. 111-127.

209. Leung, K., *Surface Potential at the Air−Water Interface Computed Using Density Functional Theory.* The Journal of Physical Chemistry Letters, 2009. **1**: p. 496.

210. Jensen, K.P. and W.L. Jorgensen, *Halide, ammonium, and alkali metal ion parameters for modeling aqueous solutions.* Journal of Chemical Theory and Computation, 2006. **2**(6): p. 1499-1509.

211. Fawcett, W.R., *Thermodynamic parameters for the solvation of monatomic ions in water.* Journal of Physical Chemistry B, 1999. **103**(50): p. 11181-11185.

212. Sciortino, F., A. Giacometti, and G. Pastore, *A numerical study of one-patch colloidal particles: from square-well to Janus.* Physical Chemistry Chemical Physics, 2010. **12**: p. 11869.

213. Fiocco, D., G. Pastore, and G. Foffi, *Effective Forces in Square Well and Square Shoulder Fluids.* Journal of Physical Chemistry B, 2010. **114**: p. 12085.

214. Hickl, P., et al., *Interaction of block copolymer micelles as probed by small angle neutron and by small angle X-ray scattering.* Colloid and Polymer Science, 1997. **275**: p. 1027.

215. Duda, Y., *Square-well fluid modelling of protein liquid-vapor coexistence.* Journal of Chemical Physics, 2009. **130**: p. 116101.

216. Young, T.M. and C.J. Roberts, *Structure and thermodynamics of colloidal protein cluster formation: Comparison of square-well and simple dipolar models.* Journal of Chemical Physics, 2009. **131**: p. 125104.

217. Barker, J.A. and D. Henderson, *What is "liquid"? Understanding the states of matter.* Review of Modern Physics, 1976. **48**: p. 587.

218. Barker, J.A. and D. Henderson, *Perturbation Theory and Equation of State for Fluids: The Square-Well Potential.* Journal of Chemical Physics, 1967. **47**: p. 2856.

219. Espindola-Heredia, R., F.d. Rio, and A. Malijevsky, *Optimized equation of the state of the square-well fluid of variable range based on a fourth-order free-energy expansion.* Journal of Chemical Physics, 2009. **130**: p. 024509.

220. Zhou, S., *Structure of a Confined Square-Well Fluid.* Journal of Physical Chemistry B, 2003. **107**: p. 3585.

221. Gil-Villegas, A., F. del Río, and A.L. Benavides, *Deviations from corresponding-states behavior in the vapor-liquid equilibrium of the square-well fluid.* Fluid Phase Equilibria 1996. **119**: p. 97.

222. Benavides, A.L., et al., *Thermodynamic and structural properties of confined discrete-potential fluids.* Journal of Chemical Physics, 2006. **125**: p. 204715.

223. Baxter, R.J., *Percus--Yevick Equation for Hard Spheres with Surface Adhesion.* Journal of Chemical Physics, 1968. **49**: p. 2770.

224. Nezbeda, I., *Percus-Yevick theory for the system of hard spheres with a square-well attraction.* Czechoslovak Journal of Physics, 1977. **27**: p. 247.

225. Yuste, S.B. and A. Santos, *A model for the structure of square-well fluids.* Journal of Chemical Physics, 1994. **101**: p. 2355.

226. Malijevsky, A., S.B. Yuste, and A. Santos, *How ``sticky'' are short-range square-well fluids?* Journal of Chemical Physics, 2006. **125**: p. 074507.

227. Cardenas, M. and M.P. Tosi, *Structure of partly quenched square-well fluids.* Physica. B, 1996. **222**: p. 143.

228. Henderson, D., W.G. Madden, and D.D. Fitts, *Monte Carlo and hypernetted chain equation of state for the square-well fluid.* Journal of Chemical Physics, 1976. **64**: p. 5026.

229. Dubinin, N.E., V.V. Filippov, and N.A. Vatolin, *Structure and thermodynamics of the one- and two-component square-well fluid.* Journal of Non-Crystalline Solids 2007. **353**: p. 1798.

230. Bergenholtz, J., et al., *HMSA integral equation theory for the square-well fluid.* Molecular Physics, 1996. **87**: p. 331.

231. Guillen-Escamilla, I., M. Chavez-Paez, and R. Castaneda-Priego, *Structure and thermodynamics of discrete potential fluids in the OZ-HMSA formalism.* Journal of Physics-Condensed Matter, 2007. **19**: p. 086224.

232. Scholl-Paschinger, E., A.L. Benavides, and R. Castaneda-Priego, *Vapor-liquid equilibrium and critical behavior of the square-well fluid of variable range: A theoretical study.* Journal of Chemical Physics, 2005. **123**: p. 234513.

233. Sharma, R.V. and K.C. Sharma, *The structure factor and the transport properties of dense fluids having molecules with square well potential, a possible generalization.* Physica. A, 1977. **89**: p. 213.

234. Andersen, H.C. and D. Chandler, *Optimized Cluster Expansions for Classical Fluids. I. General Theory and Variational Formulation of the Mean Spherical Model and Hard Sphere Percus-Yevick Equations.* Journal of Chemical Physics, 1972. **57**: p. 1918.

235. Lang, A., et al., *Structure and thermodynamics of square-well and square-shoulder fluids.* Journal of Physics-Condensed Matter, 1999. **11**: p. 10143.

236. Tang, Y. and B.C.-Y. Lu, *An analytical analysis of the square-well fluid behaviors.* Journal of Chemical Physics, 1994. **100**: p. 6665.

237. Travalloni, L., et al., *Thermodynamic modeling of confined fluids using an extension of the generalized van der Waals theory.* Chemical Engineering Science, 2010. **65**: p. 3088.

238. Denton, A.R. and H. Lowen, *The influence of short-range attractive and repulsive interactions on the phase behaviour of model colloidal suspensions.* Journal of Physics-Condensed Matter, 1997. **9**: p. 8907.

239. van Swol, F. and J.R. Henderson, *Wetting and drying transitions at a fluid-wall interface: Density-functional theory versus computer simulation.* Physical Review A, 1989. **40**: p. 2567.

240. Evans, R., J.R. Henderson, and R. Roth, *Nonanalytic curvature contributions to solvation free energies: Influence of drying.* Journal of Chemical Physics, 2004. **121**: p. 12074.

241. Roth, R. and K.M. Kroll, *Capillary evaporation in pores.* Journal of Physics-Condensed Matter, 2006. **18**: p. 6517.

242. van Swol, F. and J.R. Henderson, *Wetting and drying transitions at a fluid-wall interface. Density-functional theory versus computer simulation. II.* Physical Review A, 1991. **43**: p. 2932.

243. Singh, J.K., D.A. Kofke, and J.R. Errington, *Surface tension and vapor--liquid phase coexistence of the square-well fluid.* Journal of Chemical Physics, 2003. **119**: p. 3405.

244. Tang, Y., *First-order mean spherical approximation for inhomogeneous fluids.* Journal of Chemical Physics, 2004. **121**: p. 10605.

245. Mi, J., et al., *Prediction of phase behavior of nanoconfined Lennard-Jones fluids with density functional theory based on the first-order mean spherical approximation.* Journal of Chemical Physics, 2006. **124**: p. 144709.

246. Tang, Y., Y.-Z. Lin, and Y.-G. Li, *First-order mean spherical approximation for attractive, repulsive, and multi-Yukawa potentials.* Journal of Chemical Physics, 2005. **122**: p. 184505.

247. Yu, Y.-X. and L. Jin, *Thermodynamic and structural properties of mixed colloids represented by a hard-core two-Yukawa mixture model fluid: Monte Carlo simulations and an analytical theory.* Journal of Chemical Physics, 2008. **128**: p. 014901.

248. Mi, J., Y. Tang, and C. Zhong, *Theoretical study of Sutherland fluids with long-range, short-range, and highly short-range potential parameters.* Journal of Chemical Physics, 2008. **128**: p. 054503.

249. Tang, Y., *An accurate theory for the square-well potential: from long to short well width.* Molecular Physics, 2008. **106**: p. 2431.

250. Stewart, M.C. and R. Evans, *Wetting and drying at a curved substrate: Long-ranged forces.* Physical Review E, 2005. **71**: p. 011602.

251. Orea, P., et al., *Liquid--vapor interface of square-well fluids of variable interaction range.* Journal of Chemical Physics, 2004. **120**(24): p. 11754.

252. Henderson, J.R. and F.v. Swol, *Grand potential densities of wall--liquid interfaces approaching complete drying.* Journal of Chemical Physics, 1988. **89**: p. 5010.

253. Ebner, C., W.F. Saam, and D. Stroud, *Density-functional theory of simple classical fluids. I. Surfaces.* Physical Review A, 1976. **14**: p. 2264.

254. Lipowsky, R., et al., *Wetting, budding, and fusion-morphological transitions of soft surfaces.* Journal of Physics-Condensed Matter, 2005. **17**(31): p. S2885-S2902.

255. Sullivan, D.E., D. Levesque, and J.J. Weis, *Structure of a simple fluid near a wall. II. Comparison with Monte Carlo.* Journal of Chemical Physics, 1980. **72**(2): p. 1170-1174.

256. Huang, D.M. and D. Chandler, *Cavity formation and the drying transition in the Lennard-Jones fluid.* Physical Review E, 2000. **61**(2): p. 1501-1506.

257. Ashbaugh, H.S., *Blowing bubbles in Lennard-Jonesium along the saturation curve.* Journal of Chemical Physics, 2009. **130**(20): p. Artn 204517.

258. Oleinikova, A. and I. Brovchenko, *Effect of a fluid-wall interaction on a drying layer.* Physical Review E, 2007. **76**(4): p. 041603.

259. Hummer, G. and S. Garde, *Cavity expulsion and weak dewetting of hydrophobic solutes in water.* Physical Review Letters, 1998. **80**(19): p. 4193-4196.

260. Rasaiah, J.C., S. Garde, and G. Hummer, *Water in nonpolar confinement: From nanotubes to proteins and beyond.* Annual Review of Physical Chemistry, 2008. **59**: p. 713-740.

261. Weeks, J.D., K. Katsov, and K. Vollmayr, *Roles of Repulsive and Attractive Forces in Determining the Structure of Nonuniform Liquids: Generalized Mean Field Theory.* Physical Review Letters, 1998. **81**(20): p. 4400.

262. Rane, K.S., V. Kumar, and J.R. Errington, *Monte Carlo simulation methods for computing the wetting and drying properties of model systems.* Journal of Chemical Physics, 2011. **135**(23): p. 234102.

263. Wu, J., *Solvation of a Spherical Cavity in Simple Liquids: Interpolating between the Limits.* Journal of Physical Chemistry B, 2009. **113**(19): p. 6813-6818.

264. Henderson, J.R. and F. van Swol, *Fluctuation phenomena at a first-order phase transition.* Journal of Physics: Condensed Matter, 1990. **2**: p. 4537-4542.

265. Nijmeijer, M.J.P., et al., *Determination of the Location and Order of the Drying Transition with a Molecular-Dynamics Simulation.* Physical Review B, 1991. **44**(2): p. 834-837.

266. Xiao, C. and J.S. Rowlinson, *Drying Transition at a Square-Well Wall.* Molecular Physics, 1994. **83**(6): p. 1299-1302.

267. Evans, R., R. Roth, and P. Bryk, *Wetting at curved substrates: Non-analytic behavior of interfacial properties.* Europhysics Letters, 2003. **62**(6): p. 815-821.

268. Henderson, J.R., *Solvation of a solvophobic sphere.* Journal of Chemical Physics, 2002. **116**(12): p. 5039-5045.

269. Kuipersa, J. and E.M. Blokhuis, *Wetting and drying transitions in mean-field theory: Describing the surface parameters for the theory of Nakanishi and Fisher in terms of a microscopic model.* Journal of Chemical Physics, 2009. **131**(4): p. 044702.

270. Teshigawara, R. and A. Onuki, *Predrying transition on a hydrophobic surface: Statics and dynamics.* Physical Review E, 2011. **84**(4): p. Artn 041602.

271. Gelfand, M.P. and R. Lipowsky, *Wetting on cylinders and spheres.* Physical Review B, 1987. **36**(16): p. 8725.

272. Tang, Z.X., L.E. Scriven, and H.T. Davis, *Density-Functional Perturbation-Theory of Inhomogeneous Simple Fluids.* Journal of Chemical Physics, 1991. **95**(4): p. 2659-2668.

273. Sweatman, M.B., *Weighted density functional theory for simple fluids: Supercritical adsorption of a Lennard-Jones fluid in an ideal slit pore.* Physical Review E, 2001. **63**(3): p. 031102

274. Henderson, D. and L. Blum, *Some exact results and the application of the mean spherical approximation to charged hard spheres near a charged hard wall* Journal of Chemical Physics, 1978. **69**: p. 5441-9.

275. Bruin, C., M.J.P. Nijmeijer, and R.M. Crevecoeur, *Finite-Size Effects on Drying and Wetting Transitions in a Molecular-Dynamics Simulation.* Journal of Chemical Physics, 1995. **102**(19): p. 7622-7631.

276. Chandler, D., *Introduction to modern statistical mechanics.* 1987, New York: Oxford University Press. xiii, 274 p.

277. Nakanishi, H. and M.E. Fisher, *Multicriticality of Wetting, Pre-Wetting, and Surface Transitions.* Physical Review Letters, 1982. **49**(21): p. 1565-1568.

278. Yin, Y. and A.P. Alivisatos, *Colloidal nanocrystal synthesis and the organic-inorganic interface.* Nature, 2005. **437**(7059): p. 664-670.

279. Burda, C., et al., *Chemistry and properties of nanocrystals of different shapes.* Chemical Reviews, 2005. **105**(4): p. 1025-1102.

280. König, P.M., R. Roth, and K.R. Mecke, *Morphological Thermodynamics of Fluids: Shape Dependence of Free Energies.* Physical Review Letters, 2004. **93**(16): p. 160601.

281. Hansen-Goos, H., et al., *Solvation of Proteins: Linking Thermodynamics to Geometry.* Physical Review Letters, 2007. **99**(12): p. 128101.

282. Roth, R. and R. Evans, *The depletion potential in non-additive hard-sphere mixtures.* Europhysics Letters, 2001. **53**(2): p. 271-277.

283. Oettel, M., et al., *Depletion interaction of two spheres-Full density functional theory vs. morphometric results.* Europhysics Letters, 2009. **85**(3).

284. Kodama, R., et al., *Morphometric approach to thermodynamic quantities of solvation of complex molecules: Extension to multicomponent solvent.* Journal of Chemical Physics, 2011. **135**(4).

285. Dzubiella, J., *How Interface Geometry Dictates Water's Thermodynamic Signature in Hydrophobic Association.* Journal of Statistical Physics, 2011: p. 1-13.

286. Mecke, K.R., *Integral geometry in statistical physics.* International Journal of Modern Physics B, 1998. **12**(9): p. 861-899.

287. Hadwiger, H., *Vorlesungen über Inhalt, Oberfläche und Isoperimetrie* 1957, Berlin, Germany: Springer.

288. Hansen-Goos, H., *Entropic Forces on Bio-Molecules*. 2008, University of Stuttgart: Stuttgart.

289. Chen, B., *A Simplified Elementary Proof of Hadwiger's Volume Theorem.* Geometriae Dedicata, 2004. **105**(1): p. 107-120.

290. Mecke, K.R., T. Buchert, and H. Wagner, *ROBUST MORPHOLOGICAL MEASURES FOR LARGE-SCALE STRUCTURE IN THE UNIVERSE.* Astronomy and Astrophysics, 1994. **288**(3): p. 697-704.

291. Hendrik, H.-G. and R. Roland, *Density functional theory for hard-sphere mixtures: the White Bear version mark II.* Journal of Physics: Condensed Matter, 2006. **18**(37): p. 8413.

292. Carnahan, N.F. and K.E. Starling, *EQUATION OF STATE FOR NONATTRACTING RIGID SPHERES.* Journal of Chemical Physics, 1969. **51**(2): p. 635-&.

293. Henderson, J.R., *Potential-Distribution Theorem Mechanical Stability and Kirkwood Integral-Equation.* Molecular Physics, 1983. **48**(4): p. 715-717.

294. Marmur, A. and B. Krasovitski, *Line Tension on Curved Surfaces: Liquid Drops on Solid Micro- and Nanospheres.* Langmuir, 2002. **18**(23): p. 8919-8923.

295. Cortis, C.M., P.J. Rossky, and R.A. Friesner, *A three-dimensional reduction of the Ornstein-Zernicke equation for molecular liquids.* Journal of Chemical Physics, 1997. **107**(16): p. 6400-6414.

296. Gendre, L., R. Ramirez, and D. Borgis, *Classical density functional theory of solvation in molecular solvents: Angular grid implementation.* Chemical Physics Letters, 2009. **474**(4-6): p. 366-370.

297. Refson, K., *Moldy User's Manual*. 2003.

298. Gray, C.G. and K.E. Gubbins, *Theory of Molecular Fluids: Fundamentals* Vol. Volume 1. 1984, Oxford: Oxford University press.

299. Bopp, P.A., A.A. Kornyshev, and G. Sutmann, *Frequency and wave-vector dependent dielectric function of water: Collective modes and relaxation spectral.* Journal of Chemical Physics, 1998. **109**(5): p. 1939-1958.

300. Yu, Y.-X., et al., *Structures and correlation functions of multicomponent and polydisperse hard-sphere mixtures from a density functional theory.* The Journal of Chemical Physics, 2004. **121**(3): p. 1535-1541.